Synthesizing Nanomaterials for Energy Applications: Probing Activity as a Function of Composition, Morphology and Purity to Address Key Issues Associated with Fuel Cells and Li-Ion Batteries

A Dissertation Presented

by

Megan Elaine Scofield

to

The Graduate School

in Partial Fulfillment of the

Requirements

for the Degree of

Doctor of Philosophy

in

Chemistry

Stony Brook University

August 2016

Stony Brook University

The Graduate School

Megan Elaine Scofield

We, the dissertation committee for the above candidate for the

Doctor of Philosophy degree, hereby recommend

acceptance of this dissertation.

Dr. Stanislaus S. Wong – Dissertation Advisor
Professor, Department of Chemistry

Dr. Michael White - Chairperson of Defense
Professor, Department of Chemistry

Dr. Esther Takeuchi - Third Member of Academic Committee
Professor, Department of Chemistry

Dr. Radoslav Adzic – Outside Member
Adjunct Professor, Department of Materials Science and Engineering

This dissertation is accepted by the Graduate School

Nancy Goroff

Interim Dean of the Graduate School

Abstract of the Dissertation

Synthesizing Nanomaterials for Energy Applications: Probing Activity as a Function of Composition, Morphology and Purity to Address Key Issues Associated with Fuel Cells and Li-Ion Batteries

by

Megan Elaine Scofield

Doctor of Philosophy

in

Chemistry

Stony Brook University

2016

With the growing need to find alternative clean energy sources to fossil fuels, research into developing efficient fuel cells and batteries stands at the forefront of this grand effort. However, before mass commercialization, fundamental key issues need to be addressed. For example, fuel cells are subject to high catalyst costs and poor durability of the underlying carbon support. As a way to alleviate these issues, we have synthesized ultrathin one-dimensional (1D) alloy nanowires to probe the effect of composition, purity, and one-dimensionality upon the observed overall activity, performance, and durability.

In terms of chemical composition, crystalline ultrathin PtM alloy nanowires (NWs) (‘M’ = Fe, Co, Ru, Cu, and Au) were generated and subsequently evaluated for the hydrogen oxidation reaction (HOR). Additionally, ternary-based catalysts were synthesized (PtRuFe) in order to analyze how chemical composition influences CO tolerance as well as methanol oxidation reaction (MOR) and formic acid oxidation reaction (FAOR) activities. In both cases, we utilized a sustainably mild, ambient wet-synthesis method for the fabrication of chemically pure and crystalline systems in order to fabricate ultrathin, homogeneous alloy NWs. Moreover, in these studies, our NW systems exhibit favorable synergistic electronic effects with respect to controls.

To address another fundamental issue associated with the durability of fuel cells, we have synthesized various metal oxide and perovskite materials of different sizes and chemical compositions as supports for Pt nanoparticles (NPs). Specifically, we have demonstrated favorable metal support interactions between the Pt NPs and the $SrRuO_3$ NP supports, which lead to increased MOR activity as compared with not only the other metal oxide supports tested but also the commercial Pt NP/C standard.

In terms of Li-ion batteries, $LiFePO_4$ materials have become increasingly popular as a cathode material due to the many benefits they possess including thermal stability, durability, low cost, and long life span. However, to broaden the general appeal of this material for practical electrochemical applications, it was useful to develop a relatively mild, reasonably simple synthesis method of this cathode material. We describe a generalizable, 2-step methodology of sustainably synthesizing $LiFePO_4$ by incorporating a template-based, ambient, surfactantless, seedless, U-tube protocol in order to generate size and morphologically tailored, crystalline, phase-pure nanowires. Specifically, we demonstrate for the first time experimentally that the Fe–O3 chemical bond plays an important role in determining the overall conductivity of the material, an assertion which is further supported by recent “first-principles” calculations.

This dissertation is dedicated to my family and all that supported me during my period of study.

Table of Contents

List of Figures/Tables/Illustrations

List of Tables

List of Abbreviations

ECSA	Active electrochemical surface area
$\mathrm{H}_{\mathrm{ads}}$	Adsorbed hydrogen
$\mathrm{OH}_{\mathrm{ad}}$	Adsorbed hydroxide
$\mathrm{O}_{\mathrm{ads}}$	Adsorbed oxygen
AAEM	Alkaline anion exchange membrane
AFC	Alkaline fuel cell
θ	Angle
AAS	Atomic absorption spectroscopy
c	BET constant
$\mathrm{E}_{\mathrm{Binding}}$	Binding Energy
BET	Brunauer–Emmett–Teller
C_{H}	Capacitance associated with charges held at OHP
C_{dl}	Capacitance in the double layer
CB	Carbon black
CNT	Carbon nanotube
E_{cell}	Cell current density
cm^2	Centimeter squared
CTAB	Cetyltrimethylammonium bromide
$\Delta\mathrm{H}$	Change in Enthalpy
$\Delta\mathrm{S}$	Change in Entropy
T	Crystallite size
dec	Decade
°C	Degrees Celsius
$\mathrm{H}_{\mathrm{des}}$	Desorbed hydrogen
C_{d}	Differential capacitance
i_D	Diffusion limited current
K	Dimensionless shape vector of the crystallite size
DAFC	Direct alcohol fuel cell
DMFC	Direct methanol fuel cell
C_{H}	Double layer resistance from the Stern layer
$\mathrm{C}_{\mathrm{diff}}$	Diffusion layer capacitance
$	Dollar
EELS	Electron energy loss spectroscopy
eV	electron volt
EDAX	Energy dispersive analysis of X-rays
$\mathrm{E}_{\mathrm{Kinetic}}$	Energy of the electrons
p	Equilibrium pressure at the specific temperature for molecule adsorption
i_0	Exchange current density
fcc	Face-centered cubic
F	Faraday’s constant
FAOR	Formic acid oxidation reaction
R	Gas constant
GDL	Gas diffusion layer
ΔG	Gibbs free energy

g	Gram
E_1	Heat of adsorption for the first monolayer
E_L	Heat of liquefaction of all other layers
HRTEM	High-resolution transmission electron microscopy
HOR	Hydrogen oxidation reaction
HBE	Hydrogen binding energy
ICP	Inductively coupled plasma
IR	Infrared Spectroscopy
IHP	Inner Helmholz plane
ISS	Inner shell spectroscopy
ϕ	Instrument work function
d	Inter-plane distance
kWh	Killowatt hour
kJ	Kilojoules
i_k	Kinetic current
LIB	Li-ion battery
LSV	Linear sweep voltammogram
β	Line broadening measured at half intensity
L	Liter
MA	Mass activity
W_{e1}	Maximum electrical work
i	Measured current
MEA	Membrane electrode assembly
M	Metal
$M\text{-}H_{ad}$	Metal-adsorbed hydrogen
MOR	Methanol oxidation reaction
μC	Microcoulombs
mAh/g	Milliamp hours per gram
mg	Milligram
mV	Millivolts per decade
mol	Mole
MCFC	Molten carbonate fuel cell
ML	Monolayer
υ_m	Monolayer adsorption amount
nm	Nanometer
NP	Nanoparticle
NP/C	Nanoparticles supported on carbon
NT	Nanotube
NW	Nanowire
NNI	National Nanotechnology Initiative
NSA	Near surface alloy
NHE	Normal hydrogen electrode
n	Number of electrons
1D	One-dimensional
n	Order of the diffraction peak
OHP	Outer Helmholtz Plane

ORR	Oxygen reduction reaction
PDF	Pair distribution function
%	Percent
PFSA	Perfluorosulfonic acid
PAFC	Phosphoric acid fuel cell
Pt	Platinum
η	Polarization
E	Potential
φ	Potential at the electrode/electrolyte interface
φ_0	Potential at the electrode surface
PEMFC	Proton exchange membrane fuel cell
RHE	Reversible hydrogen electrode
p_0	Saturation pressure at the specific temperature for molecule adsorption
SEM	Scanning electron microscopy
STEM	Scanning TEM
s	Second
SAED	Selected area electron diffraction
$NABH_4$	Sodium Borohydride
SEI	Solid electrolyte interphase
SOFC	Solid oxide fuel cell
J	Specific Activity
SI	System of Units
T	Temperature
TGA	Thermogravimetric analysis
3D	Three-dimensional
υ	Total gas adsorption quantity
TEM	Transmission electron microscopy
2D	Two-dimensional
H_{upd}	Under-potential deposited hydrogen
V	Volt
XRD	X-ray diffraction
XPS	X-ray photoelectron spectroscopy
λ	X-ray wavelength
0D	Zero-dimensional

Acknowledgments

First and foremost, I would like to thank Dr. Stanislaus Wong for his never-ending effort and support to push me as a PhD student and a person. His commitment to my success has been a driving force during my research career, providing significant motivation for me to become a more knowledgeable person.

I would also like to extend gratitude to my committee chair, Dr. Michael White, and my third member, Dr. Esther Takeuchi, for their comments on my research progress that have further challenged me as a PhD student and pushed me to gain a deeper knowledge. Additionally, I would also like to thank Dr. Radoslav Adzic, not only for serving as my outside member on my committee during my defense, but also for acting as a mentor and sharing his knowledge and expertise about electrochemistry with me.

I also would like to acknowledge my fellow group members, Crystal Lewis, Haiqing Liu, Lei Wang, Yuchen Zhou, Shiyu Yue, Luyao Li, and Coray McBean for their support and help during my research career, in addition to previous group members, Dr. Jonathan Patete and Dr. Christopher Koenigsmann for their guidance in the initial stages of my research career, and providing the basis for the work completed on $LiFePO_4$. Additionally, I would like to thank Dr. James Quinn and Susan Van Horn, in addition to a number of collaborators including Dr. Dong Su, Dr. Vyacheslav Volkov, Dr. Yimei Zhu, and Dr. Jing Tao for their help with microscopy and the many discussions to aid in the data interpretation; Dr. Xiao Tong for his help with the collection of XPS results; Xiaoya Wang and Dr. Feng Wang for training me to properly assemble coin cells; Yiman Zhang and Dr. Amy Marschilok for assisting in the acquisition of electrochemical results for the work conducted on $LiFePO_4$, as well as Dr. Jianming Bai and Dr. Jinkyu Han for their contribution to the collection and interpretation of high-resolution XRD results.

Furthermore, I would also like to extend a deep thanks to Dr. Miomir Vukmirovic for our beneficial discussions in the interpretation of my electrochemical data. The faculty and staff in the Chemistry Department at Stony Brook University as well as the Condensed Matter Physics Department, Chemistry Department, and Center for Functional Nanomaterials at Brookhaven National Lab have continuously supported me, and for that, I would like to thank them as well.

Finally, I would like to sincerely thank my parents, Ceil and Robert, my many siblings, Liz, Peter, Rachel, Steve, and Sarah, along with my friends for their unconditional love and support during this strenuous 5 year period. I could not have succeeded during my PhD career without their positive reinforcement and encouragement. I would also like to specifically thank Sean for his constant advocacy and reassurance, day in and day out.

Vita, Publications and/or Fields of Study

1. “Correlating the Chemical Composition of Various Pt-based Alloyed Ultrathin Nanowires with Catalytic Activity for the Hydrogen Oxidation Reaction under Alkaline Conditions” **Scofield, Megan E.**; Zhou, Yuchen; Wang, Lei; Vukmirovic, Miomir B.; Adzic, Radoslav R.; Wong, Stanislaus S. *ACS Catal.* **2016**, v. 6(6). 3895−3908.
2. “Correlating the Chemical Composition and Size of Various Metal Oxide Substrates with the Catalytic Activity and Stability of As-Deposited Pt Nanoparticles for the Methanol Oxidation Reaction” **Scofield, Megan E.;** Koenigsmann, Christopher; Bobb-Semple, Dara; Tao, Jing; Tong; Xiao; Wang, Lei; Lewis, Crystal S.; Vukmirovic, Miomir B.; Zhu, Yimei; Adzic, Radoslav R.; Wong, Stanislaus S. *Catal. Sci. Tech.* **2015**, v. 6(7). 2435-2450.
3. “Research Update: Synthesis, properties, and applications of ultrathin metallic nanowires and associated heterostructures” Liu, Haiqing; Li, Luyao; **Scofield, Megan E.**; Wong, Stanislaus S. *APL Mater.* **2015**, v. 3(8). 080701/1-080701/15.
4. “Enhanced Performance of "Flower-like" $Li_4Ti_5O_{12}$ Motifs as Anode Materials for High-Rate Lithium-Ion Batteries” Wang, Lei; Zhang, Yiman; **Scofield, Megan E.**; Yue, Shiyu; McBean, Coray; Marschilok, Amy C.; Takeuchi, Kenneth J.; Takeuchi, Esther S.; Wong, Stanislaus S. *ChemSusChem.* **2015**, v. 8(19). 3304-3313.
5. “A Concise Guide to Sustainable PEMFCs: Recent Advances in Improving both Oxygen Reduction Catalysts and Proton Exchange Membranes” **Scofield, Megan E.**; Liu, Haiqing; Wong, Stanislaus S. *Chem. Soc. Rev.* 2015, v. 44(16). 5836-5860.
6. “Ambient synthesis, characterization, and electrochemical activity of $LiFePO_4$ nanomaterials derived from Iron phosphate intermediates” Patete, Jonathan M. (equal contribution); **Scofield, Megan E.** (equal contribution); Volkov, Vyacheslav; Koenigsmann, Christopher; Zhang, Yiman; Marschilok, Amy C.; Bai, Jianming; Han, Jinkyu; Wang, Lei; Wang, Feng; Zhu, Yimei; Graetz, Jason; and Wong, Stanislaus S. *Nano Res.* 2015, v. 8(8). 2573-2594.
7. “Tailoring the Composition of Ultrathin, Ternary Alloy PtRuFe Nanowires for the Methanol Oxidation Reaction and Formic Acid Oxidation Reaction” **Scofield, Megan E.**, Koenigsmann, Christopher; Wang, Lei; Liu, Haiqing; Wong, Stanislaus S. *Energy Environ. Sci.* 2014, v. 8(1). 350-363.
8. “Polar state in freestanding strontium titanate nanoparticles” Tyson, Trevor A.; Yu, Tian; Croft, Mark; **Scofield, Megan E.**, Bobb-Semple, Dara; Tao, Jing; Jaye, Cherno; Fischer, Daniel; Wong, Stanislaus S. *Appl. Phys. Lett.* 2014, v. 105(9). 091901/1-091901/5.
9. “Designing Enhanced One-Dimensional Electrocatalysts for the Oxygen Reduction Reaction: Probing Size- and Composition-Dependent Electrocatalytic Behavior in Noble Metal Nanowires” Koenigsmann, Christopher; **Scofield, Megan E.**; Liu, Haiqing; Wong, Stanislaus S. *J. Phys. Chem. Lett.* 2012, v. 3(22). 3385-3398.

Chapter 1 - Introduction to Nanomaterials

1.1. What is Nano?

According to the International System of Units (SI), “nano” refers to a factor of 10^{-9}. According to the National Nanotechnology Initiative (NNI), a “nanomaterial” refers to a material that possesses at least 1 dimension in the nanoscale, which is 1- 100 nm. Nanoscience refers to the study of structures and materials at the nanometer scale. Nanotechnology refers to the applications of nanoscale materials across a variety of fields including biology, chemistry, physics, engineering, and so forth. Figure 1 depicts a variety of objects along with their associated sizes in order to gain a fundamental grasp of what “nano” means.

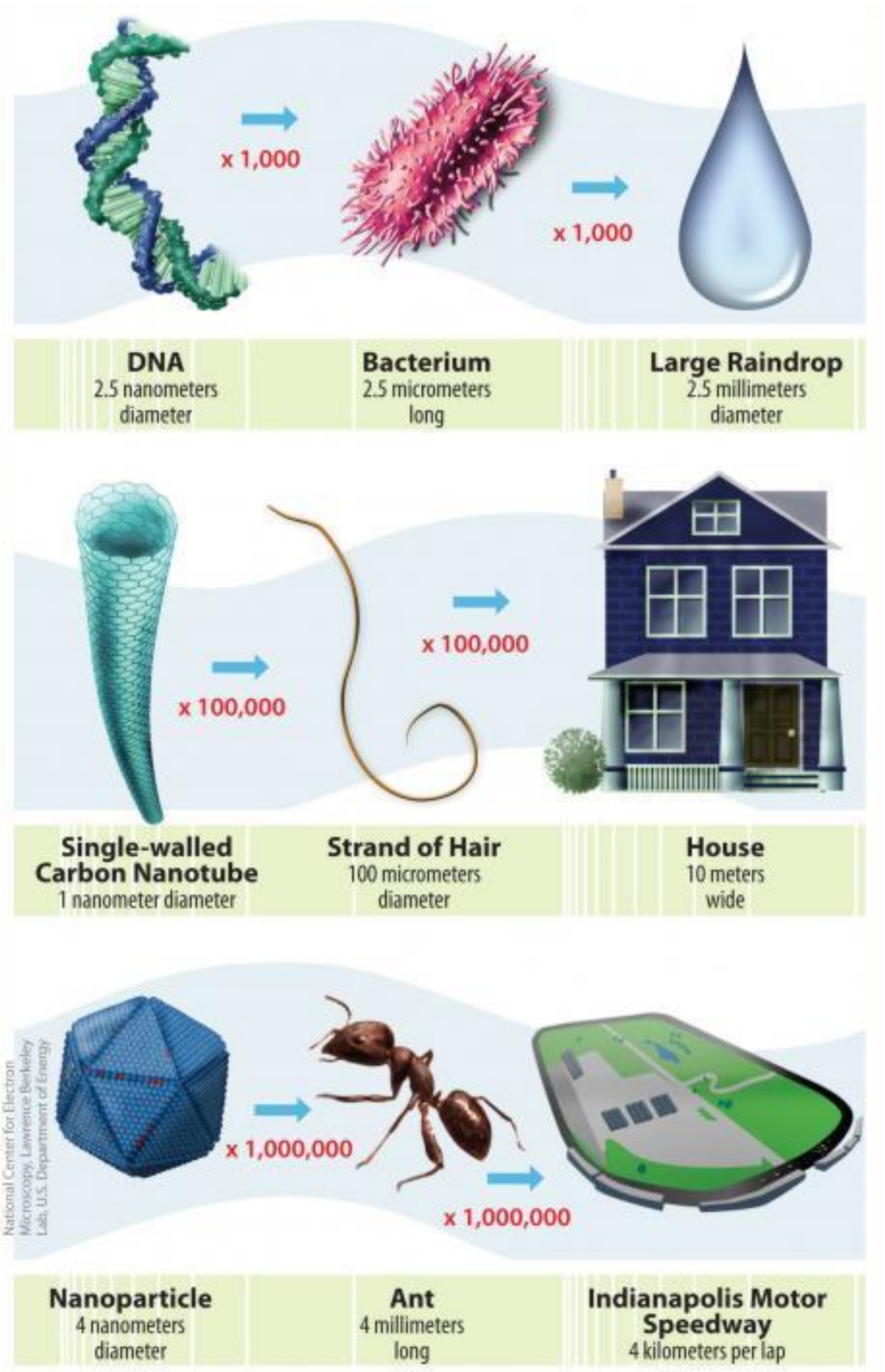

Figure 1.1. Figure including objects with their corresponding sizes. Taken from the National Nanotechnology Initiative (Nano.gov).

In recent years, nanomaterials have been explored more than ever for a number of specific reasons. Significantly, it is expected that through nanoscience, the structures of nanomaterials can be tailored so as to exhibit certain desirable properties for a range of applications. Specifically, through nanoscience, nanomaterials can be made either stronger, lighter, or more reactive, as well as can be adapted to exhibit a particular shape. A significant amount of commercial products either contain or employ nanomaterials for their production processes. Examples include (i) baseball bats in order to render them light-weight and durable, (ii) thin films on glasses in order to make then scratch-resistant or UV resistant, as well as (iii) batteries in order to increase overall power and stability. In essence, as the size of the nanomaterial changes, the properties, such as melting point, fluorescence, conductivity, reactivity, catalytic activity, and durability, can alter as well.

Another way to tailor the properties of nanomaterials is by changing their shape. Different shapes can be categorized by their dimensionality. For example, (i) nanoparticles, nanocubes, or nanopyramids, for example, are zero-dimensional (0D) nanomaterials, since all of their dimensions are confined at the nanoscale, (ii) nanowires or nanotubes are one-dimensional (1D) nanomaterials with 2 dimensions similarly restricted, (iii) nanosheets are considered as two-dimensional (2D) nanomaterials, with only 1 dimension limited, and (iv) nano-flowers or nano-urchins are three-dimensional (3D) nanomaterials, which are described by having structures resulting from and incorporating a combination of either 0D, 1D, or 2D nanomaterials. 0D and 1D materials in particular will be discussed in more detail in the sections to follow below.

Specifically, 1D nanomaterials have become a highly advantageous morphological motif as compared with 0D materials, due to their inherently increased stability, especially when employed for fuel cell applications. In part, this can be traced to the inherent asymmetry of 1D materials, which may suppress physical ripening processes as well as reduce dissolution and Ostwald ripening effects.[1, 2] Additionally, 1D materials (i) exude ‘path-directing’ effects as a result of their anisotropic shape, which are highly beneficial for electron transport applications[3] such as battery and solar applications. Moreover, the conductive properties of 1D materials can be tuned so as to either increase or decrease their overall corresponding resistivity, merely by varying their diameters.[4]

As a result, 1D nanomaterials possess a variety of beneficial attributes that should hopefully aid in solving technological issues currently affecting their 0D analogues. For example, our group[5] has previously demonstrated that 1D Pt nanowires (NWs) outperform analogous Pt nanoparticles (NPs) for ethanol oxidation, in addition to possessing lower CO stripping potentials. As stated above, 1D nanomaterials exhibit enhanced durability as compared with 0D nanomaterials, which is demonstrated in Figure 1.2. The chronoamperometry results in this Figure demonstrate enhanced stability of as-synthesized Pd NWs compared with commercial Pd NPs over a period of 1 hour.[6]

Moreover, in this thesis, our objective is to probe the effect of composition, size, and morphology of nanomaterials on activity for both fuel cells and lithium ion batteries. For example, we explore the question of how tuning the composition of ultrathin 1D Pt-based alloy nanowires affects the overall electronic structure and, in turn, governs their electrocatalytic activity. In the case of $LiFePO_4$, which is a commonly employed lithium ion battery material, we not only generate it using a facile, ambient, surfactantless synthetic method, but also examine the impact of morphology, purity, growth direction, and local coordination geometry upon the resulting electronic conductivity of the material.

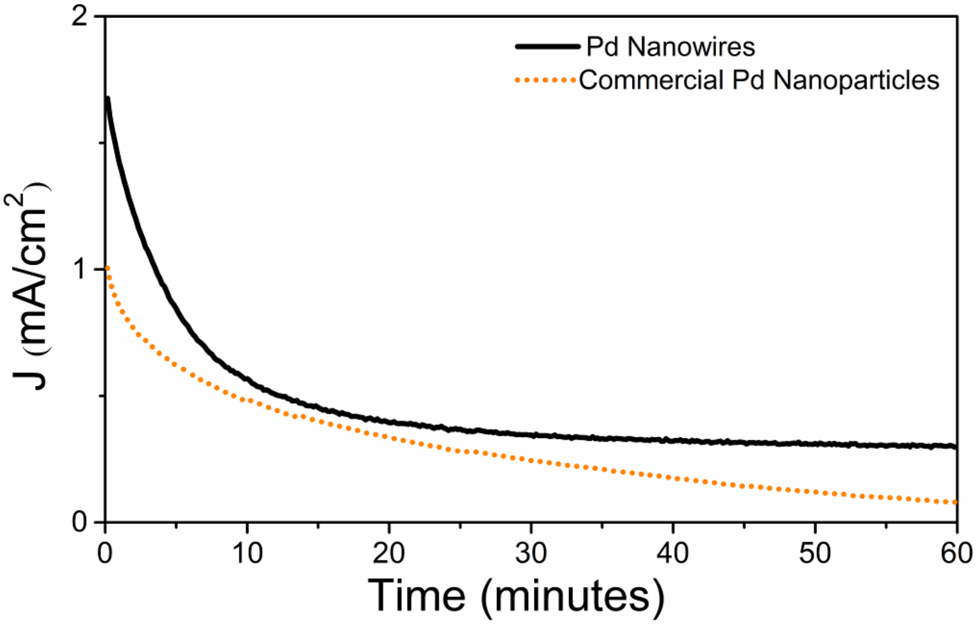

Figure 1.2. Chronoamperometry measurements for both Pd NWs and commercial Pd NPs over a period of 60 minutes, collected in an argon-saturated 0.1 M $HClO_4$ + 0.5 M HCOOH solution, obtained at a potential of 0.4 V vs RHE. Taken from Ref. 6.

1.2. Nanomaterials and their Energy-Related Applications

With the growing enthusiasm in nanomaterials due to their interesting electrical, mechanical, and optical properties as a result of the small overall size of these materials, researchers have begun to explore their function for energy-related applications, including for fuel cells, batteries, and solar cells. Both fuel cells and batteries possess anodes and cathodes at which redox reactions occur. Specifically, these redox reactions convert chemical energy to electrical energy. Moreover, batteries are considered as closed systems since energy storage and conversion occur within the battery itself, whereas fuel cells are defined more as open systems, with energy storage and conversion processes, happening separately.[7]

In this dissertation, we focus on the application of 0D and 1D nanomaterials for use in both fuel cells and Li-ion batteries. More specifically, we investigate the role of ultrathin 1D nanowires as electrocatalysts in both alkaline fuel cells (AFC) and direct methanol fuel cells (DMFC) as well as the role of metal oxide support materials as substitutes to carbon black and their overall effect upon methanol oxidation reaction (MOR) performance. Alternatively, we also consider the effect of 1D nanowires upon the performance of Li-ion batteries.

The following sections provide an introduction to fuel cells (section 1.3), with specifics pertaining to the fuel cell components utilized in this dissertation, the current status and problems associated with catalyst supports, as well as possible electrolytes that can be employed. A more in-depth description of the specific reactions investigated in this thesis, including the methanol oxidation reaction, the formic acid oxidation reaction, as well as the hydrogen oxidation reaction, along with the possible routes to tailor and optimize fuel cell catalysts can be found in sections 1.3.1 – 1.3.3, with the corresponding chemical thermodynamics associated with basic fuel cell operation discussed. Section 1.4 will address the current status of Li-ion batteries with additional information describing the structure and activity of $LiFePO_4$ nanomaterials. Section 1.5 includes the objectives of this dissertation, which incorporates a brief description of each project to provide scope and context.

1.3. Fuel Cells

With the growing demand for energy-efficient devices that possess little to no carbon footprint, fuel cells stand as a worthy option. A fuel cell is a device that electrochemically converts fuel to electricity.[7] More specifically, electrocatalysis is the study of electrode processes wherein the employed electrode material influences the specific charge-transfer reactions.[8] Many different types of fuel cells exist, including polymer electrolyte membrane fuel cells (PEMFCs), direct methanol fuel cells (DMFCs), alkaline fuel cells (AFCs), phosphoric acid fuel cells (PAFCs), molten carbonate fuel cells (MCFCs), and solid oxide fuel cells (SOFCs). With the exception of SOFCs and MCFCs, the remaining fuel cells typically employ costly precious metal catalysts, such as Pt, that render these fuel cells to be extremely expensive.

PEMFCs possess a number of advantages including the low weight and volume of the fuel cell. In addition, only oxygen, hydrogen, and water are needed for operation. Moreover, due to the low operating temperature of this type of fuel cell, it allows for quick start-ups, resulting in less damage to the fuel cell over time, thereby increasing the overall durability. Overall, these attributes enable this type of fuel cell to be suitable for transportation applications (cars, buses, trucks). However, as mentioned above, Pt is the most utilized catalyst for this type of fuel cell, effectively leading to high costs associated with fuel cell production.

DMFCs are very similar to that of PEMFCs, except for the fact that this type of fuel cell employs methanol as the fuel rather than hydrogen. Since methanol possesses a higher energy density than hydrogen, DMFCs do not experience the same fuel storage issues as PEMFCs. Moreover, DMFCs are currently used in portable devices such as cellphones and laptops.[9] A more comprehensive review will follow below.

AFCs were the first type of fuel cell to be officially commercialized, as these have been employed for space applications. AFCs are also very similar to PEMFCs except that they employ an alkaline electrolyte rather than an acidic electrolyte. However, AFCs still possess a number of challenges that need to be addressed before they can be considered to be readily commercializable. Some challenges include CO_2 poisoning, a decreased long-term durability, slow kinetics at the anode, wettability, and increased corrosion. Nevertheless, AFCs have been employed for W and kW scaled applications. A more detailed discussion of this type of fuel cell will occur below.

PAFCs use phosphoric acid as the liquid electrolyte which is contained within a silicon carbide matrix lined with Teflon. PAFCs are more tolerant to impurities as compared with the other types of fuel cells discussed above. However, they are overall less efficient at the same weight and volume, and, as a result, are large and heavy. These fuel cells are typically employed for the generation of heat and electricity as stationary devices. However, some have been utilized to power large vehicles such as buses.

MCFCs are fuel cells that utilize a molten carbonate salt mixture as the electrolyte. MCFCs operate at extremely high temperatures (600°C – 1200°C) and, as a result, can employ non-precious metal catalysts rather than expensive noble metals. Additionally, their high operating temperature allows for the conversion of fuels such as natural gas to hydrogen by a process called internal reforming, thereby making this a more cost effective system as compared with other fuel cells. However, the main disadvantage centers on the high temperature and corrosive nature of the electrolyte, thereby affecting the overall durability of the fuel cell, a parameter which is currently being investigated by many others. Moreover, MCFCs are being used for electrical utility and military applications at natural gas and coal-based power plants.[9]

SOFCs are very similar to MCFCs in that they can operate under high temperatures (< 1000°C). These systems not only reform fuel internally but remove the need for precious metal catalysts. The typical electrolyte employed in SOFCs is a hard, ceramic material that is also non-porous. This fuel cell is also the most resistant to sulfur and carbon monoxide, thereby allowing for carbon monoxide and natural gas to be employed as a potential fuel for operation. As mentioned above pertaining to MCFCs, the high temperature creates significant durability issues, in addition to slow start-ups and the need for thermal shielding. Similar to MCFCs, SOFCs tend to be used for stationary utility applications.[9] In particular, this thesis will place emphasis upon anode catalysts and support materials for both AFCs as well as DMFCs.

Components of a Fuel Cell

A fuel cell is made up of a number of components including an anode electrode, cathode electrode, ion exchange membrane, and a gas diffusion layer (GDL) material, which are all components that compose the membrane electrode assembly (MEA). The anode or the negative electrode is the electrode wherein the oxidation reaction occurs. Conversely, the cathode or the positive electrode is the location for the reduction reaction.

The ion exchange membrane exists as an ionic conductor, ultimately to provide for separation between the oxidant and fuel, thereby preventing the conduction of electrons, which subsequently travel through an external circuit. Ion exchange membranes can either be cationic or anionic. Specifically, a cationic exchange membrane possesses fixed anionic groups, allowing the transport of cations through the membrane, whereas an anionic exchange membrane is characterized by immobilized cationic groups, thereby promoting the movement of anions, i.e. the source of conductivity. The ionic groups within the membrane represent the active sites for ionic conduction. As a result, a typical polymer ion exchange membrane is highly dependent upon the associated bound and unbound water molecules at these active sites. The most commonly employed membrane was originally created by DuPont initially for space applications, known as Nafion.

The specific structure of Nafion can be found below in Figure 1.3. Nafion is a perfluorosulfonic acid (PFSA) ionomer membrane with an excellent proton conductivity of ~0.10 S/cm, when fully hydrated. However, Nafion suffers from a number of issues including (i) a decreased durability at high temperatures, as a result of an increase in the electrical resistance within the membrane, in addition to (ii) decreased conductivity at low relative humidity conditions, resulting from fewer water molecules present within the membrane itself.[10] Moreover, research has shifted to address these issues through either chemical modification of the intrinsic PFSA structure or through the synthesis of practical replacements such as polybenzimidazole- or sulfonated aromatic-based membranes.

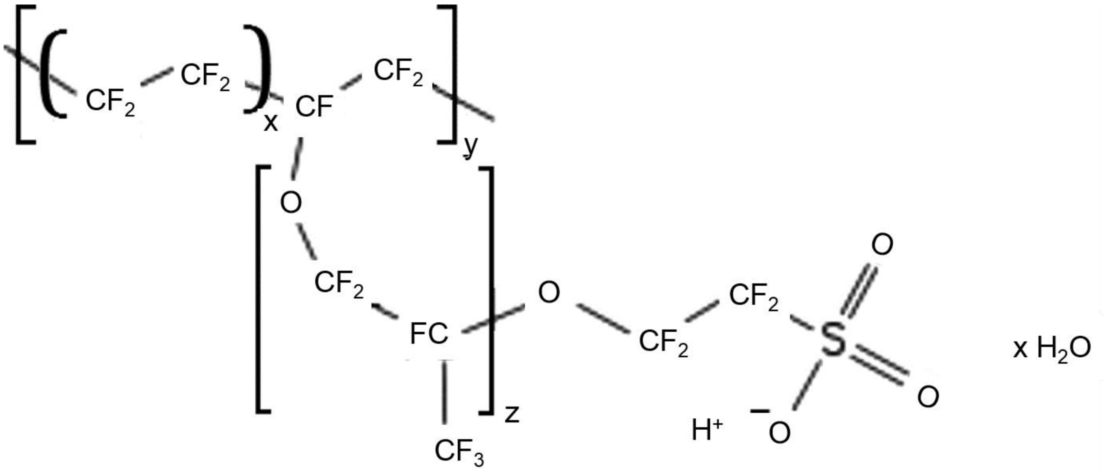

Figure 1.3. Chemical structure of Nafion. Taken from Ref. 10.

The substance promoting GDL is a porous backing material, situated typically on either side of the membrane. Moreover, the GDL is necessary to (i) diffuse gas, (ii) allow for the flow of electrons, (iii) keep water away from the electrodes, and (iv) provide for an overall mechanical support. Typically, the GDL material tends to be carbon-based, surrounded by a hydrophobic material such as Teflon, in order to prevent water from being retained within the pores of the GDL. Effective GDL materials are still under investigation, since ‘flooding’ of the electrodes is a relevant and significant problem.

Electrodes are imperative to the success of a fuel cell, since they represent the key location and denote the active sites for the specific reactions to occur. Additionally, they (i) provide for a stable interface between the electrolyte and reactant gas, (ii) conduct electrons to and from reactant sites, as well as (iii) catalyze the specific reactions.[7] The “three-phase boundary”, or the junction at which the electrolyte, reactant gas, as well as the conducting electrode meet, must be stable enough in order to ensure long-term operation and stability. Supplemental factors that influence the stability of this boundary include porosity and the wetting behavior of the electrode.

The catalyst layers reside in between the GDL material and the membrane, with one layer at the anode electrode and the other at the cathode electrode. The most commonly employed catalyst layers include the incorporation of platinum, supported onto a carbon-based material with approximately 0.5 mg needed per cm^2 of electrode area.[11] This is the result of Pt being the most effective and active catalyst for a variety of fuel cell reactions. However, Pt is sparse as well as expensive, costing approximately $34/gram.[12] A diagram indicating the average costs of each component of a fuel cell stack can be found in Figure 1.4. Moreover, based on this diagram, it is highly evident that alternatives to Pt and other costly metals need to be investigated, as the catalyst ink and application compose 34% of the fuel cell stack cost.[13]

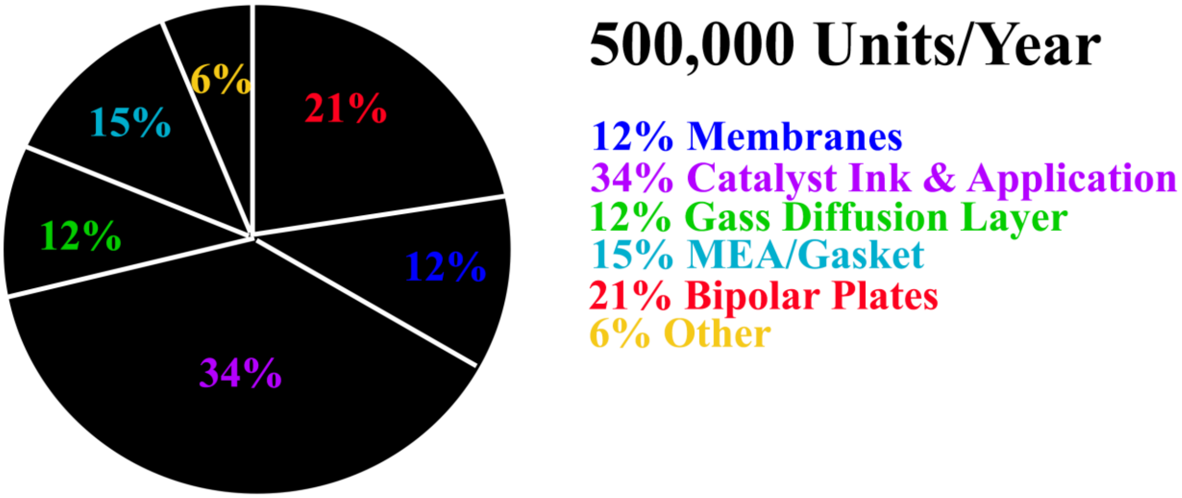

Figure 1.4. Fractional contribution of different components to a PEMFC fuel cell stack at a production rate of 500,000 units per year. Catalyst ink and application account for 34% of the total fuel cell stack cost. Adapted from Ref. 13.

Additionally, with the possibility of carbon monoxide (CO) being present either within the fuel or as a possible intermediate, there is an increased necessity to combine Pt with other, more CO-tolerant metals such as ruthenium (Ru) or tin (Sn). Therefore, there is a significant need to find low-cost, abundant alternatives that maintain similar or even improved activities and stabilities. Notwithstanding, the best performing catalysts still include Pt whether as an alloy or as a core-shell structure, or as a combination of both in order to optimize the utilization of Pt. Additionally, the specific morphology of the catalyst, such as either nanoparticles, nanowires, or nanoflowers, can optimize activity. Moreover, this thesis will specifically focus on anode-based materials, including Pt-based alloy catalysts as well as metal oxide supports.

Catalyst Supports

A conductive support material is a necessity for fuel cell catalysis not only to provide conductivity but also to promote a better dispersion of the catalyst layer, in order to otherwise optimize the surface area and active sites. Additionally, a porous support is advantageous in order to improve the gas flow. The most commonly employed support for fuel cell catalysts is carbon black (CB), due to these specific attributes. However, CB lacks thermochemical stability, leading to corrosion, and the subsequent agglomeration and decomposition of the catalyst layers.[14] That is, some have demonstrated the oxidation of carbon-based materials under conditions typical for oxygen reduction, including 0.8 – 1.2 V vs. RHE in 1 M H_2SO_4 at 65°C.[15]

Two plausible routes for the oxidation of carbon can exist, i.e. (i) reversible surface oxidation thereby generating oxygenated surface carbon, and (ii) irreversible oxidation of carbon to CO_2.[16] The former can lead to a decrease in the interaction between the Pt and the carbon surface, subsequently leading to an increase in Pt particle size. The latter gives rise to the loss of Pt, significantly decreasing the electrochemically active surface area. Additionally, CBs possesses impurities as well as recesses that trap metal nanoparticles thereby rendering them as inaccessible to the specific reactions, subsequently leading to a reduction in activity.[14] These negative attributes, in combination, can lead to a significant reduction in the overall fuel cell efficiency.

Other carbon-based materials have been explored, including carbon nanotubes, carbon nanofibers, and mesoporous carbon. Although improvements in activity have been noted for these Pt-deposited structures as compared with Pt-deposited carbon blacks, they do not fully prevent carbon oxidation. Therefore, there is a significant need to find low cost, conductive, and highly stable support materials that may also interact in a positive and favorable synergistic fashion with the catalyst layers.

Moreover, research has shifted to an investigation of non-carbon nanomaterials as support materials for fuel cell catalysts. As a part of non-carbon-containing materials, conductive oxides possess a number of benefits as compared with carbon, including high stability, resistance to corrosion, and good mechanical support, in addition to the possibility of acting either as a co-catalyst or as a means of promoting metal-support interactions.[16] For instance, a number of metal oxide materials serving as support materials have been shown to improve methanol oxidation activities as compared with the carbon-supported counterparts.[17-20]

Additionally, some metal oxide materials evince a particular bonding interaction with the as-deposited metal catalyst (group 8-10 metals) they support.[21] In particular, TiO_2 denotes the most studied and highlighted metal oxide to exhibit the precise effect known as a “strong metal-support interaction”.[21] Rather than describing the catalytic properties that result from their interactions as the term “metal-support interactions” above implies, this slightly different term indicates that it is the actual bonding interaction at the interface between the two components that results in the suppression of H_2 and CO chemisorption abilities.

A ‘strong metal-support interaction’ encompasses 2 plausible phenomena, namely an electronic and a geometric effect.[22] The geometric effect describes how metal oxide systems migrate onto the surface of the metal, ultimately creating special and localized zones of metal-metal oxide contact with enhanced properties, known as ‘encapsulation’.[21, 22] A number of metal oxide systems have displayed this effect, including vanadium oxide, niobium oxide, and manganese oxide.[23] In other cases, the metal catalyst can effectively and broadly disperse atop the metal oxide, thereby increasing its overall distribution.[21, 22] This electronic effect, in particular, is ascribed to the particular oxidation state of Ti in TiO_2, namely the Ti^{3+} oxidation state. If the titanium atom is not reduced, the “spreading” of either Pt or other metals does not visibly occur, thereby leading to agglomerations and clustering of metal atoms with reduced dispersion. In particular, both a decreased particle dispersion as well as an increased particle size can lead to reduced electrochemical surface areas, which can significantly hinder electrocatalytic performance. Therefore, it is necessary to employ or tailor catalysts so they possess small particle sizes (< 5 nm), uniform particle size distribution, as well as uniform dispersion.

However, not all metals exhibit a similar effect on reduced TiO_2. Studies conducted on Pd[24] did not display either a reduced particle size or a better dispersion, whereas Ni[25] and Ag[26] did. In addition, the metal cannot be influenced by the presence of metal oxide that is located further than a few atomic units away, as a result of screening effects. Furthermore, it has been suggested that the metal cation present within the metal oxide substrate needs to possess *d* electrons for a strong metal support interaction (i.e., the bond between the substrate and catalyst) to occur. Hence, this explains the necessity to have a TiO_2 substrate with Ti^{3+} rather than Ti^{4+}, since the latter possesses no *d* electrons for the bonding to happen. This has also shown to be true through experimental investigations, previously described and reported on.[21]

Additionally, chemical interactions between the metal particle and the metal oxide substrate can occur by 4 different methods, namely through redox reaction, alloy formation, encapsulation, or interdiffusion. The redox reaction generates an oxidized metal catalyst and a reduced metal oxide substrate. This is the most common interaction between metals and metal oxides at the interface. Alloy formation occurs when the metal overlayer forms an alloy with the cation present in the metal oxide at the interface. This interaction has been found to occur between Pt and SiO_2, Al_2O_3, and CeO_2.[27-29] The third process denotes encapsulation, wherein a small portion of a reduced metal oxide creates a thin overlayer on the metal particle.[27, 30, 31] Ultimately this process blocks active sites and leads to reduced activity. This has been observed with a number of metal particles including Pt, Rh, and Pd supported onto TiO_2 as well as CeO_2. The final case is interdiffusion, which explains either the diffusion of the metal particle into the metal oxide support or diffusion from the substrate to the metal particle.[32, 33] This leads to the formation of either interdiffusion zones or mixed ternary oxides.

Furthermore, there is a significant need to find metal oxide support materials that can facilitate a “metal-support interaction” so as to enhance the overall activity of the catalyst/substrate component. In this thesis, we evaluate the different interactions between our as-deposited Pt nanoparticles and a variety of underlying binary and ternary oxide support materials. Our results have shown that the interactions between the metal oxide support and catalyst matter significantly, as our $SrRuO_3$ supports demonstrated electron-withdrawing behavior from the Pt *d*-band. Subsequently, this bonding interaction improved the overall MOR behavior as a result of having more active sites available, i.e. less electron density present within the Pt *d*-band to bind with poisonous species such as CO. More specific details pertaining to the electronic effects found in this study and the overall impact on the electronic structures of our catalyst materials will be discussed in Chapter 5.

Electrolytes

The particular electrolyte employed within either the fuel cell or half-cell can often have a significant effect upon the particular performance of a catalyst. That is, it influences the fuel permeation rate as well as the types of catalysts chosen, in addition to the reaction rate. Moreover, with a variety of liquid electrolytes possible, these can be categorized by their pH, i.e., the presence of acidic and alkaline media. The most active metal in acidic electrolytes is Pt, with other noble metals following in activity. Due to the need to employ Pt, the overall cost of the catalyst and fuel cell can increase drastically. Moreover, with the employment of acidic electrolytes, a serious problem associated with the adsorption of anions present in the acid themselves occurs.[34] Moreover, it has been shown that the degree of coverage of ions within the electrolyte occurs in the following order: $ClO_4^- < SO_4^{-2} < NO_3^-$, as a result of their binding energy.[35] Additionally, achieved current densities in H_2SO_4 media are often less than that in $HClO_4$ due to the adsorption of sulfate ions.[36, 37] As well, it has been demonstrated that whereas sulfate ions specifically adsorb onto the Pt surface, perchlorate ions remain in the water double layer.[38, 39] Furthermore, one group has previously shown through electron energy loss spectroscopy that the sulfur atom within the (bi)sulfate ion contains more charge density as compared with the chlorine in perchlorate, thereby resulting in a larger "back-donation".[39, 40]

The use of alkaline media possesses a number of advantages compared to acidic media. In particular, metals other than Pt, specifically non-noble metals, can be as active as Pt in alkaline media.[41-45] This is due to the fact that the kinetics associated with Pt are 2 orders of magnitude slower for the anode reaction. As compared with acidic electrolyte, a minimal amount of poisoning occurs in alkaline media.[34, 46] Additionally, there is a diminished degree of degradation and corrosion of Pt-based and especially non-precious metal-based catalysts, due to the enhanced stability of non-noble metals within alkaline media, in addition to a general reduction in the amount of deterioration inherent to the overall fuel cell configuration.[47, 48] However, a serious drawback that is still under investigation is associated with the carbonation of the solution, which ultimately lowers the pH as well as decreases the current density.[41]

1.3.1. Direct Methanol Fuel Cells

Direct methanol fuel cells (DMFC) use methanol as the fuel source at the anode rather than hydrogen, with a DMFC diagram found in Figure 1.5.

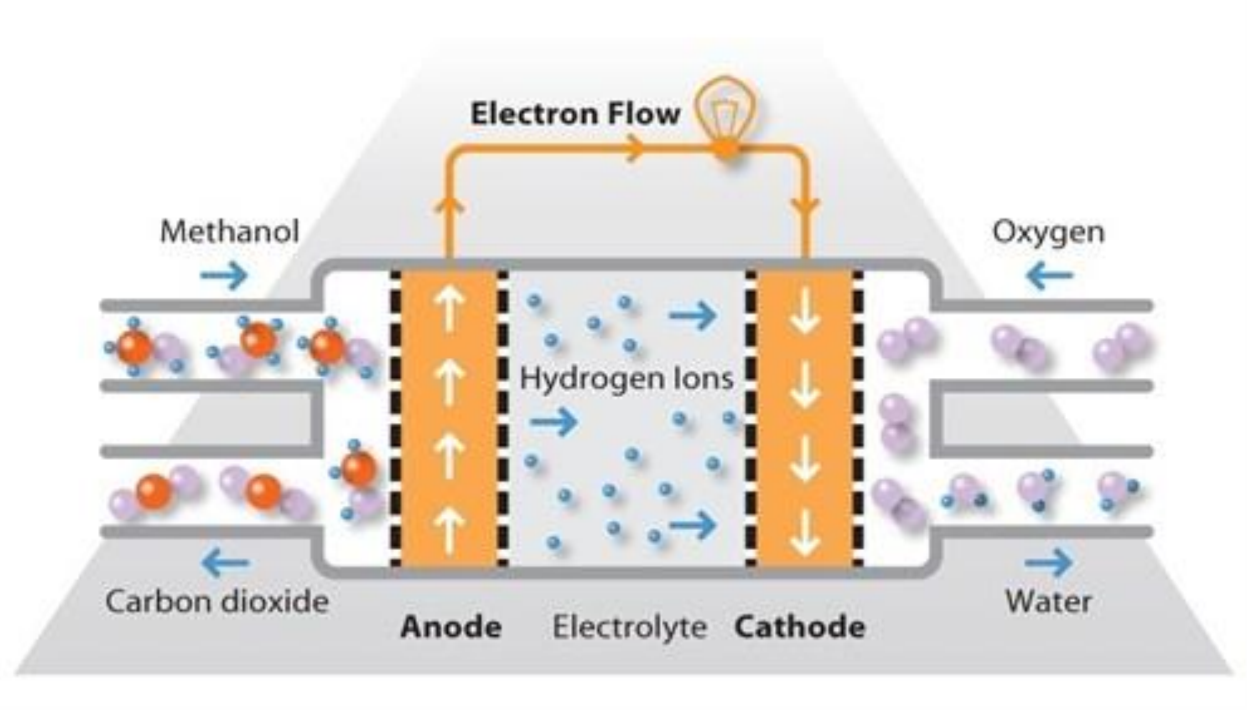

Figure 1.5. Schematic of a direct methanol fuel cell. Methanol is oxidized at the anode as the fuel, with hydrogen ions passing through the membrane to the cathode, in which oxygen reduction occurs, thereby generating water as the product. Moreover, electrons produced during the methanol oxidation reaction travel through an external circuit to the cathode to participate in the oxygen reduction reaction. Taken from fuelcelltoday.com.

The employment of either methanol or other alcohol-based fuels is significantly advantageous as compared with hydrogen due to the increased energy densities of those materials. For instance, methanol possesses an average energy density of 4.3 kWh/L, whereas hydrogen has an energy density of 2.4×10^{-4} kWh/L.[49] This is necessary for commercialization, since hydrogen storage represents a substantial problem inhibiting forward progress.

State-of-the-art electrocatalysts usually employ platinum nanoparticles at the cathode and platinum-ruthenium alloy nanoparticles at the anode, with both physisorbed onto carbon supports. Commercial electrocatalysts usually possess diameters of < 5 nm, in order to increase their surface area and to reduce the overall amount of precious metals employed, due to their high costs. However, DMFCs not only possess larger overpotentials for MOR as well as low currents, but also require a significantly larger anode catalyst loading, with typical loadings between 2 – 8 mg/cm^2.[50] Therefore, there is a driving force to find alternative catalysts to Pt with lower onset potentials and higher activities for methanol oxidation.

The overall reaction for DMFCs as well as the specific reactions at the anode and cathode half-cells are shown below in Reactions [1.1-1.3]. The methanol oxidation reaction (MOR), which can be found in Reaction [1.2], is a relatively complex 6 electron process associated with 2 plausible pathways involving the generation of formic acid, formaldehyde, or CO, with the indirect pathway (i.e., the CO-generated pathway), shown below in Figure 1.6 with red arrows. Additionally, formaldehyde can also be produced as an intermediate, highlighted by the blue arrows on top, with a reaction energy of -0.35 eV at 0.5 V. Although not shown in the schematic, the formation of formaldehyde can also lead to the generation of either formate or formic acid as another possible intermediate.

The indirect pathway (CO pathway), known as the predominant pathway, requires an ensemble of 3-5 Pt atoms for this process to occur, whereas the direct pathway (formic acid or formaldehyde) requires a small cluster of 1-2 Pt atoms.[51, 52] However, with a large cluster of Pt necessary for the indirect pathway to operate, the reaction rate is significantly lowered as a result of anion adsorption (CO, SO_4, etc). Additionally, since the indirect pathway only requires 1-2 Pt atoms, this route is significantly less hindered by anion adsorption.

Overall: $CH_3OH + 3/2\ O_2 \rightarrow CO_2 + H_2O$ $E = 1.21$ V [1.1]

Anode: $CH_3OH + H_2O \rightarrow 6H^+ + CO_2 + 6e^-$ $E° = 0.02$ V [1.2]

Cathode: $3/2\ O_2 + 6H^+ + 6e^- \rightarrow 3H_2O$ $E° = 1.23$ V [1.3]

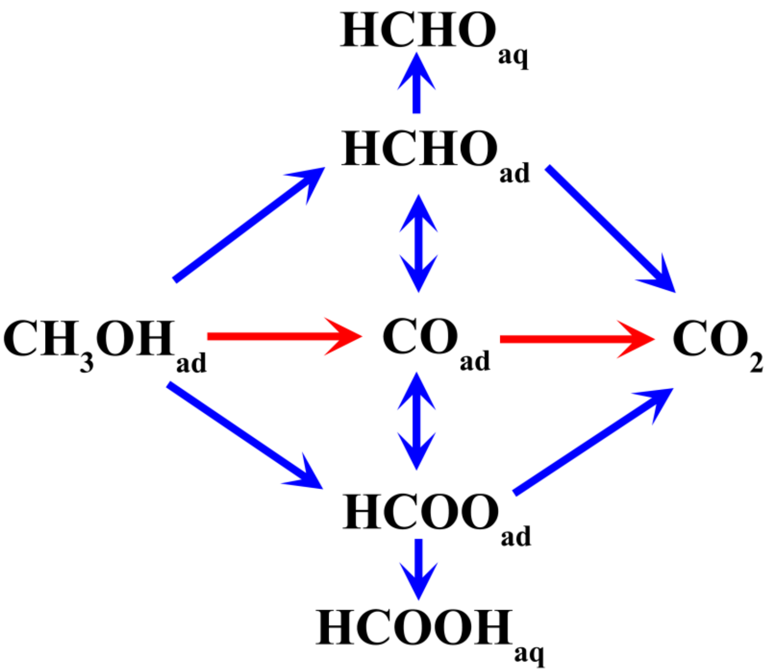

Figure 1.6. The dual pathway mechanism for the oxidation of methanol to carbon dioxide (CO_2) over Pt. The indirect pathway is highlighted by red arrows and indicates the oxidation of methanol through the carbon monoxide (CO) intermediate. The direct pathways are highlighted by blue arrows through the generation of formic acid (CHOOH) and formaldehyde (HCHO). The schematic is adapted from Ref. 52 and is based upon mechanistic steps proposed in Ref. 53.

Moreover, in the initial steps of the indirect pathway, methanol is adsorbed onto the Pt surface by a 4 electron oxidation process. The carbon is then de-hydrogenated, generating adsorbed CO with a corresponding reaction energy of -1.49 eV at 0.5 V. The removal of CO occurs very slowly due to the lack of –OH groups that would have helped to facilitate its oxidative removal from the surface. The CO essentially acts as a poisoning intermediate, thereby interfering with the MOR kinetics at low potentials since it blocks Pt active sites. However, defect sites present on the Pt surface are known to adsorb –OH groups at lower potentials, which can then help to facilitate CO oxidation.[53] Additionally, oxophilic metals can also adsorb -OH groups in order to aid in CO removal, a point which will be discussed in section 3.3. The reaction mechanism for CO removal can be found below in Reactions [1.4-1.6], which is based upon a Langmuir-Hinshelwood type reaction for the generation of CO_2.[54]

$$H_2O + * \rightarrow OH_{ads} + H^+ + e^- \quad [1.4]$$

$$CO_{ads} + OH_{ads} \rightarrow COOH_{ads} \text{ (rate-determining step)} \quad [1.5]$$

$$COOH_{ads} \rightarrow CO_2 + H^+ + e^- + 2* \qquad [1.6]$$

wherein * denotes a free surface site

Additionally, formic acid can be produced as a possible intermediate during the oxidation of methanol, otherwise known as one of the direct pathways, which can be found in Figure 1.6, as highlighted by blue arrows. Furthermore, the oxidation of formic acid can occur by 3 different pathways, i.e. the direct, indirect, and formate pathways.[55] These pathways can be found below:

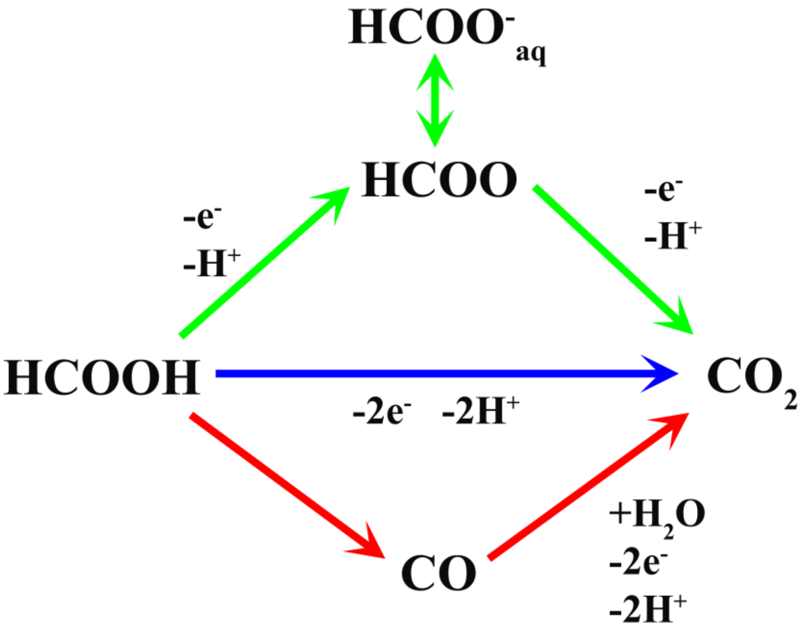

Figure 1.7. The possible reaction pathways for the oxidation of formic acid to CO_2. The direct pathway is highlighted by the blue arrow, showing the direct conversion of formic acid to CO_2. The indirect route is shown using red arrows, with the possibility of a CO intermediate. The formate pathway is represented by green arrows, with the generation of formate as an intermediate. The schematic has been adapted from Ref 52, based upon the mechanistic steps proposed in Ref. 55.

Based upon Figure 1.7, the direct route (the de-hydrogenation pathway), which is found in the middle of the scheme, describes the decomposition of formic acid to CO_2. This route only requires the presence of 1 Pt atom in order to occur and is a 2-electron process, representing the most thermodynamically favored route for the oxidation of formic acid. The indirect pathway (dehydration pathway) is highlighted by the red arrows, emphasizing the conversion of formic acid to CO by dehydration, which is a non-faradaic reaction. The CO is then re-oxidized to form CO_2, with an activation barrier of 0.99 eV at 0.5 V vs. NHE. The final pathway, i.e. the formate pathway, involves the formation of a surface formate intermediate by the conversion of formic acid. The conversion of formic acid to a hydroxy carbonyl (COOH) species possesses an activation barrier of 0.47 eV at 0.5 V vs. NHE.[52, 56] The formate intermediate is then able to react to generate CO_2, with an activation barrier of 1.1 eV. Again, in principle, this pathway only requires the presence of 1 Pt atom in order to be initiated.[52]

In practice, specific compositions of metals in addition to the particular surface geometry can yield significant impacts upon the particular reaction pathway that occurs. In other words, in this thesis, we wish to explore the roles of (i) chemical composition and (ii) physical motifs (i.e. ultrathin anisotropic 1D wires) upon the resulting small molecule oxidation reactions. Specifically, Ru is known to promote the adsorption of –OH groups at potentials lower than that necessary for the removal of adsorbed CO on Pt active sites, and this is known to be the rate-determining step for MOR. Assuming that the required ensemble of Pt atoms is present for the indirect pathway of methanol oxidation, the indirect pathway occurring through the adsorption of CO would take place at a faster rate on a PtRu nanomaterial than it would on monometallic Pt. However, the predominant route for formic acid oxidation is actually the direct pathway across a wide range of potentials. In this case, formic acid is directly oxidized to CO_2, and alloying Pt with Ru would have little to no effect upon the overall rate.

Therefore, in this thesis, the methanol oxidation reaction is investigated with the employment of various ternary PtRuFe NW catalysts (with the RuFe composition varying from 0%-30%). In addition, a number of supplementary measurements including CO stripping have been performed to determine how composition may influence the particular mechanism of methanol oxidation. It has been hypothesized that Ru highly influences the indirect pathway of methanol oxidation, but does not affect the direct pathway for oxidizing formic acid. Therefore, by systematically varying the concentrations of Ru and Fe, we can probe their collective impact upon both formic acid and methanol oxidation processes.

1.3.2. Alkaline Fuel Cells

Alkaline fuel cells have recently re-emerged as a viable candidate for commercialization due to a number of reasons.[34] First, the kinetics at the cathode are significantly faster as compared with PEMFCs, thereby allowing for the employment of non-noble metal catalysts, which would greatly reduce the overall cost of the fuel cell. Second, the ohmic polarization within AFCs, i.e. the resistance of the ion flow within the electrolyte as well as of the electron flow at the electrode, is inherently reduced.

However, a significant disadvantage of AFCs as compared with PEMFCs until recently was the carbonation of the electrolyte. This occurred as a result of CO_2 generated as either a byproduct or simply from air, thereby precipitating as a carbonate. Prior work fundamentally addressed this issue by employing alkaline anion exchange membranes (AAEM), which possess a number of beneficial attributes including the lack of precipitated carbonate as a result of low cation mobility, a simplified water management scheme, and the presence of reduced corrosion.

Moreover, AFCs are very similar to PEMFCs, in that hydrogen and oxygen are employed as fuels. However, AFCs employ an alkaline media in which the reactions are run, as opposed to an acidic electrolyte. The overall reaction can be found in Reaction [1.7] with the respective anode and cathode reactions found in Reactions [1.8-1.9]

$$\text{Overall: } 2H_2O + 2e^- \rightarrow H_2 + 2OH^- \quad [1.7]$$

$$\text{Anode: } H_2 + 2OH^- - 2e^- \rightarrow 2H_2O \quad [1.8]$$

$$\text{Cathode: } O_2 + 2H_2O + 4e^- \rightarrow 4OH^- \quad [1.9]$$

The hydrogen oxidation reaction (HOR) is the process in which hydrogen is oxidized at the anode. The kinetics of HOR are highly influenced by the crystallography of the surface, with activity increasing in the order of Pt (111) ≤ Pt (100) < Pt (110) in alkaline media at low overpotentials.[57, 58] These differences can be attributed to variations in the corresponding heats of adsorption for the active intermediate, which are structure-sensitive. In alkaline media, HOR exhibits kinetics that are almost 2 orders of magnitude slower than in acidic media.[48, 59] The different possible pathways for HOR can be found below in Reactions [1.10-1.12]:

$$\text{Tafel Reaction} \quad H_2 \rightarrow 2H_{ad} \quad [1.10]$$

$$\text{Heyrovsky Reaction} \quad H_2 + OH^- \rightarrow H_{ad} + e^- + H_2O \quad [1.11]$$

$$\text{Volmer Reaction} \quad H_{ad} + OH^- \rightarrow e^- + H_2O \quad [1.12]$$

The HOR reaction occurs either through a Tafel/Volmer route or a Heyrovsky/Volmer mechanism, based upon the rate determining step for that particular material.[57] Additionally, the particular mechanism that predominates is dependent upon the amount of hydrogen adsorbed, which is controlled by the hydrogen binding energy (HBE).[60] The specific Tafel slope can be calculated from a Tafel plot in order to determine the inherent rate-determining step for the reaction. A more detailed description of Tafel slopes can be found in Chapter 2. A pure hydrogen dissociative reaction corresponds to a Tafel slope of 30 mV/decade (Tafel step). A symmetric electron transfer reaction possesses a Tafel slope of 120 mV/decade (Heyrovsky/Volmer steps), whereas the corresponding asymmetric reaction is 240 mV/decade.[61, 62] If multiple effects (such as ligand or strain effects, which are discussed below in section 3.3) are present, slope values in between 30 – 240 mV/decade can be achieved.

Moreover, some have demonstrated that the specific potential at which a Tafel slope is collected can have a significant effect upon the value of the Tafel slope.[48, 63] For example, at low overpotentials, a pure Pt surface can achieve a Tafel slope of ~50 mV/decade, whereas at high overpotentials, a slope of ~150 mV/decade can be attained.[57] Additionally, others have acquired similar values, corresponding to pure Pt surfaces.[62, 64]

In this thesis, the effect of chemical composition upon the corresponding HOR activity of our as-synthesized ultrathin alloy PtM nanowire catalysts will be evaluated. Specifically, it has been proposed that the HBE is the underlying factor controlling HOR activity and kinetics, which can be affected and tuned by varying chemical composition.

1.3.3. Generating Highly Efficient Methanol and Hydrogen Oxidation Reaction Catalysts

Moreover, at a pure Pt anode, an overpotential of several hundred mV is necessary to reach an adequate current density for methanol oxidation. This is mainly due to the presence of adsorbed intermediates such as CO. As mentioned previously, electrocatalysts usually under 5 nm in diameter contain a significant amount of defects, which should benefit the removal of CO. However, in this size regime, CO is known to interact much more strongly as compared with bulk analogues, thereby rendering Pt as an inefficient anode electrocatalyst for MOR. Therefore, there is an inherent need to synthesize highly active anode materials that either are tolerant to CO or enable the oxidation of CO at lower potentials.

One way of optimizing mass activity and activity as a whole is by controlling the overall size of the catalyst. Much research has been conducted in order to investigate the optimal particle size for methanol oxidation. In particular, Watanabe and co-workers have demonstrated no increase in specific activity with Pt/C nanoparticles possessing diameters greater than 2 nm.[65] Additionally, another group found that Pt catalysts possessing diameters between 1 to 1.5 nm exhibited poor catalytic performance, as a result of their amorphous structure.[66]

Another method of enhancing the activity and increasing the tolerance to CO is by alloying with other metals. In particular, Pt alloyed with metals such as Ru,[67-70] Sn,[71] Ni,[72, 73] and Pb[74] as well as Pt deposited on various metal oxides such as RuO_2[75, 76] and WO_3[77] have demonstrated significant improvements in CO tolerance while also increasing their overall performance. In particular, studies have demonstrated that alloying with certain metals such as Fe, Co, Ni, Ru, and Mo increases the Pt *d*-band vacancy, an idea which has been correlated with a decrease in CO adsorption.[78] This observation is due to a decreased amount of back-donation from the Pt 5*d* electrons to the CO $2\pi^*$ orbital.[79] This type of interaction, otherwise called an electronic or ligand effect, is highly advantageous for optimizing catalyst materials. Additionally, many have investigated the relationship between surface composition and the corresponding *d*-band center as well as their impact upon overall activity.[80-83] Additional catalyst motifs exist, including both core-shell and hierarchical structures. However, the focus of this thesis is on the study of alloyed materials.

As mentioned above, PtRu is often employed for the commercial catalyst as the anode material for methanol oxidation. In particular, Ru is highly advantageous in terms of improved CO tolerance as a result of the bifunctional mechanism.[84-87] The bifunctional mechanism is a process by which a more oxophilic metal than Pt itself adsorbs hydroxyl groups at the surface at potentials lower than that for the oxidation of CO at the Pt active sites. These hydroxyl groups then facilitate the removal of CO at lower potentials, thereby generating accessible Pt active sites for methanol adsorption. In addition to Ru, other metals such as either Sn, As, or Si as well as metal oxides such as $Ni(OH)_2$ have demonstrated the ability to dissociate water at low potentials in order to aid in the removal of CO.[84, 87-89]

Additionally, the strain effect denotes another result of either alloying or forming a core-shell motif, which occurs when the lattice constants of two (or more) metals are different from one another. This phenomenon leads to variations in the chemical properties of the individual metals. Norskov and co-workers previously demonstrated that strained surfaces can have a significant impact upon the desorption of CO and well as the chemisorption of oxygen, as a result of shifted *d*-band centers.[90] That is, a tensile strain causes an expansion of the overall lattice, which leads to an upshift in the *d*-band center, thereby strengthening interactions with adsorbates. Conversely, a compression strain has the opposite effect, substantively shifting the *d*-band center further away from the Fermi level and thereby weakening adsorbate interactions. Moreover, some have turned to alloying with multiple metals in order to optimize effects.[81, 91-95]

In addition, tailoring the morphology can yield a drastic impact upon performance. Specifically, 1D nanomaterials possess a number of beneficial aspects that make them ideal catalyst materials including high aspect ratios, fewer lattice boundaries, a limited number of deleterious defects, and long segments of smooth crystal planes. Although 3D structures are not explicitly discussed in this thesis, these nanomaterials also possess a number of benefits such as higher surface area-to-volume ratios, which can improve upon available contact regions[96, 97] in addition to reduced diffusion lengths, as a result of their nanometer-sized building blocks.[98, 99]

Moreover, previous research within our group has demonstrated an increase in methanol oxidation activity by employing Pt NW catalysts as compared with their NP counterparts.[5, 100] In fact, the Pt NWs exhibited a shift in the CO stripping peak to lower potentials as compared with the Pt NP system, an observation which was attributed to a specific arrangement of surface-terrace defect sites. Additionally, the reduced amount of low coordination atoms of the 1D structure is beneficial, since CO binds more strongly at these sites.[101, 102]

AFCs possess inherently different problems as compared with DMFCs due to the employment of an alkaline electrolyte. Although AFCs do not have problems associated with CO poisoning at the anode, they do exhibit kinetics 2 orders of magnitude lower for Pt as compared with an acidic electrolyte.[48, 59] Therefore, this allows for the substitution of Pt with non-precious metals. Ni-based catalysts are among the most active non-precious metal alternatives to Pt for the hydrogen oxidation reaction.[45, 103-105] For instance, Yan and co-workers synthesized a CoNiMo NP catalyst and found a 20x improvement in HOR activity as compared with an electroplated Ni catalyst.[45] However, currently, the study of non-precious metal catalysts remains a topic of intensive research, as alternatives are still unable to achieve either the same or even better activity as compared with Pt.[105, 106] Therefore, many have incorporated Pt into their different structures, forming either alloy, core-shell, or hierarchical motifs.

Moreover, the different types of effects described above, including strain and electronic effects, are still applicable for the hydrogen oxidation reaction. In effect, altering the *d*-band center of a synthesized catalyst has a noticeable result upon the HOR kinetics and the overall activity, since HOR is kinetically limited. For example, Wang and co-workers demonstrated that 2 Pt monolayers (ML) deposited onto a Ru nanotube (NT) generated a weakened HBE of -0.33 eV, i.e. a value closer to 0 as compared with a Pt (111) surface (-0.48 eV).[107] Additionally, Yan and co-workers also provided evidence for a decrease in HBE as compared with electroplated Ni (-0.51 eV) for their CoNiMo catalyst (-0.43 eV).[44]

Although the strain effect and ligand effect are dominant factors influencing HOR kinetics and activity, it had been proposed that the bifunctional effect also plays a role in controlling HOR kinetics. In fact, it had been theoretically proposed that OH_{ad} is a key reactant species in HOR, and that the presence of a more oxophilic metal should improve the reaction kinetics and activity of Pt.[108] However, another group experimentally tested this hypothesis by investigating the electrochemical activity of commercial alloy PtRu NPs and Pt NP/C.[109] Ultimately, this group found that the PtRu NP/C outperformed Pt NP/C, an observation which they ascribed to an optimized hydrogen binding energy (HBE) value, as a result of an electronic effect imparted onto Pt by Ru. Their rationale rested on the observation that PtRu NP/C did not give rise to a lower onset potential for CO desorption as compared with Pt NP/C, which would have provided for significant evidence for the presence of an oxophilic effect.

Furthermore, by taking into account size, composition, morphology, as well as the resulting geometric and electronic effects, catalysts can be optimally tailored in order to generate high activities and enhanced durability for their respective catalytic reactions. That objective denotes one of the main themes of this thesis.

Chemical Thermodynamics

The change in the Gibbs free energy (ΔG) for a specific electrochemical reaction can determine the maximum electrical work (W_{e1}), obtained by a fuel cell at a constant temperature and pressure. The specific equation can be found below Equation [1.1], with n representing the number of electrons participating in the reaction, F as Faraday's constant (96,487 coulombs/mol), and E denoting the ideal potential for the cell. The state function for determining the Gibbs free energy can be found in Equation [1.2], with ΔH representing a change in enthalpy, ΔS highlighting a change in entropy, and T as temperature.

$$W_{e1} = \Delta G = -nFE \qquad [1.1]$$

$$\Delta G = \Delta H - T\Delta S \qquad [1.2]$$

Based upon these equations, the ideal cell voltage in which H_2 and O_2 react is determined to be 1.229 V from liquid water. Moreover, as the temperature of the cell increases, there is a linear decrease in cell voltage.[7] However, a number of irreversible processes can lead to decreases in the ideal cell voltage. These losses are specified as polarization or overpotential, including activation polarization, concentration polarization, and ohmic polarization processes.[7]

The generation of losses due to activation is a result of sluggish kinetics. Therefore, in order to improve upon the current losses, better catalysts need to be developed. Concentration polarization is caused by the slow diffusion of reactants and products to and from a reaction site. The larger the current density generated by a fuel cell, the greater the concentration loss. Moreover, ohmic polarization is triggered by resistance including both resistance of the ion flow within the electrolyte as well as of the electron flow at the electrode. Ways to reduce the ohmic losses within the cell include (i) reducing the width of the membrane as well as employing one with higher ionic conductivity, (ii) better contact between bipolar plates and the GDL material, as well as (iii) less spatial separation between catalysts. As a result, the overall cell equation is:

$$E_{cell} = \Delta E - \eta_{activation} - \eta_{ohm} - \eta_{concentration} \qquad [1.3]$$

At low current densities, the major loss is ascribed to activation polarization, with the cell potential achieved being very close to the theoretical potential. As the current density increases, ohmic losses also contribute to the overall decrease in cell potential. As high current densities, the concentration polarization also contributes. Moreover, typically, a fuel cell operates around 0.7 V in order to achieve a reasonable efficiency.

Additionally, a number of factors influence the electrode reaction rate and current including either mass transfer, electron transfer, chemical reactions occurring before or after electron transfer, or other surface reactions such as adsorption and desorption.[110] An example of a general pathway at the electrode can be found in Figure 1.8. A simple reaction includes mass transfer of a reactant to the electrode, followed by electron transfer from a non-adsorbed species, and mass transfer of the product to the solution. However, in most cases, more convoluted steps occur, including either multiple reaction pathways, various electron transfer processes, or alterations of the electrode surfaces.

The rate-determining step of a particular reaction is the step that limits the magnitude of the current.[110] A rate-determining step is defined as the step that is particularly sluggish in either removing relevant products or generating specific reactant materials. For example, the rate-determining step for methanol oxidation on Pt is the oxidation of adsorbed CO. Moreover, a steady-state current can be achieved when the rate of each reaction step is the same.

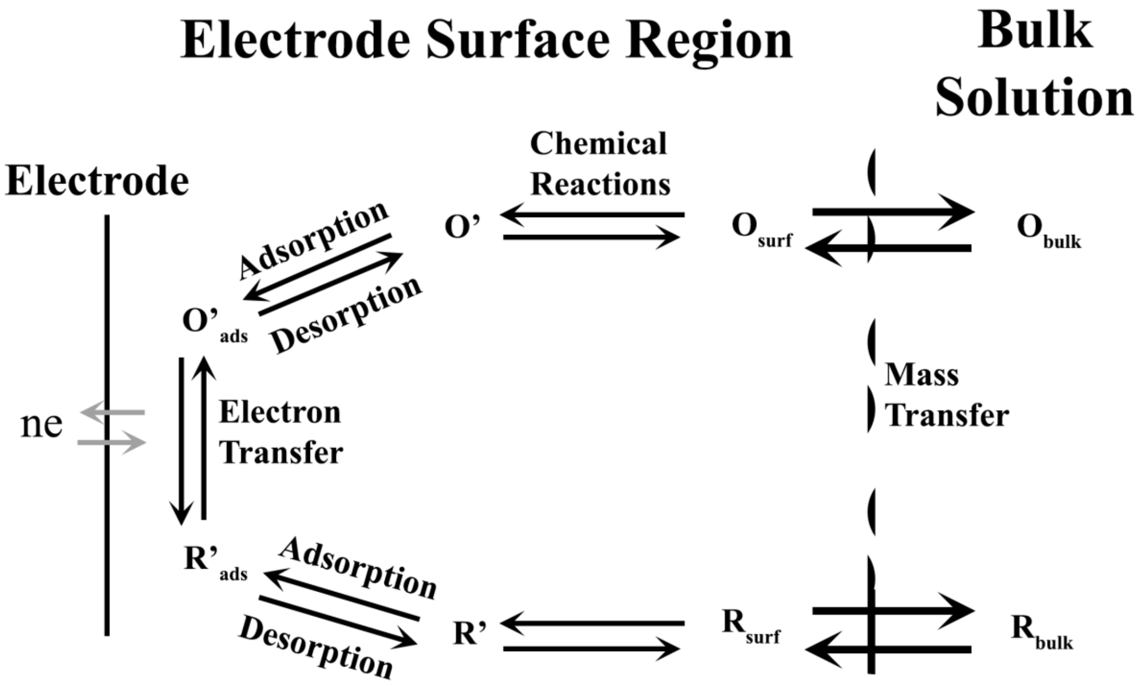

Figure 1.8. Pathway of a general electrode reaction. A simple reaction depicting mass transfer of a reactant from the bulk solution to the electrode, followed by electron transfer from a non-adsorbed species to the adsorbed species, and mass transfer of the product to the bulk solution. Adapted from Ref. 110.

Various types of mass transfer can affect the electrochemical reaction including:[110]

- Migration: Transport of a charged body as a result of an electrical field
- Diffusion: Transport of a charged body as a result of a concentration gradient
- Convection: Transport as a result of either stirring or natural density gradients

However, in most cases, not all three are occurring simultaneously; that is, one or more of the possible mass transfer types are prevented, either by adding an inert electrolyte to reduce migration or through the lack of stirring to inhibit convection.

1.4. Li-ion Batteries

A battery is an electrochemical cell or cells that are in contact to generate electrical energy.[7] Li-ion batteries (LIB) are composed of a positive electrode, typically some sort of carbon containing material such as graphene, as well as a negative electrode containing Li such as $LiFePO_4$ or $LiCoO_2$, separated by a Li-ion conducting electrolyte. Li-ion batteries are employed for a variety of applications, including consumer electronics such as phones, radios/speakers, and computers, as well as cars, tractors, warehouse equipment, and so forth. Additionally, due to their high energy density and flexibility in design, LIBs account for ~63% of the world's total battery sales.[111]

It is highly advantageous to use a Li-based material at the cathode, since it is the most electropositive (-3.04 V vs. RHE) and the lightest metal (6.94 g/mol), thereby promoting the high energy density of the battery. Modern LIBs extract Li from an oxide host material at the cathode and into either a carbon-, silicon-, or tin-based material at the anode. The capacity of the oxide is determined by the solid-solution range of the Li. Additionally, within the initial cycle, a solid electrolyte interphase (SEI) forms at the anode, thereby leading to a decrease in the amount of Li present, as these ions permeate into the SEI layer.

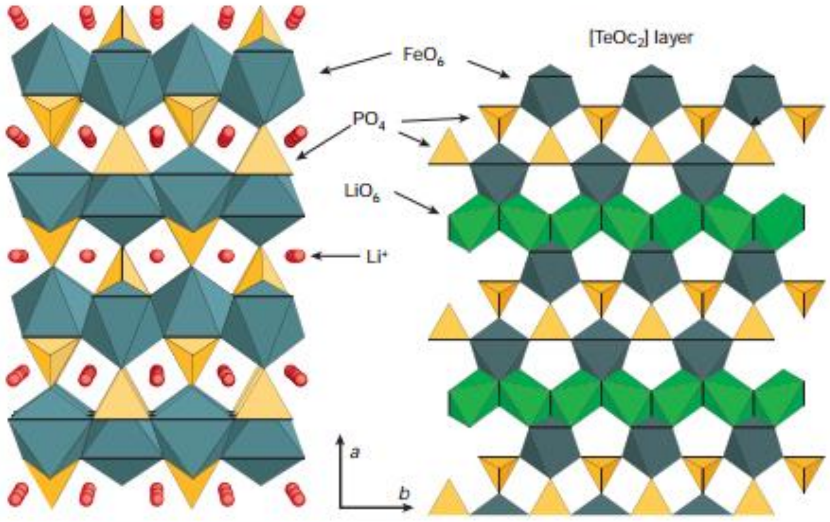

Figure 1.9. $LiFePO_4$ olivine crystal structure projected along the [001] plane. Li ions are in red with the FeO_6 octahedra in blue and PO_4 tetrahedra in yellow. The right depicts the distorted hexagonal close packed (*hcp*) structure with two oxygen-dense layers. Li ions can diffuse through the [001] or [010] plane. Taken from Ref. 111.

$LiFePO_4$ denotes a common cathode material, with an olivine-type structure, composed of FeO_6 corner-sharing octahedra and PO_4 tetrahedral anions, which can be found in Figure 1.9. However, in order to address the poor electronic conductivity of the material, carbon additives and low temperature synthesis routes are often needed to be employed. Moreover, as a result, 90% of the theoretical capacity (165 mAh/g) associated with $LiFePO_4$ can be utilized.[111] Moreover, in this thesis, we will discuss the optimization of size, morphology, and purity of $LiFePO_4$ nanostructures as cathode materials for LIB applications.

1.5. Objectives of Current Work

The purpose of this thesis is to characterize the as-prepared nanomaterials as well as to analyze their discrete properties in the context of key fuel cell and battery applications discussed above. Specifically, 2 chapters will focus on the synthesis and subsequent application of monometallic, binary, and ternary metallic nanowires for the MOR, FAOR, and HOR, respectively, with the former two reactions occurring in acidic media and the latter under alkaline conditions. Additionally, 1 chapter will center on the synthesis of Pt deposited metal oxide and ternary oxide support materials for optimization of performance in the methanol oxidation reaction. Lastly, 1 chapter will discuss the synthesis and possible use of $LiFePO_4$ NWs for Li-ion battery-related applications.

As a means of providing relevant background and context, the synthetic methods employed to generate the various 0D and 1D nanomaterials as well as the suite of characterization techniques utilized within this thesis will be discussed in detail in Chapter 2.

To summarize the overall objectives of this thesis, we aim to investigate:

(i) the effect of Pt-based alloy nanowires on the overall performance of methanol oxidation, formic acid oxidation, and hydrogen oxidation. This will be completed through the investigation of how by tailoring composition, electronic effects can emerge that subsequently "alter" the electronic structures of our alloy nanowires. We will then investigate how these chemically modified structures influence activity, durability and kinetics of the specific reaction being tested.

(ii) the effect of metal oxide support materials upon the catalytic activity of supported Pt NPs for the methanol oxidation reaction. This will be accomplished not only by analyzing the bonding environment between the catalyst and support material that leads to manifested metal-support interactions but also by correlating catalyst particle size and surface area with achieved activity and durability.

(iii) the effect of composition, morphology, bond structure, and phase purity of $LiFePO_4$ NWs on the electrochemical performance as a cathode material for Li-ion batteries. This will be realized through a variety of advanced techniques to characterize the local bonding environment as well as the orientation and growth direction of our as-synthesized NWs that we will subsequently correlate with theoretical predictions.

To investigate each of the topics and projects described in this thesis and summarized in Sections 1.5.1 through 1.5.4, a range of characterization techniques has been employed, and these will be further described in more detail in their corresponding Chapters. Nonetheless, these scientific issues are relevant, if not even critically pertinent, to understanding structure-property relationships for fuel cell and battery applications. Therefore, this thesis focuses on considering how the electronic structure of a nanomaterial can be tailored and tuned in a way so as to become more beneficial for a particular application. In so doing, we explore the bonding environment as well as interactions between the metals and metal oxide species serving in the roles of catalysts, catalyst supports, and cathode materials. These structure-induced electronic effects are examined from the perspective of modifications to the size, chemical composition, and morphology of our nanomaterials.

1.5.1. PtRuFe NWs for the Methanol Oxidation Reaction and Formic Acid Oxidation Reaction (Chapter 3)

In the search for alternatives to conventional Pt electrocatalysts, we have synthesized ultrathin, ternary PtRuFe NWs, possessing different chemical compositions in order to probe their CO tolerance as well as electrochemical activity as a function of composition for both (i) the methanol oxidation reaction and (ii) the formic acid oxidation reaction. As-prepared ‘multifunctional’ ternary NW catalysts exhibited both higher MOR and FAOR activity as compared with mono-metallic Pt NWs, binary Pt_7Ru_3 and Pt_7Fe_3 NWs, and commercial catalyst control samples. In terms of synthetic novelty, we utilized a sustainably mild, ambient wet-synthesis method never previously applied to the fabrication of crystalline, pure ternary systems in order to fabricate ultrathin, homogeneous alloy PtRuFe NWs with a range of controlled compositions. These NWs were subsequently characterized using a suite of techniques including X-ray diffraction (XRD), transmission electron microscopy (TEM), selected area electron diffraction (SAED), and energy dispersive analysis of X-rays (EDAX) in order to verify not only the incorporation of Ru and Fe into the Pt lattice but also their chemical homogeneity, morphology, as well as physical structure and integrity. Lastly, these NWs were electrochemically tested in order to deduce the appropriateness of conventional explanations such as (i) the bi-functional mechanism as well as (ii) the ligand effect to account for our MOR and FAOR reaction data. Specifically, methanol oxidation appears to be predominantly influenced by the Ru content, whereas formic acid oxidation is primarily impacted by the corresponding Fe content within the ternary metal alloy catalyst itself.

1.5.2. PtM (M = Ru, Fe, Co, Fe, Cu, Au) for the Hydrogen Oxidation Reaction (Chapter 4)

With an increased interest in the development of hydrogen fuel cells as a plausible alternative to combustion engines, recent work has focused on creating AFC, which employ an alkaline environment. Working in alkaline as opposed to acidic media yields a number of tangible benefits, including (i) the ability to use cheaper and plentiful precious-metal-free catalysts, due to their increased stability; (ii) a reduction in the amount of degradation and corrosion of Pt-based catalysts; and (iii) a longer operational lifetime for the overall fuel cell configuration. However, in the absence of Pt, no catalyst has achieved similar activities to that of Pt. Herein, we have synthesized a number of crystalline ultrathin PtM alloy NWs ('M' = Fe, Co, Ru, Cu, and Au) in order to replace a portion of the costly Pt metal without compromising on activity while simultaneously adding in metals known to exhibit favorable synergistic ligand and strain effects with respect to the host lattice. In fact, our experiments confirm theoretical insights about a clear and correlative dependence between measured activity and chemical composition. We have conclusively demonstrated that our as-synthesized alloy NW catalysts yield improved HOR activities as compared with a commercial Pt standard as well as with our as-synthesized Pt NWs. The Pt_7Ru_3 NW system, in particular, quantitatively achieved an exchange current density of 0.493 mA/cm^2, which is higher than the corresponding data for Pt NWs alone. Additionally, the HOR activities follow the same expected trend as their calculated HBE values, thereby confirming the critical importance and correlation of HBE with the observed activities.

1.5.3. Synthesis, Characterization and Electrochemical Testing of Metal Oxide and Perovskite Nanomaterials for the Methanol Oxidation Reaction (Chapter 5)

The performance of electrode materials in conventional DMFCs is constrained by (i) the low activity of the catalyst materials relative to their overall cost, (ii) the poisoning of the active sites due to the presence of partially oxidized carbon species (such as but not limited to CO, formate, and acetate) produced during small molecule oxidation, and (iii) the lack of catalytic stability and durability on the underlying commercial carbon support. Therefore, as a viable alternative, we have synthesized various metal oxide and perovskite materials of different sizes and chemical compositions as supports for Pt NPs. Our results including unique mechanistic studies demonstrate that the $SrRuO_3$ substrate with immobilized Pt NPs at its surface evinces the best methanol oxidation performance as compared with all of the other substrate materials tested herein, including commercial carbon itself. Additionally, data from electron energy loss spectroscopy (EELS) and X-ray photoelectron spectroscopy (XPS) confirmed the presence of electron transfer from bound Pt NPs to surface Ru species within the $SrRuO_3$ substrate itself, thereby suggesting that favorable metal support interactions are responsible for the increased MOR activity of Pt species with respect to the underlying $SrRuO_3$ composite catalyst material.

1.5.4. Synthesis and Characterization of 1D $LiFePO_4$ Nanomaterials (Chapter 6)

$LiFePO_4$ materials have become increasingly popular as a cathode material due to the many benefits they possess including thermal stability, durability, low cost, and long life span. Nevertheless, to broaden the general appeal of this material for practical electrochemical applications, it would be useful to develop a relatively mild, reasonably simple synthesis method of this cathode material. Herein, we describe a generalizable, 2-step methodology of sustainably synthesizing $LiFePO_4$ by incorporating a template-based, ambient, surfactantless, seedless, U-tube protocol in order to generate size and morphologically tailored, crystalline, phase-pure nanowires. The purity, composition, crystallinity, and intrinsic quality of these wires were systematically assessed using TEM, high-resolution TEM (HRTEM), scanning electron microscopy (SEM), XRD, SAED, EDAX, and high-resolution synchrotron XRD. From these techniques, we were able to determine that there is an absence of any obvious defects present in our wires, supporting the viability of our synthetic approach. Electrochemical analysis was also employed to assess their electrochemical activity. Although our nanowires do not contain any noticeable impurities, we attribute their less than optimal electrochemical rigor to differences in the chemical bonding between our $LiFePO_4$ nanowires and their bulk-like counterparts. Specifically, we demonstrate for the first time experimentally that the Fe–O3 chemical bond plays an important role in determining the overall conductivity of the material, an assertion which is further supported by recent “first-principles” calculations. Nonetheless, our ambient, solution-based synthesis technique is capable of generating highly crystalline and phase-pure energy-storage-relevant nanowires that can be tailored so as to fabricate different sized materials of reproducible, reliable morphology.

1.6. References

1. Garbarino, S.; Ponrouch, A.; Pronovost, S.; Gaudet, J.; Guay, D., *Electrochemistry Communications* **2009,** *11* 1924-1927.
2. Koenigsmann, C.; Wong, S. S., *Energy & Environmental Science* **2011,** *4* 1161-1176.
3. Wang, C.; Waje, M.; Wang, X.; Tang, J. M.; Haddon, R. C.; Yan, *Nano Letters* **2004,** *4* 345-348.
4. Smith, P. A.; Nordquist, C. D.; Jackson, T. N., *Applied Physics Letters* **2000,** *77* 1399-1401.
5. Zhou, W.-P.; Li, M.; Koenigsmann, C.; Ma, C.; Wong, S. S.; Adzic, R. R., *Electrochimica Acta* **2011,** *56* 9824-9830.
6. Liu, H.; Adzic, R. R.; Wong, S. S., *ACS Applied Materials & Interfaces* **2015,** *7* 26145-26157.
7. Winter, M.; Brodd, R. J., *Chemical Reviews* **2004,** *104* 4245-4270.
8. Bockris, J. O. M.; Reddy, A. K. N., *Modern Electrochemistry*. Plenum Press: New York, 1970.
9. Aricò, A. S.; Bruce, P.; Scrosati, B.; Tarascon, J.-M.; van Schalkwijk, W., *Nature Materials* **2005,** *4* 366-377.
10. Scofield, M. E.; Liu, H.; Wong, S. S., *Chemical Society Reviews* **2015,** *44* 5836-5860.
11. Sun, Y.; Zhou, T.; Pan, Q.; Zhang, X.; Guo, J., *RSC Advances* **2015,** *5* 60237-60245.
12. Bullion, J. Platinum price per gram.
13. James, B. D.; Kalinoski, J.; Baum, K., *Manufacturing Cost Analysis of Fuel Cell Systems*. U.S. Department of Energy: Arlington, VA, USA, 2011.
14. Sharma, S.; Pollet, B. G., *Journal of Power Sources* **2012,** *208* 96-119.
15. Kangasniemi, K. H.; Condit, D. A.; Jarvi, T. D., *Journal of The Electrochemical Society* **2004,** *151* E125-E132.
16. Antolini, E.; Gonzalez, E. R., *Solid State Ionics* **2009,** *180* 746-763.
17. Abida, B.; Chirchi, L.; Baranton, S.; Napporn, T. W.; Kochkar, H.; Léger, J.-M.; Ghorbel, A., *Applied Catalysis B: Environmental* **2011,** *106* 609-615.
18. Yu, N.; Kuai, L.; Wang, Q.; Geng, B., *Nanoscale* **2012,** *4* 5386-5393.
19. Hua, H.; Hu, C.; Zhao, Z.; Liu, H.; Xie, X.; Xi, Y., *Electrochimica Acta* **2013,** *105* 130-136.
20. Xiao, Y.; Zhan, G.; Fu, Z.; Pan, Z.; Xiao, C.; Wu, S.; Chen, C.; Hu, G.; Wei, Z., *Electrochimica Acta* **2014,** *141* 279-285.
21. Tauster, S. J., *Accounts of Chemical Research* **1987,** *20* 389-394.
22. Fu, Q.; Wagner, T., *Surface Science Reports* **2007,** *62* 431-498.
23. Tauster, S. J.; Fung, S. C., *Journal of Catalysis* **1978,** *55* 29-35.
24. Baker, R. T. K.; Prestridge, E. B.; McVicker, G. B., *Journal of Catalysis* **1984,** *89* 422-432.
25. Raupp, G. B.; Dumesic, J. A., *Journal of Catalysis* **1986,** *97* 85-99.
26. Baker, R. T. K.; Prestridge, E. B.; Murrell, L. L., *Journal of Catalysis* **1983,** *79* 348-358.
27. Bernal, S.; Calvino, J. J.; Cauqui, M. A.; Gatica, J. M.; Larese, C.; Pérez Omil, J. A.; Pintado, J. M., *Catalysis Today* **1999,** *50* 175-206.
28. Penner, S.; Wang, D.; Su, D. S.; Rupprechter, G.; Podloucky, R.; Schlögl, R.; Hayek, K., *Surface Science* **2003,** *532–535* 276-280.

29. Wang, D.; Penner, S.; Su, D. S.; Rupprechter, G.; Hayek, K.; Schlögl, R., *Journal of Catalysis* **2003,** *219* 434-441.

30. Fu, Q.; Wagner, T.; Olliges, S.; Carstanjen, H.-D., *The Journal of Physical Chemistry B* **2005,** *109* 944-951.

31. Bernal, S.; Calvino, J. J.; Cauqui, M. A.; Gatica, J. M.; López Cartes, C.; Pérez Omil, J. A.; Pintado, J. M., *Catalysis Today* **2003,** *77* 385-406.

32. Raj, R.; Saha, A.; An, L.; Hasselman, D. P. H.; Ernst, P., *Acta Materialia* **2002,** *50* 1165-1176.

33. Yu, Y.; Mark, J.; Ernst, F., *Journal of Materials Science* **2006,** *41* 7785-7797.

34. Antolini, E.; Gonzalez, E. R., *Journal of Power Sources* **2010,** *195* 3431-3450.

35. Snell, K. D.; Keenan, A. G., *Electrochimica Acta* **1982,** *27* 1683-1696.

36. Lamy, C., *Electrochimica Acta* **1984,** *29* 1581-1588.

37. Leiva, E. P. M.; Giordano, M. C., *Journal of The Electrochemical Society* **1983,** *130* 1305-1312.

38. Smirnov, P.; Wakita, H.; Yamaguchi, T., *The Journal of Physical Chemistry B* **1998,** *102* 4802-4808.

39. Teliska, M.; Murthi, V. S.; Mukerjee, S.; Ramaker, D. E., *The Journal of Physical Chemistry C* **2007,** *111* 9267-9274.

40. Olivera, P. P.; Parito, M.; Sellers, H., Electronic structure calculations of polyatomic oxyanions adsorbed on metal surfaces. In *Interfacial Electrochemistry*, Wieckowski, A., Ed. Marcel-Dekker: New York, 1999; p 63.

41. Merle, G.; Wessling, M.; Nijmeijer, K., *Journal of Membrane Science* **2011,** *377* 1-35.

42. Kruusenberg, I.; Mondal, J.; Matisen, L.; Sammelselg, V.; Tammeveski, K., *Electrochemistry Communications* **2013,** *33* 18-22.

43. Xing, Z.; Li, Q.; Wang, D.; Yang, X.; Sun, X., *Electrochimica Acta* **2016,** *191* 841-845.

44. Li, X.; Popov, B. N.; Kawahara, T.; Yanagi, H., *Journal of Power Sources* **2011,** *196* 1717-1722.

45. Sheng, W.; Bivens, A. P.; Myint, M.; Zhuang, Z.; Forest, R. V.; Fang, Q.; Chen, J. G.; Yan, Y., *Energy & Environmental Science* **2014,** *7* 1719-1724.

46. Kadirgan, F.; Beden, B.; Leger, J. M.; Lamy, C., *Journal of Electroanalytical Chemistry and Interfacial Electrochemistry* **1981,** *125* 89-103.

47. Durst, J.; Siebel, A.; Simon, C.; Hasche, F.; Herranz, J.; Gasteiger, H. A., *Energy & Environmental Science* **2014,** *7* 2255-2260.

48. Sheng, W.; Gasteiger, H. A.; Shao-Horn, Y., *Journal of The Electrochemical Society* **2010,** *157* B1529-B1536.

49. Narayan, S. R.; Valdez, T. I., *Electrochem. Soc. Interface* **2008,** *17* 40-45.

50. Wang, C.-H.; Chen, L.-C.; Chen, K.-H., *Electrocatalysis of Direct Methanol Fuel Cells: From Fundamentals to Applications*. John Wiley and Sons: 2009; p 606.

51. Cuesta, A., *Journal of the American Chemical Society* **2006,** *128* 13332-13333.

52. Neurock, M.; Janik, M.; Wieckowski, A., *Faraday Discussions* **2008,** *140* 363-378.

53. Housmans, T. H. M.; Koper, M. T. M., *The Journal of Physical Chemistry B* **2003,** *107* 8557-8567.

54. Lai, S. C. S.; Lebedeva, N. P.; Housmans, T. H. M.; Koper, M. T. M., *Topics in Catalysis* **2007,** *46* 320-333.

55. Chen, Y. X.; Heinen, M.; Jusys, Z.; Behm, R. J., *Angewandte Chemie International Edition* **2006,** *45* 981-985.

56. Yu, X.; Pickup, P. G., *Journal of Power Sources* **2008,** *182* 124-132.
57. Markovic, N. M.; Sarraf, S. T.; Gasteiger, H. A.; Ross, P. N., *Journal of the Chemical Society, Faraday Transactions* **1996,** *92* 3719-3725.
58. Marković, N. M.; Ross Jr, P. N., *Surface Science Reports* **2002,** *45* 117-229.
59. Bagotzky, V. S.; Osetrova, N. V., *Journal of Electroanalytical Chemistry and Interfacial Electrochemistry* **1973,** *43* 233-249.
60. Mahoney, E. G.; Sheng, W.; Yan, Y.; Chen, J. G., *ChemElectroChem* **2014,** *1* 2058-2063.
61. Krischer, K.; Savinova, E. R., *Handbook of Heterogeneous Catalysis*. Wiley-VCH Verlag GmbH & Co. KGaA: 2008.
62. St. John, S.; Atkinson, R. W.; Unocic, K. A.; Unocic, R. R.; Zawodzinski, T. A.; Papandrew, A. B., *ACS Catalysis* **2015,** *5* 7015-7023.
63. Shinagawa, T.; Garcia-Esparza, A. T.; Takanabe, K., *Scientific Reports* **2015,** *5* 13801.
64. Conway, B. E.; Bai, L., *Journal of Electroanalytical Chemistry* **1986,** *198* 149-175.
65. Watanabe, M.; Saegusa, S.; Stonehart, P., *Journal of Electroanalytical Chemistry and Interfacial Electrochemistry* **1989,** *271* 213-220.
66. Song, Y.; Garcia, R. M.; Dorin, R. M.; Wang, H.; Qiu, Y.; Coker, E. N.; Steen, W. A.; Miller, J. E.; Shelnutt, J. A., *Nano Letters* **2007,** *7* 3650-3655.
67. Jambunathan, K.; Jayaraman, S.; Hillier, A. C., *Langmuir* **2004,** *20* 1856-1863.
68. Moore, J. T.; Corn, J. D.; Chu, D.; Jiang, R.; Boxall, D. L.; Kenik, E. A.; Lukehart, C. M., *Chemistry of Materials* **2003,** *15* 3320-3325.
69. Yajima, T.; Uchida, H.; Watanabe, M., *The Journal of Physical Chemistry B* **2004,** *108* 2654-2659.
70. Fachini, E. R.; Díaz-Ayala, R.; Casado-Rivera, E.; File, S.; Cabrera, C. R., *Langmuir* **2003,** *19* 8986-8993.
71. González, M. J.; Peters, C. H.; Wrighton, M. S., *The Journal of Physical Chemistry B* **2001,** *105* 5470-5476.
72. Park, K.-W.; Choi, J.-H.; Sung, Y.-E., *The Journal of Physical Chemistry B* **2003,** *107* 5851-5856.
73. Liu, F.; Lee, J. Y.; Zhou, W., *The Journal of Physical Chemistry B* **2004,** *108* 17959-17963.
74. Casado-Rivera, E.; Volpe, D. J.; Alden, L.; Lind, C.; Downie, C.; Vázquez-Alvarez, T.; Angelo, A. C. D.; DiSalvo, F. J.; Abruña, H. D., *Journal of the American Chemical Society* **2004,** *126* 4043-4049.
75. Villullas, H. M.; Mattos-Costa, F. I.; Bulhões, L. O. S., *The Journal of Physical Chemistry B* **2004,** *108* 12898-12903.
76. Liu, H.; Iglesia, E., *The Journal of Physical Chemistry B* **2005,** *109* 2155-2163.
77. Park, K.-W.; Ahn, K.-S.; Nah, Y.-C.; Choi, J.-H.; Sung, Y.-E., *The Journal of Physical Chemistry B* **2003,** *107* 4352-4355.
78. Xu, C.; Wang, L.; Mu, X.; Ding, Y., *Langmuir* **2010,** *26* 7437-7443.
79. Igarashi, H.; Fujino, T.; Zhu, Y.; Uchida, H.; Watanabe, M., *Physical Chemistry Chemical Physics* **2001,** *3* 306-314.
80. Demirci, U. B., *Journal of Power Sources* **2007,** *173* 11-18.
81. Stamenkovic, V. R.; Mun, B. S.; Arenz, M.; Mayrhofer, K. J. J.; Lucas, C. A.; Wang, G.; Ross, P. N.; Markovic, N. M., *Nat Mater* **2007,** *6* 241-247.
82. Wu, J.; Yang, H., *Accounts of Chemical Research* **2013,** *46* 1848-1857.

83. Stamenkovic, V. R.; Mun, B. S.; Mayrhofer, K. J. J.; Ross, P. N.; Markovic, N. M., *Journal of the American Chemical Society* **2006,** *128* 8813-8819.
84. Watanabe, M.; Uchida, H., Catalysts for the electro-oxidation of small molecules. In *Handbook of Fuel Cells*, John Wiley & Sons, Ltd: 2010.
85. Roth, C.; Benker, N.; Buhrmester, T.; Mazurek, M.; Loster, M.; Fuess, H.; Koningsberger, D. C.; Ramaker, D. E., *Journal of the American Chemical Society* **2005,** *127* 14607-14615.
86. Gojković, S. L.; Vidaković, T. R.; Đurović, D. R., *Electrochimica Acta* **2003,** *48* 3607-3614.
87. Zhou, W.; Zhou, Z.; Song, S.; Li, W.; Sun, G.; Tsiakaras, P.; Xin, Q., *Applied Catalysis B: Environmental* **2003,** *46* 273-285.
88. Permyakova, A. A.; Han, B.; Jensen, J. O.; Bjerrum, N. J.; Shao-Horn, Y., *The Journal of Physical Chemistry C* **2015,** *119* 8023-8031.
89. Huang, W.; Wang, H.; Zhou, J.; Wang, J.; Duchesne, P. N.; Muir, D.; Zhang, P.; Han, N.; Zhao, F.; Zeng, M.; Zhong, J.; Jin, C.; Li, Y.; Lee, S.-T.; Dai, H., *Nat Commun* **2015,** *6*.
90. Mavrikakis, M.; Hammer, B.; Nørskov, J. K., *Physical Review Letters* **1998,** *81* 2819-2822.
91. Qiu, J.-D.; Wang, G.-C.; Liang, R.-P.; Xia, X.-H.; Yu, H.-W., *The Journal of Physical Chemistry C* **2011,** *115* 15639-15645.
92. Guo, S.; Zhang, S.; Sun, X.; Sun, S., *Journal of the American Chemical Society* **2011,** *133* 15354-15357.
93. Huang, T.; Wang, X.; Zhuang, J.; Cai, W.-B.; Yu, A., *Electrochemical and Solid-State Letters* **2009,** *12* B112-B115.
94. Jeon, M. K.; Won, J. Y.; Lee, K. R.; Woo, S. I., *Electrochemistry Communications* **2007,** *9* 2163-2166.
95. Wang, Z.-B.; Yin, G.-P.; Shao, Y.-Y.; Yang, B.-Q.; Shi, P.-F.; Feng, P.-X., *Journal of Power Sources* **2007,** *165* 9-15.
96. Zhao, Y.; Tao, C.; Xiao, G.; Wei, G.; Li, L.; Liu, C.; Su, H., *Nanoscale* **2016,** *8* 5313-5326.
97. Banerjee, S.; Wong, S. S., *Journal of the American Chemical Society* **2004,** *126* 2073-2081.
98. Mao, Y.; Kanungo, M.; Hemraj-Benny, T.; Wong, S. S., *The Journal of Physical Chemistry B* **2006,** *110* 702-710.
99. Wang, L.; Zhang, Y.; Scofield, M. E.; Yue, S.; McBean, C.; Marschilok, A. C.; Takeuchi, K. J.; Takeuchi, E. S.; Wong, S. S., *ChemSusChem* **2015,** *8* 3304-3313.
100. Koenigsmann, C.; Zhou, W.-p.; Adzic, R. R.; Sutter, E.; Wong, S. S., *Nano Letters* **2010,** *10* 2806-2811.
101. Karmazyn, A. D.; Fiorin, V.; Jenkins, S. J.; King, D. A., *Surface Science* **2003,** *538* 171-183.
102. Hammer, B., *Topics in Catalysis* *37* 3-16.
103. Kenjo, T., *Journal of The Electrochemical Society* **1985,** *132* 383-386.
104. Kiros, Y.; Schwartz, S., *Journal of Power Sources* **2000,** *87* 101-105.
105. Zhuang, Z.; Giles, S. A.; Zheng, J.; Jenness, G. R.; Caratzoulas, S.; Vlachos, D. G.; Yan, Y., *Nat Commun* **2016,** *7*.
106. Gasteiger, H. A.; Kocha, S. S.; Sompalli, B.; Wagner, F. T., *Applied Catalysis B: Environmental* **2005,** *56* 9-35.

107. Elbert, K.; Hu, J.; Ma, Z.; Zhang, Y.; Chen, G.; An, W.; Liu, P.; Isaacs, H. S.; Adzic, R. R.; Wang, J. X., *ACS Catalysis* **2015,** *5* 6764-6772.
108. Strmcnik, D.; Uchimura, M.; Wang, C.; Subbaraman, R.; Danilovic, N.; van der Vliet, D.; Paulikas, A. P.; Stamenkovic, V. R.; Markovic, N. M., *Nature Chemistry* **2013,** *5* 300-306.
109. Wang, Y.; Wang, G.; Li, G.; Huang, B.; Pan, J.; Liu, Q.; Han, J.; Xiao, L.; Lu, J.; Zhuang, L., *Energy & Environmental Science* **2015,** *8* 177-181.
110. Bard, A. J.; Faulkner, L. R., *ELECTROCHEMICAL METHODS: Fundamentals and Applications*. 2 ed.; JOHN WILEY & SONS, INC.: 2001.
111. Tarascon, J.-M.; Armand, M., *Nature* **2001,** *414* 359.

Chapter 2 – Description of Synthesis, Characterization, and Experimental Methods

2.1.Synthesis Methods

A vast amount of synthetic methods exists for the formation of 0D and 1D nanomaterials, including but not limited to hydrothermal,[1] molten salt,[2] sol-gel,[3, 4] electrospinning, template-directed,[5-7] and solution-based syntheses.[8] Two different philosophical approaches can be discussed for the synthesis of nanomaterials, namely bottom-up and top-down protocols. The bottom-up approach involves the self-assembly of smaller components into a larger material, whereas the top-down approach refers to the etching or successive cutting of a bulk material to generate smaller components.[9] The bottom-up approach allows for a better systematic control over the synthesis of nanomaterials whereas the top-down approach has the potential for problems such as damage to the overall surface structure as well as the introduction of defects and/or contaminants. A general scheme depicting both approaches can be found in Figure 2.1. The next few sections will describe a variety of techniques, i.e. all bottom-up approaches, utilized to synthesize the different nanomaterials within this thesis.

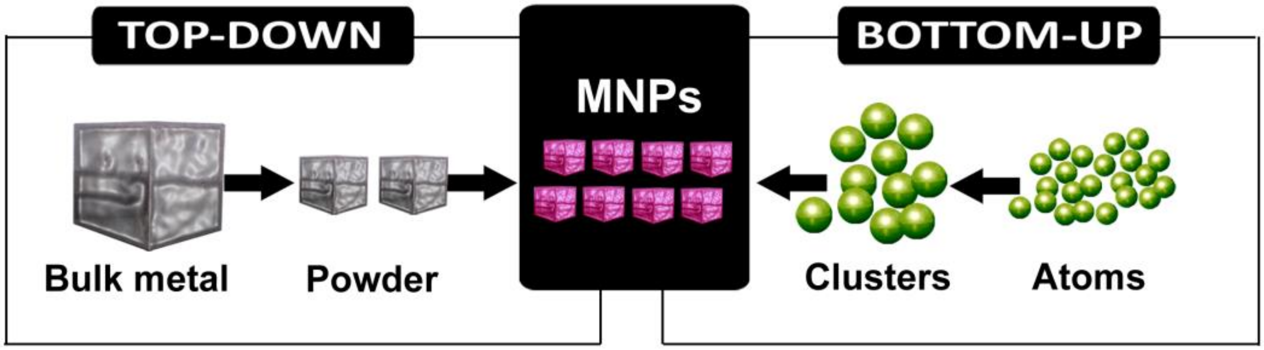

Figure 2.1. Scheme depicting both a bottom-up and top-down approach for the synthesis of metal nanoparticles. Taken from Ref 9.

2.1.1. Hydrothermal Synthesis

Hydrothermal synthesis involves a heterogeneous reaction in a closed system under high temperature and pressure conditions utilizing aqueous solvent that ultimately dissolves and recrystallizes materials that otherwise would not form under ambient conditions.[10] This type of synthetic method allows for the control over a significant amount of reaction parameters including reaction time, temperature, and pressure as well as the specific solvents and precursors.

This particular technique can not only generate monodisperse but also highly homogenous materials. Hydrothermal synthetic methods possess a number of potential advantages over other synthesis processes in terms of the characteristics of the resulting products, including high purity, homogeneity, crystal symmetry, narrow particle size distributions, and the possibility of scale-up procedures for increased product generation.[10, 11] The high pressures employed for this method allow for the generation of highly crystalline materials, at relatively low temperatures, since typical operating temperatures reside between 100 and 200°C. This technique can be employed to synthesize a range of materials including ZnO nanowire arrays,[12] Bi_2WO_6 nanoplates,[13] TiO_2/graphene composites,[14] SnO_2 microspheres,[15] and many others. This method has been utilized to synthesize both the TiO_2 nanoparticles[16] and 40 nm $SrTiO_3$ nanoparticles[17] within this thesis.

2.1.2. Molten Salt Synthesis

The molten salt method possesses significant advantages as compared with other methods, particularly its ability to scale up to large quantities as well as its generalizable nature. In a typical reaction, precursors are combined with a salt mixture, either with or without a surfactant in order to dictate morphology, in a boat and placed within a furnace for a specified period of time at a certain temperature. In fact, a number of factors influence the nature of the resulting materials synthesized including (i) the size and composition of the salt employed, (ii) the melting point of the salt or salt mixture, (iii) the reaction time and temperature, and (iv) the chemical composition and morphology of the precursors.[18] Control over all of these parameters can lead to the corresponding ability to fine tune the nature of the resulting products so as to create the desired composition and morphology.

More specifically, a molten salt consists of either a compound or compounds that can melt to generate a liquid state that possesses a certain degree of ionic properties.[19] Typically, an acid acts as an oxide acceptor, whereas a base acts as an oxide donor in the overall reaction.[20] The salt mixture employed generally consists of either sulfates or chlorides that are mixed with the starting materials and heated to the designated reaction temperature.[19] The specific salt employed also dictates the reaction temperature, due to its specific melting point. The range of reaction temperatures can be further expanded by creating mixtures of various salts. Moreover, a variety of materials such as $BaTiO_3$ nanostrips,[21] $SrRuO_3$ nanoparticles,[2] MnO_2 nanowires,[22] TiO_2 nanorods,[23] and $BiFeO_3$ nanocubes.[24] In particular, the 113 nm $SrTiO_3$ nanoparticles[25] and 146 nm $SrRuO_3$ nanoparticles[22] studied in this thesis were synthesized via this method.

2.1.3. Sol-Gel Synthesis

Similar to other synthetic methods, the sol-gel technique is highly versatile. The sol-gel process possesses 6 steps:[26]

(i) Formation of the sol. This is usually characterized by either an alkoxide or solvated metal solution;

(ii) Gelation process, which is typically indicative of the formation of an oxide. This step results in an increase in the viscosity of the solution.

(iii) ‘Syneresis’, or aging of the gel, in which polycondensation reactions occur to form a solid. This leads to a contraction in the gel network as well as the removal of liquid from the pores. Phase transformations usually occur during this step.

(iv) Drying of the gel, in which other liquids are further removed from the gel. If the gel is dried thermally, the resulting material is called a xerogel. If the liquids are removed under supercritical conditions, the resulting substance is an aerogel.[27, 28] Aerogels tend to maintain an overall porous structure, maintaining pore volumes of up to 98%. By contrast, xerogels may shrink during the process of drying and give rise to a far less porous structure.

(v) Dehydration of the product through removal of the –OH groups at the surface. This usually occurs under a heating protocol.

(vi) Decomposition of the gel at high temperatures, usually exceeding 800°C. The last step is more than often necessary in order to crystallize the resulting material, since prior to that step, the material is usually amorphous.[28]

While the sol-gel method yields a number of benefits, a significant disadvantage is the lack of control over morphology. However, variations in pH as well as specific solvent can have some impact on the resulting morphology.[29] Moreover, many types of nanomaterials have been synthesized using this method including NiO nanoparticles,[30] ZnO-coated $LiMnPO_4$ particles,[31] $NiCoFe_2O_4$ nanoparticles,[32] and TiO_2 nanoplates.[33] In this thesis, 35 nm RuO_2 nanoparticles[34] were synthesized by this method.

2.1.4. Template-Directed Synthesis

Template-directed synthesis methods are known to be rather simple, environmentally friendly, and highly applicable to the synthesis of a variety of materials.[18] The use of a template removes the necessity of a surfactant to initiate one-dimensional growth. In a standard synthesis, the template serves as a spatially confining framework for the growth of particular materials. The pores of the template possess a particular size, which dictates the overall diameter of the products. In general, the chemical and structural properties of the membrane allow for significant control over the morphology and size of the synthesized material. A variety of 1D nanomaterials have been synthesized within our group employing this method, including $Pd_{1-x}Pt_x$ nanowires,[35] Ru nanowires,[7] Cu nanowires,[5] and $YMnO_3$ nanowires.[4] Others have, by analogy, produced V_2O_5 nanowires,[36] Co_3O_4 nanowires,[36] $BaTiO_3$ nanorods,[37] and $Sr_2Nb_2O_7$ nanorods.[37] More importantly, this method was used to synthesize the $LiFePO_4$ nanowires[38] discussed in this thesis.

2.1.5. Solution-Based Synthesis

Solution-based methods possess distinct advantages over all other synthetic methods due to their inherent simplicity, ability to scale-up, as well as their flexibility to be tailored.[39] For instance, precursors, solvents, surfactants, and oxidizing/reducing agents can be substituted and replaced with potentially a wide array of more environmentally friendly choices. In addition, variations in specific reaction parameters such as the pH, the reaction time, temperature, concentration, stirring rate, and so on can also be explored.[40]

Moreover, solution-based strategies have been employed to synthesize a wide array of nanomaterials to date such as spinel cobalt oxide nanoparticles,[41] $BiNnO_4$ nanopowders,[42] ZnO nanorods,[43] $Li_4Ti_5O_{12}$ mesoporous nanoclusters,[44] as well as the Pt-based alloy nanowires synthesized within this thesis.[45-47]

2.2.Characterization Methods

2.2.1. Electron Microscopy Characterization Methods

2.2.1.1.Transmission Electron Microscopy

Transmission electron microscopy (TEM) is a microscopy technique employed to characterize the morphology of a material, in which an electron beam is focused and passed through a material at a high voltage. The electron beam then comes in contact with lenses that generate an image based upon the interaction between the electron beam and the material. Typically, this image is magnified and focused onto either a layer of film or detected by a CCD camera. Moreover, 2 types of TEM images can be collected, namely a ‘bright-field’ image or ‘dark-field’ image. In a bright-field image, only unscattered electrons are collected, which results in a darker image. We explain this result based on fewer electrons reaching the image plane due to more scattered electrons. Conversely, in a ‘dark-field’ image, scattered electrons are collected, giving rise to the brighter ‘appearance’ of the material.

TEMs have the capability for detecting individual atoms, when magnifying in high resolution. This type of microscopy is called high-resolution TEM, or HRTEM. Using HRTEM, useful information pertaining to the atomic structure as well as the growth direction can be collected. However, this type of characterization method does not necessarily provide for a qualitative understanding of the sample as a whole. TEM instruments have the ability to image contrast due to the different adsorptive capabilities of electrons as a result of variations in the composition as well as in the thicknesses of the sample materials. However, accelerating voltages need to be considered prior to analysis, since damage can occur to the sample as a result of the incident electron beam energy.

TEM instruments can help to discern variations in morphology, composition, chemical purity, electronic structure, and crystal orientation. As a result, this characterization technique is employed in a variety of fields, including nanotechnology, biology, cancer research, virology, materials research, as well as polymer research. An example of a TEM instrument and its individual components can be found in Figure 2.2. Additionally, the nature of the interaction of a TEM electron beam with a specimen is highlighted in Figure 2.4.

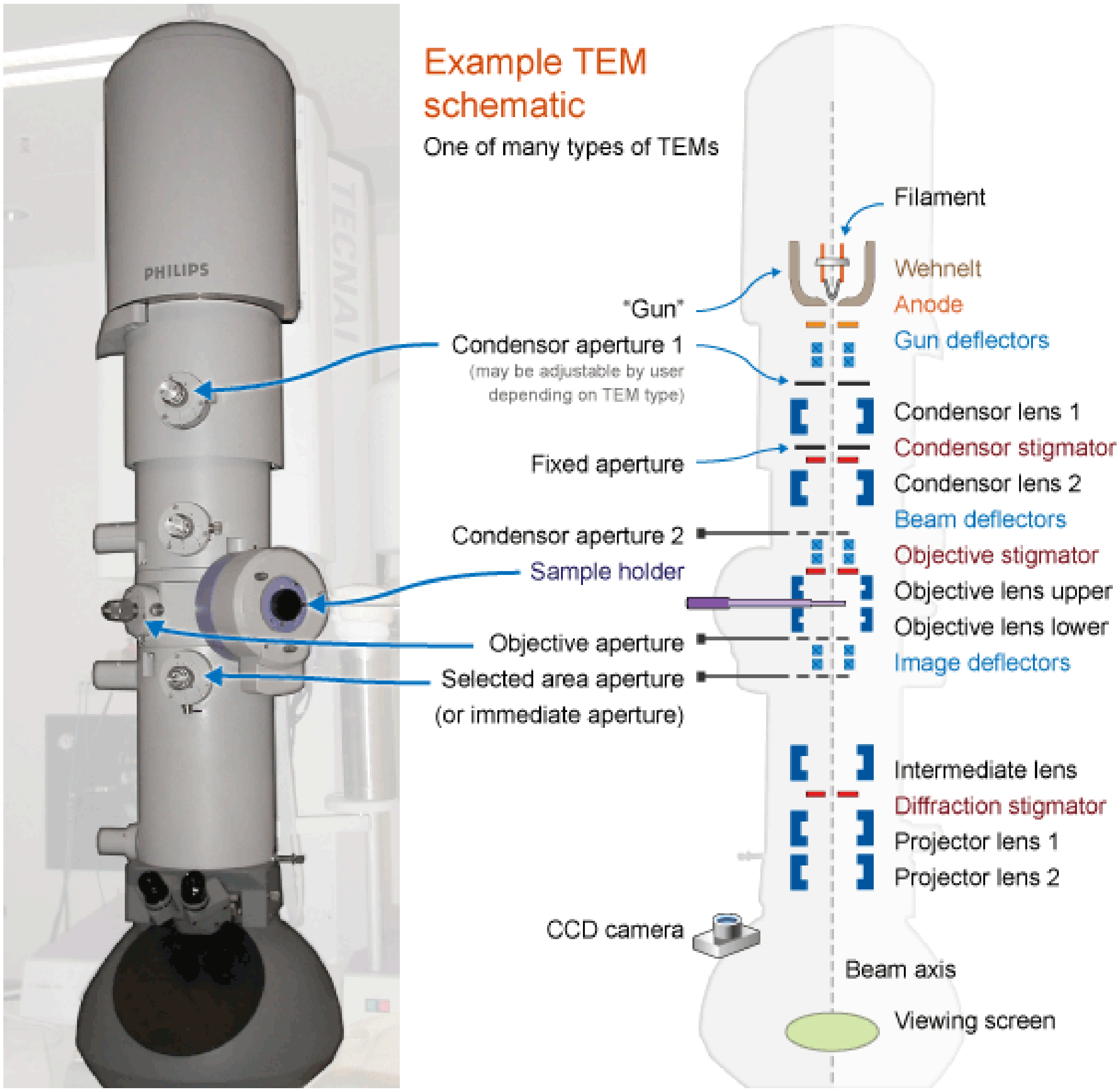

Figure 2.2. Depiction of transmission electron microscope and individual components. Taken from the Australian Microscopy and Microanalysis Research Facility Website.

2.2.1.2.Selected Area Electron Diffraction

As an ancillary and complementary data set for the TEM, a selected area electron diffraction (SAED) pattern can be collected and can be generated, when electrons are diffracted by the atoms within a specific material, determined by the crystal structure. With the electrons being scattered at different angles by the single crystalline material, the resulting image will consist of an array of spots, with each spot corresponding to a specific diffraction condition of the material's crystal structure. As the sample is rotated or tilted, different diffraction spots will appear, corresponding to new diffraction conditions. If the material is polycrystalline and possesses many different constituent subcrystals with various orientations, rings are formed as a result of an averaging of the spots, similar to what is attained by XRD, thereby allowing for identification. That is, the distances between the central spot and the rings correspond to the various d-spacings of the material.

2.2.1.3.Scanning Electron Microscopy

A scanning electron microscope (SEM) is another specialized instrument that aids in characterizing morphology. Specifically, the instrument scans a focused electron beam across the material being analyzed. These electrons interact with the atoms at the surface generating signals associated with the surface structure and topography. These signals are produced by different types of scattered electrons. Back-scattered electrons are electrons that have been elastically scattered with the same energy that they had prior to hitting the specimen. Heavier materials tend to back-scatter electrons more strongly, and hence, appear brighter in SEM images. Back-scattered electrons are highly useful for analyzing the shape and size of materials. Additionally, secondary electrons result from inelastic scattering when coming into contact with the sample, and contain significant amount of information about the surface of the material. Although some SEM instruments yield spatial resolutions better than 1 nm, typically this technique is used to characterize larger materials.

2.2.2. X-Ray Characterization Methods

2.2.2.1. X-ray Diffraction

X-ray diffraction (XRD) is a technique used to identify the particular atomic structure of a crystalline material. Specifically, X-rays are generated when a focused electron beam shoots electrons through a high voltage field at a material. As the electrons bombard the material, inner shell electrons are ejected as a result of an ionization process. Once a free electron fills the shell, an X-ray photon is emitted, corresponding to the energy of the material. Additional X-rays are also generated when the electron beam hits the target material.

Synchrotron XRD is slightly different in that electrons or positrons are shot under near light speed conditions around a circular ring. As a result, the intensity of the synchrotron electron beam is at least 2 orders of magnitude stronger and more intense than the sources associated with a standard X-ray tube.[48]

When X-rays hit the desired material, some photons will be deflected and change direction, a process known as scattering. If the wavelength does not change, meaning only momentum is transferred, this is called either elastic scattering or Thompson scattering. These are the X-rays measured, since they carry information about the material. If energy from the X-rays is transferred to the atoms, the scattered X-rays will possess a different wavelength, a process which is called either inelastic scattering or Compton scattering.

The acquired XRD patterns can provide important information, pertaining to the sample material. In particular, (i) the position of the diffraction peaks is defined by both the size and composition of the material, (ii) the intensity ratio of the peaks is controlled by the location and type of atoms within the unit cell, and (iii) the shape and width of these peaks are determined by the intrinsic structural properties of the material, such as strain, defects, and crystallite size. In order to calculate the crystallite size of one's material, the Scherrer equation below, i.e. Equation [2.1], is employed, wherein T is the mean crystallite size of the material, K is the dimensionless shape vector of the crystallite size, which is typically around 0.9, λ is the X-ray wavelength, β is the line broadening measured at half intensity after subtracting the instrumental line broadening, and cos θ is the Bragg angle, which is the angle between the X-ray beam and a given set of crystalline planes.

$$T = \mathrm{K}\lambda / \beta\cos\theta \qquad [2.1]$$

Additionally, as mentioned above, the XRD patterns are directly related to the atomic distances within the structure analyzed. Bragg's Law, i.e. Equation [2.2] below, can help to determine the conditions necessary for diffraction peaks to be observed, with 'd' representing the inter-plane distance, 'n' corresponding to the order of the diffraction peak, λ affiliated with the wavelength of the X-ray, and θ associated with the scattering angle. A visual representation of Bragg's law can be found in Figure 2.3.

$$2d \sin\theta = n\lambda \qquad [2.2]$$

The main method used in this thesis will pertain to powder XRD, which means that our samples are studied in powder form. A powder sample contains crystalline domains that are randomly oriented within the material. As a result, data consisting of either the d-spacings or 2θ values will be collected. Additionally, high-resolution synchrotron XRD will also be discussed.

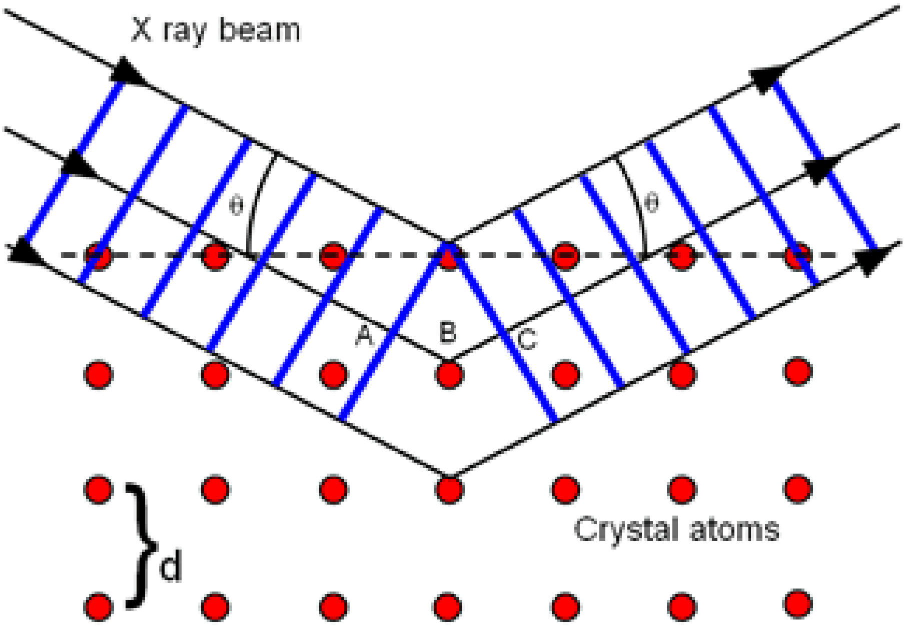

Figure 2.3. X-ray diffraction theory, corresponding to Bragg's Law. Reflection of X-ray beams (black arrows) by crystal atoms (red circles) within a sample. θ corresponds to the scattering angle as a result of the X-rays being deflected by atoms within the sample. The θ value can be used to determine the d-spacings of the material. Taken from iop.org.

2.2.2.2.X-Ray Photoelectron Spectroscopy

X-ray photoelectron spectroscopy (XPS) is a technique employed to determine the surface chemistry of a material. XPS can determine the elemental composition, empirical formula, and the electronic states of the elements within the material. In this technique, the surface of a material is irradiated by soft (low energy) X-rays, such as either an Al Kα X-ray source (hν = 1486.6 eV) or a Mg Kα X-ray source (hν = 1253.6 eV), a process which cause electrons to be ejected from the top 10 nm of the material. The electrons will only be ejected if their binding energy is lower than the intrinsic energy of the X-ray source itself. The XPS instrument simultaneously measures the kinetic energy of the emitted electrons. For example, Pt metal possesses a binding energy of 71 eV, corresponding to the *4f* region ($4f_{7/2}$ peak).

In a typical spectrum, the peak intensities correspond to the amount of material at the surface, whereas the peak positions pertain to the elemental and chemical composition. In order to determine the binding energy of the electron, or the amount of energy needed to remove the electron from the surface, information about the kinetic energy as well as the photon energy is often needed. The equation used to determine the specific binding energies ($E_{Binding}$) for a particular element can be found below:

$$E_{Binding} = E_{Photon} - (E_{Kinetic} + \phi) \qquad [2.3]$$

E_{Photon} corresponds to the specific energy of the photons being used, $E_{Kinetic}$ is related to the energy of the electrons measured by the instrument, and ϕ (work function correction) is the instrument correction factor that accounts for the kinetic energy given up by the photoelectron when being adsorbed by the detector.[49] The binding energy is influenced by a number of factors including (i) the element from which the electron was removed, (ii) the specific orbital from which the electron was removed, and (iii) the chemical state of the atom from which the electron was ejected.

2.2.2.3.Energy Dispersive Analysis of X-Rays

Energy dispersive analysis of X-rays (EDAX) is an analytical tool used to determine the elemental makeup and chemical composition of a material. By analogy with the other X-ray techniques above, an electron beam is focused onto a sample. The X-rays cause electrons to be ejected from an inner shell such as either the K or L shell, thereby causing a higher energy electron to settle in the hole that was created. During the process of an electron being ejected from an outer shell, such as the M shell, thereby filling the inner shell vacancy, an X-ray corresponding to the difference in energy between the shells is emitted and detected by the EDX spectrometer.[50] Figure 2.4 describes electron beam interactions with the sample, thereby leading to information associated with EDX (or EDS in figure), electron energy loss spectroscopy (which will be discussed in detail below), as well as electron diffraction, all occurring within a TEM.

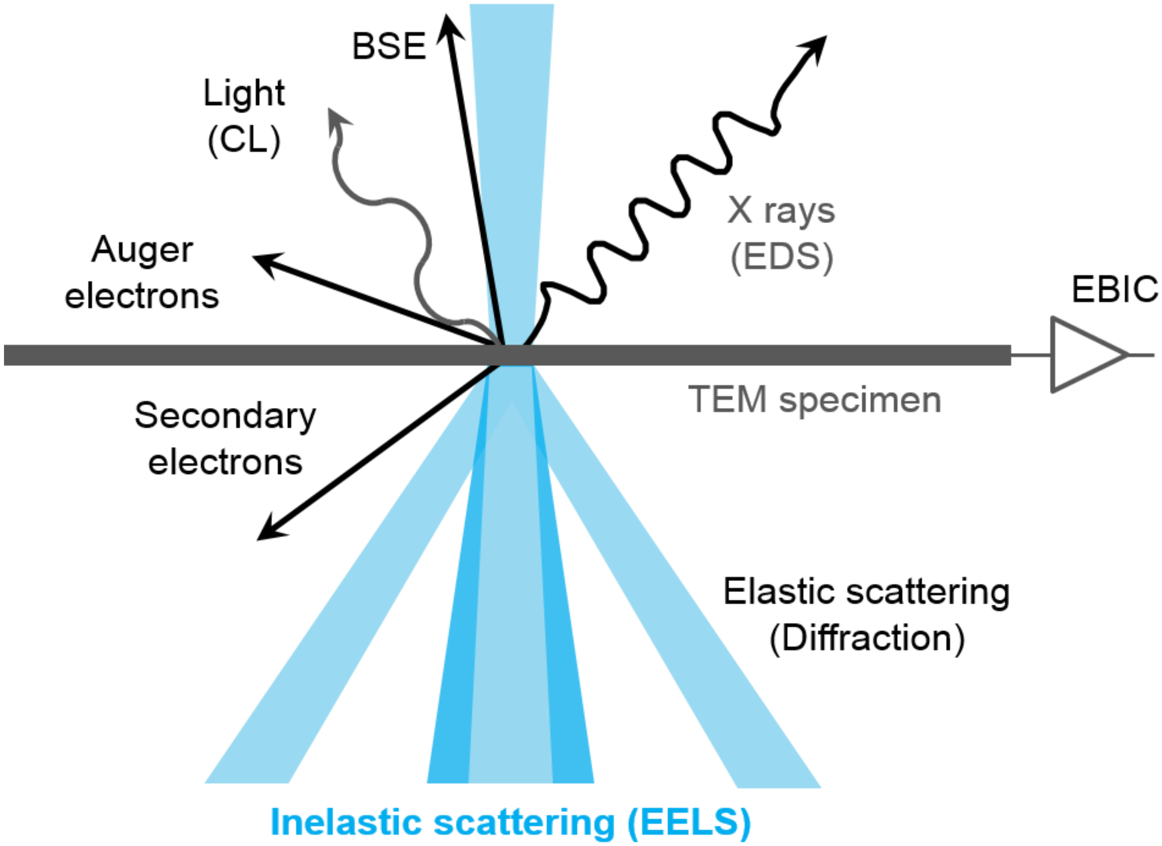

Figure 2.4. TEM beam interaction. An electron beam is focused onto a sample, with some being scattered elastically (back-scattered electrons – BSE) and inelastically. In order for the sample to de-excite, energy is given off through either Auger electrons, photons, or X-rays. Electrons that are scattered inelastically are analyzed for EELS analysis, elastically-scattered electrons are used for diffraction analysis, and X-rays are used for EDS analysis. Taken from gatan.com

2.2.2.4.Electron Energy Loss Spectroscopy

Electron energy loss spectroscopy (EELS) is a technique that probes the atomic composition, valence and conduction band properties, chemical bonding, and surface properties. In this technique, a beam of electrons is focused onto the specific material being analyzed. Once the electrons hit the surface of the material, some electrons are scattered inelastically, ultimately losing energy. This causes the sample to be in the excited state, so the material will need to give off energy to return to its ground state. The amount of energy given off can be quantified and is manifested in the form of either Auger electrons or X-rays. The scattered electrons that come off the sample are then detected, and the electron energy loss signal is measured.

As compared with EDX spectroscopy, EELS is better for detecting and characterizing elements with low atomic numbers, particularly starting with carbon.[51] In addition, it is more facile to identify different forms of information associated with metals, such as oxidation states as compared with EDX. This is mainly due to the difference in energy resolution between the two techniques (up to 80% detection rate at low counts for EELS vs. < 1% for EDX).[52]

2.2.3. Surface Area Characterization Methods

2.2.3.1.Brunauer–Emmett–Teller Theory

The Brunauer-Emmett-Teller (BET) technique involves the physical adsorption of molecules, such as nitrogen, carbon dioxide, argon, and so forth, onto a material’s surface followed by its subsequent removal in order to determine the overall surface area of the material. BET theory is based upon a monolayer to multi-adsorption model updated from the Langmuir theory, with three hypotheses: (i) the gas molecules adsorb onto the surface infinitely as multi-layers, (ii) there are no interactions between the individual layers, and (iii) the Langmuir theory (which will be described below) can be used to describe each adsorption layer.[53]

The Langmuir theory is based upon 5 assumptions:

(i) there are a fixed number of active sites on the surface, (ii) all sites are of equal shape and size, (iii) every active site can only adsorb one gaseous molecule with each, releasing the same amount of heat energy, (iv) there is an dynamic equilibrium between the site and the gaseous molecules, and (v) the adsorption of molecules can only form a monolayer.[54]

The Langmuir theory does not necessarily account for a variety of factors. More particularly, this model only holds true under low pressure conditions wherein the gaseous molecules are in vapor phase and multilayers of gaseous molecules cannot form. Additionally, it assumes that the surface of the material is homogeneous. However, the active sites are not necessarily identical in size and shape. More importantly, it does not account for the weak interactions between the gaseous molecules. In fact, it assumes no interactions, in addition to a lack of randomness in adsorption. BET theory differs to some degree from the Langmuir theory and incorporates five slightly modified assumptions:

(i) the various gases only adsorb onto individual sites of a well-defined surface, one molecule per site, (ii) an adsorbed molecule can act as a single adsorption site for another molecule, (iii) the top layer of molecules is in equilibrium with the gas phase, (iv) the desorption of a molecular layer is kinetically limited (i.e. each molecule layer has its own heat of adsorption, the aggregate of all other layers except for the initial layer is assumed to be a condensed species, and therefore the heat of adsorption is equal to the heat of liquefaction), and (v) at the saturation pressure, an infinite amount of molecular layers exist.[55]

However, some disadvantages nevertheless exist with the BET model. Similar to the Langmuir model, a homogeneous surface is assumed. Additionally, some adsorbate interaction is accounted for but lateral interactions between the molecules are neglected. Finally, the heats of adsorption for all layers beyond that of the initial monolayer are assumed to be equal.

The BET equation, Equation [2.4], which is an adsorption isotherm equation, can be found below with p and p_0 corresponding to equilibrium and saturation pressure at the specific temperature for molecule adsorption, with υ pertaining to the total gas adsorption quantity assuming multilayer adsorption and υ_m corresponding to the monolayer adsorption amount.

Additionally, the values are needed to solve for c, the BET constant, Equation [2.5], E_1 which corresponds to the heat of adsorption for the first monolayer, E_L which is affiliated with the heat of liquefaction of all other layers, and R, corresponding to the gas constant with T representing the temperature in Kelvin.

$$\frac{1}{\upsilon[\frac{p_0}{p-1}]} = \left[\frac{c-1}{\upsilon_m c}\right]\left[\frac{p}{p_0}\right] + \frac{1}{\upsilon_m \mathrm{c}} \qquad [2.4]$$

$$c = e^{\frac{(E_1 - E_L)}{RT}} \qquad [2.5]$$

In order to create a BET plot, the value determined from this specific part of Equation [2.4], i.e. $(1/\upsilon[p_0/p1])$, is plotted along the y-axis with (p/p_0) plotted along the x-axis. The slope (A) as well as y-intercept (I) are then used to determine υ_m, or a monolayer-adsorbed gas quantity in Equation [2.6], as well as c, the BET constant related to the heats of adsorption in Equation [2.7].

$$\upsilon_m = \frac{1}{A + I} \qquad [2.6]$$

$$c = 1 + \frac{A}{I} \qquad [2.7]$$

2.3.Electrochemical Characterization Methods for Fuel Cells

2.3.1. Cyclic Voltammetry

Cyclic voltammetry is a potentiodynamic electrochemical method used to study the electrochemical properties of a system. With this method, the potential is swept as a function of either time. Once a certain potential is reached, it reverses direction. An anodic current occurs when electron flow travels from the solution to the electrode, whereas a cathodic current is characterized by an electron flow taking place from the electrode to the solution. Examples of CVs can be found in Figure 2.5 as well as Figure 2.6. The characteristics found in these CVs provide information about the surface structure, active sites, and the interaction with various adsorbates. Some common adsorbates include hydrogen, oxygen, and carbon monoxide. The various regions of a CV will be discussed below with Figure 2.5 depicting two CVs corresponding to the Pt (111) surface in both acid and alkaline media.

2.3.1.1.Hydrogen Adsorption/Desorption Region

The hydrogen adsorption/desorption region or hydrogen underpotential deposition region (H_{upd}) is characterized by atomic hydrogen that is adsorbed onto a specific metal substrate at a potential that is positive to the Nernst potential (0.0 V vs. RHE) for the hydrogen evolution reaction (HER).[56] The maximum saturation coverage (1 monolayer) of H_{upd} on Pt is 0.66/Pt, which may be attributed to the repulsive lateral interaction in the hydrogen adlayer.[56] The specific bond energies for underpotentially deposited hydrogen adsorbed to a Pt (111) surface in either acidic or alkaline environments are ~ 240 – 250 kJ/mol.[56]

The hydrogen adsorption region (i.e. 0.05 V – 0.375 V) on a Pt (111) surface in both acid (H_2SO_4) and alkaline (KOH) electrolytes is characterized by flat broad peaks attributed to solely hydrogen adsorption/desorption rather than a combination of that with anion adsorption. Examples of representative CVs collected on Pt (111) surfaces in both acid (H_2SO_4) as well as alkaline (KOH) media can be found in Figure 2.5. In acid, hydrogen adsorption occurs via Reaction [2.1], whereas Reaction [2.2] describes adsorption in alkaline media:[56]

$$\mathrm{Pt} + \mathrm{H_3O^+} + e^- \rightarrow \mathrm{Pt\text{-}H_{upd}} + \mathrm{H_2O} \quad [2.1]$$

$$\mathrm{Pt} + \mathrm{H_2O} + e^- \rightarrow \mathrm{Pt\text{-}H_{upd}} + \mathrm{OH^-} \quad [2.2]$$

At slightly more positive potentials (i.e. 0.4 – 0.6 V) in H_2SO_4, additional reversible peaks can be seen, which are attributed to the reversible adsorption of (bi)sulfate anions. In KOH as well as $HClO_4$, peaks can also be found between 0.6 – 0.85 V, which are attributed to the reversible adsorption of hydroxyl anions.[56] Specifically, the bond energy for the adsorption of hydroxyl groups on a Pt (111) surface in an alkaline electrolyte is approximately 136 kJ/mol.[56] Moreover, the charge of the H_{upd} region is commonly used to calculate the electrochemical accessible surface area (ECSA) of Pt catalysts.

In this dissertation, we use the H_{upd} region (both hydrogen adsorption and desorption region) in order to determine the average surface area of our catalysts. The charge of the H_{upd} region can be used to determine the geometric surface area of Pt catalysts. Moreover, the integration area accounts for both the hydrogen adsorption and desorption charges, as well as the correction for the double layer charge. The double layer region is the region where there is no faradaic process. For Pt it resides between H_{upd} and Pt-OH formation. A representative CV corresponding to synthesized Pt NWs including labeled H_{upd} regions, oxide regions, as well as double layer regions, demonstrating the double layer correction, is highlighted as Figure 2.6.

The theoretical charge for a monolayer of adsorbed hydrogen is converted to the geometric surface area using the conversion factor (i.e. 210 $\mu C/cm^2$ – the charge needed to desorb hydrogen).[57] In addition, this region can provide insight into the types of active sites present, including information about variations in hydrogen binding energy (HBE) in addition to the surface structure of the catalysts.

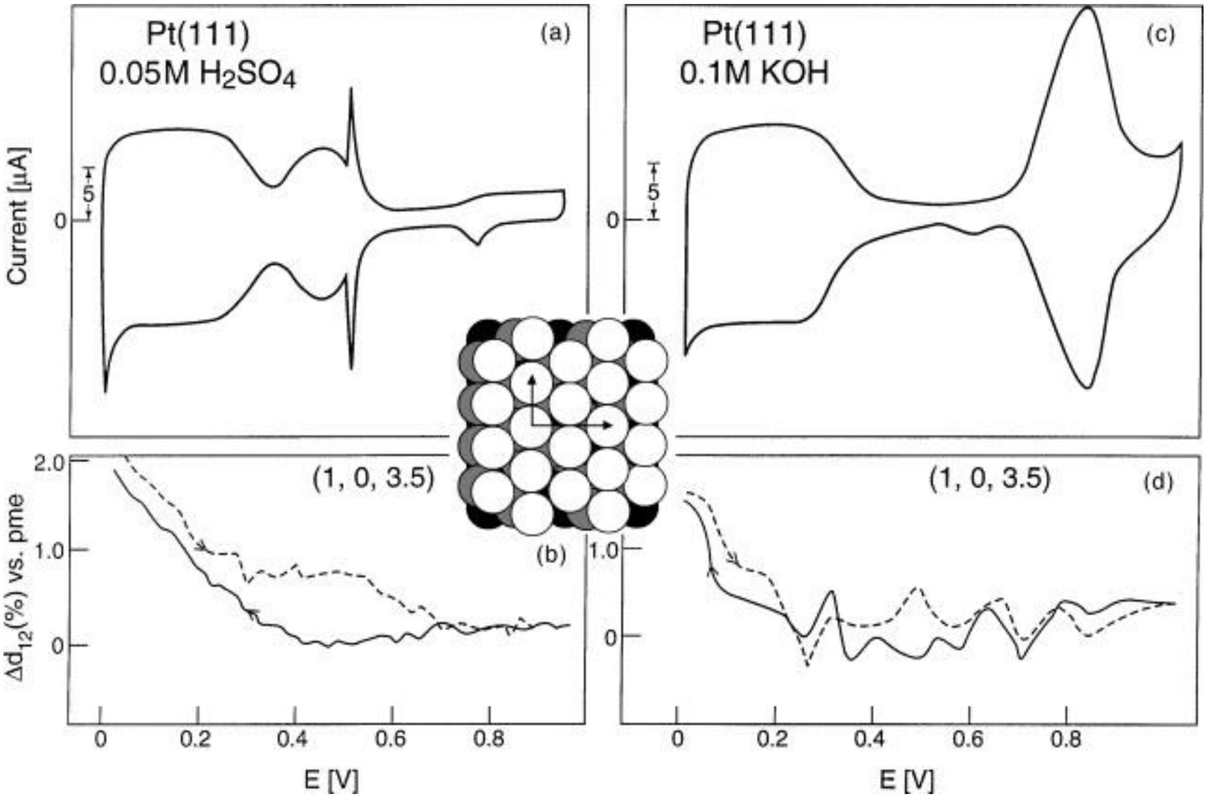

Figure 2.5. Cyclic voltammetry of the Pt (111) surface in an electrochemical cell: (a) in H_2SO_4 and (c) in 0.1 M KOH. The potential was scanned at 50 mV/s. Changes in inter-layer spacing (Δd_{12}) measured from the potential of minimum expansion (PME) (e.g., the least coverage by any adsorbates) on scanning the potential at 2 mV/s (b) in H_2SO_4 and (d) in 0.1 M KOH. Insert: ideal model for the Pt(1 1 1)-(1 × 1) surface. Electrode potential E is given vs. the reversible hydrogen electrode (RHE). Taken from Ref. 54.

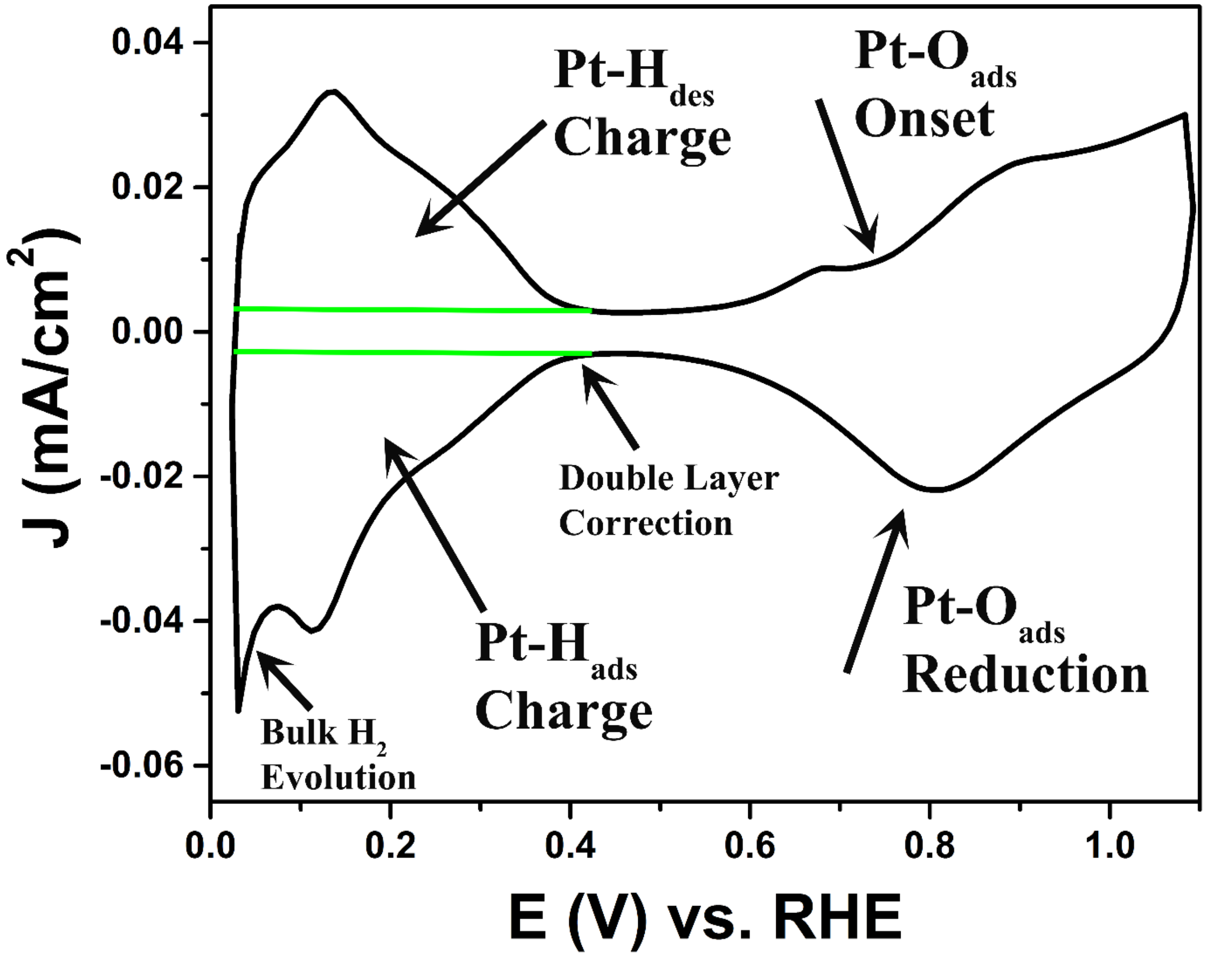

Figure 2.6. A representative CV, corresponding to synthesized Pt NWs is shown with the H_{upd} regions (hydrogen adsorption/desorption) and oxide regions labeled. The green vertical lines indicate the double layer correction, when determining the integrated H_{ads} and H_{des} charges.

2.3.1.2.Oxide Region

The oxide region is characterized by the adsorption of oxygen in the anodic sweep, followed by the subsequent desorption during the cathodic sweep. This can be seen in (c) of Figure 2.5 between 0.6 V – 0.85 V. At low temperatures (< 500 K) and low pressures, the saturation coverage for atomic oxygen is 0.25 monolayer ML on Pt (111) with the oxygen atoms situated in 3-fold hollow sites.[56] This region provides for insight about how a particular catalyst binds oxygen, more specifically, the strength of binding oxygen. The oxide adsorption and reduction regions (Pt-O_{ads}) on our synthesized Pt NW system are explicitly highlighted in Figure 2.6.

2.3.1.3.Double Layer Region

The double layer region or electrical double layer typically resides between 0.6 V – 0.75 V in H_2SO_4 electrolyte, as seen in (a) of Figure 2.5. Moreover, the double layer region of our as-synthesized Pt NW sample in an $HClO_4$ electrolyte can be found in Figure 2.6. The first model of the double layer was proposed by Helmholtz, and can be found in (a) of Figure 2.7. In the double layer region, the metal surface possesses a surface charge in which oppositely charged ions electrostatically rearrange at the surface in order for the overall layer to remain neutral. As a result, a potential drop occurs at this region, designated as the outer Helmholtz Plane (OHP).

In the Gouy-Chapman model found in (b) of Figure 2.7, which made significant improvements based upon the Helmholtz model, the existence of a diffuse layer is generated. Rather than having negative stationary ions at the interface counterbalancing the positive charge at the metal surface, the ions are free to move throughout solution. The greatest concentration of charge would exist at the interface, with charge decreasing as the distance increases. As the electrode becomes more charged, the diffuse layer should become more compact, thereby leading to a rise in the differential capacitance (C_d). An increase in electrolyte capacitance is also noted, when there is a corresponding increase in electrolyte concentration. However, this model assumes that ions can approach the surface extremely closely and does not account for the size and atomic radii of the ions.

A later model generated by Stern adapted and updated the Helmholtz and Gouy-Chapman models to incorporate and take into account a number of additional factors including the chemical nature of the metal and solvent, the type and amount of solute, the presence of diffusion/mixing, as well as the localized structures of both the metal surface and ions in solution. In this particular model, free ions are depicted to move throughout the liquid as a result of electrostatic interactions and thermal motion. However, in this model, the potential drop is expanded to include these mobile ions. This model can be found in (c) of Figure 2.7.

A number of parameters are neglected by this updated model, including the ion pairing effect within the double layer, the presence of nonspecific interactions between the ions and charged surface, as well as the fact that the capacitance associated with charges held at OHP (C_H) is currently defined as being independent of potential. Additional derivations and equations are necessary to take into account of these factors.

Moreover, some additional modifications have been made over the years to attempt to address these important issues, with the Bockris/Devanthan/Müller model being the most widely accepted. They collectively postulated that solvent molecules maintain a fixed alignment with the electrode surface. That is, the first layer of solvent molecules possesses an orientation dictated by the charge associated with the electric field. The inner Helmholz plane (IHP) passes through the centers of these specific molecules. Adsorbed molecules or partially solvated molecules exist within this plane, with fully solvated molecules residing outside the IHP, with the OHP passing through the center of these molecules. Finally, the diffuse layer exists outside of the OHP. Although this is the most widely accepted model as a result of addressing the role of the solvent in the double layer, this model still fails to address issues associated with the distribution of charges on the electrode side. Nevertheless, this is the model that is most widely employed by electrochemists, since it accounts for most of the interactions present within the double layer region.

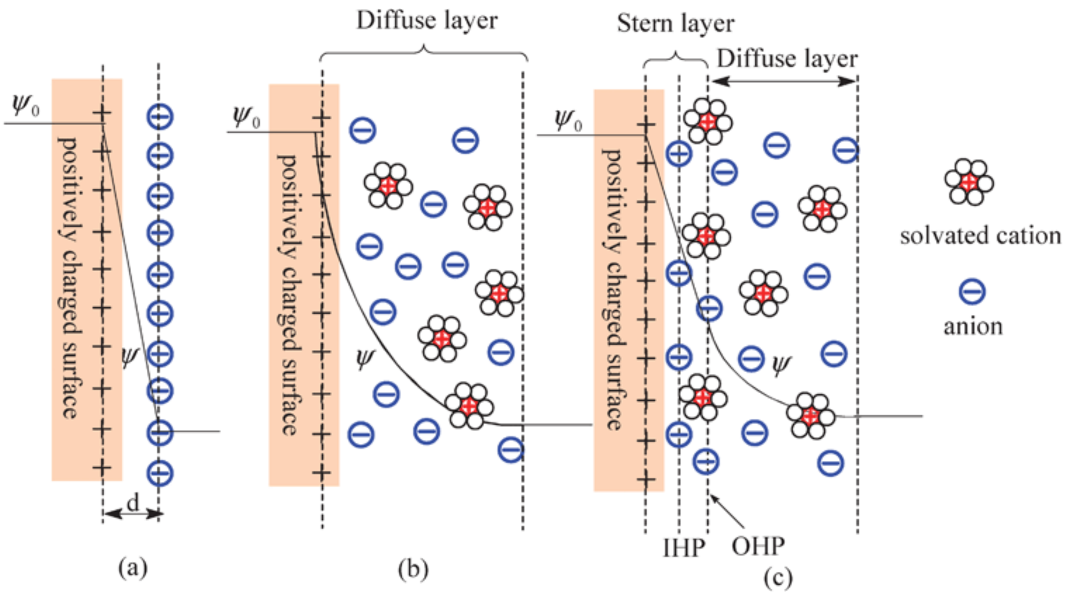

Figure 2.7. Models of the electrical double layer at a positively charged surface: (a) the Helmholtz model, (b) the Gouy–Chapman model, and (c) the Stern model, showing the inner Helmholtz plane (IHP) and outer Helmholtz plane (OHP). The IHP refers to the distance of closest approach of specifically adsorbed ions (generally anions) and OHP refers to that of the non-specifically adsorbed ions. The OHP is also the plane where the diffuse layer begins. *d* is the double layer distance described by the Helmholtz model. φ_0 and φ are the potentials at the electrode surface and the electrode/electrolyte interface, respectively. Taken from Ref. 56.

The equation to determine the capacitance of the electrical double layer can be found below in Equation [2.8]:

$$\frac{1}{C_{dl}} = \frac{1}{C_H} + \frac{1}{C_{diff}} \qquad [2.8]$$

In this equation, C_{dl} represents the capacitance in the double layer, C_H references the compact double layer resistance from the Stern layer, and C_{diff} corresponds to the diffusion layer capacitance, with both regions being shown in (c) of Figure 2.7. Multiple factors can influence the double layer capacitance at a planer electrode surface, including the electric field at the electrode, the types of electrolyte ions present, the chemical affinity between the adsorbed ions and the electrode surface, as well as the employed electrolyte.[58]

2.3.2. CO Stripping Voltammetry

CO stripping is another technique utilized to not only remove impurities at the surface, but also quantify the ECSA of catalysts, using 410 $\mu C/cm^2$ – the charge needed to desorb CO. In this technique, a monolayer of CO is adsorbed onto the surface and subsequently stripped to form CO_2 molecules. CO generally binds onto metals through electron transfer from the 5σ orbital to the metal, followed by back-donation of *d* electrons from the metal to the unfilled anti-binding $2\pi^*$ orbital of CO.[56] Additionally, since CO is either often generated as an intermediate in reactions, such as methanol oxidation or ethanol oxidation, or is present within the fuel itself such as H_2, it is a useful tool to analyze CO oxidation performance for certain catalysts that may be exposed to it.

2.3.3. Chronoamperometry

Chronoamperometry (CA) is a potential step technique, where the potential is stepped and the corresponding current produced is measured. Moreover, this relevant technique is employed to probe surface poisoning at a particular potential as a function of time. Although there is no specific requirement for duration of stability testing, it is generally accepted that 1 to 2 hours is adequate to evaluate any poisoning of the surface or degradation of the catalyst. Additionally, the potential chosen should be within the onset region for oxidation. This is necessary, since the generation of poisonous species is often simultaneously occurring with the utilization of the fuel. Typically, a sharp decrease will happen in the initial 2 minutes for most surfaces, due to poisoning of the active sites.[59] This sharp decrease has even been shown to be ~ 2 orders of magnitude lower during the 2 minute period than the initial current achieved.[60] However, the decrease in activity varies significantly, based upon the specific material.[61-64] That is, a more CO tolerant catalyst may possess only a slight drop in activity as compared with Pt, which is highly susceptible to CO poisoning. Moreover, Figure 2.8 (B) demonstrates a significant drop in the initial stages of chronoamperometry, due to significant poisoning of the active sites.

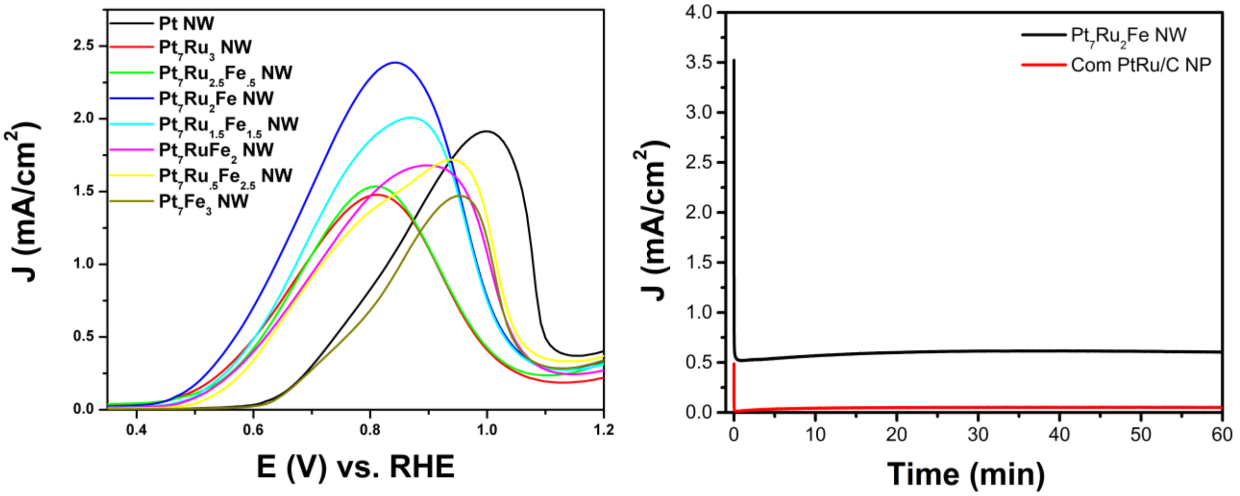

Figure 2.8. (A) Methanol oxidation reaction activities in argon-saturated 0.1 M $HClO_4$ electrolyte with 0.5 M CH_3OH at a scan rate of 20 mV/sec for a variety of binary and ternary Pt-based catalysts. (B) Chronoamperometry measurements collected for 1 hour at 0.65 V vs. RHE for our as-synthesized Pt_7Ru_2Fe NWs and commercial PtRu NP/C. Adapted by permission of The Royal Society of Chemistry from Ref. 46.

2.3.4. Determining Methanol Oxidation, Formic Acid Oxidation and Hydrogen Oxidation Reaction Performance

The particular measurements collected throughout this thesis are necessary in order to make correlations between composition and activity as well as durability. Certain parameters such as scan rate or electrolyte concentration can have a distinctive impact on the overall activity and stability of catalysts. Moreover, at a fast scan rate, i.e. 100 mV/sec, high currents are achieved, due to increased resistance, thereby resulting in unreliable results. However, at slow scan rates, depending on how fast the reaction proceeds, certain peaks may be missing due to the reaction occurring faster than the scan. Moreover, in most cases, a scan rate between 10 mV/sec to 50 mV/sec is accepted. Additionally, electrolyte concentrations can highly affect catalyst performance. As mentioned in Chapter 1, certain ions, such as either sulfate or perchlorate ions present in the electrolyte, can adsorb onto the surface and block active sites. By increasing the concentration of these particular ions in solution, less active sites will be available for the particular reaction being tested. For example, Wright and co-workers demonstrated that with increasing perchloric electrolyte concentrations (i.e. 0.05 to 2.0 M), the Pt (111) ORR activity decreased dramatically, due to specific adsorption at the Pt active sites.[65]

Hydrogen oxidation reaction (HOR) activities were determined from polarization curves collected in an H_2-saturated 0.1 M KOH electrolyte with the electrode rotating at various rotation rates (i.e. 400 rpm, 900 rpm, 1600 rpm, 2000 rpm, 2500 rpm) at a scan rate of 20 mV/s. Moreover, rotation is often needed during the reaction, since the diffusion of hydrogen is often impacted by rotation rate. With this method, the activities can be determined by the Koutecky-Levich equation, Equation [2.9], found below:

$$\frac{1}{I} = \frac{1}{I_k} + \frac{1}{I_D} \qquad [2.9]$$

The kinetic HOR current (I_k) can be determined from the current collected at the reversible potential, i.e. 0.0 V vs. RHE (I) as well as the current obtained in the diffusion-limited region (I_D), which in our case, was achieved at 0.2 V vs. RHE. Once I_k has been calculated, it is subsequently normalized to the ECSA, determined from either the H_{upd} or CO stripping charges, to obtain the exchange current density (i_0). Exchange current densities are used to evaluate catalytic activity, close to the reversible potential (i.e. 0.0 V), since this is the potential wherein HOR is kinetically limited.[66]

Additionally, Tafel plots can be created in order to determine the rate-determining step for HOR. Moreover, a Tafel plot analyzes the kinetics associated with a particular region as a function of overpotential, or the potential beyond the reduction potential determined by thermodynamics. The magnitude of the Tafel slope can be used to help in determining the rate-limiting step for the overall reaction. The hydrogen oxidation reaction proceeds either by the Tafel/Volmer or Heyrovsky/Volmer routes. These processes are additionally described in Reactions [2.3 to 2.5], with the specific reactions found below. For a Pt (111) surface at low overpotentials (< 0.05 V), the Tafel/Volmer route dominates with a Tafel slope of 50 mV/decade. However, at high overpotentials (> 0.05 V), the Heyrovsky/Volmer route occurs, evincing 150 mV/decade in 0.1 M KOH solution.[67]

Tafel Reaction $H_2 \rightarrow 2H_{ad}$ [2.3]

Heyrovsky Reaction $H_2 + OH^- \rightarrow H_{ad} + e^- + H_2O$ [2.4]

Volmer Reaction $H_{ad} + OH^- \rightarrow e^- + H_2O$ [2.5]

An example of HOR curves collected over a range of rotation rates (400, 9000, 1600, 2000, 2500 rpm) as well as a corresponding Tafel plot can be found in Figure 2.9.

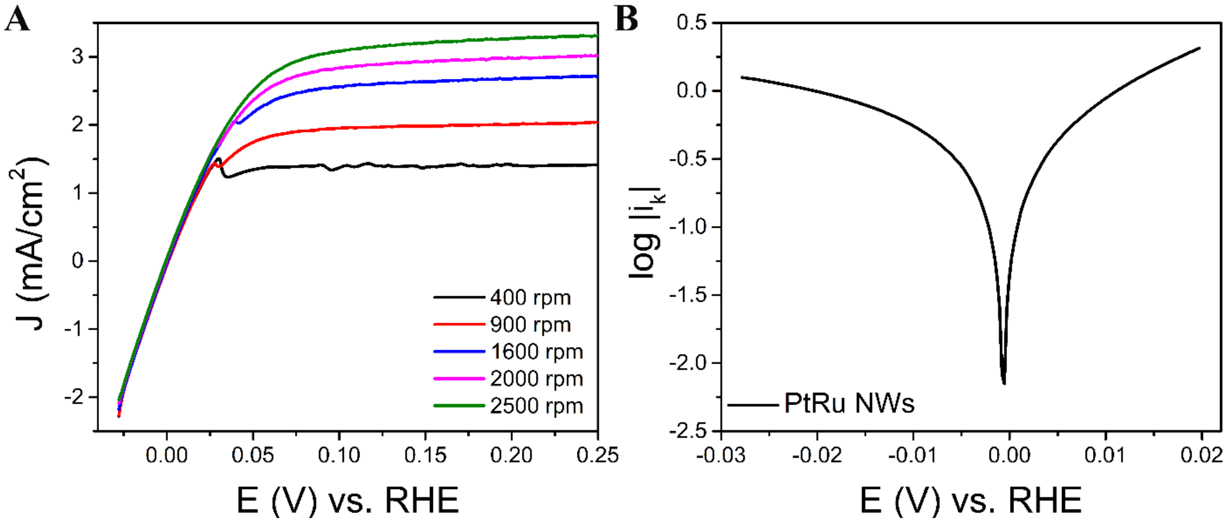

Figure 2.9. (A) HOR curves collected in hydrogen-saturated 0.1 M KOH solution at rotation rates of 400 rpm, 900 rpm, 1600 rpm, 2000 rpm, and 2500 rpm for the Pt_7Ru_3 NW catalyst. The curves are normalized to the geometric surface area of the electrode. (B) Corresponding Tafel plot using data collected in a hydrogen-saturated 0.1 M KOH solution at 2500 rpm. Adapted with permission from *ACS Catal.*, **2016**, *6*, pp 3895–3908. Copyright 2016 American Chemical Society.

Methanol oxidation reaction (MOR) activities or formic acid oxidation reaction activities (FAOR) were determined by linear sweep voltammograms in either an Ar-saturated 0.1 M $HClO_4$ or H_2SO_4 electrolyte at a scan rate of 20 mV/s with either 0.5 M methanol or 0.5 M formic acid added to the cell as the fuel. Examples of MOR curves can be found in (A) of Figure 2.8 for our as-synthesized binary and ternary NW catalysts. The activities for methanol and formic acid oxidation are determined by picking a current from the onset of oxidation, which is then subsequently standardized to the ECSA of Pt. These current values are correlated with the kinetics associated with the particular reaction. After the standardization process, either MOR or FAOR activity values are generated at a particular potential. Moreover, the specific activity can also be standardized to the geometric surface area of the electrode, if the ECSA cannot be specifically determined or relied upon. Moreover, another way of standardizing activity is through either the mass of the catalyst or the precious metal content, otherwise called mass activity (MA). Multiple routes exist to determine the mass of the catalyst including inductively coupled plasma (ICP) mass spectrometry, atomic absorption spectroscopy (AAS), or thermogravimetric analysis (TGA). Although mass activities have not been calculated within this manuscript, it serves as a useful tool to compare with the performance of other catalyst materials.

2.4.Electrochemical Characterization Methods for Li-ion Batteries

2.4.1. Electrochemical Cycling

Similar to fuel cells, Li-ion batteries are also cycled within a potential window for a period of time, thereby generating a current at a particular voltage. In a typical discharged state, Li is extracted from an oxide host at the cathode and incorporated into a carbon/silicon/tin material at the anode. During charge and discharge cycles, various types of polarization can occur to yield a difference in potential at equilibrium and under current flow. These types of polarization include ohmic overpotential, activation overpotential, and mass transport overpotential. Activation overpotential occurs when the kinetics of the reaction are limited and thereby shift the specific potential to a higher voltage. Ohmic overpotentials occur as a result of proton transfer resistance at intermediate current densities. Lastly, mass transport overpotentials exist when the concentration of a reactant material is too low at high current densities, thereby leading to mass transport losses. These types of overpotentials cause variations in the theoretically determined voltage and capacity of the battery. Additional information concerning cycling can be found in Section 2.4.1.

2.5.Synthesis and Characterization Methods used in this Thesis

2.5.1. Synthesis

2.5.1.1.Pt-based Ultrathin Nanowires

The synthesis of monometallic, binary, and ternary metal-based nanowire networks has been accomplished by a solution technique, based on confining metal growth within a soft template, consisting of a network of inverse wormlike micelles.[45, 68] In typical experiments to synthesize our series of ternary PtRuFe nanowires as an example, for the relevant metal precursors, we prepared an aqueous mixture of hexachloroplatinic acid hydrate ($H_2PtCl_6{\cdot}6H_2O$, Alfa Aesar, 99.9%, 1.5 mM), ruthenium (III) chloride hydrate ($RuCl_3{\cdot}xH_2O$, Acros Organics, 35-40% Ru, 1.5 mM) and iron (III) nitrate nonahydrate ($Fe(NO_3)_3{\cdot}9H_2O$, Aldrich, 98+%, 1.5 mM) in appropriate, stoichiometrically determined quantities. These solutions were then combined with a solution of cetyltrimethylammonium bromide (CTAB, Fluka, 40 mM) in chloroform (Acros, 99.8%), while under stirring. Subsequently, 40 mL of H_2O was added under stirring for an additional 30 min. An aqueous solution of sodium borohydride ($NaBH_4$, Alfa Aesar, 98%

powder) was then used to reduce the metal ions encapsulated within the inverse micellar network, as denoted by a color change from a dark green to a dark gray/black hue. After an additional 20 minutes of stirring, as-synthesized nanowires were centrifuged. The supernatant was discarded and subsequently washed three times with 2 mL of ethanol followed by centrifugation for 2 min at 6000 rpm.

Binary PtRu, PtFe, PtCo, PtAu, and PtCu NW were prepared analogously using precursor concentrations of 2 mM, using ruthenium (III) chloride hydrate ($RuCl_3 \cdot xH_2O$, Acros Organics, 35-40% Ru), iron (III) nitrate nonahydrate ($Fe(NO_3)_3 \cdot 9\ H_2O$, Aldrich, 98+%), cupric chloride ($CuCl_2 \cdot 2\ H_2O$, J.T. Baker), cobalt chloride ($CoCl_2$, Aldrich, 97%), or hydrogen tetrachloroaurate (III) hydrate ($HAuCl_4 \cdot x\ H_2O$, Alfa Aesar, 99.999% metals basis, Au 49% min), respectively, in the absence of the third precursor. Monometallic Pt NWs were also synthesized following the same method, employing hexachloroplatinic acid hydrate ($H_2PtCl_6 \cdot 6H_2O$, Alfa Aesar, 99.9%, 4 mM) as the sole precursor.

The surfactant ‘contaminant’ was removed using an effective cleaning protocol.[69] Upon isolation of the NWs, these nanomaterials were subsequently dispersed and ‘washed’ in *n*-butylamine (Acros Organics, 99+%, 0.5 mg catalyst/mL) by sonication for approximately 30 seconds. The solution was then left to stir for 3 days at 400 rpm. The NWs were subsequently collected upon centrifugation at 5000 rpm for 5 minutes. The product was dispersed in 10 mL methanol and sonicated for 15 minutes. The solution was centrifuged again with the entire process repeated for an additional 2 times. The catalyst was later re-dispersed into ethanol prior to additional use. Finally, the *n*-butylamine residue was finally removed by a combination of selective CO adsorption and subsequent CO stripping techniques, as described in section 3.3.1.

2.5.1.2.TiO_2 Nanoparticles (11.4 nm in diameter)

TiO_2 nanoparticles have been synthesized via a two-step hydrothermal protocol, previously developed by our group.[16] In particular, 0.5217 g of commercial anatase TiO_2 (Sigma Aldrich, 99.8% metals basis) is immersed in an aqueous solution of 94 mL of sodium hydroxide (NaOH) (EMD, 10 M) in water in a 120 mL autoclave, and stirred until it is homogeneous. The autoclave is then heated to 120°C and left for 24 h. After the 24 h reaction, the resulting mixture was transferred to a centrifuge tube, sonicated with water, and ultimately centrifuged. The supernatant was subsequently removed from the bottom of the tube, prior to isolation of a fine titanate powder, after additional washing steps with HCl (EMD, ACS Grade) in order to remove residual NaOH.

To convert the hydrogen titanate nanostructures into the corresponding TiO_2 particles, 0.05 g of the hydrogen titanate was added to 16 mL of H_2O in a 23 mL autoclave and heated to 170°C for 24 h. The resulting material was washed with H_2O to remove any excess acid.

2.5.1.3.RuO_2 Nanoparticles (35.0 nm in diameter)

RuO_2 nanoparticles[34] have been fabricated, as follows: 0.42 g of $RuCl_3 \cdot x\ H_2O$ (Acros Organics, 35-40% Ru) was added to 3.5 mL ethanol (Alfa Aesar, anhydrous, denatured, HPLC grade) to create a 1.5 mM solution, which was stirred vigorously until completely dissolved. Subsequently, 1.2 mL of propylene oxide (Fisher Scientific) was added as the gelation agent, and the mixture was continuously stirred until a gel was created. Once the gel was formed, the mixture was covered with parafilm at room temperature and allowed to sit for 24 h. The material was then calcined in a tube furnace at 600°C for 2 h with a ramp rate of 10°C/min. After cooling, the resulting mixture was treated with H_2O_2 (Fisher Scientific, 50% stabilized, certified) in order to oxidize any Ru metal, still remaining.

2.5.1.4. $SrTiO_3$ Nanoparticles (40.7 nm in diameter)

$SrTiO_3$ particles[17] were synthesized by employing a previously published hydrothermal protocol. Specifically, TiO_2 (Sigma Aldrich, 99.8% metals basis, 0.18 g, 2.3 mmol) was mixed in a 20 mL aqueous solution of KOH (~45% purity for HPLC, Fluka, 1.26 g, 23 mmol) and $Sr(OH)_2 \cdot 8\ H_2O$ (Alfa Aesar, 99% metal basis, 0.508 g, 2.3 mmol) within a 23 mL autoclave. This mixture was heated to 150°C for 3 days. The autoclave was later cooled to room temperature. The resulting white powder was washed with water and then air dried overnight.

2.5.1.5. $SrRuO_3$ Nanoparticles (37.3 nm in diameter)

In a typical synthesis described in the prior literature for 40 nm diameter $SrRuO_3$ nanoparticles,[70] 0.1 g of both $RuCl_3 \cdot xH_2O$ (Acros Organics, 35-40% Ru) and strontium acetate ($Sr(CH_3COO)_2$) (Alfa Aesar) were added to 20 mL H_2O, and stirred for 10 minutes, until the mixture was rendered homogeneous. KOH (Fluka, ~45%, for HPLC) was added in until the pH attained a value of 13, and the solution was subsequently stirred for 1 h. The mixture was then removed from stirring, and left to stand at room temperature for 3 h. Afterwards, the material was washed with H_2O for three times, filtered, and dried overnight at 80°C. The material was ground with a mortar and pestle, and calcined at 600°C for 5 h.

2.5.1.6. $SrTiO_3$ Nanoparticles (146.0 nm in average diameter)

In a typical synthesis used without modification,[25] strontium oxalate, anatase TiO_2 (Sigma Aldrich, 99.8% metals basis), NaCl (Merck, bulk), and NP-9 (Sigma Aldrich) in an effective molar ratio of 1: 1: 20: 3 were mixed and subsequently ground with a mortar and pestle for 25 min. The mixture was then transferred to a crucible and placed in a tube furnace for 3.5 h at 850°C with a ramp rate of 10°/min. The material was subsequently cooled to room temperature, washed with de-ionized water for several times, and later dried overnight.

2.5.1.7.$SrRuO_3$ Nanoparticles (146.0 nm in average diameter)

Based on our prior studies, larger $SrRuO_3$ nanoparticles[2] were prepared by combining and mixing strontium hydroxide ($Sr(OH)_2 \cdot 8H_2O$ (Alfa Aesar, 99% metal basis)), RuO_2 nanoparticles (prepared from Section 2.1.2), NaCl / KCl (1: 1) (Merck, bulk; Mallinckrodt, Baker), and 1% mineral oil (Acros Organics, pure) in Triton X-100 (EM Industries) with an effective mole ratio of 1: 1: 20: 3 using a mortar and pestle. The mixture was ground for 25 min prior to transfer to a crucible. The material was then heated to 700°C at a ramp rate of 5°C/min with a continuous flow of air, and later quenched by immediate removal from the furnace. The product was washed twice with distilled water, centrifuged, and dried overnight.

2.5.1.8.Pt Nanoparticles

Platinum nanoparticles[71, 72] were synthesized and deposited in situ on the metal oxide substrates by the following route. Specifically, a combination of hexachloroplatinic acid hydrate ($H_2PtCl_6 \cdot 6\ H_2O$, Alfa Aesar, 99.9%, an experimentally determined optimal mass loading of 50%) and the individual metal oxide substrate being tested was placed in 5 mL H_2O and sonicated for 30 min. Subsequently, an aqueous solution of 0.1 g sodium borohydride ($NaBH_4$, Alfa Aesar, 98% powder) was added, and the mixture was further sonicated for an extra 15 min. The resulting solution was washed with distilled water and ethanol for several more times, centrifuged, and ultimately dispersed in ethanol as an ink (2 mg of catalyst / mL of ethanol).

2.5.1.9.$FePO_4$ Nanowires

The synthesis of amorphous $FePO_4$ occurred between Fe^{3+} and PO_4^{3-} precursor solutions. Moreover, the Fe^{3+} precursor solution was produced by combining anhydrous ferric chloride, $FeCl_3$ (EM Science, 98%) with 0.1 M aqueous solution of HCl (EMD, 38%), to prepare a solution with a concentration of Fe^{3+} of 0.05 M. A surplus amount of acid was added to the precursor solution in order to enhanced the solubility of $FeCl_3$ in addition to preventing the generation of $Fe(OH)_x$ impurities in the NWs. $Fe(OH)_x$ impurities decompose into iron oxide during crystallization, which is undesired. The second precursor solution containing phosphate was generated by dissolving sodium phosphate dodecahydrate, tribasic (Acros Organics, 98%) in water, to generate a PO_4^{3-} concentration of 0.05 M.

Amorphous $FePO_4$ NWs were generated employing the U-tube method. A polycarbonate track-etched Nucleopore membrane (Whatman Co., U.K.), with pore size diameters of either 50 or 200 nm, was sonicated in distilled water, in order to wet the the internal channels, while also removing any air bubbles that may be present in the pores. The template was then placed between two half-cells of the glass U-tube device. Both the Fe^{3+} precursor solution and the PO_4^{3-} solution were simultaneously added to either sides of the U- tube apparatus, maintaining the solution level on both sides. This is necessary to ensure the diffusion of both precursors simultaneously within the pores of the template. Nucleation and growth begins to occur when the two solutions converge within the pores, generating $FePO_4$ NWs that possess diameters mimicking the diameters of the pores within the commercial template. After a period of 24 hours, the arms of the U-tube are emptied, and the template is removed from the device.

During the 24 hour period, a thin layer of excess amorphous material will generally form on the outside of the membrane, which is subsequently physically removed by hand. Moreover, $Fe(OH)_x$ impurities can also be generated within the template during the reaction, which can be determined by the presence of orange-colored material. These particular sections within the template were removed with a scissor in order to ensure the purity of the sample. The $FePO_4$ NWs were subsequently removed from the template by dissolving the template in in CH_2Cl_2 (Acros, 99.5%). The resultant was then washed with CH_2Cl_2 multiple times using centrifugation, following additional washes in ethanol. The product was finally dispersed in ethanol and dried at 80°C overnight.

2.5.1.10. $FePO_4$ Nanoparticles

Additionally, a bulk $FePO_4$ sample was generated by simultaneously mixing the two precursor solutions (equal volume) mentioned above, in a beaker, which was allowed to stir in air for 1 hour. The resulting material was washed and centrifuged with water multiple times. The product was then dispersed in ethanol and dried overnight at 80°C.

2.5.1.11. Lithiation of $FePO_4$ Nanomaterials

The amorphous iron phosphate precursors are lithiated by chemical means employing a previously established protocol.[73, 74] Specifically, the $FePO_4$powders are dispersed in lithium iodide (Aldrich, 99.9%) in acetonitrile (EMD, 99.8%), so that a1 M solution is created, and the ratio of $FePO_4$: Li is 1: 3. Using Shlenk conditions to create a nitrogen atmosphere, the solution is stirred continuously for 24 hours. After the 24 hour period, the products are washed and centrifuged in acetonitrile until the solution is no longer yellow, but colorless. After the washing step, the products are annealed in a tube furnace for 5 hours at 550°C in a flowing 5% H_2/ Ar atmosphere. The crystalline, lithiated materials are removed from the boat by sonication in water. It is necessary to use not only a short period of time but also a weak sonicator, as both can damaged the resulting NWs, which will be discussed in Chapter 6. After removal, the NWs are washed with water and dispersed in ethanol.

2.5.2. Detailed Description of Structural Characterization Methods

2.5.2.1.X-Ray Characterization

Powder diffraction samples were prepared by dispersing the relevant ultrathin NW samples into ethanol and drop casting the resulting slurry onto a glass microscope slide. Powder diffractograms of as-prepared NWs were obtained either on a Scintag diffractometer, operating in the Bragg-Brentano configuration with Cu Kα radiation (λ =1.54 Å), with diffraction patterns acquired from 35° to 85° at a scanning rate of 0.25° min^{-1} or a Rigaku Ultima III Diffractometer, operating in the Bragg configuration by using Cu Ka radiation (1.54 Å), with the diffraction data collected at a scanning rate of 1° min^{-1}.

Powder diffraction samples of our metal oxide-based supports were prepared by drying either the relevant metal oxide support or the various catalyst samples. Powder diffractograms were obtained on a Scintag diffractometer, operating in the Bragg-Brentano configuration with Cu Kα radiation (λ = 1.54 Å). Diffraction patterns were collected from 2θ values of either 20° or 30° to 80° at a scanning rate of 1° per minute.

To obtain the powder XRD patterns of our $LiFePO_4$-related materials, a concentrated slurry of the product in ethanol was sonicated and subsequently deposited onto a glass microscope slide, which was allowed to sit and dry to create a uniform layer of product. Diffraction patterns were initially obtained on a Scintag diffractometer, operating in the Bragg-Bretano configuration using Cu Kα radiation (λ = 1.54 Å) with a range of 10 to 70° at a scan rate of 0.25° per minute. High-resolution XRD data were acquired using the X14A beamline of the National Synchrotron Light Source (NSLS) at Brookhaven National Laboratory. This station is equipped with a position-sensitive silicon strip detector, located at a distance of 1433 mm from the sample and operating at a wavelength of 0.7788 Å. Structural and compositional information were derived by Rietveld refinements of the XRD patterns using the TOPAS 4.1 program.

For XPS analysis, the solid samples were prepared by dispersing the powder samples in ethanol and subsequently drop-casting them onto a Si wafer. They were analyzed within the vacuum chamber of an XPS instrument (Model SPECS Phoibos 100 electron energy analyzer).

The chamber was evacuated to a base pressure of about $2 \cdot 10^{-10}$ torr. XPS spectra were either collected using an Al Kα X-ray source (hν = 1486.6 eV) or a Mg Kα X-ray source (hν = 1253.6 eV) (model XR 50). The reported spectra have been referenced to the C 1s peak located at 285.0 eV.[75]

2.5.2.2.Electron Microscopy

The structural morphology and crystallinity of as-prepared materials were characterized by TEM obtained with a Technai12 BioTwinG2 TEM instrument, equipped with an AMT XR-60 CCD camera system. EDAX was performed on a Leo 1550 field-emission SEM (FE-SEM), operating at an accelerating voltage of either 5 kV or 20 kV. HRTEM and SAED patterns were acquired on a JEOL 2100F instrument at accelerating voltages of 200 kV with a beam size of 2 Å. Additional HRTEM images, SAED patterns, HAADF imaging, and the collection of defocused diffraction patterns were obtained using a JEOL 3000F microscope, equipped with a field-emission gun operating at an accelerating voltage of 300 kV.

The electron energy loss experiments on the metal oxide supports were carried out with a double Cs-corrected JEOL JEM-ARM200F TEM. EELS were obtained using the scanning probe module as part of the dual EELS data acquisition mode, so that the absolute energy loss value could be efficiently calibrated. The Gatan Digital Micrograph software package was used for routine analysis of the spectra. More than ten EELS spectra were obtained from each individual sample, with representative results, highlighted in the Figures.

HAADF, scanning TEM (STEM) images and EELS measurements on the binary NW catalysts were acquired using an aberration-corrected Hitachi HD 2700C equipped with a modified Gatan Enfina ER spectrometer. Samples were prepared for measurement by dispersing solid powder in ethanol, sonicating the resulting suspension for 2 min, and ultimately evaporating one drop onto a 300 mesh Cu grid, coated with a lacey C film.

2.5.3. Electrochemical Characterization Methods

2.5.3.1. Preparation of the Electrode.

Electrochemical characterization of all synthesized materials was performed with the samples supported onto a glassy carbon electrode (GCE; 5 mm, Pine Instruments). Initially, the electrode was polished to a mirror finish using an aluminum oxide powder slurry (0.050 μm particle size). Prior to deposition of the catalyst, the GCE surface was pre-modified with a thin layer of Vulcan XC-72R carbon in order to serve as a carbonaceous support structure for the as-prepared NWs, when tested for methanol, formic acid, and hydrogen oxidation reactions. No carbon support was utilized in particular experiments when alternative, non-carbonaceous supports were specifically employed as a replacement for carbon.

When testing for methanol and formic acid oxidation, the catalyst samples were dispersed in ethanol (at a concentration of 2 mg/mL) and were then loaded onto a carbon-modified GCE by adding two drops (i.e. 5 μL per drop) of the catalyst dispersion onto the surface, which was subsequently allowed to dry in air. When the NW samples were tested for hydrogen oxidation, a concentration of 0.2 mg/mL was used with no addition of carbon support. Quantitatively, the loading protocol yielded either ~20 μg_{metal} cm_{disk}^{-2} or 14 μg_{Pt} cm_{disk}^{-2} for Pt-based alloy systems. In all cases, the GCE was then sealed with one 5 μL drop of an ethanolic 0.025% Nafion solution, prepared from a 5% stock solution.

Prior to electrochemical analysis, the catalyst-loaded GCE was immersed into fresh aliquots of water, so as to remove any impurities. In order to prepare the commercial standards, alloy-type $Pt_{1-x}Ru_x$ (‘x’ = 0.5) NPs and Pt NPs with a 20% precious metal content (ETek) were rendered into catalyst ink dispersions (1 mg/mL) in 25% isopropyl alcohol in water and deposited directly onto the surface of polished GCE for characterization.

The binary and ternary-based NW samples tested for methanol and formic acid oxidation were placed in 0.1 M perchloric acid (Fisher Scientific, optima grade) solutions, the Pt-deposited metal oxide supports were collected in 0.1 M sulfuric acid solutions, and the binary NW samples tested for hydrogen oxidation were collected in 0.1 M potassium hydroxide solutions, each created using high-purity water possessing a resistivity value of 18.2 MΩ•cm. Pt foil and an Ag/AgCl combination (3 M Cl^-) served as the counter and reference electrodes, respectively. All potentials have been reported with respect to the reversible hydrogen electrode (RHE).

2.5.3.2.Cyclic Voltammetry

The corresponding electrochemical properties of the monometallic, binary, and ternary catalysts were examined by CV as well as using CO stripping voltammetry. CVs were obtained in the desired argon-saturated electrolyte at a scan rate of 20 mV/s. The adsorption of a monolayer of CO was accomplished by immersing the electrodes into a CO-saturated perchloric acid (Fisher Scientific, Optima grade) electrolyte for a period of 30 min. Subsequently, the electrode was transferred to a deoxygenated electrolyte solution, so as to obtain the corresponding CO stripping CV. The CO stripping process was implemented in order to remove *n*-butylamine from the NW surface in order to expose available active sites. The presence of CO effectively displaces residual *n*-butylamine, since CO possesses a higher affinity for adsorption and can be subsequently removed upon cycling. Additionally, in 0.1 M KOH, the adsorption of a monolayer of CO was accomplished by bubbling in CO gas through the electrochemical cell for 15 minutes of reaction. After 15 minutes, the electrode was then immersed in a CO-saturated KOH solution, and it was held at a potential of 0.1 V vs. RHE (within the hydrogen adsorption region) for a period of 45 minutes in order to electrochemically adsorb the CO. Subsequently, in the absence of the electrode, the cell was bubbled with Ar alone to remove the CO gas. After 20 minutes, the electrode was transferred to the deoxygenated electrolyte solution, so as to measure the corresponding CO stripping CV.

The ECSA was calculated from the integrated hydrogen adsorption (H_{ads}) determined in the cyclic voltammetry analysis, utilizing 210 $\mu C/cm^2$ as the conversion factor. As-obtained ECSA values represent a reasonable estimate of the active Pt sites in the system.

2.5.3.3.Evaluation of MOR, HOR, and FAOR Kinetics

The MOR kinetics were measured by first obtaining CVs at a scan rate of 20 mV/s in a deoxygenated 0.5 M methanol (Fisher Scientific, Optima grade) solution, supported in a 0.1 M $HClO_4$ electrolyte. Typically, an LSV was obtained in the anodic sweep direction, so as to collect the MOR kinetics curves. The observed current was subsequently normalized to the Pt surface area, which can be determined from the H_{ads} charge. After the initial LSV, the collection of the MOR CVs was repeated to ensure that the surface of the catalyst was sufficiently stable in order to generate more reproducible CVs. In the case of the metal oxide supports studied, Tafel plots were generated from MOR CVs, collected at a scan rate of 1 mV/s.

The analogous formic acid oxidation kinetics data were acquired in a 0.1 M $HClO_4$ electrolyte in the presence of a 0.5 M formic acid solution (EMD, 98% ACS reagent grade). The same electrochemical parameters described above were applied. All electrodes in this thesis have been tested and run under identical conditions, in order to establish a self-consistent comparison amongst all of the electrodes.

The HOR kinetics data were acquired by first obtaining CVs using a scan rate of 20 mV/s in a H_2-saturated solution, dispersed within a 0.1 M KOH electrolyte. Typically, an LSV was obtained in the anodic sweep direction, so as to amass individual HOR kinetics curves, obtained between -0.05 and 0.3 V vs. RHE at varying rotation speeds (i.e. 400, 900, 1600, 2000, and 2500 rpm). The observed current was subsequently normalized to the geometric surface area of the electrode. After the initial LSV, collection of the HOR CVs was repeated a number of times to ensure that the surface of the catalyst was sufficiently stable to generate more reproducible CVs. All of the electrodes tested herein have been probed and run under identical conditions, in order to establish a self-consistent comparison amongst all of the electrodes analyzed. In particular, the activity of our samples has been compared with respect to that of Pt NP/C (Etek), serving as a commercial standard and control.

2.5.3.4.Stability Measurements

Chronoamperometry was also run in order to test the stability of our as-prepared catalysts. Chronoamperograms were obtained in a de-oxygenated 0.5 M methanol solution, supported in a 0.1 M $HClO_4$ electrolyte. The electrodes were submerged and tested, while the potentials were maintained at a value of 0.65 V (for ternary NW catalysts) and 0.7 V (for metal oxide supports) for a period of one hour. These specific potentials were used, due to the fact that they reside within the onset region of all of the catalysts tested herein, thereby allowing for an appropriate comparison of relative activity.

2.5.3.5.Battery Testing

The electrochemical performance of the 200 nm diameter $LiFePO_4$ nanowires and bulk-like particles were measured on an Arbin BT-2000 test station. Both $LiFePO_4$ nanomaterials were investigated electrochemically by investigating their capacity as a function of cycle number. For electrochemical studies, an electrode preparation method[76, 77] was specifically chosen in order to take into account the small amount of nanoscale $LiFePO_4$ generated ambiently, resulting in our $LiFePO_4$ materials being mixed with 10 weight % carbon black and 10 weight % Teflon (PTFE) powder. The mixture was ground in a mortar and pestle for 30 min to form a wafer. The wafer was then rolled out and placed in a drying oven under vacuum for 24 hours at 80°C to ensure hydration removal.

A coin cell configuration was used with pure lithium foil as the anode; 1.0 M $LiPF_6$ dissolved in EC/DMC (1:1) solution was utilized as the electrolyte, in addition to a separator for the cell. Specifically, under an inert argon atmosphere within a glove box environment, the electrodes were placed in the bottom terminal of a 2032 coin cell configuration to which electrolyte was added. An insulating polymer membrane was then placed over the electrode and a gasket was introduced to completely seal the cathode half-cell itself. A piece of lithium metal ribbon was layered on top of the separator, followed by a metal plate collector. Finally, a spring was placed on top of the collector to hold the components in place, and the top terminal of the coin cell was subsequently pressed into the setup to seal the cell. The assembled battery was then cycled between 2.0 V and 3.6 V at room temperature.

Electrodes containing iron phosphate were prepared using commercial and synthesized samples of $FePO_4$. The commercial samples were obtained from Aldrich (iron (III) phosphate dihydrate, Fe content of 29%) and prepared by drying at 500°C (with purity determined by thermogravimetric analysis) to remove the water, prior to electrochemical evaluation. Electrodes consisting of $FePO_4$ (85%), carbon black (5%), graphite (5%), and polyvinylidene difluoride (5%) on battery grade aluminum foil were prepared using the standard doctor blade method. Two electrode cells were prepared versus lithium metal electrodes with an electrolyte of 1 M $LiPF_6$ in the presence of 1:1 ethylene carbonate: dimethylcarbonate. The cells were cycled at 30°C under voltage ranges of 2.0 – 3.6 V and 1.5 - 4.0 V at 0.18 or 0.018 mA/cm^2 rates.

2.6.References

1. Tiano, A. L.; Papaefthymiou, G. C.; Lewis, C. S.; Han, J.; Zhang, C.; Li, Q.; Shi, C.; Abeykoon, A. M. M.; Billinge, S. J. L.; Stach, E.; Thomas, J.; Guerrero, K.; Munayco, P.; Munayco, J.; Scorzelli, R. B.; Burnham, P.; Viescas, A. J.; Wong, S. S., *Chemistry of Materials* **2015,** *27* 3572-3592.
2. Tiano, A. L.; Santulli, A. C.; Koenigsmann, C.; Feygenson, M.; Aronson, M. C.; Harrington, R.; Parise, J. B.; Wong, S. S., *Chemistry of Materials* **2011,** *23* 3277-3288.
3. Santulli, A. C.; Feygenson, M.; Camino, F. E.; Aronson, M. C.; Wong, S. S., *Chemistry of Materials* **2011,** *23* 1000-1008.
4. Patete, J. M.; Han, J.; Tiano, A. L.; Liu, H.; Han, M.-G.; Simonson, J. W.; Li, Y.; Santulli, A. C.; Aronson, M. C.; Frenkel, A. I.; Zhu, Y.; Wong, S. S., *The Journal of Physical Chemistry C* **2014,** *118* 21695-21705.
5. Lewis, C. S.; Wang, L.; Liu, H.; Han, J.; Wong, S. S., *Crystal Growth & Design* **2014,** *14* 3825-3838.
6. Han, J.; McBean, C.; Wang, L.; Jaye, C.; Liu, H.; Fischer, D. A.; Wong, S. S., *The Journal of Physical Chemistry C* **2015,** *119* 3826-3842.
7. Koenigsmann, C.; Semple, D. B.; Sutter, E.; Tobierre, S. E.; Wong, S. S., *ACS Applied Materials & Interfaces* **2013,** *5* 5518-5530.
8. Koenigsmann, C.; Sutter, E.; Adzic, R. R.; Wong, S. S., *The Journal of Physical Chemistry C* **2012,** *116* 15297-15306.
9. Domènech, B.; Bastos-Arrieta, J.; Amanda Alonso, J. M. s.; Muñoz, M.; Muraviev, D. N., *Bifunctional Polymer-Metal Nanocomposite Ion Exchange Materials*. InTech: 2012.
10. Byrappa, K.; Adschiri, T., *Progress in Crystal Growth and Characterization of Materials* **2007,** *53* 117-166.
11. Lu, A.-H.; Salabas, E. L.; Schüth, F., *Angewandte Chemie International Edition* **2007,** *46* 1222-1244.
12. Greene, L. E.; Law, M.; Goldberger, J.; Kim, F.; Johnson, J. C.; Zhang, Y.; Saykally, R. J.; Yang, P., *Angewandte Chemie International Edition* **2003,** *42* 3031-3034.
13. Zhang, C.; Zhu, Y., *Chemistry of Materials* **2005,** *17* 3537-3545.
14. Liang, Y.; Wang, H.; Sanchez Casalongue, H.; Chen, Z.; Dai, H., *Nano Research* **2010,** *3* 701-705.
15. Demir-Cakan, R.; Hu, Y.-S.; Antonietti, M.; Maier, J.; Titirici, M.-M., *Chemistry of Materials* **2008,** *20* 1227-1229.
16. Mao, Y.; Wong, S. S., *Journal of the American Chemical Society* **2006,** *128* 8217-8226.
17. Chen, C.; Dai, Q.; Miao, C.; Xu, L.; Song, H., *RSC Advances* **2015,** *5* 4844-4852.
18. Mao, Y.; Park, T.-J.; Zhang, F.; Zhou, H.; Wong, S. S., *Small* **2007,** *3* 1122-1139.
19. Segal, D., *Journal of Materials Chemistry* **1997,** *7* 1297-1305.
20. Lux, H., *Zeitschrift für Elektrochemie* **1939,** *45* 303-309.
21. Deng, H.; Qiu, Y.; Yang, S., *Journal of Materials Chemistry* **2009,** *19* 976-982.
22. Peng, R.; Wu, N.; Zheng, Y.; Huang, Y.; Luo, Y.; Yu, P.; Zhuang, L., *ACS Applied Materials & Interfaces* **2016,** *8* 8474-8480.
23. Tseng, L.-T.; Luo, X.; Bao, N.; Ding, J.; Li, S.; Yi, J., *Materials Letters* **2016,** *170* 142-146.
24. Chen, J.; Xing, X.; Watson, A.; Wang, W.; Yu, R.; Deng, J.; Yan, L.; Sun, C.; Chen, X., *Chemistry of Materials* **2007,** *19* 3598-3600.

25. Mao, Y.; Banerjee, S.; Wong, S. S., *Journal of the American Chemical Society* **2003,** *125* 15718-15719.

26. Cushing, B. L.; Kolesnichenko, V. L.; O'Connor, C. J., *Chemical Reviews* **2004,** *104* 3893-3946.

27. Livage, J.; Henry, M.; Sanchez, C., *Progress in Solid State Chemistry* **1988,** *18* 259-341.

28. Hench, L. L.; West, J. K., *Chemical Reviews* **1990,** *90* 33-72.

29. Niederberger, M., *Accounts of Chemical Research* **2007,** *40* 793-800.

30. Zorkipli, N. N. M.; Kaus, N. H. M.; Mohamad, A. A., *Procedia Chemistry* **2016,** *19* 626-631.

31. Rajammal, K.; Sivakumar, D.; Duraisamy, N.; Ramesh, K.; Ramesh, S., *Ionics* **2016,** 1-6.

32. de Biasi, R. S.; de Souza Lopes, R. D., *Ceramics International* **2016,** *42* 9315-9318.

33. Yang, H.; Duh, J.-G., *RSC Advances* **2016,** *6* 37160-37166.

34. Walker, J.; Bruce King, R.; Tannenbaum, R., *Journal of Solid State Chemistry* **2007,** *180* 2290-2297.

35. Koenigsmann, C.; Sutter, E.; Chiesa, T. A.; Adzic, R. R.; Wong, S. S., *Nano Letters* **2012,** *12* 2013-2020.

36. Lakshmi, B. B.; Patrissi, C. J.; Martin, C. R., *Chemistry of Materials* **1997,** *9* 2544-2550.

37. Limmer, S. J.; Seraji, S.; Wu, Y.; Chou, T. P.; Nguyen, C.; Cao, G. Z., *Advanced Functional Materials* **2002,** *12* 59-64.

38. Patete, J. M.; Scofield, M. E.; Volkov, V.; Koenigsmann, C.; Zhang, Y.; Marschilok, A. C.; Wang, X.; Bai, J.; Han, J.; Wang, L.; Wang, F.; Zhu, Y.; Graetz, J. A.; Wong, S. S., *Nano Research* **2015,** *8* 2573-2594.

39. Wang, X.; Li, Y., *Inorganic Chemistry* **2006,** *45* 7522-7534.

40. Tiano, A. L.; Koenigsmann, C.; Santulli, A. C.; Wong, S. S., *Chemical Communications* **2010,** *46* 8093-8130.

41. Gunnewiek, R. F. K.; Mendes, C. F.; Kiminami, R. H. G. A., *Advanced Powder Technology*.

42. Balamurugan, C.; Lee, D. W.; Maheswari, A. R.; Parmar, M., *RSC Advances* **2014,** *4* 54625-54630.

43. Wang, D.; Song, C., *The Journal of Physical Chemistry B* **2005,** *109* 12697-12700.

44. Sun, L.; Kong, W.; Wu, H.; Wu, Y.; Wang, D.; Zhao, F.; Jiang, K.; Li, Q.; Wang, J.; Fan, S., *Nanoscale* **2016,** *8* 617-625.

45. Song, Y.; Garcia, R. M.; Dorin, R. M.; Wang, H.; Qiu, Y.; Coker, E. N.; Steen, W. A.; Miller, J. E.; Shelnutt, J. A., *Nano Letters* **2007,** *7* 3650-3655.

46. Scofield, M. E.; Koenigsmann, C.; Wang, L.; Liu, H.; Wong, S. S., *Energy & Environmental Science* **2015,** *8* 350-363.

47. Scofield, M. E.; Zhou, Y.; Yue, S.; Wang, L.; Su, D.; Tong, X.; Vukmirovic, M. B.; Adzic, R. R.; Wong, S. S., *ACS Catalysis* **2016,** 3895-3908.

48. Drenth, J., *Principles of Protein X-Ray Crystallography*. Springer-Verlag New York: New York, 2007; p XIV, 332.

49. Morgan, P.; Drews, J.; Dhiman, R.; Nielson, P., Nanostructured Materials in Different Dimensions for Sensing Applications. In *Nanotechnological Basis for Advanced Sensors*, Reithmaier, J. P.; Paunovic, P.; Kulisch, W.; Popov, C.; Petkov, P., Eds. Springer: 2011; p 257.

50. Goldstein, J., *Scanning Electron Microscopy and X-ray Microanalysis: Third Edition*. Plenum: 2003.

51. Leapman, R., EELS Quantitative Analysis. In *Transmission Electron Energy Loss Spectrometry in Materials Science and The EELS Atlas*, Wiley-VCH Verlag GmbH & Co. KGaA: 2005; pp 49-96.
52. von Harrach, H.; Klenov, D.; Freitag, B.; Schlossmacher, P.; Collins, P.; Fraser, H., *Microscopy and Microanalysis* **2010,** *16* 1312-1313.
53. Langmuir, I., *Journal of the American Chemical Society* **1916,** *38* 2221-2295.
54. Masel, R. I., *Principles of Adsorption and Reaction on Solid Surfaces*. Wiley Interscience: 1996.
55. Brunauer, S.; Emmett, P. H.; Teller, E., *Journal of the American Chemical Society* **1938,** *60* 309-319.
56. Marković, N. M.; Ross Jr, P. N., *Surface Science Reports* **2002,** *45* 117-229.
57. Bard, A.; Faulkner, L., *Electrochemical Methods: Fundamentals and Applications*. John Wiley & Sons, Inc: 2001.
58. Zhang, L. L.; Zhao, X. S., *Chemical Society Reviews* **2009,** *38* 2520-2531.
59. Parsons, R.; VanderNoot, T., *Journal of Electroanalytical Chemistry and Interfacial Electrochemistry* **1988,** *257* 9-45.
60. Motoo, S.; Furuya, N., *Journal of Electroanalytical Chemistry and Interfacial Electrochemistry* **1985,** *184* 303-316.
61. Yang, H.; Zhang, J.; Sun, K.; Zou, S.; Fang, J., *Angewandte Chemie International Edition* **2010,** *49* 6848-6851.
62. Jayaraman, S.; Jaramillo, T. F.; Baeck, S.-H.; McFarland, E. W., *The Journal of Physical Chemistry B* **2005,** *109* 22958-22966.
63. Liu, Z.; Ling, X. Y.; Su, X.; Lee, J. Y., *The Journal of Physical Chemistry B* **2004,** *108* 8234-8240.
64. Wang, J.; Xi, J.; Bai, Y.; Shen, Y.; Sun, J.; Chen, L.; Zhu, W.; Qiu, X., *Journal of Power Sources* **2007,** *164* 555-560.
65. Attard, G. A.; Brew, A.; Hunter, K.; Sharman, J.; Wright, E., *Physical Chemistry Chemical Physics* **2014,** *16* 13689-13698.
66. Rheinländer, P. J.; Herranz, J.; Durst, J.; Gasteiger, H. A., *Journal of The Electrochemical Society* **2014,** *161* F1448-F1457.
67. Schmidt, T. J.; Ross Jr, P. N.; Markovic, N. M., *Journal of Electroanalytical Chemistry* **2002,** *524–525* 252-260.
68. Yang, S.; Hong, F.; Wang, L.; Guo, S.; Song, X.; Ding, B.; Yang, Z., *The Journal of Physical Chemistry C* **2010,** *114* 203-207.
69. Liu, H.; Koenigsmann, C.; Adzic, R. R.; Wong, S. S., *ACS Catalysis* **2014,** *4* 2544-2555.
70. Atta, N. F.; Galal, A.; Ali, S. M., *International Journal of Electrochemical Science* **2012,** *7* 725-746.
71. Mayavan, S.; Mandalam, A.; Balasubramanian, M.; Sim, J.-B.; Choi, S.-M., *Materials Research Bulletin* **2015,** *67* 215-219.
72. Qiu, J.-D.; Wang, G.-C.; Liang, R.-P.; Xia, X.-H.; Yu, H.-W., *The Journal of Physical Chemistry C* **2011,** *115* 15639-15645.
73. Zhou, H.; Yiu, Y.; Aronson, M. C.; Wong, S. S., *Journal of Solid State Chemistry* **2008,** *181* 1539-1545.
74. Zhang, F.; Mao, Y.; Park, T.-J.; Wong, S. S., *Advanced Functional Materials* **2008,** *18* 103-112.

75. Duan, T. L.; Pan, J. S.; Ang, D. S., *ECS Journal of Solid State Science and Technology* **2015,** *4* P364-P368.
76. Song, Y.; Yang, S.; Zavalij, P. Y.; Whittingham, M. S., *Materials Research Bulletin* **2002,** *37* 1249-1257.
77. Yuan, L.-X.; Wang, Z.-H.; Zhang, W.-X.; Hu, X.-L.; Chen, J.-T.; Huang, Y.-H.; Goodenough, J. B., *Energy & Environmental Science* **2011,** *4* 269-284.

Chapter 3: Tailoring the Composition of Ultrathin, Ternary Alloy PtRuFe Nanowires for the Methanol Oxidation Reaction and Formic Acid Oxidation Reaction

3.1. Introduction

With the growing demand for alternative energy sources, much research effort has focused on the development of DMFCs as a viable energy conversion device. Specifically, DMFCs consist of both an anode and a cathode at which the oxidation of methanol and the reduction of oxygen can respectively occur.[1, 2] Specifically, equations 1 and 2 highlight the overall cell reaction for the DMFC.

$$CH_3OH + 3/2\ O_2 \rightarrow CO_2 + 2\ H_2O \qquad [3.1]$$

$$CH_3OH + H_2O \rightarrow CO_2 + 6H^+ + 6e^- \qquad [3.2]$$

In this work, we are primarily preoccupied with understanding the methanol oxidation reaction, occurring at the anode half-cell. Typically, Pt-based materials are used as MOR catalysts, due to their relatively high catalytic activities. However, this has proven to be problematic, since platinum is expensive because of its relative scarcity. Moreover, when Pt is incorporated into a catalyst, deleterious effects, such as surface poisoning, particle ripening, and dissolution, often arise,[3, 4] all of which lead to a decrease in the number of active sites available for MOR and thereby contribute to poor kinetics and durability.[5]

One strategy to enhance the catalytic activity of Pt has been to incorporate other electrochemically active, more plentiful metals, such as ruthenium for example, thereby forming homogeneous $Pt_{1-x}Ru_x$ alloys. Specifically, very high efficiency values have already been observed in $Pt_{1-x}Ru_x$ systems using a range of Ru concentrations (‘x’ = 0.07-0.33). The presence of 30% Ru dopant, as in the Pt_7Ru_3 system, yielded exceptionally high activities.[6-8] As such, we used this particular binary alloy composition as our explicit ‘starting point’ control sample from which to seek out possible permutations of this overall 30% metal dopant for creating ever more electrochemically active catalysts.

In PtRu systems, the MOR reaction proceeds through a plausible *'bifunctional mechanism'*, wherein adsorbed hydroxide species at the Ru site facilitate the oxidation and removal of the CO intermediate adsorbed onto the Pt active sites.[9-12] Consequently, more Pt active sites become accessible for methanol oxidation, thereby enhancing catalytic performance at lower overpotentials.[11-14] Although binary alloys clearly represent a positive step forward, there is a functional need for improvement, due to issues such as long-term catalytic durability, which ultimately hinder the current commercial viability of DMFCs.

As such, in recent years, efforts have shifted beyond the use of bimetallic catalysts to the study of more complex ternary 'platforms', incorporating three different transition metals. Specifically, ternary systems including but not limited to PtRuNi,[3, 10, 15, 16] PtRuFe,[17-20] PtRuSn,[3] PtRuMo,[3] PtRuRh,[21] and PtRuAu[22] have been investigated as potential electrocatalysts for MOR. The addition of this extra metal not only decreases the overall cost of the catalyst by reducing the amount of Pt utilized but also improves catalytic activity through a favorable synergistic electronic interaction between the Pt active sites and the transition metal dopants.[4, 10, 11]

Specifically, the inherent structural coupling between the dopant metal lattice and the Pt lattice forces a compression strain upon the Pt lattice, due to the shorter interatomic distance of the dopant sites as compared with Pt. This so-called *"ligand effect"* therefore increases the *d*-orbital overlap, contributing to a down-shift in energy for the weighted center of the *d*-band. In effect, electron density is withdrawn from the Pt *d*-band towards that of the dopant metals. In terms of practical consequences for catalysis, the lower weighted center of the *d*-band contributes to a lowered CO affinity as a result of a concomitant weakening of the overlap between the Pt *d*-

orbitals and the CO π^*-orbitals. Hence, CO coverage is effectively reduced, which correspondingly increases the number of exposed Pt active sites available for MOR.

In this light, utilizing a combinatorial computational approach, Nørskov and co-workers[19] analyzed a wide array of ternary and quaternary alloy electrocatalysts, and determined that PtRuCo, PtRuNi, as well as PtRuFe catalysts exhibited significantly higher CO tolerance values as compared with binary PtRu catalysts. Experimentally, PtRuNi nanoparticles synthesized by Park et al.[3] demonstrated that the incorporation of Ni into a PtRu alloy resulted in an increase in specific activity, which was as much as ~2.2-fold higher as compared with that of the PtRu catalyst, an observation attributable to electron transfer from Ni to Pt. Similarly, Yu et al.[18] synthesized and compared the activity of multiple ternary nanoparticle electrocatalysts, i.e. PtRuM ('M' = Co, Ni, Fe); in particular, both PtRuCo and PtRuNi electrocatalysts evinced a favorable 50 mV negative shift in the onset potential for MOR. Moreover, Sun and co-workers[23] synthesized FePtPd nanowires possessing different chemical compositions in order to analyze their MOR activity as compared with that of PtFe, PtPd, and Pt catalysts. They found that their $Fe_{28}Pt_{38}Pd_{34}$ electrocatalysts also exhibited a favorable negative shift in onset potential for methanol oxidation as well as a corresponding increase in the peak current density as compared with both binary alloy and Pt analogues. All of these examples demonstrate and corroborate the notion that by incorporating a third transition metal, such as Fe, CO tolerance can be increased, and as a result, the activity can be enhanced due to the availability of active sites.

Moreover, PtRuM electrocatalysts (wherein 'M' = Co, Ni, and Fe, i.e. incorporating first row transition metals) have become particularly appealing, because Fe, for instance, represents a more plentiful, lower cost, and reasonably less toxic alternative, especially as compared with bulk Pt. Hence, due to the attractiveness of Fe as a viable catalytic component and potential replacement for Ru, the purpose of this work has been to systematically explore Fe-based PtRuM electrocatalysts with the aim of correlating chemical composition with electrochemical activity in order to understand and fine tune the preparation of electrocatalysts for enhanced performance in both MOR and FAOR.The other key point is that by incorporating Fe within this ternary alloy architecture, we have been able to demonstrate an increase in electrochemical stability by nearly 4-fold as compared with commercial PtRu standards. In so doing, we have potentially addressed and mitigated for a serious limitation preventing the widespread commercialization of anode materials, an issue which had been previously commented upon by our group and others.[24, 25]

As an additional parameter to tailoring chemical composition, we have also been interested in exploring the effect of electrocatalyst morphology upon corresponding activity. Specifically, it is known that the use of anisotropic 1D structures such as NWs and NTs has led to significant improvements in electrocatalytic performance as compared with traditional, conventional 0D morphologies such as nanoparticles. The rationale is that crystalline 1D nanostructures possess (a) high aspect ratios, (b) improved stability, (c) short segments of smooth crystal planes, and (d) a low number of deleterious surface defect sites, all of which are desirable attributes for fuel cell catalysts.[26] Recent results from our group confirm this hypothesis.[20, 27, 28] Furthermore, when the diameter of the 1D wire is decreased toward the ultrathin size regime (< 5 nm), we are able to minimize the presence of not only deleterious intrinsic defect sites but also lattice boundary imperfections, which tend to alter the surface energy of the Pt. All of these factors suggest that ultrathin PtRuFe NWs represent a particularly favorable structural paradigm for the synthesis of high-performance electrocatalysts.

In this study therefore, we have synthesized ultrathin, ternary PtRuFe NW electrocatalysts using an ambient, wet synthesis method that has not, to the best of our knowledge, ever before been applied to the successful generation of multi-functional ternary metal-based catalysts. Solution-based techniques are advantageous for the production of electrocatalysts, since they represent potentially straightforward, reasonably mild, high-yield, scalable, and cost-efficient processes. Specifically, the methodology[29, 30] used herein involves the reduction of metal precursors with sodium borohydride in the presence of a so-called ‘soft template’, created by the CTAB surfactant within a two-phase water-chloroform system. One of the advantages of this technique is that because the nucleation and growth of the wires is fundamentally controlled by the size and shape of the ‘soft template’ pores, one can rather easily create porous, high surface area networks of interconnected, ‘wormlike’ metallic nanowires, possessing average diameters of as small as 1.9 nm. Utilizing this protocol,[29, 30] we were therefore able to tune the relative concentrations of Ru and Fe precursors, and fabricate a range of homogeneous alloyed ultrathin NWs, as confirmed by our structural characterization data.

We have investigated not only the CO tolerance but also the electrochemical activity of our NWs as a function of Ru and Fe content. Specifically, as discussed earlier, using Pt_7Ru_3 as our ‘starting’ catalyst composition, upon the addition of 10% Fe to replace Ru content, the resulting Pt_7Ru_2Fe NW catalyst gave rise to a negative shift of ~230 mV in onset potentials for CO stripping as well as to ~11 times higher MOR activity as compared with our monometallic Pt NW controls, rendering this as our best catalyst tested for MOR. Moreover, these results suggest significant improvements by comparison with currently available, commercial PtRu nanoparticle (NP) standards (i.e. 1.52 mA/cm^2 versus 0.15 mA/cm^2 @ 0.7 V vs. RHE). Moreover, as we increased the amount of Fe present in the samples from 10% to 25% and correspondingly decreased the Ru content from 20% to 5%, we observed a shift in the onset for CO absorption towards higher potentials, thereby indicating the presence of delayed kinetics. As a result, from an analysis of our data based on the volcano-type trend observed in Figure 3.7, the Pt_7Ru_2FeNW catalyst represented a particularly attractive option for MOR.

To further explore the effects associated with varying the concentrations of the dopant metals, these catalysts were additionally for performance in formic acid oxidation. It should be noted that ternary catalysts have rarely been tested for activity with respect to both complementary reactions, namely methanol oxidation and formic acid oxidation, which thereby renders this study as both significant and novel. Specifically, when these catalysts were purposely used to oxidize formic acid, we noted that $Pt_7Ru_{1.5}Fe_{1.5}$ NWs maintained the lowest onset potential as compared with the other ternary samples, even Pt_7Ru_2Fe NWs.

As a result, from our data for both MOR and FAOR, we have been able to demonstrate that the actual chemical composition of the catalyst counts, because this parameter can be specifically used to finely tune the activity of our NWs for enhanced performance. These data therefore highlight a promising strategy for using chemistry to rationally and controllably optimize activities for both MOR and FAOR.

3.2. Results and Discussion

3.2.1. Ambient Synthesis and Characterization of PtRuFe NWs

In this study, for the first time, we have adapted an ambient wet synthesis technique to prepare ternary alloy nanowires under relatively mild reaction conditions. By appropriately manipulating the stoichiometric ratios of the metal precursors, we are able to correspondingly vary the constituent concentrations of each metal within the NWs, thereby allowing for the fabrication of homogeneous alloys with tunable compositions. The structure, purity, and crystallinity of our ultrathin ternary NWs were analyzed using a suite of structural characterization techniques including XRD, TEM, and HRTEM.

Specifically, Figure 3.1 highlights powder XRD patterns obtained on our ternary PtRuFe NWs as well as controls consisting of binary Pt_7Ru_3, Pt_7Fe_3 as well as monometallic Pt NWs. All seven NW samples possessed peaks located at 39°, 46° and 67°, which can be ascribed to the corresponding (111), (200), and (220) planes of an underlying Pt *fcc* framework structure (JCPDS database #04-0802). It is evident that the patterns are devoid of peaks that can be attributed to either the elemental ruthenium or iron phases (JCPDS database #06-0663 and #85-1410, respectively), thereby suggesting that reduction of the precursors can result in the formation of uniform alloys. Moreover, no apparent peaks ascribable to any possible impurities within the nanowires could be observed, indicative of the reasonably high purity of our samples. Nevertheless, for the PtRuFe NWs, slight shifts to higher 2θ are noted for the Pt (111) peak, likely due to the contraction of the Pt lattice by the incorporation of both Ru and Fe. The broadness of the peaks can potentially be attributed to both the inherently small sizes of the NWs tested (i.e. diameters under 5 nm) as well as to their intrinsic segmented texture.

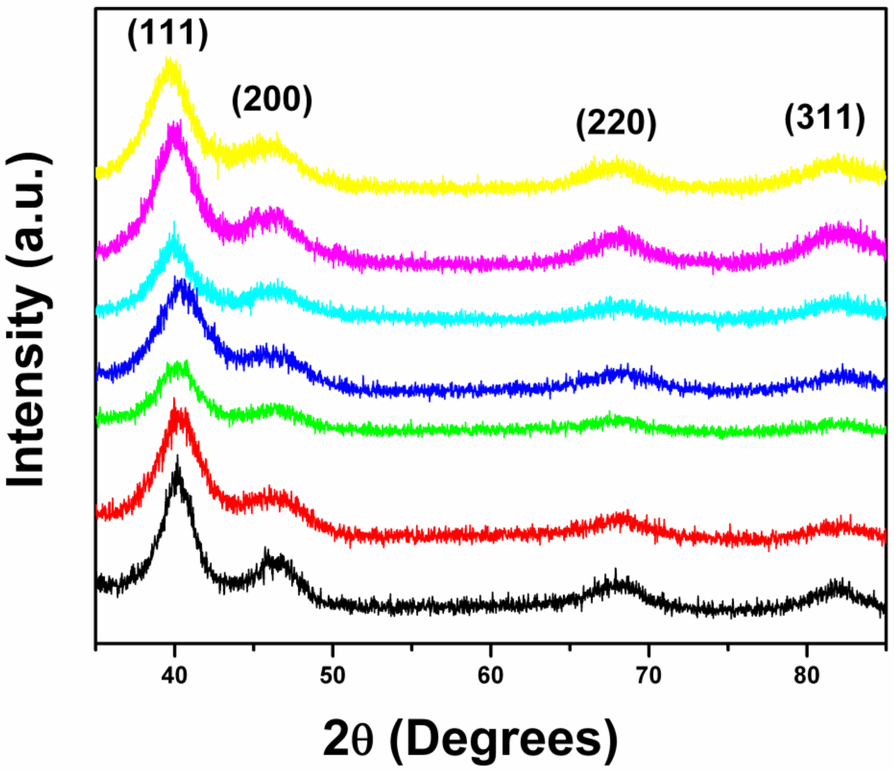

Figure 3.1. XRD patterns for Pt NWs (black), Pt_7Ru_3 NWs (red), Pt_7Ru_2Fe NWs (green), $Pt_7Ru_{1.5}Fe_{1.5}$ NWs (blue), Pt_7RuFe_2 NWs (baby blue), $Pt_7Ru_{.5}Fe_{2.5}$ NWs (magenta), and Pt_7Fe_3 NWs (yellow), respectively. All peaks are labeled and correspond to a Pt *fcc* structure (JCPDS database #04-0802). Reproduced by permission of The Royal Society of Chemistry.

Figures 3.2, 3.3, and 3.4 collectively illustrate the morphological analysis of all of our as-synthesized electrocatalysts using TEM, HRTEM, and SAED. Figure 3.2 suggests that we were able to synthesize the desired NW structural motif for all compositions prepared. All samples possess an average cross-sectional diameter in the range of 1.9 to 2.2 nm, as shown in Table 3.1. The usefulness and relevant applicability of our wet synthesis method are evident, as the nanowires produced are effectively homogeneous and monodisperse and moreover, their diameters are reasonably uniform, even while possessing a host of chemical compositions.

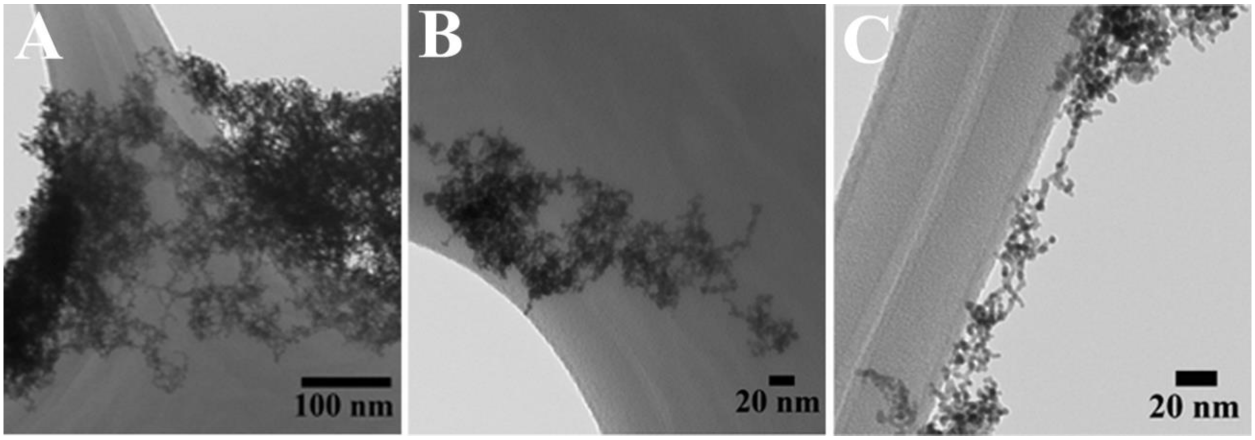

Figure 3.2. Representative TEM micrographs of the overall network-like nanowire structure. Specifically, images pertaining to (A) Pt_7Ru_3 NWs, (B) $Pt_7Ru_{1.5}Fe_{1.5}$ NWs, and (C) Pt_7Ru_2Fe NWs. Reproduced by permission of The Royal Society of Chemistry.

Higher-resolution TEM images (Figures 3.3B, E, H and Figures 3.4B, E, H, K) confirm that the interconnected nanowires are segmented and consist of constituent single-crystalline segments with lengths exceeding 100 nm.[31] These data are consistent with the selected area electron diffraction patterns (Figures 3.3C, F, I and Figures 3.4C, F, I, L), which collectively indicate that all of the samples maintain a polycrystalline texture. The corresponding lattice parameters were determined from the SAED data as well as deduced from the HRTEM images, and are summarized in Table 1 along with their calculated theoretical parameters. Specifically, the alloy-type NWs possessed measured *d*-spacings that correspond to the (111) plane of these various alloys, and these values are actually all within experimental error. The slight contraction in the lattice parameters with respect to that of elemental Pt is consistent with that of prior reports in the literature, due to the incorporation of Ru and Fe into the Pt lattice, thereby causing a slight contraction of the *fcc* lattice. As a result, the SAED patterns and the XRD data further confirm the notion that we can design and subsequently generate highly uniform and homogeneous alloyed nanowires, possessing a variety of desired compositions.

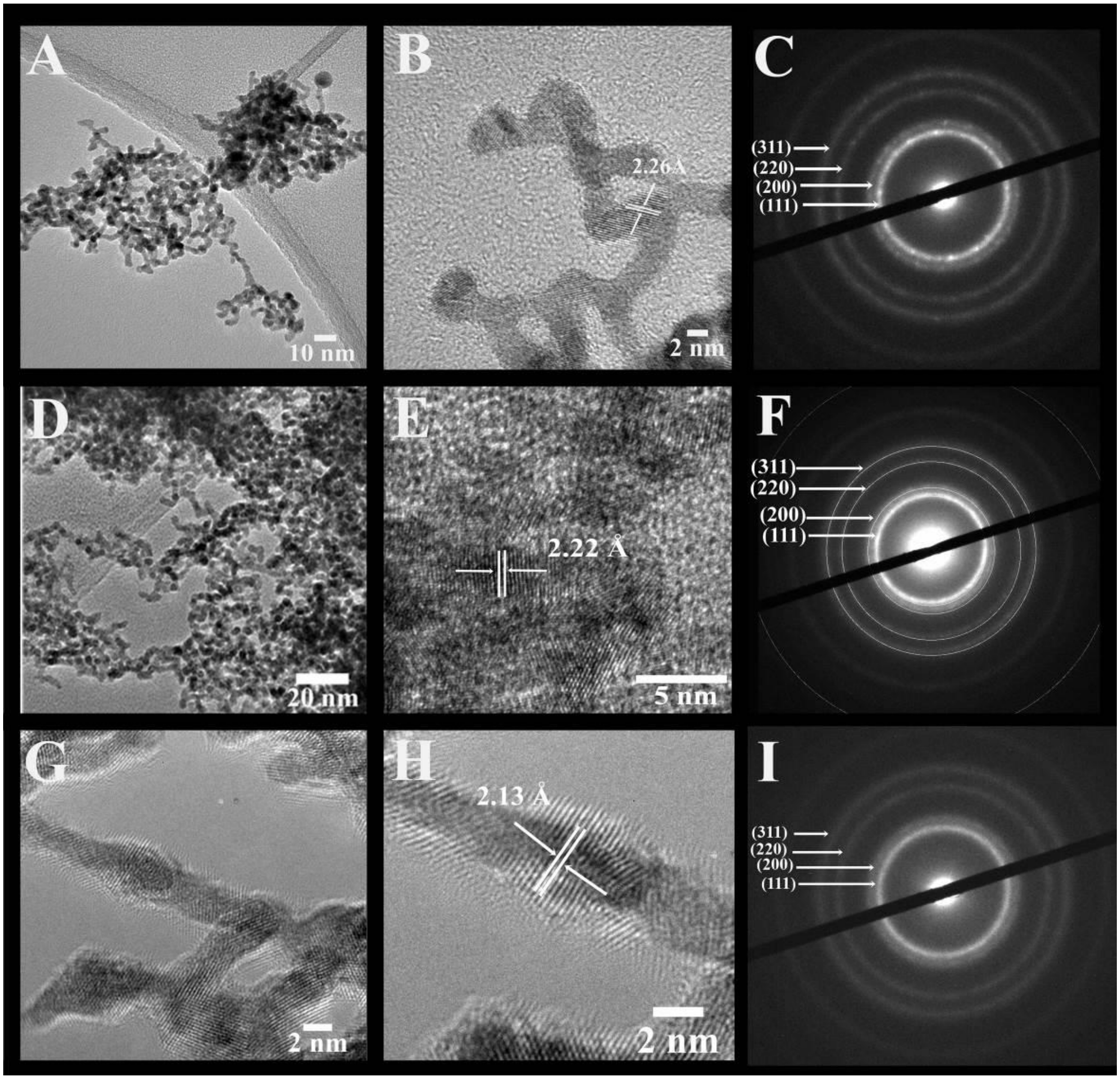

Figure 3.3. Representative high resolution TEM micrographs (A, D, G), higher magnification HRTEM images with measured *d*-spacings (B, E, H), and associated single area electron diffraction patterns (C, F, I) for Pt NWs (A-C), Pt_7Ru_3 NWs (D-F), and Pt_7Fe_3 NWs (G-I), respectively. Reproduced by permission of The Royal Society of Chemistry.

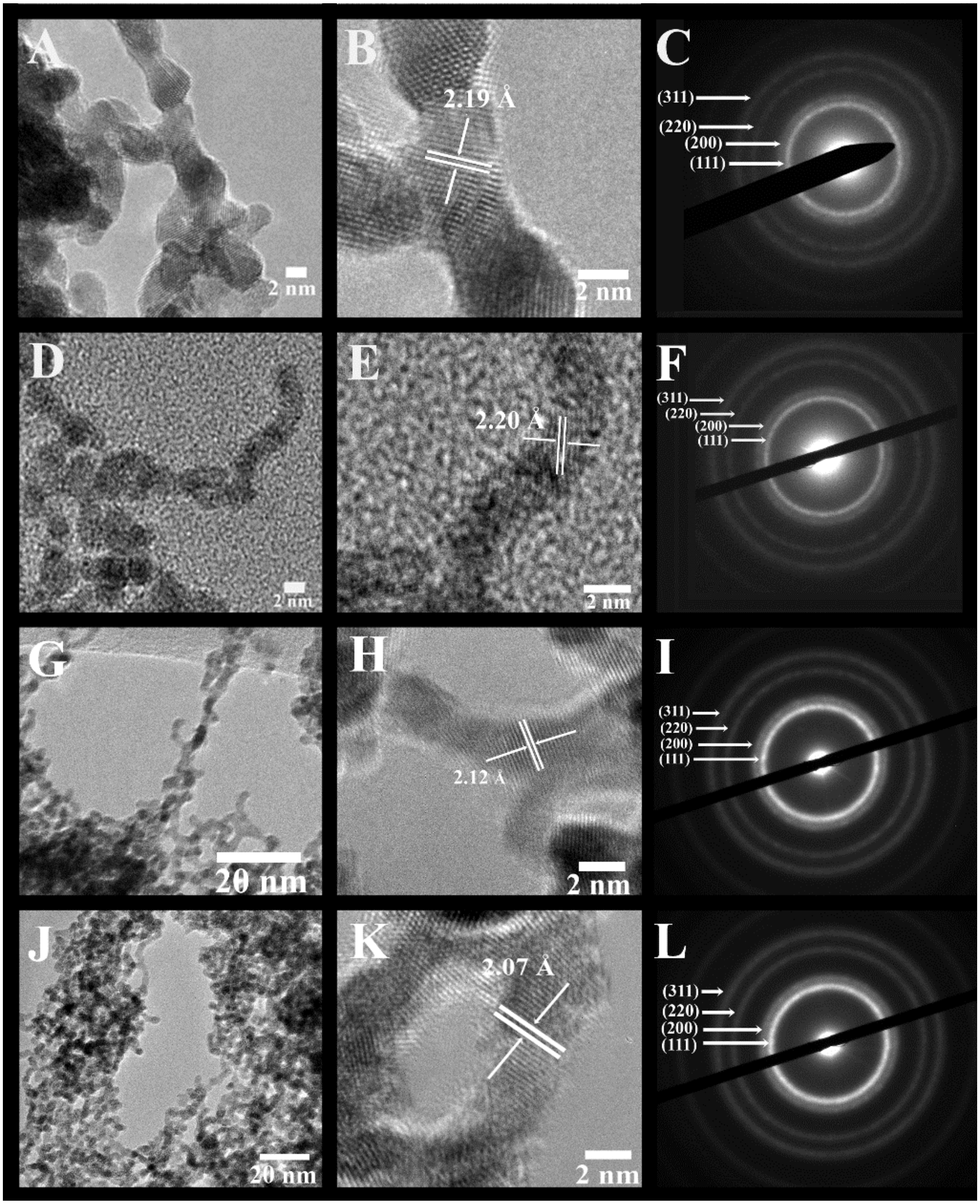

Figure 3.4. Representative high resolution TEM micrographs (A, D, G, J), higher magnification HRTEM images with measured *d*-spacings (B, E, H, K), and associated single area electron diffraction patterns (C, F, I, L) for Pt_7Ru_2Fe NWs (A-C), $Pt_7Ru_{1.5}Fe_{1.5}$ NWs (D-F), Pt_7RuFe_2 NWs (G-I) and $Pt_7Ru_{.5}Fe_{2.5}$ NWs (J-L), respectively. Reproduced by permission of The Royal Society of Chemistry.

To complement these data, the actual chemical composition of our nanowire samples was determined using energy dispersive X-ray spectroscopy (EDAX). The elemental results are presented in Table 3.1, and are consistent with the expected chemical compositions based on the precursor concentrations used and the NWs we intended to synthesize. As a result, both Fe and Ru are present in these samples with their chemical compositions predicted within experimental error. Thus, the XRD data coupled with the TEM and SEM-EDAX measurements together confirm that there is a high degree of correlation between the chemical composition of the precursor solutions and the corresponding composition of the resulting NWs.

Catalyst	**Pt % Comp.**	**Ru % Comp.**	**Fe % Comp.**	**Avg. Diameter**	**Measured (SAED)**	**Measured (HRTEM)**	**Calculated**
Pt NWs	100%	-	-	1.9 ± .3 nm	2.26 Å	2.26 Å	2.260 Å
Pt_7Ru_3 NWs	72%	28%	-	2.0 ± .4 nm	2.22 Å	2.22 Å	2.068 Å
$Pt_7Ru_{2.5}Fe_{.5}$ NWs	73%	22%	5%	2.1 ± .3 nm	2.22 Å	2.21 Å	2.079 Å
Pt_7Ru_2Fe NWs	72%	19%	9%	2.2 ± .4 nm	2.22 Å	2.20 Å	2.077 Å
$Pt_7Ru_{1.5}Fe_{1.5}$ NWs	69%	14%	17%	2.1 ± .4 nm	2.12 Å	2.19 Å	2.064 Å
Pt_7RuFe_2 NWs	70%	9%	21%	2.0 ± .2 nm	2.25 Å	2.12 Å	2.076 Å
$Pt_7Ru_{.5}Fe_{2.5}$ NWs	73%	4%	23%	1.9 ± .3 nm	2.24 Å	2.07 Å	2.099 Å
Pt_7Fe_3 NWs	67%	-	33%	2.0 ± .2 nm	2.22 Å	2.13 Å	2.067 Å

Table 3.1. Atomic percent compositions for each of the metals present in each catalyst as well as the average diameters of each of the nanowires synthesized, from experimental measurements. Measured and calculated lattice *d*-spacings from both high-resolution TEM images as well as single area electron diffraction patterns, corresponding to the (111) plane of the Pt *fcc* lattice. Reproduced by permission of The Royal Society of Chemistry.

3.2.2. Correlating Composition of Homogeneous Alloy Catalysts with MOR

As shown in Figure 3.5A and 3.5B, CVs were obtained for Pt NWs, Pt_7Ru_3 NWs, Pt_7Fe_3 NWs and the four ternary PtRuFe NWs in order to investigate and correlate the impact of altering Ru and Fe ratios on electrochemical performance. Regarding the substructure of the

CVs, the shape and location of the observed hydrogen and oxygen adsorption features associated with the Pt_7Ru_3 NW catalyst are consistent with prior reports of homogeneous $Pt_{1-x}Ru_x$ alloy type nanowires.[32, 33] Interestingly, a significant upshift of the oxide reduction peak of ~200 mV is noted, as the Fe content is increased from 10% to 25% in the Pt_7Ru_2Fe and $Pt_7Ru_{.5}Fe_{2.5}$ catalysts, respectively. Figure 3.6 depicts the linear trend between onset potential and changes in atomic composition. This apparent shift in the oxide reduction peak suggests a weakening of the interaction with the oxygen adsorbate and has been observed by previous groups.[7, 33, 34]

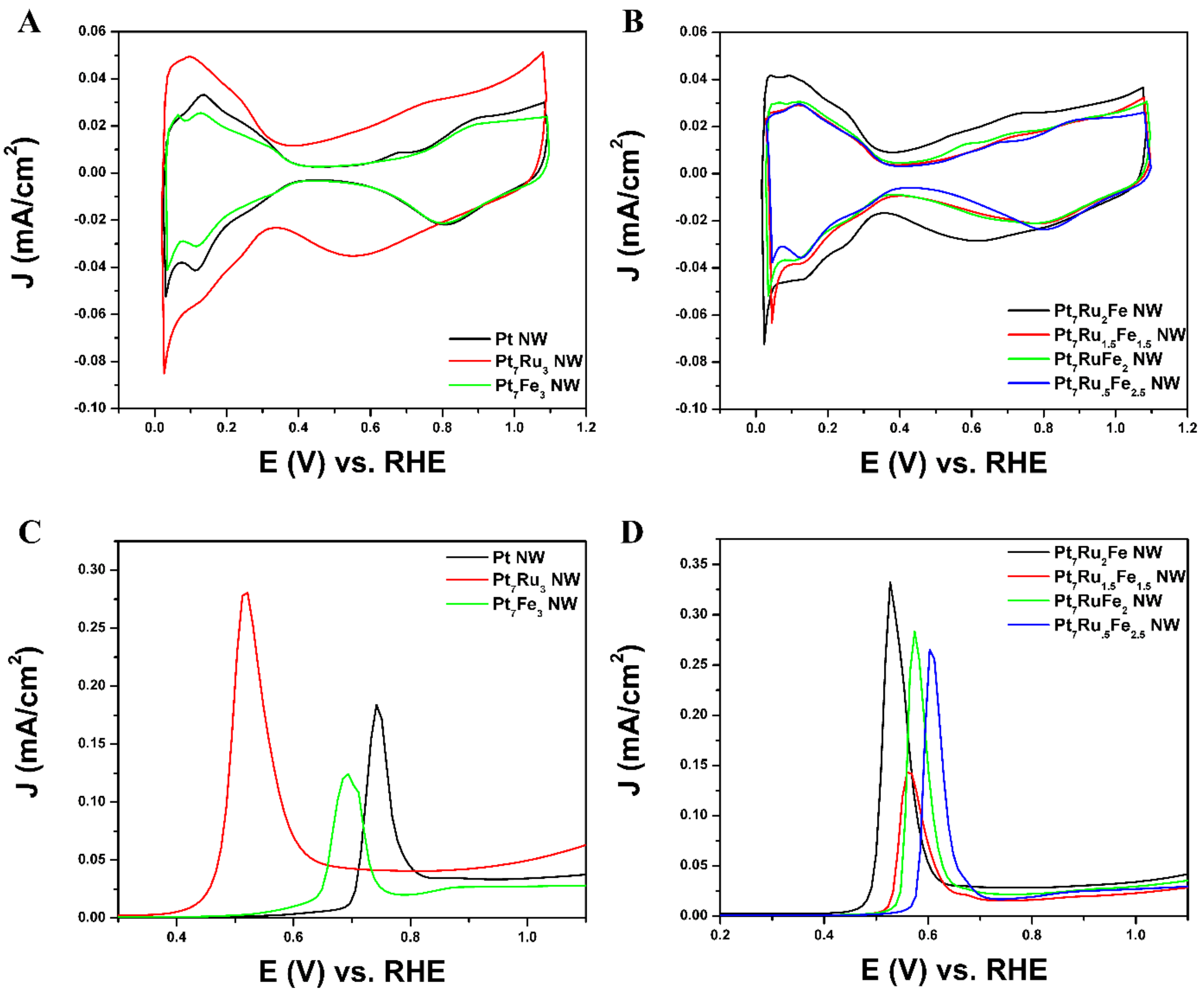

Figure 3.5. Representative CV curves in an argon saturated 0.1 M $HClO_4$ solution, obtained at a scan rate of 20 mV/s with the current normalized to ECSA for (A) Pt NWs, Pt_7Ru_3 NWs, Pt_7Fe_3 NWs and (B) Pt_7Ru_2Fe NWs, $Pt_7Ru_{1.5}Fe_{1.5}$ NWs, Pt_7RuFe_2 NWs, $Pt_7Ru_{.5}Fe_{2.5}$ NWs , respectively. (C) Representative CO stripping LSV curves for Pt NWs, Pt_7Ru_3 NWs, Pt_7Fe_3 NWs and (D) Pt_7Ru_2Fe NWs, $Pt_7Ru_{1.5}Fe_{1.5}$ NWs, Pt_7RuFe_2 NWs, $Pt_7Ru_{.5}Fe_{2.5}$ NWs, respectively. Reproduced by permission of The Royal Society of Chemistry.

We attribute this observation to a restructuring effect associated with our as-processed nanowires. Specifically, dissolution is known to occur for a variety of transition metals, including Fe, Ni, and Co, especially when localized at the surface and exposed to anodic potentials.[35] Therefore, as the amount of Ru decreases and is effectively substituted with increasing Fe content, any Fe present within these alloys would tend to be preferentially consolidated and incorporated as part of the nanowire core due to the likely dissolution and subsequent removal of Fe at the exposed surface. As a result, the dissolution of iron and concomitant formation of a Pt-rich surface typically results in improved catalytic performance owing to the unique structural and electronic effects imparted by the interactions between the Pt-rich surface and the alloy-type core.[36-38] Corroborating evidence for the enrichment of Pt at the catalytic interface is also apparent in the hydrogen adsorption region, which shows increasing Pt-like character as the Fe content is increased from 10 – 25%; such an observation has also been noted for Pt_7Fe_3 NWs.

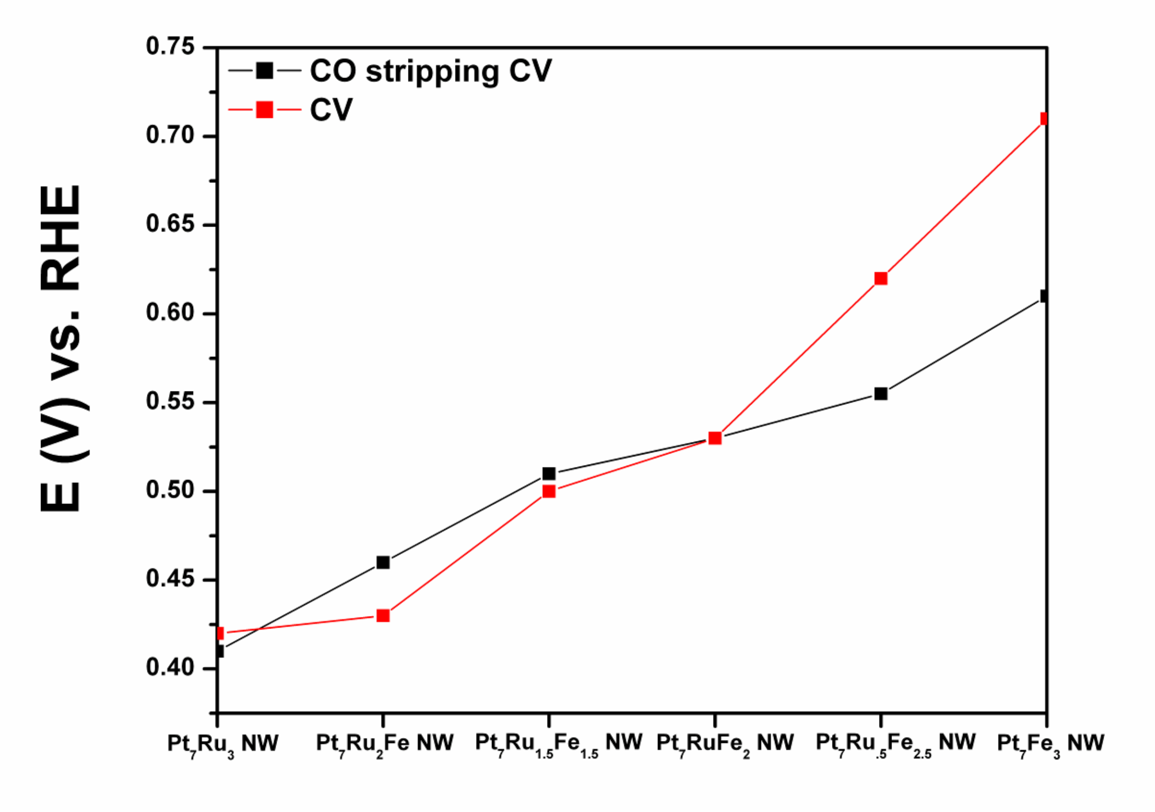

Figure 3.6. A plot investigating the trend in onset potential for CO stripping (black) and the onset of oxygen reduction (red) as a function of composition, ranging from Pt_7Ru_3 NWs to Pt_7Fe_3 NWs. Reproduced by permission of The Royal Society of Chemistry.

Although it is evident from the H_{ads} results that Pt is increasingly enriched at the catalytic interface as a function of decreasing amounts of Ru present within the catalyst due to preferential Fe surface dissolution, it is interesting to note that the onset of oxide formation is similar to that observed for Pt_7Ru_3 NWs as well as for Fe-doped Pt_7Ru_2Fe NWs, with the onset for the $Pt_7Ru_{1.5}Fe_{1.5}$ NWs as well as for the remaining ternary catalysts analyzed shifted slightly to higher potentials, denoting behavior similar to that for the Pt_7Fe_3 NW catalyst. To explain all of these data, it is known that in the case of $Pt_{1-x}Ru_x$ alloys, the presence of Pt-Ru pair sites increases MOR catalytic performance by facilitating the oxidation of adsorbed CO species at potentials lower than those observed on elemental Pt as a result of a process referred to as 'carbonyl-spillover'.[39, 40] That is, in the presence of Ru, adsorbed CO species generated by the rapid dehydrogenation of methanol at Pt active sites can functionally 'spill over' and react with Ru-OH species, thereby forming CO_2. Thus, the CV results suggest that the Fe-doped PtRu NWs may actually benefit from the complementary beneficial effects of (i) the bifunctional mechanism, wherein –OH species dissociated from water and adsorbed onto the Ru surface catalyze the removal of CO adsorbed onto Pt active sites at lower potentials, thereby increasing the overall activity of $Pt_{1-x}Ru_x$–based alloys, as well as (ii) the favorable electronic effects associated with PtFe alloys, in which the presence of Fe functionally lowers the *d*-band center of the Pt, thereby resulting in more *d*-band vacancies and therefore, overall less susceptible to poisoning of active sites by CO species formed as intermediates in the indirect oxidation of methanol.[3, 6, 41, 42]

In order to evaluate the methanol oxidation performance, all seven catalysts were tested electrochemically in comparison with commercial PtRu/C serving as a standard and the resulting linear sweep voltammograms (LSVs) are shown in Figure 3.7. Pt_7Ru_2Fe NWs evinced the highest MOR activity, generating an activity of 2.27 mA/cm^2 at 0.8 V vs. RHE; analogous $Pt_7Ru_{1.5}Fe_{1.5}$ Pt_7RuFe_2, $Pt_7Ru_{.5}Fe_{2.5}$, Pt_7Ru_3, and Pt_7Fe_3 NWs yielded lower activities with values of 1.86 mA/cm^2, 1.46 mA/cm^2, 1.35 mA/cm^2, 1.46 mA/cm^2, and 0.67 mA/cm^2, respectively.

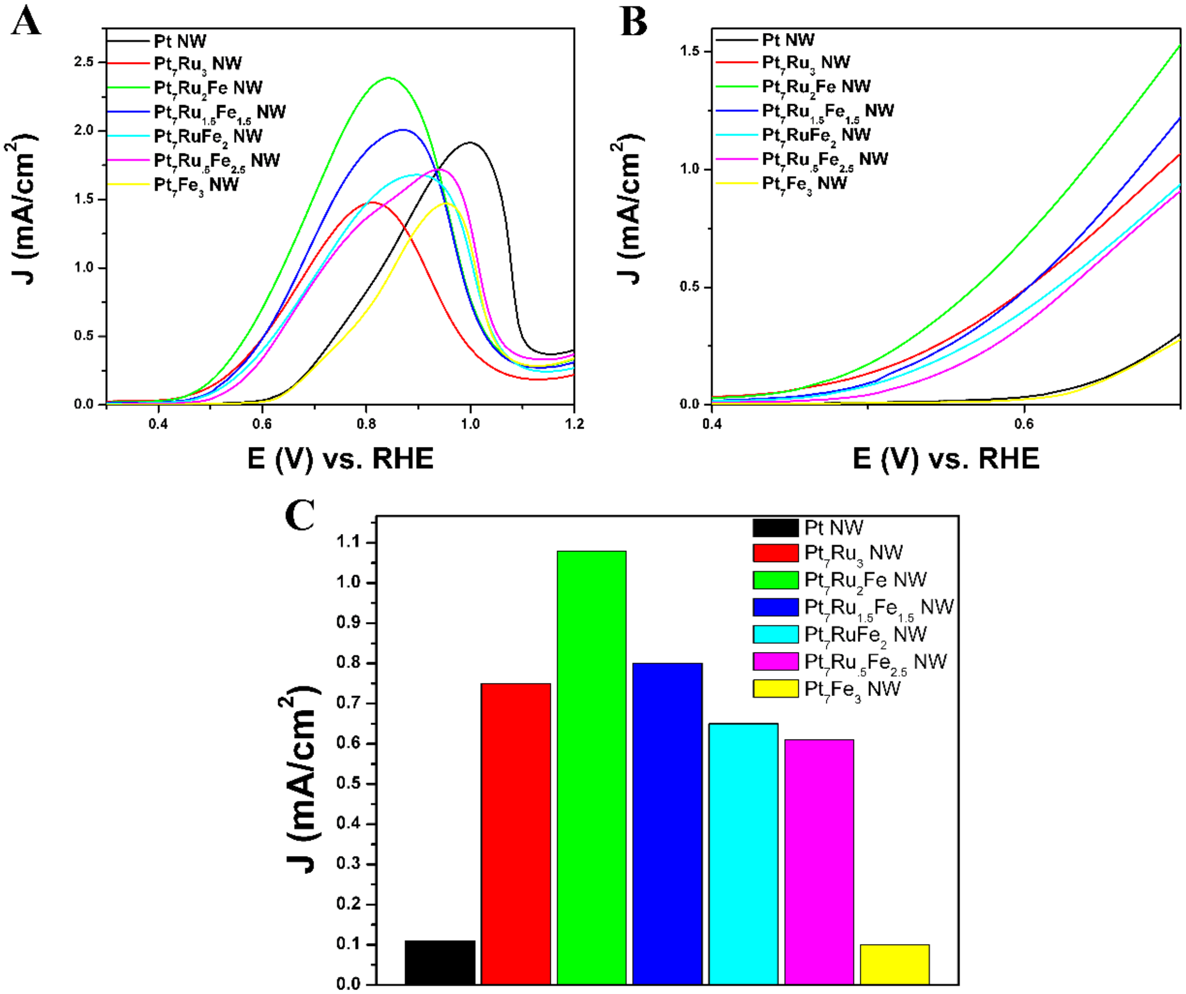

Figure 3.7. (A) Cyclic voltammograms for the methanol oxidation reaction in an argon saturated 0.1 M $HClO_4$ + 0.5 M MeOH solution, obtained at a scan rate of 20 mV/s with the current normalized to ECSA. (B) Magnification of the MOR onset region highlighted between 0.4 V - 0.7 V vs. RHE. (C) Bar graph highlighting MOR activity at E (V) vs. RHE = 0.65 V for Pt NWs, Pt_7Ru_3 NWs, Pt_7Ru_2Fe NWs, $Pt_7Ru_{1.5}Fe_{1.5}$ NWs Pt_7RuFe_2 NWs, $Pt_7Ru_{.5}Fe_{2.5}$ NWs and Pt_7Fe_3 NWs, respectively. Reproduced by permission of The Royal Society of Chemistry.

Analyzing the onset region shown in Figure 3.7B, it is apparent that Pt_7Ru_2Fe possessed the lowest onset potential of all the NWs tested with a potential of ~ 0.44 V. Figure 3.7C depicts a bar graph comparing the MOR activity at a representative potential of 0.65 V, which was in the onset region of the LSV. From these data, we measured a specific activity of 1.10 mA/cm^2 for our best MOR catalyst tested, namely Pt_7Ru_2Fe NWs, which is 11-fold higher than that of Pt_7Fe_3 and Pt NWs (0.10 mA/cm^2) and almost 2-times greater as compared with our ‘starting point’, i.e. our as-synthesized Pt_7Ru_3 NWs (0.75 mA/cm^2). Moreover and importantly, we demonstrated a volcano-type trend in activity across our series of samples, further supporting our claim that composition is crucial to electrocatalytic performance. Moreover, the numbers reproducibly obtained with our ternary NWs are higher in magnitude as compared with other reports of PtRuFe catalysts,[6, 20, 27] and even significantly outperformed conventional commercial standards, such as PtRu NP/C, as can be observed in Figure 3.8.

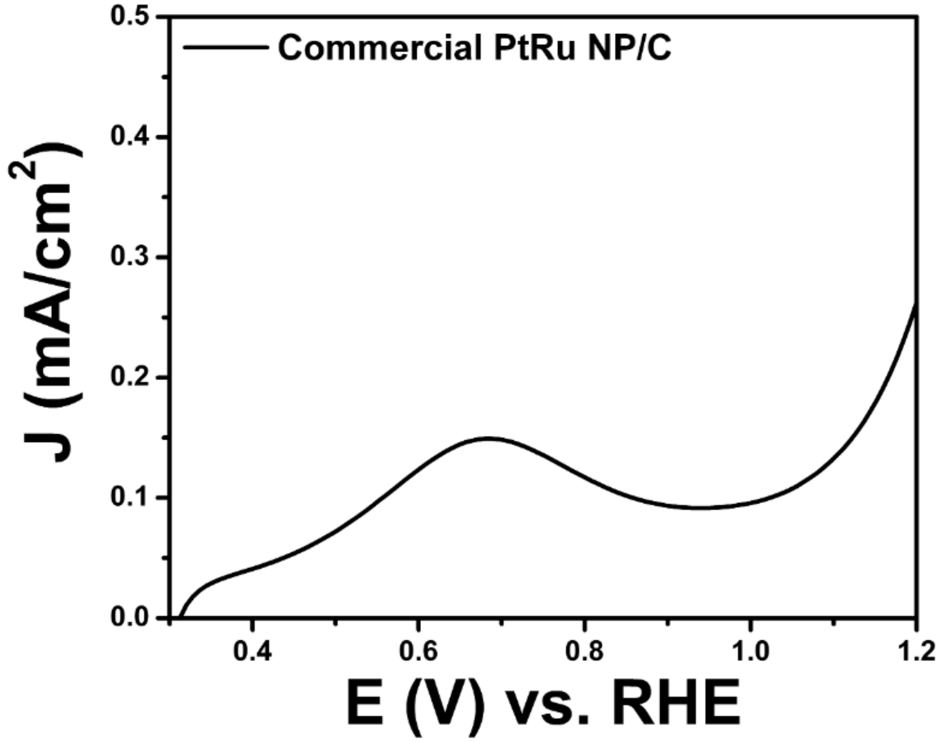

Figure 3.8. MOR activity measured for commercial PtRu NP/C with a 1:1 molar ratio. Reproduced by permission of The Royal Society of Chemistry.

3.2.3. Correlating Composition of Alloy Catalysts with MOR and FAOR Mechanisms

One of the aims of our study has been to gain insights into the observed enhancements, i.e. encouraging shifts in potential and activity, in our trimetallic Fe-containing PtRuFe NWs and to determine if these phenomena are dependent upon and can therefore be tuned by predictively tailoring chemical composition. Therefore, in experiments aimed at completing our activity analysis and understanding the overall potential of our catalysts, we investigated the performance of our nanowires toward the catalytic oxidation of CO and formic acid, which represent two potential critical intermediates in the oxidation of methanol.

3.2.3.1. MOR

To date, two distinctive MOR oxidation pathways have been proposed in the literature to explain the measured enhancement in performance for simulated bimetallic alloy systems.[43-45] In the case of the *conventional "CO pathway"* or *indirect pathway*, it is calculated that the rate-determining step is the dehydrogenation of CHO_{ads} to CO, which has a considerable energy barrier of 0.98 eV. The indirect pathway is anticipated to be more significant if adsorbed OH species are not available at the catalytic interface. By contrast, calculations reveal that a *direct, CO-free pathway* is favored, wherein formic acid (HCOOH) is rapidly produced as a weakly bound intermediate species by the reaction of the CHO_{ads} with OH_{ads}. In this *CO-free pathway*, the scission of the O-H bond of HCOOH represents the rate determining step with a significantly lower energy barrier of 0.75 eV. Thus, the theoretical results suggest that the *direct pathway* should prevail in the case wherein adsorbed OH species are readily available, leading to the formation of HCOOH as the primary intermediate. Therefore, the *direct pathway* is readily distinguishable from its indirect counterpart by the collective presence of $HCOOH_{ads}$ and OH_{ads} species in the former, as opposed to the predominant occurrence of only CO_{ads} in the latter.

A number of factors can influence the principal pathway, such as potential, flow rate, and methanol concentration.[46] Currently, experimental evidence for both mechanisms relies primarily on the measured MOR kinetics and an *ex situ* spectroscopic analysis of electrocatalysts. Therefore, it is necessary to study the oxidation behavior of both methanol and formic acid in order to pinpoint the effects that promote enhanced performance.

Initially, CO stripping LSVs were collected to analyze the CO tolerance of each catalyst, as observed in Figure 3.5C and 3.5D. The currents measured for each sample were normalized to the electrochemically active surface area, which was determined from the hydrogen adsorption region (H_{ads}). As can be observed, the CO onset potential for the Pt NWs (black line) occurs at ~0.69 V. As more Ru is added (30 atom %), the onset is shifted to a lower potential (i.e. ~0.41 V), consistent with the bi-functional mechanism; the presence of additional Ru sites enables OH species to be adsorbed at lower potentials, thereby facilitating the removal of adsorbed CO species from Pt active sites. The CO stripping onsets for the various ternary catalysts are shown as a function of NW composition in Figure 3.6 and show that there is a monotonous trend between NW composition and the CO stripping onset potential.

This apparent and proportional increase in CO onset potential with a corresponding rise in Fe content in the composition of ternary NW catalysts is consistent with the relative enrichment of Pt at the interface, due to selective dissolution of Fe sites which correspondingly promotes the formation of a Pt surface layer with an alloy core. Such behavior can also be explained by the corresponding decrease in Ru content, which is responsible for adsorbing OH species that assist in subsequent CO oxidation on the Pt surface. All of these trends are consistent with prior reports, although the onset potentials measured in the Fe-doped, ultrathin NWs are measurably lower as compared with values observed for analogous systems.[20, 27]

Although this trend in CO onset potential (i.e. systematic decrease with increasing Ru metal content) supports the presence of the bifunctional mechanism, it does not fully describe the complicated and synergistic interactions between Pt, Ru, and Fe, and their combined effect upon the resulting MOR mechanism. However, as previously mentioned during the analysis of the CV data, the catalyst possessing only 10% Fe dopant to replace Ru gave rise to a similar onset potential for oxide adsorption as that of control Pt_7Ru_3 NWs, an observation which further corroborates the viability of a ligand effect, in which the presence of Fe is less conducive to the formation of an adsorbed CO intermediate. In effect, the Pt_7Ru_2Fe nanowires were found to give rise to the lowest onset potential and highest MOR activity (Figure 3.7), presumably due to a diminished affinity towards CO and the corresponding presence of more available Pt active sites for MOR.

In terms of the effect of the ultrathin NW morphology, recent work by our group[47] and others[48-50] has shown that the segmented texture results in the production of well-ordered smooth crystalline planes along the single crystalline segments as well as defect sites present at the interconnects between segments. Typically, active sites bind rather strongly to CO, thereby requiring a higher potential for its removal. Defect sites, on the other hand, require a lower potential for the elimination of CO species.[45, 51]As a result, elemental ultrathin Pt NWs are particularly active toward alcohol oxidation due to their overall enhanced ability to oxidize CO. That is, since CO can be oxidized at relatively lower potentials as compared with their larger diameter nanowire analogues, ultrathin Pt nanowires provide for more active sites to be available for MOR. Hence, on the basis of our CO stripping results, we show that the CO oxidation performance of ultrathin nanowires can be further enhanced by tailoring chemical composition.

3.2.3.2. FAOR

To further investigate the relative contributions of the bi-functional mechanism and ligand effect with respect to our results, formic acid oxidation was investigated as well for all of our catalysts, using Pt NWs as a standard reference. The data are shown in Figure 3.9. Typically, FAOR can occur either directly (Equation 3.3) or indirectly (Equation 3.4) through the generation of the intermediate CO.[52] The indirect CO-mediated pathway is less favorable to occur on the surfaces of Pt-based catalysts, due to possible poisoning effects.

$$HCOOH \rightarrow CO_2 + 2e^- + 2H^+ \quad [3.3]$$

$$HCOOH \rightarrow CO + H_2O \rightarrow CO_2 + 2\,e^- + 2H^+ \quad [3.4]$$

Figure 3.9A depicts the onset region for formic acid oxidation. As can be observed, for all nanowires analyzed, our $Pt_7Ru_{1.5}Fe_{1.5}$ NW catalyst not only possesses the lowest onset potential (0.38 V) for the oxidation of formic acid but also exhibits the fastest kinetics for the reaction, as indicated by its steepest slope. Figure 3.9B highlights a bar graph, describing the overall activity of each catalyst towards FAOR measured at a potential of 0.65 V.

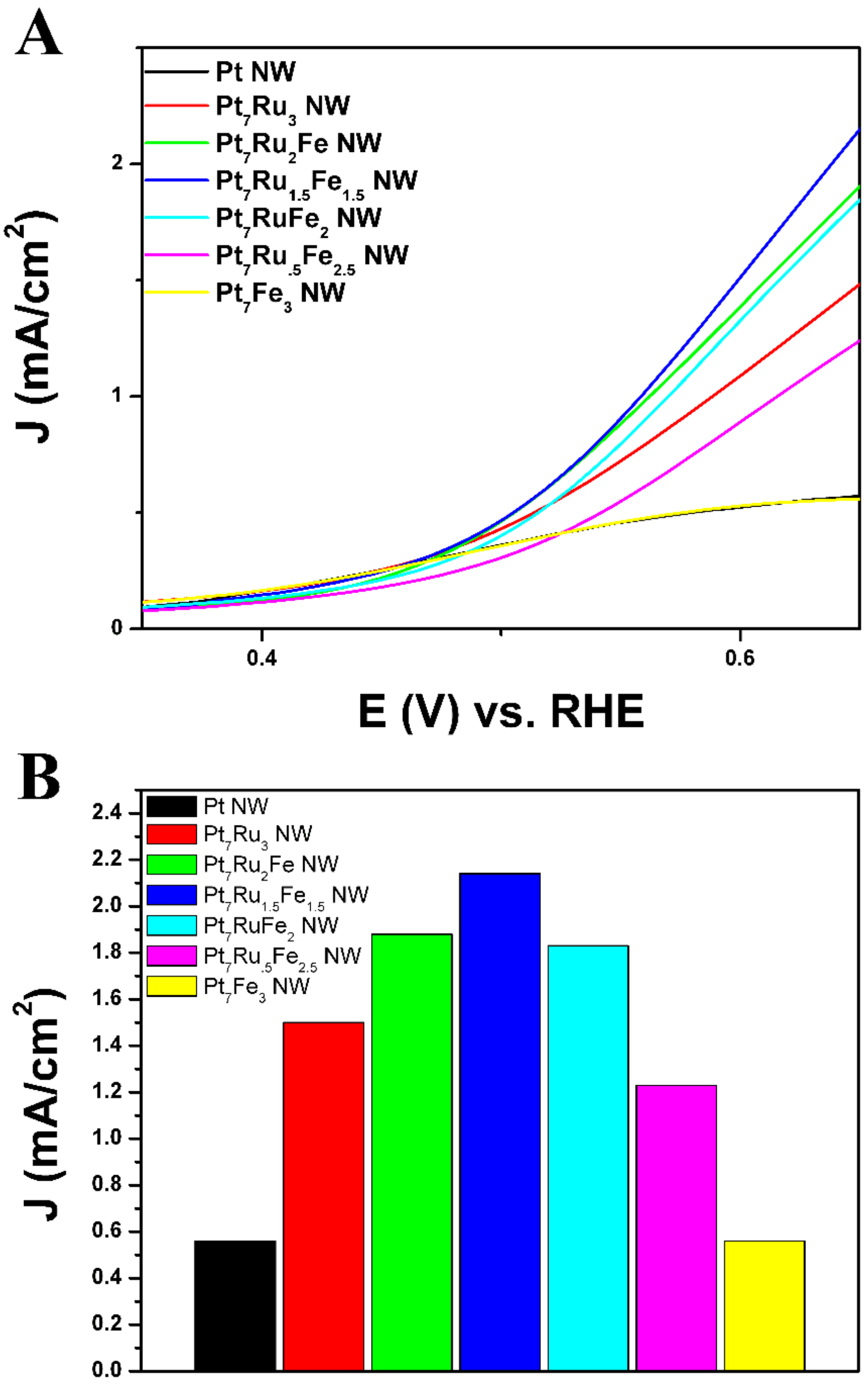

Figure 3.9. (A) Cyclic voltammograms for the formic acid oxidation reaction in an argon saturated 0.1 M $HClO_4$ + 0.5 M HCOOH solution, obtained at a scan rate of 20 mV/s with the current normalized to ECSA. (B) Bar graph demonstrating FAOR activity at E(V) vs. RHE = 0.65 V for Pt NWs, Pt_7Ru_3 NWs, Pt_7Ru_2Fe NWs, $Pt_7Ru_{1.5}Fe_{1.5}$ NWs Pt_7RuFe_2 NWs, $Pt_7Ru_{.5}Fe_{2.5}$ NWs and Pt_7Fe_3 NWs, respectively. Reproduced by permission of The Royal Society of Chemistry.

Of the samples tested, the $Pt_7Ru_{1.5}Fe_{1.5}$ NW catalyst yielded the highest activity (2.15 mA/cm^2), which is nearly four times that of as-prepared Pt NWs (0.58 mA/cm^2). We noted that the activities of the remaining catalysts also follow a volcano-type trend, similar to what had been previously found for the MOR data in Figure 3.7. These catalysts achieved FAOR activities of 1.90 mA/cm^2 (Pt_7Ru_2Fe NWs), 1.83 mA/cm^2 (Pt_7RuFe_2 NWs), 1.22 mA/cm^2 ($Pt_7Ru_{.5}Fe_{2.5}$ NWs), 1.50 mA/cm^2 (Pt_7Ru_3 NWs) and 0.55 mA/cm^2 (Pt_7Fe_3 NWs), respectively which all fall slightly below that of $Pt_7Ru_{1.5}Fe_{1.5}$ NWs on either side of the table. Moreover, our ternary catalysts also outperformed that of commercial PtRu NP/C, as can be observed in Figure 3.10.

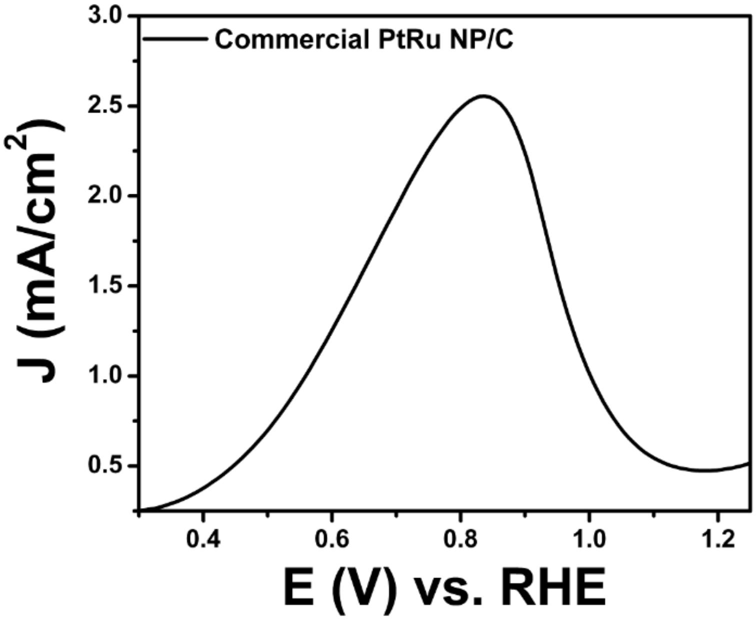

Figure 3.10. Formic acid oxidation for commercial alloy PtRu NP/C with a 1:1 ratio. Reproduced by permission of The Royal Society of Chemistry.

A similar onset potential value for both Pt_7Ru_2Fe NW and $Pt_7Ru_{1.5}Fe_{1.5}$ NW catalysts indicated that the parameter of onset potential was not necessarily influenced by their corresponding CO stripping abilities. More specifically, we found that catalysts possessing the lowest onset for the methanol oxidation reaction and formic acid oxidation reaction did not necessarily give rise to the lowest onset potential for CO stripping.

3.2.4. Comparison of and Insights into MOR and FAOR Data.

As a result, by rationally tailoring chemical composition of Pt-based alloys within the 30% overall metal dopant (i.e. RuM content) window that we worked with in recognition of the high performance of Pt_7Ru_3 alloys serving as our 'base' control composition, we have been able to precisely optimize the most advantageous percentage permutation of metals for each of the reactions analyzed herein. Specifically, by adding in only 10% Fe to replace Ru as part of the PtRuM alloy, we synthesized a catalyst with the lowest onset potential for MOR, indicative of faster reaction kinetics, as well as the highest activity for the MOR process. By adding in 15% Fe to replace Ru in the PtRuM alloy, we generated not only a lower onset but also a higher overall electrochemical activity for FAOR, presumably because of the combination of (i) the extra Fe content, which yielded a decreased affinity for poisoning species (such as CO) and therefore a shift of the formic acid absorption to lower potentials, as well as (ii) the presence of 15% Ru content associated with removing poisonous species from Pt active sites at lower potentials. Overall, these results therefore suggest that catalysts need to be precisely tailored in terms of chemistry in order to synthesize the ideal alloy composition for each reaction.

In Figure 3.5, in effect, we were able to observe two distinctive trends, one specifically related to Ru content and another associated with the Fe content. In the cathodic sweep, a shift to lower potentials occurred with the addition of more Ru dopant within a PtRu catalyst as compared with pure Pt, possibly as a result of the bi-functional mechanism.[9] Upon the subsequent addition of 10% Fe to replace Ru, no apparent shift in the oxide reduction peak was visible, as compared with the Pt_7Ru_3 catalyst control, suggesting that there may have been the same amount of –OH species absorbed onto the surface.

Such an observation would suggest the presence of a ligand effect.[36] By contrast, by adding in 15% -30% Fe and correspondingly decreasing overall Ru content, the catalysts became more 'noble' as compared with Pt_7Ru_3 NW catalyst, due to the relative increase of Pt at the surface (i.e. through the ligand effect) as noted by the shift to higher potentials for the reduction of oxide species. The fact that the Pt_7Fe_3 NW catalyst evinced a similar onset as compared with Pt can be explained in terms of this phenomenon. Overall, based solely on the surface structure analysis of these catalysts by CV, the Pt_7Ru_2Fe NW catalyst appeared to exhibit the highest catalytic activity towards MOR.

As a result herein, we have demonstrated that both the oxidation of methanol and formic acid are governed by two contrasting trends. Specifically, methanol oxidation appears to be predominantly influenced by the Ru content, whereas formic acid oxidation is primarily impacted by the corresponding Fe content within the ternary metal alloy catalyst itself. Therefore, by carefully optimizing and tuning chemical composition, we have tried to create a synergistic balance between these two competing behaviors to generate the best compromise catalyst for the overall methanol oxidation reaction, in this case, the Pt_7Ru_2Fe NW catalyst.

To take these results a step further, chronoamperometric experiments (Figure 3.11) were run in order to probe the stability of our as-prepared nanowire catalysts during methanol oxidation. We were able to demonstrate that by using this unique ternary alloy system, we could readily increase catalyst stability as compared with a commercial PtRu NP standard. Overall, once these catalysts became stable, our ternary NW catalyst maintained higher steady state current densities of 0.605 mA/cm^2 over the whole time range of 60 minutes as compared with a conventional PtRu NP/C catalyst (current density of 0.051 mA/cm^2), thereby suggesting not only increased stability but also greater catalytic activity for our NW species.

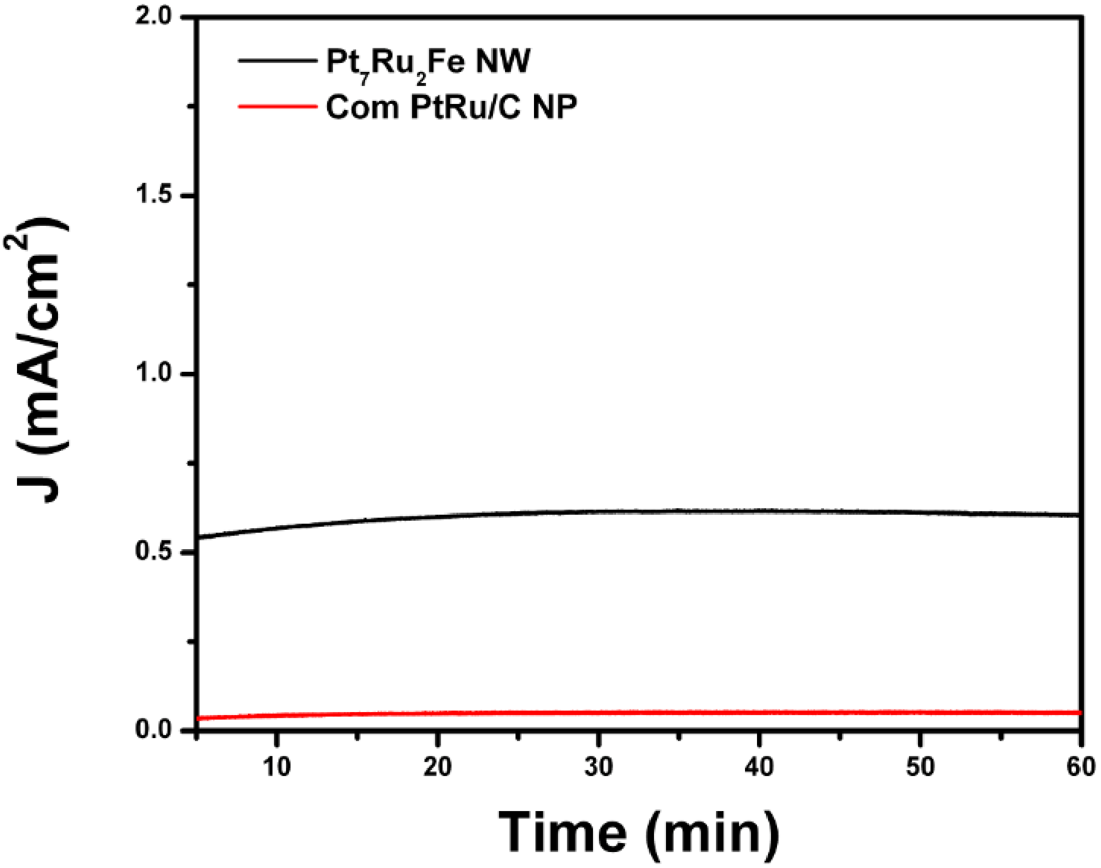

Figure 3.11. Chronoamperometry measurements of optimized Pt_7Ru_2Fe NW catalysts as compared with commercial standards (i.e. PtRu NP/C) in an argon saturated 0.1 $HClO_4$ + 0.5 M CH_3OH solution, obtained at a potential of 0.65 V vs. RHE for a period of 60 min. Reproduced by permission of The Royal Society of Chemistry.

The enhanced stability of NWs versus NPs has been previously ascribed to stronger NW interactions with the carbon support as well as to an inherently greater NW structural stability, especially under acidic MOR conditions.[23] It should also be noted that commercial Pt NP/C achieve comparable steady state current densities as compared with that of the PtRu NP/C.[25] These results simply reinforce the fact that our ternary Pt_7Ru_2Fe system represents a more active and stable catalyst for MOR as compared with conventional and even commercial choices.

3.3. Conclusions and Future Work

Previous work had provided evidence that ternary PtRuM (M = Ni, Co and W) alloys could be considered as promising anodes for DMFCs.[24] Therefore, herein, as a variation of that theme, starting from a high-performance binary Pt_7Ru_3 sample as a ‘base control’, we have successfully synthesized ternary PtRuM nanowire catalysts possessing various atomic compositions of metal dopants (Ru and Fe), utilizing an inverse micellar protocol that had not as yet been previously applied to such chemically complex electrocatalytic systems. As comparative controls, we also reproducibly generated Pt_7Ru_3 NWs, Pt_7Fe_3 NWs, and Pt NWs to probe the effect of tailoring chemical composition upon the corresponding electrochemical activity. As-generated NW catalysts possessed diameters of approximately 2 nm and expected chemical compositions, as determined from EDAX data. HRTEM demonstrated that our as-synthesized nanowires were polycrystalline in nature and consisted of short segments of crystalline planes, as further corroborated by SAED patterns.

The collected CVs gave rise to shifts in the oxide region, suggesting that interactions between Pt, Ru, and Fe can be explained in the context of the bifunctional mechanism (associated with the alloying of Ru) and the ligand effect (ascribed to the presence of Fe in the alloy core). Specifically, the Pt_7Ru_2Fe and Pt_7Ru_3 NW catalysts possessed the lowest onset of formation of Ru-OH species even with a mere 10% loss of Ru and a corresponding 10% increase in Fe content, suggestive of a ligand induced effect, likely as a result of the presence of Fe lowering the *d*-band center of Pt and, thereby altering the electronic properties of the overall alloy. However, with either a 15%, 20%, or even 25% addition of Fe and the concomitant loss of Ru, the onset potential shifted to higher potentials, as was seen by the catalysts containing 20%

and 25% Fe as well, implying that the addition of 10% Fe may actually represent the optimal PtRuFe composition for enhanced activity, since it evinced the lowest onset for MOR activity.

Such a finding would also suggest that the CO tolerance of the catalyst is not necessarily correlated with its corresponding MOR activity, since we determined that the Pt_7Ru_3 NW catalyst possessed a better CO tolerance as compared with the Pt_7Ru_2Fe NW catalyst but maintained a lower MOR activity. However, we noted that the $Pt_7Ru_{1.5}Fe_{1.5}$ NW catalyst represents the most optimized catalyst amongst the ones tested for formic acid oxidation reaction, since the observed electrochemical enhancement may be due to the synergistic interactions between Fe and Ru, since no significant changes in the CVs, such as shifts to lower potentials in the oxide region, were observed. The stability and durability of our optimized Pt_7Ru_2Fe NW catalyst as compared with a commercial PtRu NP standard were subsequently tested by chronoamperometry. We noted that our NW system evinced a higher stability, further demonstrating its practicality and real potential as a stable, active, and viable MOR catalyst.

Overall, our multifunctional catalysts not only demonstrated a decreased affinity towards CO as compared with our as-synthesized Pt catalyst control and commercial PtRu standards but also exhibited both higher MOR and FAOR activity as compared with as-prepared binary Pt_7Ru_3 and Pt_7Fe_3 NWs, monometallic Pt NWs, and commercial catalyst samples. We will continue to investigate the effect of purposely tailoring the chemical compositions of ternary metal catalysts by utilizing additional first row transition metals to enhance performance. Nevertheless, our work on this new class of reasonably sustainably produced ternary nanowire catalysts represents a promising avenue for designing new architectural motifs with relevance for fuel cell applications.

3.4. References

1. Choi, W. C.; Jeon, M. K.; Kim, Y. J.; Woo, S. I.; Hong, W. H., *Catalysis Today* **2004,** *93-95* 517-522.
2. Wasmus, S.; Küver, A., *Journal of Electroanalytical Chemistry* **1999,** *461* 14-31.
3. Kang, D. K.; Noh, C. S.; Kim, N. H.; Cho, S.-H.; Sohn, J. M.; Kim, T. J.; Park, Y.-K., *Journal of Industrial and Engineering Chemistry* **2010,** *16* 385-389.
4. Qiu, H.; Zou, F., *ACS Applied Materials & Interfaces* **2012,** *4* 1404-1410.
5. Joo, S. H.; Choi, S. J.; Oh, I.; Kwak, J.; Liu, Z.; Terasaki, O.; Ryoo, R., *Nature* **2001,** *412* 169-172.
6. Huang, T.; Liu, J.; Li, R.; Cai, W.; Yu, A., *Electrochemistry Communications* **2009,** *11* 643-646.
7. Long, N. V.; Yang, Y.; Thi, C. M.; Minh, N. V.; Cao, Y.; Nogami, M., *Nano Energy* **2013,** *2* 636-676.
8. Sieben, J. M.; Duarte, M. M. E., *International Journal of Hydrogen Energy* **2012,** *37* 9941-9947.
9. Gómez de la Fuente, J. L.; Martínez-Huerta, M. V.; Rojas, S.; Hernández-Fernández, P.; Terreros, P.; Fierro, J. L. G.; Peña, M. A., *Applied Catalysis B: Environmental* **2009,** *88* 505-514.
10. Ribeiro, V. A.; Correa, O. V.; Neto, A. O.; Linardi, M.; Spinacé, E. V., *Applied Catalysis A: General* **2010,** *372* 162-166.
11. Godoi, D. R. M.; Perez, J.; Villullas, H. M., *The Journal of Physical Chemistry C* **2009,** *113* 8518-8525.
12. Wang, H.; Alden, L. R.; DiSalvo, F. J.; Abruña, H. c. D., *Langmuir* **2009,** *25* 7725-7735.
13. Strasser, P.; Fan, Q.; Devenney, M.; Weinberg, W. H.; Liu, P.; Norskov, J. K., *The Journal of Physical Chemistry B* **2003,** *107* 11013-11021.
14. Velázquez-Palenzuela, A.; Brillas, E.; Arias, C.; Centellas, F.; Garrido, J. A.; Rodríguez, R. M.; Cabot, P.-L., *Journal of Power Sources* **2012,** *208* 306-315.
15. Liu, F.; Lee, J. Y.; Zhou, W. J., *Small* **2006,** *2* 121-128.
16. Wang, Z. B.; Yin, G. P.; Shi, P. F.; Sun, Y. C., *Electrochemical and Solid-State Letters* **2006,** *9* A13-A15.
17. Wang, D.-Y.; Chou, H.-L.; Lin, Y.-C.; Lai, F.-J.; Chen, C.-H.; Lee, J.-F.; Hwang, B.-J.; Chen, C.-C., *Journal of the American Chemical Society* **2012,** *134* 10011-10020.
18. Huang, T.; Liu, J.; Li, R.; Cai, W.; Yu, A., *Electrochemistry Communications* **2009,** *11* 643-646.
19. Strasser, P.; Fan, Q.; Devenney, M.; Weinberg, W. H.; Liu, P.; Nørskov, J. K., *The Journal of Physical Chemistry B* **2003,** *107* 11013-11021.
20. Jeon, M. K.; Won, J. Y.; Lee, K. R.; Woo, S. I., *Electrochemistry Communications* **2007,** *9* 2163-2166.
21. Kawaguchi, T.; Rachi, Y.; Sugimoto, W.; Murakami, Y.; Takasu, Y., *Journal of Applied Electrochemistry* **2006,** *36* 1117-1125.
22. Kageyama, S.; Murakami, A.; Ichikawa, S.; Seino, S.; Nakagawa, T.; Daimon, H.; Ohkubo, Y.; Kugai, J.; Yamamoto, T. A., *Journal of Materials Research* **2012,** *27* 1037-1045.
23. Guo, S.; Zhang, S.; Sun, X.; Sun, S., *Journal of the American Chemical Society* **2011,** *133* 15354-15357.
24. Koenigsmann, C.; Wong, S., *Energy and Environmental Science* **2011,** *4* 1045-1528.
25. Yuan, Q.; Huang, D.-B.; Wang, H.-H.; Zhou, Z.-Y., *Langmuir* **2014,** *30* 5711-5715.

26. Cademartiri, L.; Ozin, G. A., *Advanced Materials* **2009,** *21* 1013-1020.
27. Jeon, M. K.; Lee, K. R.; Daimon, H.; Nakahara, A.; Woo, S. I., *Catalysis Today* **2008,** 123-126.
28. Koenigsmann, C.; Scofield, M.; Liu, H.; Wong, S., *The Journal of Physical Chemistry Letters* **2012,** *3*.
29. Song, Y.; Garcia, R. M.; Dorin, R. M.; Wang, H.; Qiu, Y.; Coker, E. N.; Steen, W. A.; Miller, J. E.; Shelnutt, J. A., *Nano Letters* **2007,** *7* 3650-3655.
30. Yang, S.; Hong, F.; Wang, L.; Guo, S.; Song, X.; Ding, B.; Yang, Z., *The Journal of Physical Chemistry C* **2009,** *114* 203-207.
31. Koenigsmann, C.; Santulli, A. C.; Gong, K.; Vukmirovic, M. B.; Zhou, W.-p.; Sutter, E.; Wong, S. S.; Adzic, R. R., *Journal of the American Chemical Society* **2011,** *133* 9783-9795.
32. Koenigsmann, C.; Semple, D. B.; Sutter, E.; Tobierre, S. E.; Wong, S. S., *ACS Applied Materials & Interfaces* **2013,** *5* 5518-5530.
33. Antolini, E., *Materials Chemistry and Physics* **2003,** *78* 563-573.
34. Stamenkovic, V. R.; Mun, B. S.; Mayrhofer, K. J. J.; Ross, P. N.; Markovic, N. M., *Journal of the American Chemical Society* **2006,** *128* 8813-8819.
35. Toda, T.; Igarashi, H.; Uchida, H.; Watanabe, M., *Journal of The Electrochemical Society* **1999,** *146* 3750-3756.
36. Xu, C.; Li, Q.; Liu, Y.; Wang, J.; Geng, H., *Langmuir* **2012,** *28* 1886-1892.
37. Strasser, P.; Koh, S.; Anniyev, T.; Greeley, J.; More, K.; Yu, C.; Liu, Z.; Kaya, S.; Nordlund, D.; Ogasawara, H.; Toney, M. F.; Nilsson, A., *Nature Chemistry* **2010,** 454-460.
38. Toda, T.; Igarashi, H.; Watanabe, M., *Journal of The Electrochemical Society* **1998,** *145* 4185-4188.
39. Stolbov, S.; Ortigoza, M. A.; Adzic, R.; Rahman, T. S., *The Journal of Chemical Physics* **2009,** *130* 124714/1-124714/5.
40. Sasaki, K.; Wang, J. X.; Balasubramanian, M.; McBreen, J.; Uribe, F.; Adzic, R. R., *Electrochimica Acta* **2004,** *49* 3873-3877.
41. Zhang, X.; Zhang, F.; Guan, R.-F.; Chan, K.-Y., *Materials Research Bulletin* **2007,** *42* 327-333.
42. Ehteshami, S. M. M.; Jia, Q.; Halder, A.; Chan, S. H.; Mukerjee, S., *Electrochimica Acta* **2013,** *107* 155-163.
43. Zhong, W. H.; Liu, Y. X.; Zhang, D. J., *Journal of Physical Chemistry C* **2012,** *116* 2994-3000.
44. Yuan, D.; Gong, X.; Wu, R., *Journal of Chemical Physics* **2008,** *128* 064706.
45. Rossmeisl, J.; Ferrin, P.; Tritsaris, G. A.; Nilekar, A. U.; Koh, S.; Bae, S. E.; Brankovic, S. R.; Strasser, P.; Mavrikakis, M., *Energy and Environmental Science* **2012,** *5* 8335-8342.
46. Wang, H.; Loffler, T.; Baltruschat, H., *Journal of Applied Electrochemistry* **2001,** *31* 759-765.
47. Zhou, W.-P.; Li, M.; Koenigsmann, C.; Ma, C.; Wong, S. S.; Adzic, R. R., *Electrochimica Acta* **2011,** *56* 9824-9830.
48. Wang, S.; Jiang, S. P.; Wang, X.; Guo, J., *Electrochimica Acta* **2011,** *56* 1563-1569.
49. Si, F.; Ma, L.; Liu, C.; Zhang, X.; Xing, W., *RSC Advances* **2012,** 401-403.
50. Xia, B. Y.; Wu, H. B.; Yan, Y.; Lou, X. W. D.; Wang, X., *Journal of the American Chemical Society* **2013,** *135* 9480-9485.
51. Lai, S. C. S.; Lebedeva, N. P.; Housmans, T. H. M.; Koper, M. T. M., *Topics in Catalysis* **2007,** *46* 320-333.

52. Xu, J.; Yuan, D.; Yang, F.; Mei, D.; Zhang, Z.; Chen, Y.-X., *Physical Chemistry Chemical Physics* **2013,** *15* 4367-4376.

Chapter 4 - Role of Chemical Composition in the Enhanced Catalytic Activity of Pt-Based Alloyed Ultrathin Nanowires for the Hydrogen Oxidation Reaction under Alkaline Conditions

4.1. Introduction

With an increased interest in the development of hydrogen fuel cells as a plausible alternative to internal combustion engines, recent work has focused on creating viable AFCs, which employ an alkaline medium as opposed to acid as the primary electrolyte. In effect, AFCs possess a number of important benefits associated with the presence of a more favorable and desirable alkaline electrolyte medium. Specifically, these include (i) the ability to use non-precious metal catalysts due to their increased stability, (ii) a diminished degree of degradation and corrosion of Pt-based catalysts, and (iii) a general reduction in the amount of deterioration inherent to the overall fuel cell configuration.[1-3]

Additionally, the reaction that occurs at the cathode, namely the oxygen reduction reaction (ORR), tends to possess faster kinetics in alkaline media.[1, 4] However, there remains a significant need for improvement at the anode side of the fuel cell where the oxidation of hydrogen occurs, because unfortunately, the kinetics for this reaction process are inherently slower in alkaline media versus in acid electrolytes. In particular, despite the fact that platinum is known to be the most active metal for initiating HOR in alkaline media, it unfortunately still exhibits 2 orders of magnitude slower kinetics than what is measured in corresponding acid electrolytes.[2, 3] Moreover, existing catalysts are particularly susceptible to CO poisoning. Therefore, to mitigate for all of these issues, there is a tangible need to create unconventional geometries possessing superior HOR kinetics in alkaline media whose performance inherently surpasses that of elemental, monometallic Pt.

One strategy is by generating alternative architectures, i.e. structures that incorporate monometallic nanomaterials as constituent components of a larger whole. Such an approach encompasses efforts to generate new and interesting classes of hierarchical architectures such as alloy and core-shell motifs, wherein the local electronic environment of Pt for example can be systematically altered through corresponding variations in structure and composition.

However, the rationale for the expected improvement in both activity and kinetics with these novel materials in alkaline media is still a matter of controversy. In effect, contradictory theories have been proposed to explain enhancements observed with alloyed structures in particular. Some have suggested that the enhanced activity of these catalysts originates from the increased oxophilicity of the alloyed metal. In particular, Markovic and co-workers[5] have theoretically proposed that OH_{ad} is a key reactant species in HOR, and that the presence of a more oxophilic metal should improve the reaction kinetics and activity of Pt. A different group[6] experimentally tested this hypothesis by investigating the electrochemical activity of commercial PtRu and of Pt NP/C control samples. Ultimately, this group discovered that PtRu NP/C achieved higher activities than Pt NP/C but ascribed the enhancement to an optimized HBE, which was attributed to an electronic effect imparted onto Pt by Ru as opposed to an oxophilic effect. Their rationale rested on the observation that PtRu NP/C did *not* possess a lower onset potential for CO desorption as compared with Pt NP/C, which would have provided for incontrovertible evidence for the presence of an oxophilic effect.

In this light, herein, we aim to more systematically address this key mechanistic question by synthesizing Pt-based metallic alloys wherein we take the advantage of the combination of both a ‘ligand effect’ and a ‘lattice strain effect’. By the ‘ligand effect’,[7-9] we refer to a phenomenon in which the electronic properties of the active sites of one transition metal are modified by the introduction of another metal. Specifically, it should manifest itself in the corresponding adjustment of the M-H_{ad} interaction, which we believe to be the rate-determining step for HOR.[6] That is, our PtM NWs (wherein M = a plentiful transition metal) should evince enhanced HOR kinetics, as H should be bound *less* strongly onto alloyed surfaces. Furthermore, by the term 'lattice strain effect', we refer to changes in the surface Pt-Pt bond distance as a result of the incorporation of other transition metals, thereby leading to changes in the *d*-band center of Pt.[10-13] Throughout this paper, we use the term 'electronic effects' to embody, encompass, and incorporate the synergistic association of both ligand and lattice strain effects.

Indeed, Pt-based alloyed systems have previously been investigated by computational analysis, and it has been postulated that the structural and electronic interactions between the two alloyed metals should promote more facile HOR kinetics due to changes in the 'effective' hydrogen binding energy.[14, 15] Previous theoretical work performed by Nørskov and co-workers[16] calculated the HBEs for various individual metals, and found that a number of them possessed HBEs that were very favorable for hydrogen oxidation. Specifically, this work[15] also suggested that the incorporation of certain metals such as Ni, Co, Fe, Cu, and Ru into Pt-containing alloys represents viable options for achieving hydrogen binding with an "optimal" HBE, i.e. a value closer to 0 as compared with Pt bulk itself. Additional work performed by Wang and co-workers[17] implied that by alloying Pt with a metal possessing a comparatively stronger hydrogen binding energy, one could conceivably shift the overall HBE to more favorable values, i.e. to weaker HBE values as compared with pure Pt itself.

For optimal HOR performance, we ultimately seek a weakening in the hydrogen binding energy as compared with Pt, an assertion supported by others.[17] In effect, there is a strengthening of the HBE as the *d*-band center moves closer to the Fermi level of a metal such as Pt.[10, 18] Our goal is the opposite, and therefore, our objective has been to create alloyed nanomaterials that demonstrate a weakening in HBE by moving the *d*-band center away from the Pt Fermi level.

Hence, based upon previous HBE calculations associated with various transition metals,[16, 19] we can potentially tailor novel electrocatalysts with improved HOR kinetics by deliberatively and systematically altering the alloy composition and therefore, control the corresponding variations in HBE. Hence, our goal has been to correlate composition with activity. Additionally, our objective of replacing expensive noble metals with cheaper, more abundant metals is essential for designing electrocatalysts for mass production.

Apart from rationally varying the chemical compositions of our Pt-based alloy structures, we have also tailored the morphology of our catalysts. In effect, crystalline 1D catalysts have previously been shown to possess high aspect ratios, fewer potentially deleterious defect sites, and short segments of crystalline planes, all of which contribute to the enhanced activity of 1D systems as compared with their 0D counterparts.[20-22] Furthermore, anisotropic nanostructures such as Pt NWs maintain a favorable downshift in the Pt *d*-band, which contributes to a weaker d-π^* interaction with the adsorbed CO, thereby improving Pt's ability to oxidize adsorbed CO at potentials closer to the thermodynamic potential for MOR.[23] Moreover, the surfaces of 1D morphologies can be tuned so as to preferentially display different crystal facets.[8, 21] In addition, the rates of dissolution and ripening processes have been demonstrated to be significantly slower in the case of 1D nanostructures, by comparison with commercial Pt NP/C. All of these findings suggest that 1D architectures represent promising motifs for HOR catalysts.

Our last novel variation for HOR has been to reduce the average diameters of our 1D nanowires tested to the ultrathin size regime (< 5 nm). In doing so, we should be able not only to decrease the amount of defect sites present in the wire, which has been previously shown to favorably alter the surface energy of Pt but also to minimize any lattice boundary defects. Indeed, the presence of defects contributes to the degradation of Pt, since lower coordination Pt surface sites are more prone to irreversible oxidation.[21]

Overall, in this study, we not only intend to verify the theoretical results proposed by Mavrikakis and co-workers[15] by experimentally synthesizing a series of ultrathin 1D Pt-based binary alloys with controllable composition and subsequently testing their HOR activities within an alkaline electrolyte but also propose to investigate the combined roles of the ‘ligand effect’ and the ‘lattice strain effect’ in governing HOR activity. Our work represents the first systematic *correlation of HOR activity with key structural parameters* that notably influence surface chemistry and the presence of active sites for a variety of binary alloy nanowire systems, operating in alkaline media. Our overall results highlight that our intrinsic activities can be deliberatively improved upon and optimized through a judicious combination of (i) morphology, (ii) chemical composition, and (iii) size. Specifically, we have observed that excellent HOR activity values, whose trend approximates that of previous theoretical predictions,[15] can be specifically achieved with 1D anisotropic motifs, characterized by both < 5 nm diameters and well-chosen Pt-based alloyed compositions.

To create our test materials, we have employed an ambient and facile wet synthesis method,[24, 25] which we have previously applied to the generation of ultrathin ternary PtRuFe nanowire systems,[26] in order to produce ultrathin Pt-based binary alloy NW systems. This protocol involves the reduction of metal precursors with sodium borohydride in the presence of a so-called ‘soft template’, created by the CTAB surfactant within a two-phase water-chloroform system. One of the advantages of this technique is that the wire dimensionality is fundamentally controlled by the size and shape of the ‘soft template’ pores, and hence, it is rather straightforward to create porous, high surface area networks consisting of interconnected, ‘wormlike’ metallic nanowires, possessing average diameters of as little as 1.9 nm. In terms of desirable chemical compositions, it has been reported that the presence of 30% Ru dopant, as in the Pt_7Ru_3 system, yielded exceptionally high activities.[27-29] As such, we used this particular binary alloy composition as our explicit ‘starting point’ from which to generate possible permutations for other Pt-based alloys, so as to create a family of effective electrochemically active catalysts.

4.2. Results and Discussion

4.2.1. Ambient Synthesis and Characterization of Pt and PtM (M=Ru, Fe, Co, Au, Cu) NWs

We have sought to use an ambient solution-based synthesis method to synthesize families of binary ultrathin nanowires with consistent composition and structure. In this study, our objective has been to correlate the precise composition of various Pt-based binary nanowire systems with the resulting hydrogen oxidation reaction performance, occurring at the anode. The targeted structural objective of achieving a Pt-based alloy NW structure should not only minimize the catalyst cost but also provide a chemical means for modifying and tuning the overall HBE of the NW, likely the most important determinant of HOR activity,[16] to a value close to the optimal value of zero. Recent work[17] by Wang and co-workers corroborates the intent of our own study, as they demonstrated that creating Pt-based structures, incorporating a transition metal that possesses a stronger binding affinity with hydrogen, diminishes the intrinsic binding affinity of Pt for hydrogen, thereby decreasing the resulting HBE to a more favorable value as compared with that of monometallic Pt alone.

The chemical composition and crystallinity of our nanowires have been examined by XRD, as shown in Figure 4.1. All catalysts evince a foundational Pt *fcc* lattice with no apparent peaks ascribable to any possible impurities within the nanowires observed, which is indicative of the reasonably high purity of our samples. Specifically, the four peaks detected can be assigned to the (111), (200), (220), and (311) planes of an underlying Pt *fcc* framework structure (JCPDS database #04-0802), respectively.

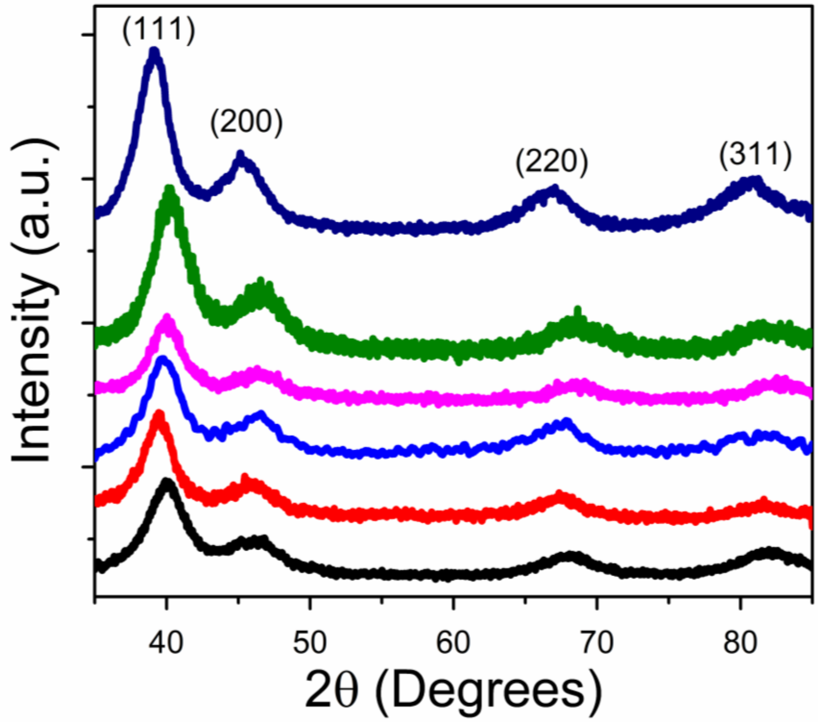

Figure 4.1. XRD patterns for Pt NWs (black), Pt_7Ru_3 NWs (red), Pt_7Co_3 NWs (blue), Pt_7Fe_3 NWs (magenta), Pt_7Cu_3 NWs (green), and Pt_7Au_3 NWs (navy), respectively. All peaks have been labeled and can be ascribed to a Pt *fcc* structure (JCPDS database #04-0802). Reprinted with permission from *ACS Catal.*, **2016**, *6*, pp 3895–3908. Copyright 2016 American Chemical Society.

The morphology of each catalyst has also been investigated in Figures 4.2 and 4.3. The TEM images in Figures 4.2 and 4.3 (A, D, G) demonstrate the overall anisotropic one-dimensional morphology expected for each catalyst. Figures 4.2 and 4.3 (B, E, H) highlight higher magnification TEM (HRTEM) images from which we were able to measure various *d*-spacings and to subsequently correlate these values with the expected overall lattice structure of the as-synthesized catalysts. In each case, the measured *d*-spacings were found to be within experimental error of the expected *d*-spacings for the active Pt (111) plane (i.e. 2.26 Å). Again, it should be mentioned that the *d*-spacings for all of the Pt-based binary alloys with the exception of the PtAu sample (Figure 4.3H) evinced a minor decrease in the *d*-spacing value, likely ascribable to the smaller lattice size of each of the incorporated alloyed metals. By contrast, we note that the Au lattice (i.e. 0.4079 nm) is slightly larger than that of Pt itself (i.e. 0.392 nm), and therefore its presence leads to an expansion of the overall Pt lattice. These small variations in the *d*-spacing values nevertheless validate the presence of lattice strain effects associated with each of the catalysts, which can subsequently impact upon the observed Pt surface electronic properties.[13] This effect on HOR activity will be discussed further in Section 2.3.

Overall, the HRTEM images demonstrate that the nanowires are composed of short crystalline segments associated with single-crystalline planes.[22] SAED patterns for each of the catalysts were taken and are presented in Figures 4.2 and 4.3 (C, F, I); these data can be used to further evaluate the lattice structure of the various alloys. In each case, rings associated with the Pt (111), (200), (220), and (311) lattice planes can be observed. It was not evident that we could conclusively assign rings to either individual metallic Ru (Fig. 4.2F), Fe (Fig. 4.2I), Co (Fig. 4.3C), Cu (Fig. 4.3F), or Au (Fig. 4.3I) lattice planes. Hence, together with the XRD data, our collective results are consistent with the full incorporation of the second transition metal with Pt within a relatively uniform and homogeneous alloyed NW structure. Additionally, the presence of ring patterns as opposed to well-defined arrays of sharp discrete dots further confirms the overall polycrystalline nature of the catalysts.

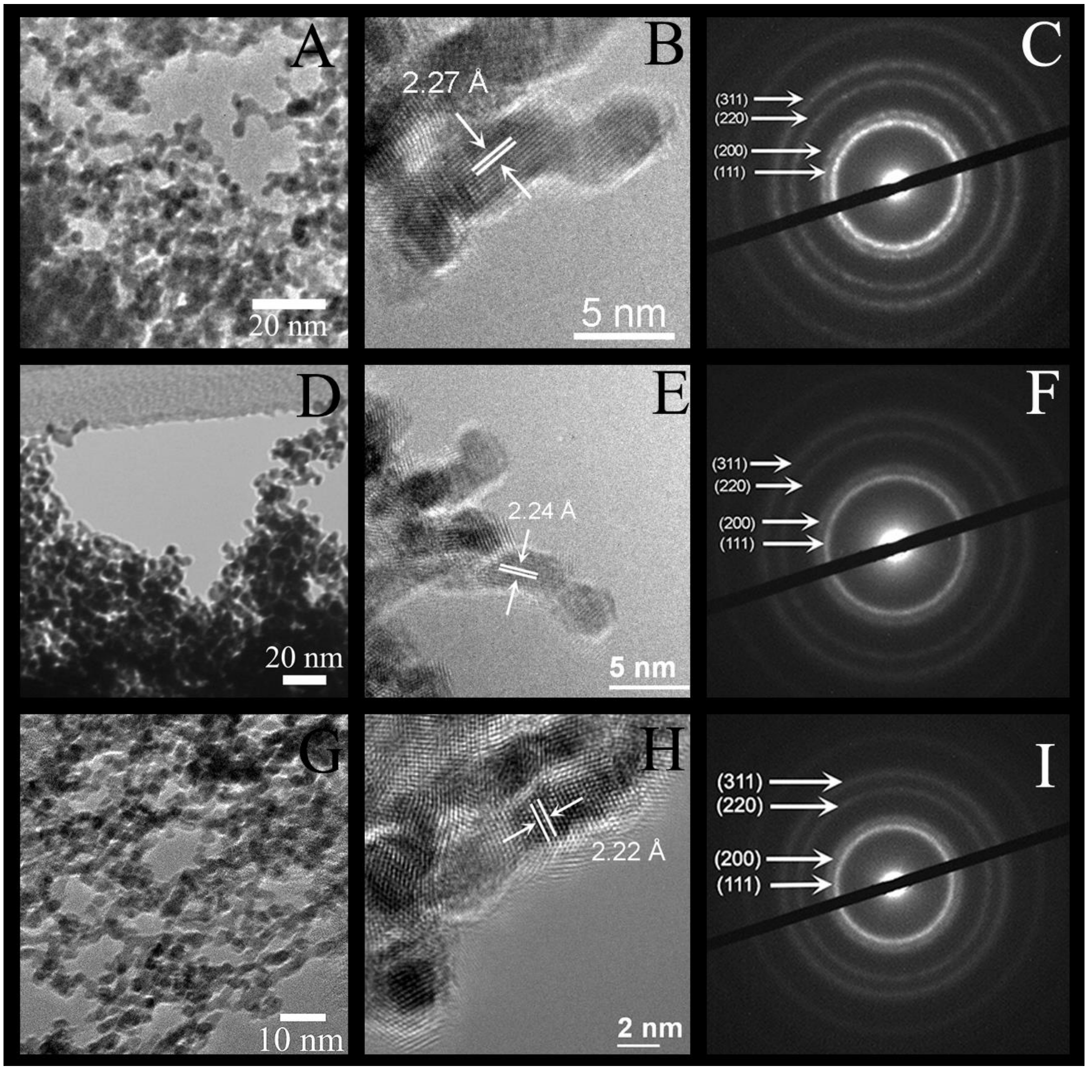

Figure 4.2. (A, D, and G) Representative high-resolution TEM images, (B, E, and H) higher magnification HRTEM images with both measured *d*-spacings, and (C, F, and I) associated single area electron diffraction patterns for (A-C) Pt NWs, (D-F) Pt_7Ru_3 NWs, and (G-I) Pt_7Fe_3 NWs, respectively. Reprinted with permission from *ACS Catal.*, **2016**, *6*, pp 3895–3908. Copyright 2016 American Chemical Society.

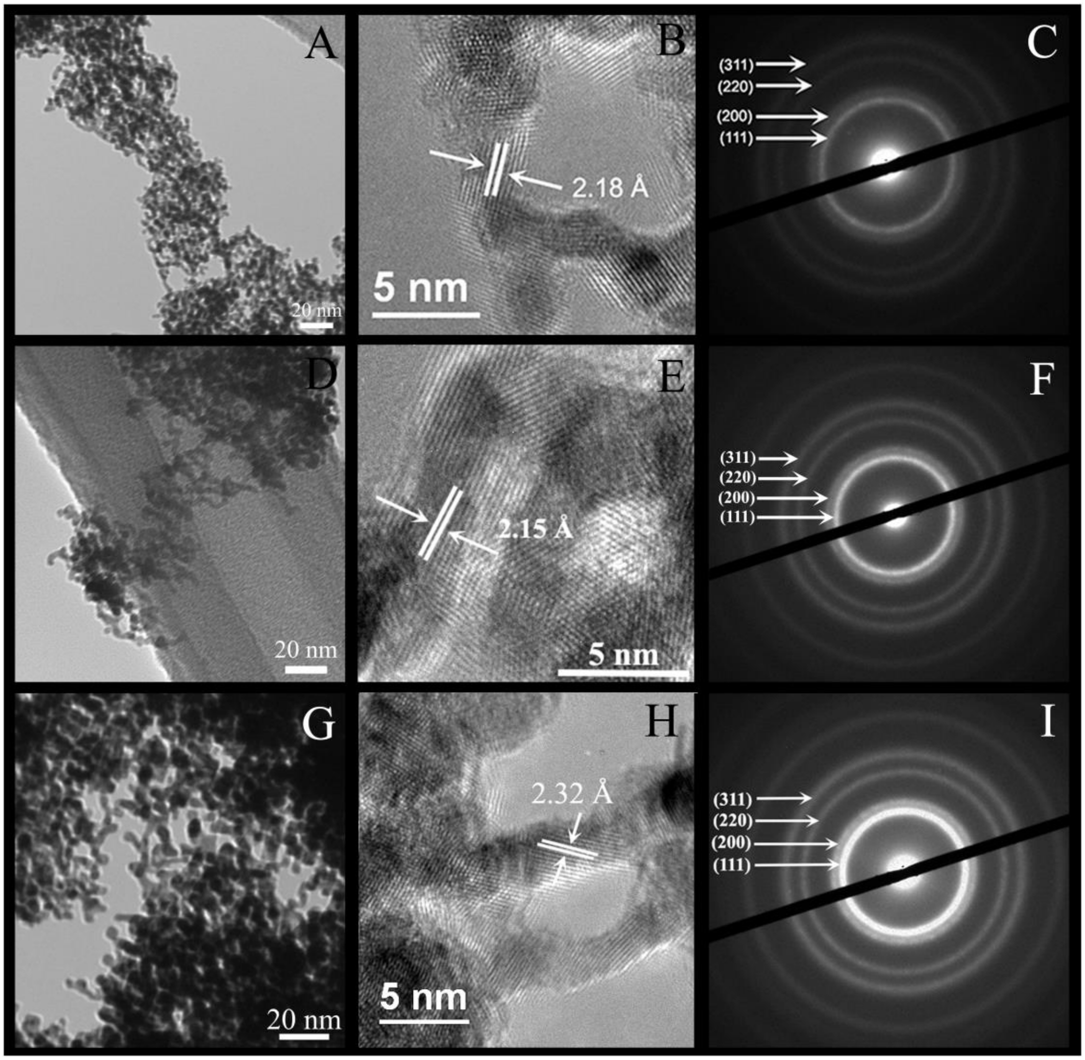

Figure 4.3. (A, D, and G) Representative high-resolution TEM images, (B, E, and H) higher-magnification HRTEM images with both measured *d*-spacings, and (C, F, and I) associated single area electron diffraction patterns for (A-C) Pt_7Co_3 NWs, (D-F) Pt_7Cu_3 NWs, and (G-I) Pt_7Au_3 NWs, respectively. Reprinted with permission from *ACS Catal.*, **2016**, *6*, pp 3895–3908. Copyright 2016 American Chemical Society.

Table 4.1 consists of data on the various atomic percent compositions associated with the binary alloys. The expected 70: 30 molar ratio was originally chosen due to the increased activity observed for the Pt_7Ru_3 alloy, as discussed in the Introduction. For this reason, a 70: 30 molar ratio has been extended to cover the composition of these binary alloys for HOR testing. The actual atomic percent compositions for each of these catalysts are within experimental error of the expected 70: 30 expected ratio, as determined by EDAX analysis. Additionally, Table 4.1 reports on the average diameters of each of the binary alloy catalysts tested as well as of the measured *d*-spacing values, derived from the TEM and HRTEM images in Figures 4.2 and 4.3. All of the measured *d*-spacing values are in accordance with corresponding data determined for other similar Pt-based alloy nanostructures described in the literature.[30-34]

Material	**Expected Atomic % Composition**	**Actual Atomic % Composition**	**Average Diameter (nm)**	**Average Pt d-spacing (Å)**
Pt NWs	100	100	2.1 ± 0.1	2.27 ± 0.05
PtRu NWs	70-30	74 - 26 (± 0.5)	2.09 ± 0.2	2.24 ± 0.03
PtCo NWs	70-30	73 - 27 (± 2.1)	2.2 ± 0.2	2.18 ± 0.05
PtFe NWs	70-30	67 - 33 (± 2.3)	1.91 ± 0.3	2.22 ± 0.06
PtCu NWs	70-30	72 - 28 (± 0.7)	2.19 ± 0.2	2.15 ± 0.08
PtAu NWs	70-30	69 - 31 (± 2.2)	2.19 ± 0.3	2.32 ± 0.02

Table 4.1. Table characterizing the binary alloyed nanowires tested. Columns relate to the nanowire material tested, the expected and actual % chemical compositions, the average measured diameters (nm), as well as average measured *d*-spacings (Å). The actual atomic % compositions presented were determined from EDAX analysis. Reprinted with permission from *ACS Catal.*, **2016**, *6*, pp 3895–3908. Copyright 2016 American Chemical Society.

XPS spectra for each binary NW catalysts analyzed are presented in Figure 4.4 and Figure 4.5, respectively. For each of the samples, regions associated with the Pt $4f_{7/2}$ (i.e. the lower energy peak) and the Pt $4f_{5/2}$ (i.e. the higher energy peak) orbitals have been studied. In Figure 4.4A, the behavior of the *4f* peaks ascribed to Pt, PtRu, PtFe, and PtCo, respectively, has been evaluated. We note that the Pt $4f_{7/2}$ peak corresponding to the Pt NWs, serving as a control, is located at 69.44 eV. As expected, all 3 alloyed catalysts give rise to peaks that have been shifted to higher binding energies as compared with Pt itself, a finding indicative of electron removal from the Pt *d*-band. In particular, the specific locations for each of these Pt $4f_{7/2}$ peaks are situated at 71.49 eV, 70.69 eV, and 70.11 eV for PtRu, PtFe, and PtCo, respectively. Based upon these data, it is reasonable to assert that all of these alloyed catalysts should evince better HOR kinetics as compared with the Pt NW system alone, because of a downward shift in the Pt *d*-band center in these systems, which is consistent with a weaker adsorption of hydrogen at the surface, i.e. a lower HBE.[15]

In Figure 4.4B, the pure Pt NW system is compared with both the PtCu as well as the PtAu NW systems. By analogy with the other metal alloyed NWs, a shift to higher potentials was observed for the PtCu system, as manifested in a peak position of 70.06 eV as compared with 69.44 eV for Pt. Again, this result is consistent with electron depletion from the Pt *d*-band and a corresponding lessening in the HBE as compared with pure Pt. By contrast, the PtAu system gives rise to a peak location (i.e. 69.41 eV) which is slightly decreased as compared with that of Pt itself (i.e. 69.44 eV). Au is known to donate electron density to Pt and thereby cause an upshift in the Pt *d*-band center. Such a scenario would lead to a stronger adsorption of hydrogen as compared with Pt alone, i.e. a higher HBE.[15] As such, the key point of our results is that measurable XPS shifts versus that of pure Pt occur upon alloying Pt with another metal, suggesting the importance and relevance of ligand and strain effects.

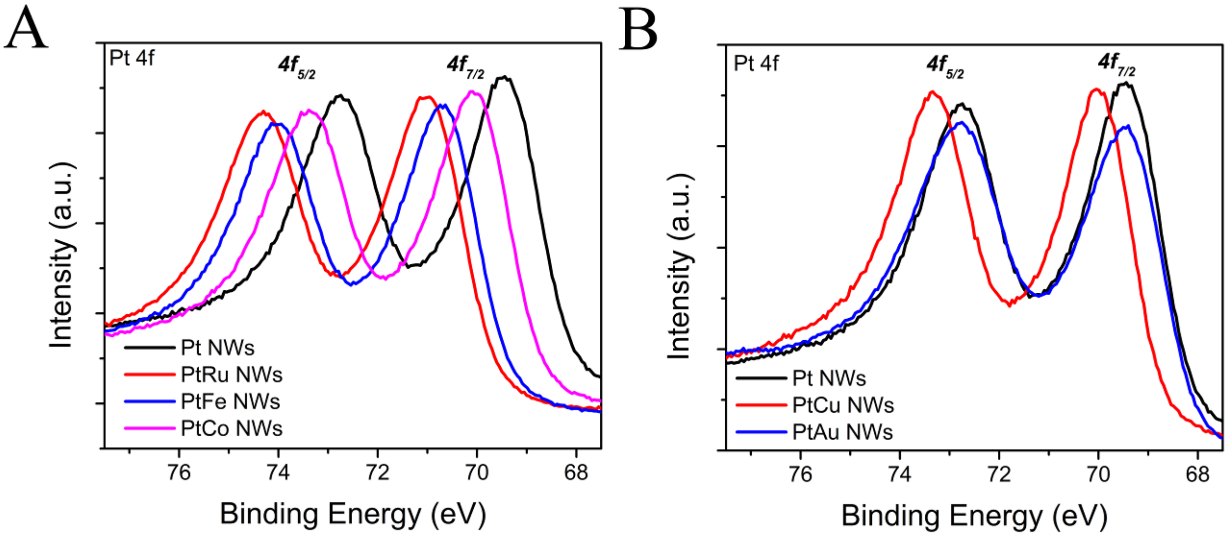

Figure 4.4. XPS spectra associated with the Pt *4f* region for the various binary catalysts tested. (A) Pt NWs (black), Pt_7Ru_3 NWs (red), Pt_7Fe_3 NWs (blue), and Pt_7Co_3 NWs (magenta), as well as (B) Pt NWs (black), Pt_7Cu_3 NWs (red), and Pt_7Au_3 NWs (blue), respectively. Reprinted with permission from *ACS Catal.*, **2016**, *6*, pp 3895–3908. Copyright 2016 American Chemical Society.

The corresponding XPS regions associated with the individual 'M' metal within each alloyed PtM catalyst are shown in Figure 4.5 along with fits provided using the CasaXPS program. We postulate that the Co, Fe, as well as Cu elements should all be affected by a slight surface oxidation upon exposure to air, an inevitable consequence of PtM alloy formation under either ambient or wet-solution conditions.[35-39] Hence, their signature peak positions will be slightly offset from expected values for these particular elements.

Figure 4.5A highlights the raw and fitted data for the Ru *3d* region. We note the presence of a Ru $3d_{3/2}$ peak situated at 285.71 eV and a Ru $3d_{5/2}$ peak located at 279.27 eV, which are consistent with the presence of metallic Ru within the Pt alloy. Figures 4.5B, 4.5C, and 4.5D feature the raw and fitted data for the Fe *2p* region, Co *2p* region, and Cu *2p* region, respectively, for the corresponding metal alloys. We were able to identify Fe $2p_{3/2}$ and $2p_{1/2}$ peaks placed at 709.4 eV and 722.8 eV; Co $2p_{3/2}$ and $2p_{1/2}$ peaks located at 779.67 eV and 795.54 eV; and finally, Cu $2p_{3/2}$ and $2p_{1/2}$ peaks positioned at 929.89 eV and 949.65 eV, respectively. In each case, based upon the fitting results, the peaks can be primarily ascribed to the expected pure metallic species. Moreover, Figure 4.5E corresponds to the Au *4f* region with no oxide present. The Au $4f_{7/2}$ and $4f_{5/2}$ peaks reside at 81.3 eV and 84.96 eV, respectively, denoting data in good agreement with what would be expected upon alloying with Pt.[40-44]

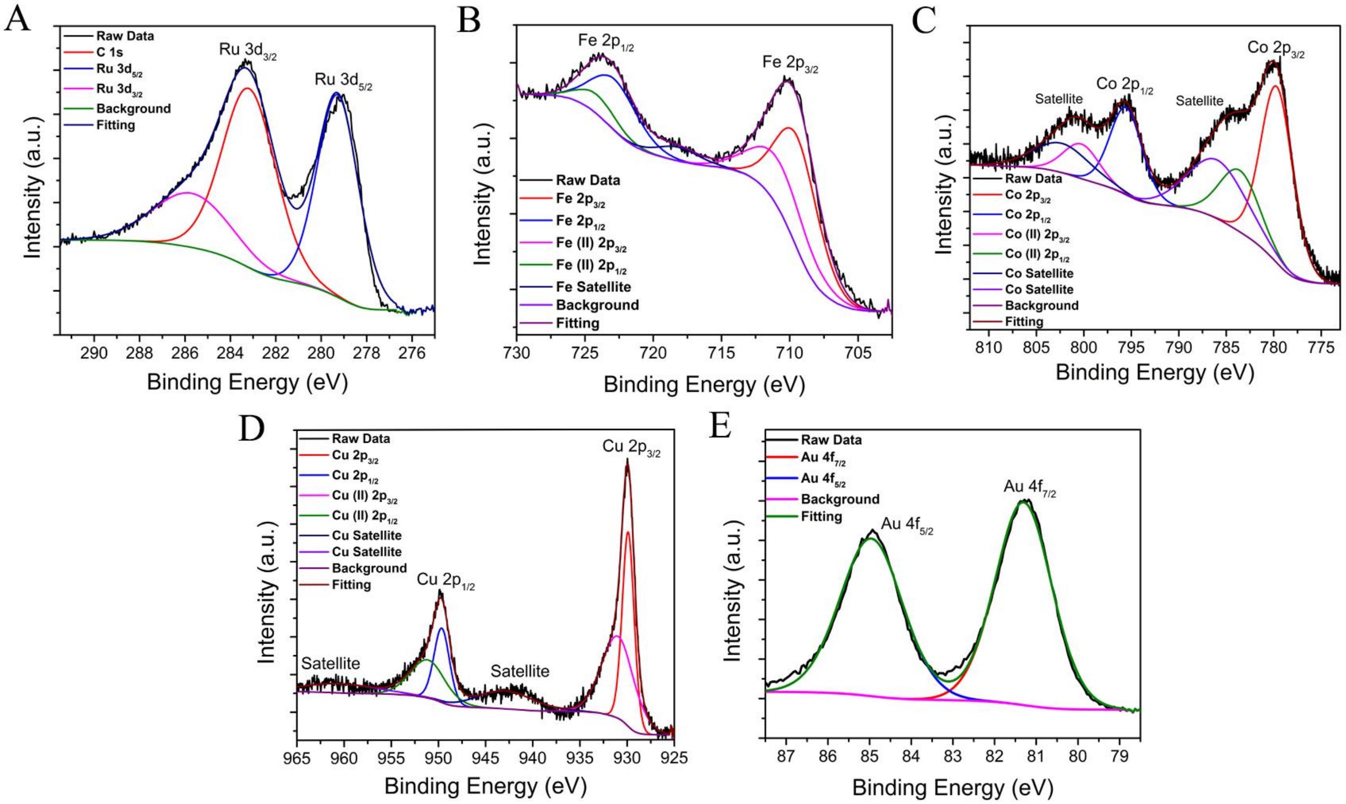

Figure 4.5. XPS spectra associated with the 'M' in various PtM binary catalysts tested. (A) Ru *3d* region for the Pt_7Ru_3 NWs, (B) Fe *2p* region for the Pt_7Fe_3 NWs, (C) Co *2p* region for the Pt_7Co_3 NWs, (D) Cu *2p* region for the Pt_7Cu_3 NWs, and (E) Au *4f* region for the Pt_7Au_3 NWs, respectively. The raw data for each metal have been fitted using the CasaXPS program with fittings for each. Reprinted with permission from *ACS Catal.*, **2016**, *6*, pp 3895–3908. Copyright 2016 American Chemical Society.

In addition to the XPS analysis, HAADF images as well as EELS line scan profiles have been acquired in Figures 4.6 and 4.7 in order to probe the surface homogeneity of our alloyed nanowires. All of the HAADF images (Figures 4.6A, 4.6C, 4.6E, 4.7A, and 4.7C) are consistent with an overall ultrathin nanowire network structure with individual constituent nanowires possessing average diameters of ~ 2 nm. The STEM-EELS line scans in Figure 4.6B, 4.6D, and 4.6F, as well as in Figure 4.7B and 4.7D are strongly indicative of the spatial uniformity and chemical homogeneity of the alloy NW structure, because the data do not support the idea of a well-defined core-shell motif. As a caveat, we observe that in Figure 4.7D, the Pt and Au signals could not be fully differentiated from each other, since the Au edge substantially overlaps with the Pt edge, as can be seen in Figure 4.8. Nevertheless, it is reasonable to assert that even with some degree of surface Au segregation, the line scan data remain consistent with an overall alloyed NW formation.

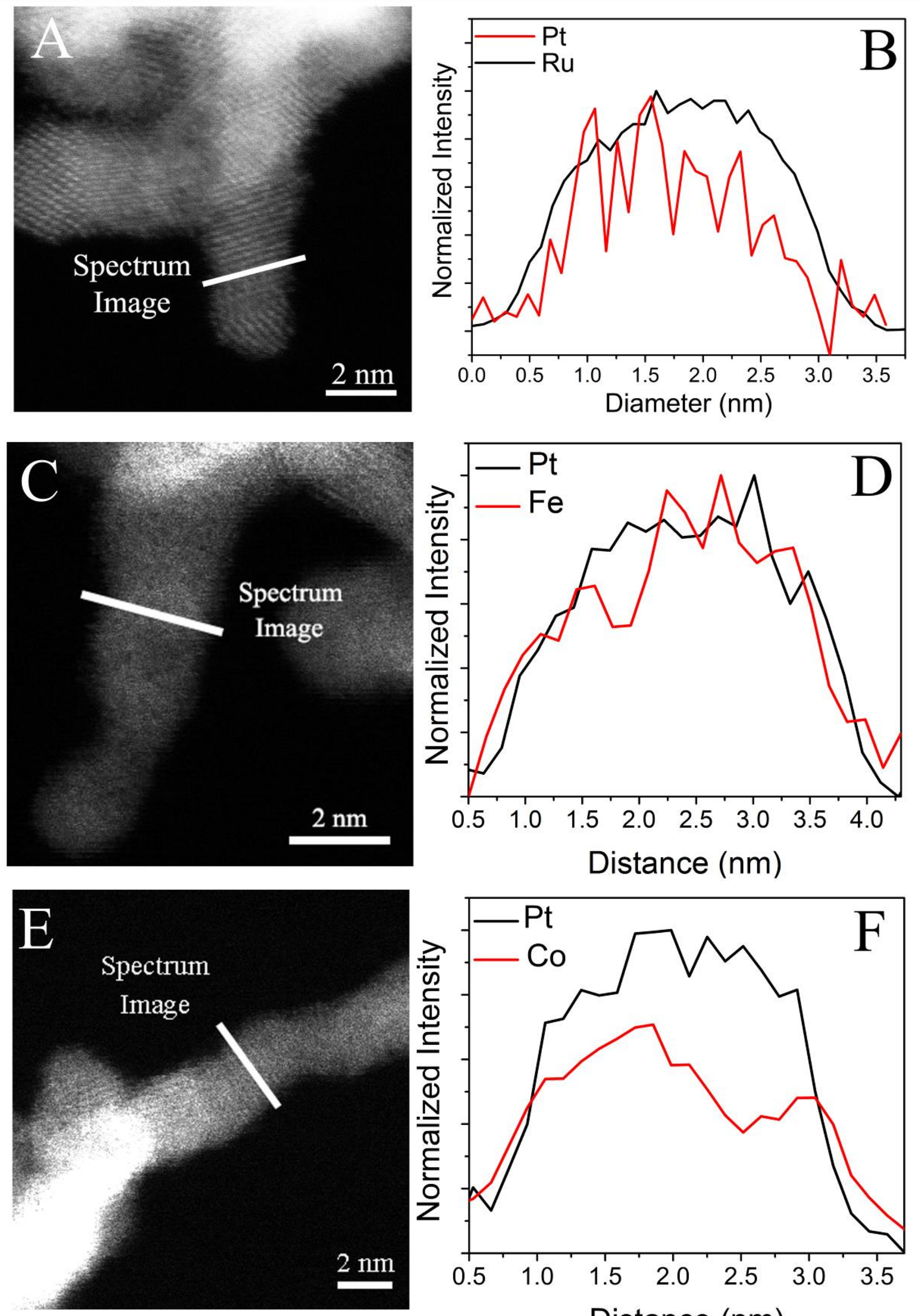

Figure 4.6. (A, C, and E) HAADF images and the corresponding (B, D, and F) EELS line-scan profiles, highlighting the elemental spatial distribution of each of the nanowire catalysts. (A-B) Pt_7Ru_3 NWs, (C-D) Pt_7Fe_3 NWs, and (E-F) Pt_7Co_3 NWs, respectively. Reprinted with permission from *ACS Catal.*, **2016**, *6*, pp 3895–3908. Copyright 2016 American Chemical Society.

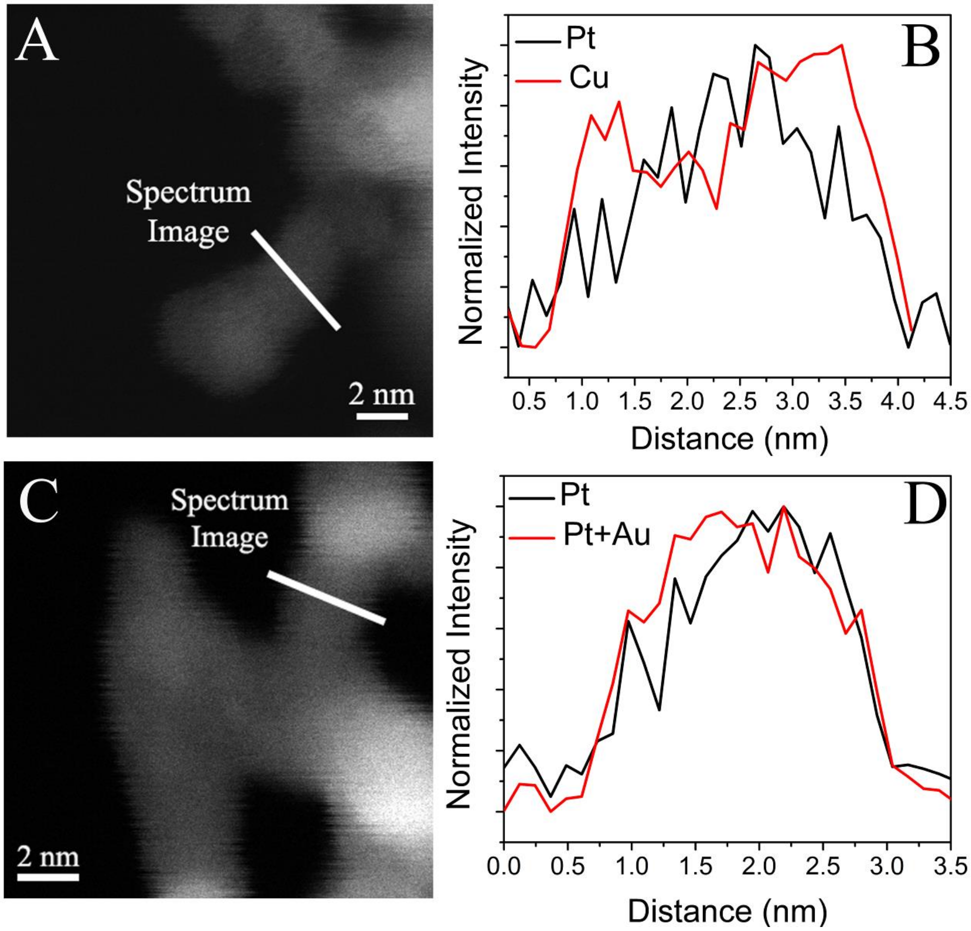

Figure 4.7. (A and C) HAADF images and the corresponding (B and D) EELS line-scan profiles, illustrating the elemental spatial distribution of each of the nanowire catalysts. (A-B) Pt_7Cu_3 NWs and (C-D) Pt_7Au_3 NWs, respectively. Reprinted with permission from *ACS Catal.*, **2016**, *6*, pp 3895–3908. Copyright 2016 American Chemical Society.

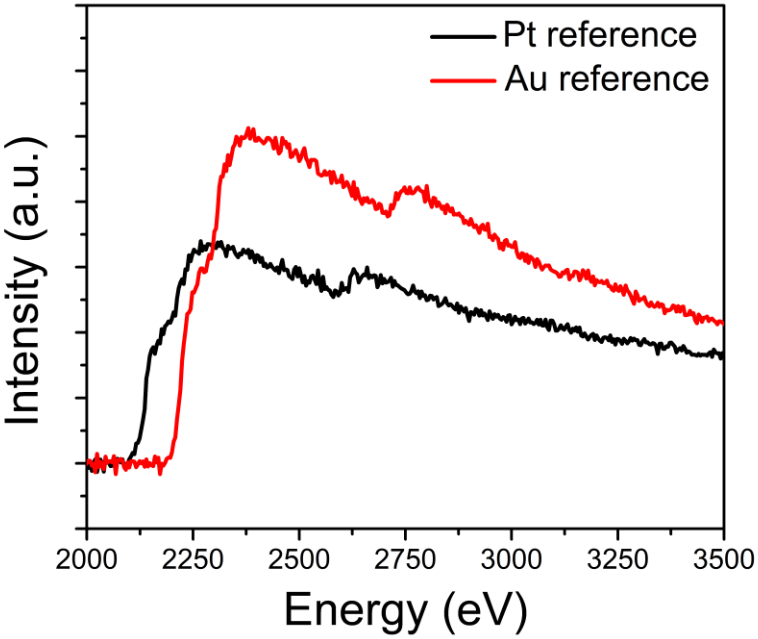

Figure 4.8. EELS spectra for Pt and Au reference samples, respectively. Reprinted with permission from *ACS Catal.*, **2016**, *6*, pp 3895–3908. Copyright 2016 American Chemical Society.

4.2.2. Evaluating Hydrogen Oxidation Reaction Activities of Synthesized Binary Alloy Catalysts

Cyclic voltammograms for each binary alloy catalyst are shown in Figures 4.9A and 4.9B with the corresponding H_{upd} charges determined from these CVs presented in Table 4.2. Figure 4.9A pertains to results associated with 'M' maintaining stronger HBEs than Pt, whereas Figure 4.9B highlights data involved with 'M' possessing weaker HBEs than Pt.[16] In Figure 4.9A, all of the catalysts give rise to CVs which are similar in nature to those of Pt, a finding which would further confirm the likely alloyed nature of the catalysts themselves. More specifically, all catalysts yielded peaks located at ~ 0.2 to 0.45 V vs. RHE, which can be ascribed to Pt-H interactions on the (110) and (100) planes of Pt.[3, 45]

Typically, it is relatively difficult to differentiate among the shifts within the hydrogen adsorption region for all of the catalysts analyzed. However, there are noticeable shifts in the hydrogen adsorption region to lower potentials for all alloyed PtM catalysts as compared with the elemental Pt NW system; for instance, the Pt(110) facet for the PtRu NW system is located at 0.205 V vs. RHE as compared with 0.257 V vs. RHE for the analogous Pt NW system. Based upon prior research, these observations make sense, as these alloyed systems likely demonstrate a weakening in the hydrogen binding interaction with their surfaces, which can be correlated with corresponding improvements in HOR kinetics.[6] These shifts in HBEs are likely a consequence of electronic effects imparted upon the Pt lattice by the addition through alloying of as much as 30% transition metal content.

In fact, as compared with Pt itself, all catalysts further demonstrate the presence of a noticeable ‘electronic effect’, as manifested in shifts in the oxide region. Specifically, the Pt_7Ru_3 NW catalyst demonstrates the presence of an oxide region shifted to lower potentials as compared with monometallic Pt, with the –OH reduction peak occurring at 0.68 vs. RHE.[6, 46] Additionally, the positions of the –OH reduction peaks of the other alloy catalysts tested, i.e. Pt_7Co_3 NWs and Pt_7Fe_3 NWs, are located at 0.7 V and 0.71 V vs. RHE, respectively, which are situated in the region between those of PtRu NWs and of pure Pt NWs themselves (i.e. 0.75 V vs. RHE). Therefore, it is reasonable to conclude that the Pt_7Co_3 NWs, Pt_7Fe_3 NWs, and Pt_7Ru_3 NWs all exhibit a perceptible electronic effect, due to the incorporation of ‘M’ within the Pt lattice as compared with the as-synthesized Pt NW system.

Moreover, these CV data correlate well with the XPS results in Figure 4.4. Specifically, the measured XPS shifts in the Pt *4f* region to higher binding energies are also suggestive of a decrease in the oxygen binding energy.[5, 17] In this vein, the PtRu, PtFe, and PtCo systems all gave rise to anticipated shifts in the oxide regions to lower potentials. Therefore, in the context of our CV results in Figure 4.9A, it would be expected that the Pt_7Ru_3 NW system should in fact give rise to the 'best' HOR kinetics due to the observation of the largest shift in the hydrogen adsorption region (i.e. to lower potentials) as compared with monometallic Pt.

Furthermore, in Figure 4.9B, we collected CVs associated with PtCu and PtAu NWs in addition to that for Pt NWs. The PtCu NW catalyst yielded a CV slightly different that of monometallic Pt in the hydrogen adsorption region (0.2 V – 0.5 V vs. RHE), with PtCu exhibiting one peak in the hydrogen adsorption region as opposed to two peaks. This feature is more prominent in Figure 4.10, which represents a larger window (0.0 V – 0.45 V vs. RHE) of the hydrogen adsorption region; this finding will be discussed further in Section 2.3. Additionally, the CV profile of PtAu NW catalyst gave rise to an extra peak located at ~ 1.1 V vs. RHE in the cathodic sweep, a feature which has been previously attributed to the presence of hydroxyl adsorption onto surface Au.[47] In essence, we find that the hydrogen adsorption regions for both PtCu and PtAu are shifted to lower onset potentials as compared with Pt alone, behavior consistent with an 'electronic' effect. Additionally, shifts can clearly be seen in the oxide region of the CVs of our alloyed nanowires as compared with the Pt NW system alone, thereby substantiating our assertion. Based upon these CVs, it would appear that the PtAu NW catalyst should possess the best HOR ability among all of these 3 catalysts, due to the lowest onset potential observed in the hydrogen adsorption region. However, due to the inherently weak HBEs associated with both Cu and Au, previous research has suggested that alloys incorporating these metals may not necessarily demonstrate enhanced HOR performance.[17]

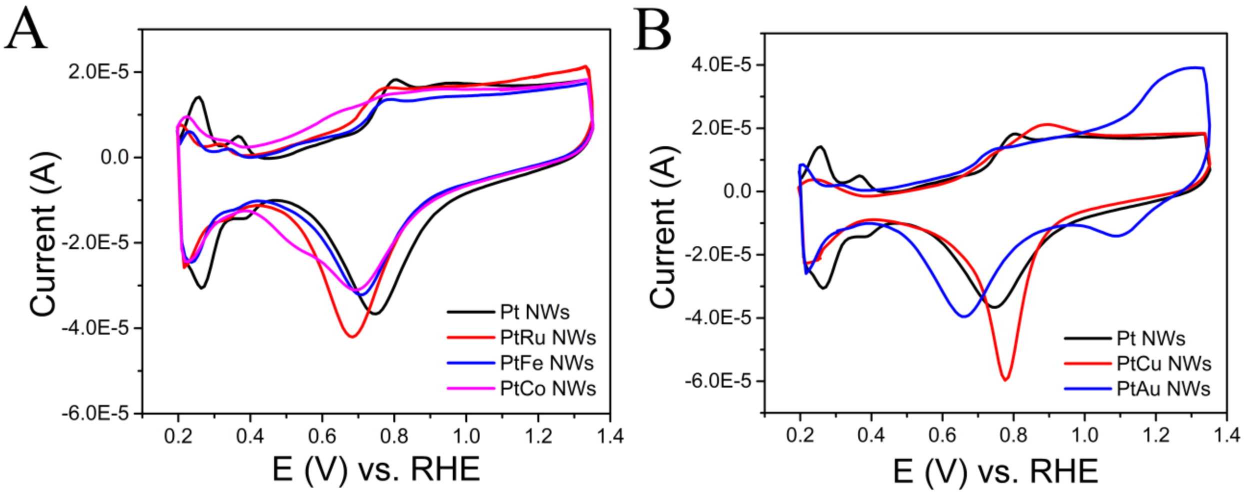

Figure 4.9. Cyclic voltammograms collected in an argon-saturated 0.1 M KOH solution and obtained at a scan rate of 20 mV/sec. (A) Pt NWs (black), Pt_7Ru_3 NWs (red), Pt_7Fe_3 NWs (blue), and Pt_7Co_3 NWs (magenta), as well as (B) Pt NWs (black), Pt_7Cu_3 NWs (red), and Pt_7Au_3 NWs (blue), respectively. Reprinted with permission from *ACS Catal.*, **2016**, *6*, pp 3895–3908. Copyright 2016 American Chemical Society.

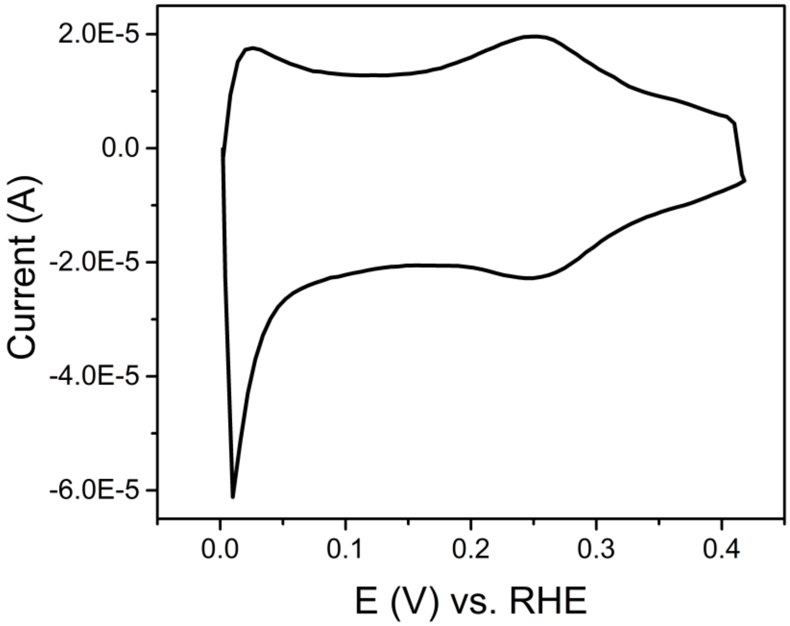

Figure 4.10. Hydrogen adsorption and underpotential deposition region collected in an Ar-saturated 0.1 M KOH electrolyte for Pt_7Cu_3 NWs. Reprinted with permission from *ACS Catal.*, **2016**, *6*, pp 3895–3908. Copyright 2016 American Chemical Society.

The corresponding CO stripping CVs are presented in Figure 4.11 with the analogous CO stripping charges determined from these data, highlighted in Table 4.2. From Figure 4.11A, we find that all of the NW catalyst systems possess shallow initial onsets for CO stripping between 0.4 V – 0.5 V vs. RHE. In effect, the Pt NW system gives rise to a similar CO stripping profile to those achieved by others.[47, 48] Specifically, we find 2 distinctive peaks corresponding to features associated with Pt(111) and Pt(110)/Pt(100) species.[48] Notably, PtRu gave rise to onsets for both peaks at detectably lower potentials than for all other catalyst systems.

In addition, the calculated electrochemical surface areas, determined from the CO stripping charge for both PtRu (0.270 cm^2) as well as Pt (0.271 cm^2), are almost identical, which would be expected, since both Ru and Pt possess similar affinity for CO.[49] We note that PtFe as well as PtCo evince broader CO stripping peaks that have been shifted to lower potentials as compared with Pt alone, a scenario indicative of their more facile capacity for removing CO from their surfaces.

In Figure 4.11B, the CO stripping abilities of Pt are compared with those of both PtCu and PtAu, respectively. With PtAu, we observed a shift to lower potentials for the removal of CO from the surface, whereas for PtCu, we detected only an ill-defined CO stripping peak. For PtCu in particular, this result may be a consequence of a surface rearrangement or reconstruction of Pt atoms as a result of Cu dissolution, a point which will be further discussed in Section 2.3.

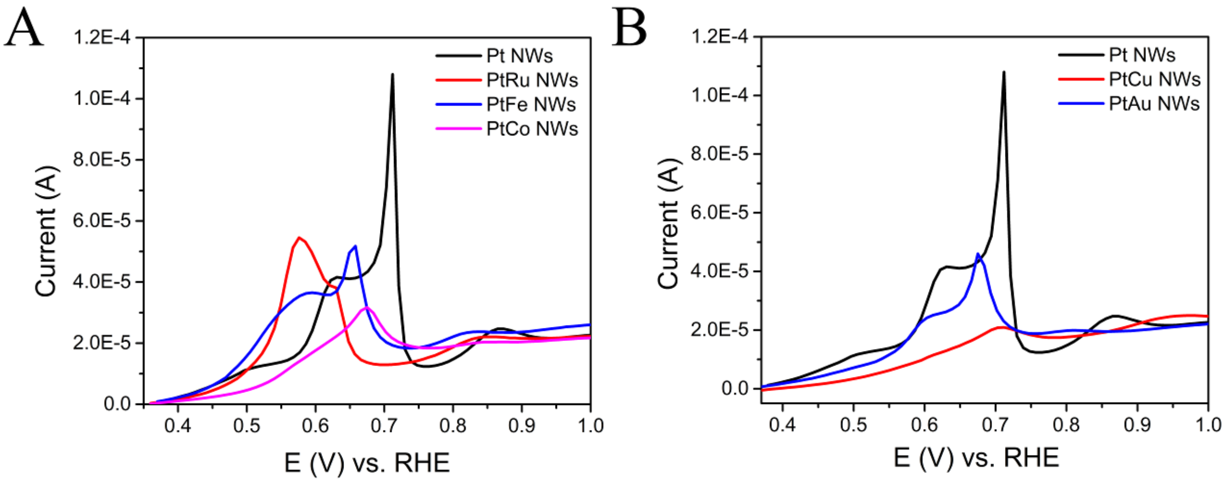

Figure 4.11. CO stripping CVs collected in an argon-saturated 0.1 M KOH solution and generated using a scan rate of 20 mV/sec. (A) Pt NWs (black), Pt_7Ru_3 NWs (red), Pt_7Fe_3 NWs (blue), and Pt_7Co_3 NWs (magenta), as well as (B) Pt NWs (black), Pt_7Cu_3 NWs (red), and Pt_7Au_3 NWs (blue), respectively. Reprinted with permission from *ACS Catal.*, **2016**, *6*, pp 3895–3908. Copyright 2016 American Chemical Society.

4.2.3. Correlating Composition of Alloy Catalysts with Hydrogen Oxidation Reaction Activities

A rotating disc electrode was employed to evaluate the hydrogen oxidation reaction performance, with all current normalized to the geometric surface area of the electrode. Figure 4.12A compares the performance of as-synthesized Pt NWs with that of binary alloy catalysts composed of 70 atom % Pt and 30 atom % Fe, Co, and Ru, respectively, at a rotation rate of 1600 rpm. Additional HOR curves for each catalyst at various rotating speeds (i.e. 400, 900, 1600, 2000, and 2500 rpm, respectively) can be found in Figure 4.13 with data associated with a commercial Pt NP/C standard displayed in Figure 4.14.

Specifically, our Pt_7Ru_3 NW catalyst was able to achieve a diffusion limited current at lower potentials, which is suggestive of improved HOR kinetics, i.e. a more facile ability to oxidize hydrogen. Corresponding data on Pt alloyed with both Au and Cu (30 at. %) can be found in Figure 4.12B. Specifically, the Pt_7Cu_3 NW catalyst arrived at the diffusion limited current density at ~ 0.2 V, whereas the Pt_7Au_3 NW catalyst only attained this value at ~0.25 V. This observation would indicate relatively slower HOR kinetics for this particular Pt_7Au_3 composition, as compared with the other catalysts. Moreover, based upon both Figures 4.12A and 4.12B, we found that the Pt_7Ru_3 NW catalyst yielded the lowest potential at which the diffusion limited current was reached, a result signifying its remarkably enhanced HOR abilities.

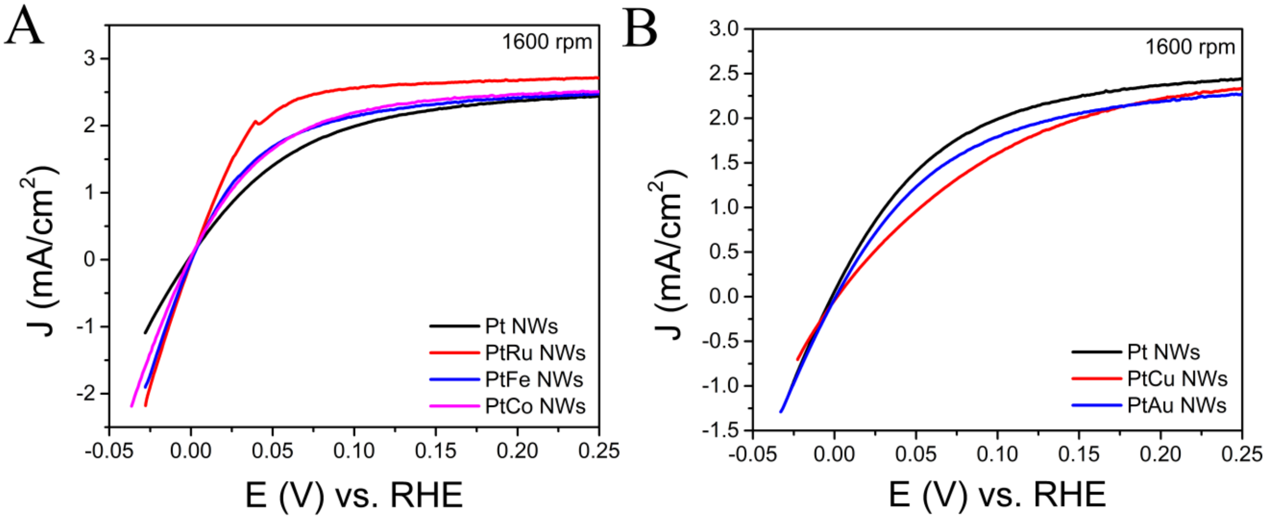

Figure 4.12. Hydrogen oxidation reaction cyclic voltammograms acquired in a hydrogen-saturated 0.1 M KOH solution and collected at 1600 rpm, with the current normalized to the geometric surface area of the electrode. (A) Pt NWs (black), Pt_7Ru_3 NWs (red), Pt_7Fe_3 NWs (blue), and Pt_7Co_3 NWs (magenta), as well as (B) Pt NWs (black), Pt_7Cu_3 NWs (red), and Pt_7Au_3 NWs (blue), respectively. Reprinted with permission from *ACS Catal.*, **2016**, *6*, pp 3895–3908. Copyright 2016 American Chemical Society.

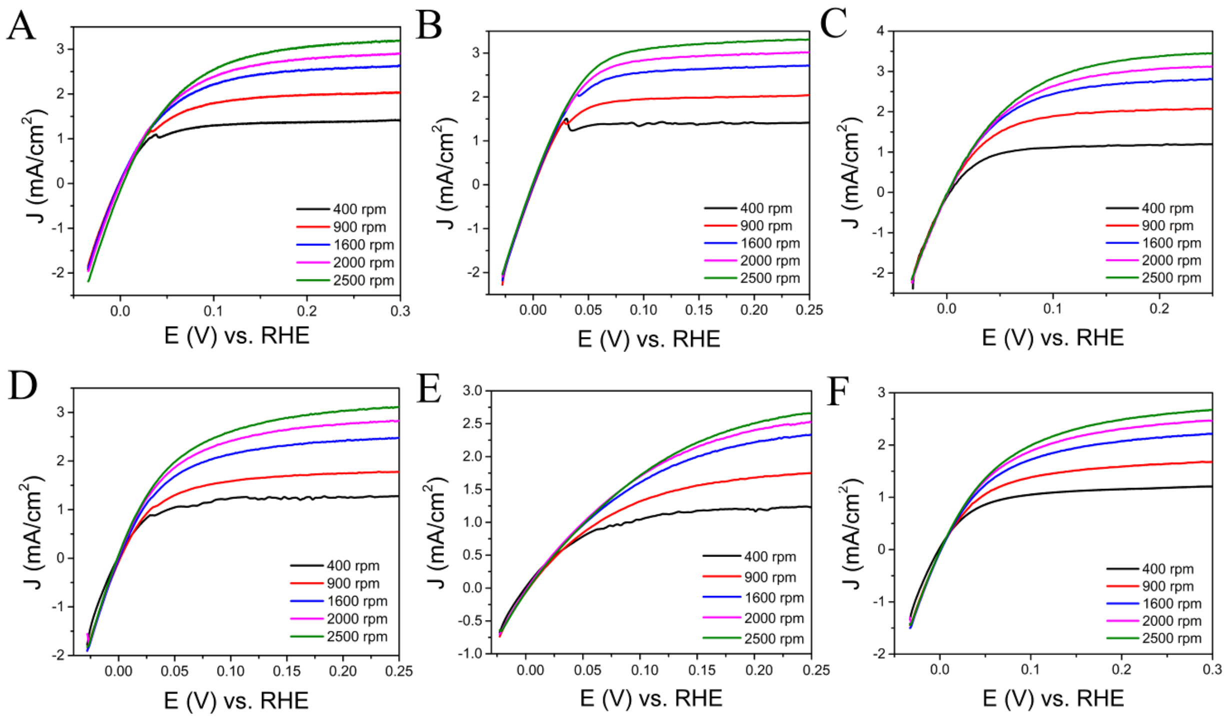

Figure 4.13. Hydrogen oxidation reaction curves obtained in a hydrogen-saturated 0.1 M KOH electrolyte at varying rotation speeds (i.e. 400, 900, 1600, 2000, and 2500 rpm, respectively). All curves are normalized to the geometric surface area of the electrode. (A) Pt NWs, (B) Pt_7Ru_3 NWs, (C) Pt_7Fe_3 NWs, (D) Pt_7Co_3 NWs, (E) Pt_7Cu_3 NWs, and (F) Pt_7Au_3 NWs, respectively. Reprinted with permission from *ACS Catal.*, **2016**, *6*, pp 3895–3908. Copyright 2016 American Chemical Society.

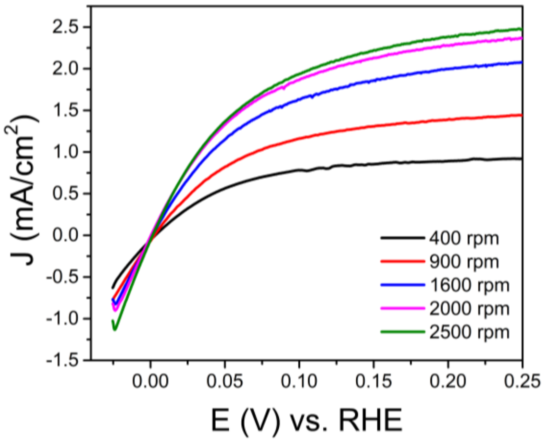

Figure 4.14. Hydrogen oxidation reaction curves acquired in a hydrogen-saturated 0.1 M KOH electrolyte at varying rotation speeds (i.e. 400, 900, 1600, 2000, and 2500 rpm) normalized to the geometric surface area of the electrode for commercial Pt/C. Reprinted with permission from *ACS Catal.*, **2016**, *6*, pp 3895–3908. Copyright 2016 American Chemical Society.

A bar graph can be found in Figure 4.15, summarizing the HOR exchange current densities obtained at 2500 rpm with respect to the computed trend in HBE values, previously determined by Mavrikakis et al.[15] for all catalysts. In essence, exchange current densities have been used to evaluate catalytic activity, close to the reversible potential (i.e. 0.0 V), since this is the potential where HOR is kinetically limited.[50] Hence, the calculation of this parameter, which has been standardized to the H_{upd} charges, allows for a more realistic, sensible, and quantifiably interpretable comparison of the various activities associated with the different catalyst materials tested.[51] Specifically, exchange current density values therefore been calculated using the kinetic currents derived from data acquired from the Tafel plots (Figure 4.17) in the context of the Koutecky-Levich equation divided by the H_{upd} charges determined from Figure 4.9.

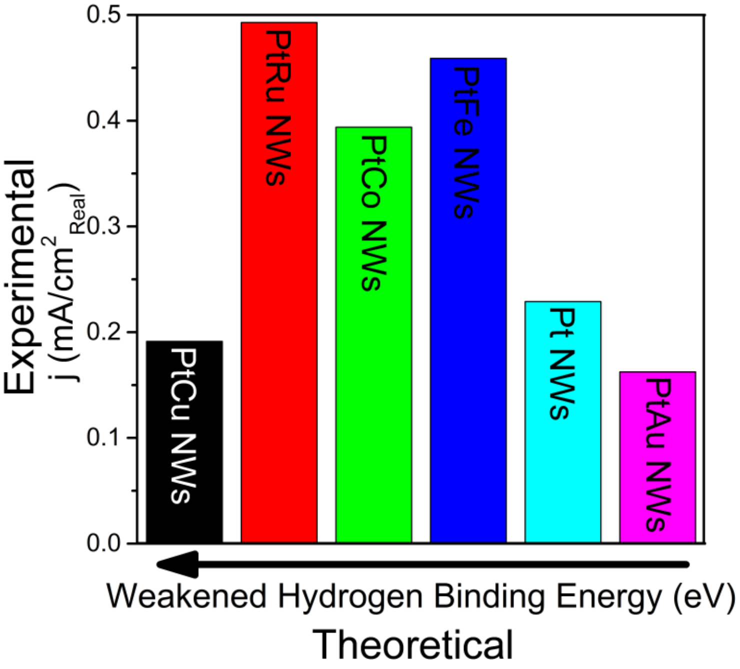

Figure 4.15. Bar graph highlighting experimental HOR exchange current densities as a function of the corresponding trend based on calculated surface HBE values for models of 'near surface alloys' for Pt NWs, Pt_7Ru_3 NWs, Pt_7Fe_3 NWs, Pt_7Co_3 NWs, Pt_7Cu_3 NWs, and Pt_7Au_3 NWs, respectively. The trend shown for the theoretical HBE values was based upon the data presented in Ref. 15. Reprinted with permission from *ACS Catal.*, **2016**, *6*, pp 3895–3908. Copyright 2016 American Chemical Society.

Based on all of these data, the effect of alloying cannot be underestimated. There is a clear correlative dependence between activity and chemical composition, with the Pt_7Ru_3 NW catalyst demonstrating the highest exchange current density measured of 0.493 mA/cm^2, as would be expected based on other reports in the literature.[6, 52] The addition of Ru promotes a more effective and prominent 'electronic' effect, which, as suggested by the XPS results, is a particularly key and influential variable with respect to determining HOR activity.[2, 45, 46]

As mentioned previously, this 'electronic effect' includes contributions from both the 'ligand effect' as well as the 'lattice strain effect'. The 'ligand effect' alters the *d*-band overlap of both Pt and 'M', as it involves either the withdrawal or addition of electron density to the Pt *d*-band, thereby effectively modifying the local electronic structure of Pt. By contrast, the 'lattice strain effect' is caused by either a compressive or tensile strain at the surface, i.e. a 'perturbation' of the Pt lattice with consequences for its electronic structure, since it has been shown to affect the position of its *d*-band center as well.[10] We have verified the presence of these synergistic electronic effects through measured XPS shifts in the Pt *4f* region of each binary catalyst analyzed (Figure 4.4) as well as in shifts observed in the hydrogen and oxide regions of the CVs presented in Figure 4.9, corroborated by variations in the *d*-spacing values achieved for all alloyed structures as compared with Pt. The remaining alloyed catalysts achieved exchange current densities of 0.459 mA/cm^2, 0.394 mA/cm^2, 0.162 mA/cm^2, and 0.191 mA/cm^2, respectively, corresponding to Pt_7Fe_3 NWs, Pt_7Co_3 NWs, Pt_7Au_3 NWs, and Pt_7Cu_3 NWs, with 0.229 mA/cm^2 and 0.202 mA/cm^2 pertaining to as-synthesized Pt NWs and commercial Pt/C NPs, respectively. The results are summarized in Table 4.2. These data confirm and substantiate the measured activity values, which had been collected at 0.05 V vs. RHE, normalized to the geometric surface area of the electrode, also located in Table 4.2.

Catalyst	Calculated Pt electrochemical surface area from the H_{upd} region (cm^2)	Calculated Pt electrochemical surface area from the CO stripping region (cm^2)	Activity Measured at 0.05 V vs. RHE ($mA/cm^2_{geometic}$)	Exchange current density (mA/cm^2_{real})
Pt	0.27	0.271	1.38	0.229
PtRu	0.176	0.273	2.2	0.493
PtFe	0.159	0.285	1.68	0.459
PtCo	0.168	0.267	1.64	0.394
PtCu	0.129	0.134	0.97	0.191
PtAu	0.155	0.227	1.23	0.162

Table 4.2. Computed Pt electrochemical surface areas calculated from the H_{upd} regions and CO stripping regions, respectively. Corresponding activities at 0.05 V vs. RHE normalized to the geometric surface area of the electrode compared with normalized HOR exchange current densities for all catalysts determined from a combination of data from Tafel plots in Figure 4.17 as well as from calculated H_{upd} charges. Reprinted with permission from *ACS Catal.*, **2016**, *6*, pp 3895–3908. Copyright 2016 American Chemical Society.

It is worth noting that the Pt NW catalyst gives rise to a better overall HOR performance as compared with commercial Pt NP/C. This observation is most likely due to the one-dimensional nature of the nanowire catalyst. As discussed earlier, 1D nanomaterials possess a number of beneficial attributes that can lead to such enhancements. In this particular case, the favorable combination of short segments of smooth crystal planes, fewer potentially deleterious defect sites, and higher aspect ratios collectively lead to enhanced performance as compared with their 0D analogues.[21]

The main goal of this study has been to correlate HOR exchange current densities (and as a result, activities) with theoretically calculated HBEs for the various alloys, with the calculated HBEs associated with a number of near surface alloys (NSA) performed by Mavrikakis et al.[15] ‘Near surface alloys’ denote alloy structures that possess different compositions at their surfaces as compared with the bulk of the material. In Figure 4.15, we correlate the experimental HOR exchange current densities (and by analogy, activities) of our various NW catalysts tested herein with the corresponding trend predicted by Mavrikakis. Since NSAs possess periodic extended single crystal surfaces which are vastly different than that of ultrathin alloy nanowires experimentally studied herein, the exact HBE values themselves cannot be precisely assigned to any particular chemical composition.

Hence, the HBE values in order of ‘decreasing activity’, based upon these calculations, can be summarized, as follows: PtCu (-2.32 eV), PtRu (-2.42 eV), PtCo (-2.62 eV), PtFe (-2.65 eV), Pt (-2.72 eV), and PtAu (-3.01 eV), respectively. Though the order of experimental activities associated with the PtFe and PtCo NW systems appears to be ostensibly switched as compared with theory, nonetheless, it is reasonable to assert that both the measured specific activities and the calculated HBEs are within error of each other.

Additionally, based on these findings, it would appear that our data for the PtCu NW system do not fall within the expected trend; PtCu would have been expected to possess the best HOR kinetics due to its comparatively decreased (and by extension, more favorable) HBE as compared with Pt. However, previous work performed on PtCu alloys in alkaline media by Strasser and co-workers[53] demonstrated that when cycling at high potentials (> 0.55 V vs. RHE), Cu forms an oxide species that dissolves *in situ* and subsequently re-deposits onto the surface of the Pt, thereby not only blocking active Pt sites but also causing –OH groups to adsorb onto Pt, since Pt is more oxophilic. In order to test this theory, HOR was performed on the PtCu NW system, immediately following catalyst deposition and prior to any CVs collected (Figure 4.16). In essence, CVs are normally acquired to not only clean the surface but also evaluate the extent of both the hydrogen and oxide adsorption and desorption taking place. However, in the very process of cycling the test system to higher potentials in order to probe the relevant oxide region, as previously stated, Cu oxide can form and inhibit activity by blocking Pt active sites.

Therefore, we found that in the absence of CV data acquisition prior to HOR testing, the HOR activity significantly improves as compared with prior results (i.e. 0.97 mA/cm^2) with the PtCu system; in effect, we achieved a value of 1.64 mA/cm^2 at 0.05 V vs. RHE.

In order to demonstrate that this dramatic improvement in HOR activity could be ascribed to the lack of surface Cu oxide species, the other alloyed catalysts were also tested as control samples, again in the absence of any prior CV data collection. As can be seen in Figure 4.16 and Table 4.3, in the absence of any previous CV measurements, the HOR activities of the Pt (i.e. 0.94 mA/cm^2), PtRu (i.e. 2.19 mA/cm^2), PtFe (i.e. 1.59 mA/cm^2), PtCo (i.e. 1.49 mA/cm^2), and PtAu (i.e. 1.07 mA/cm^2) systems, respectively, are actually within experimental error of the corresponding HOR activities achieved with initially running the cycling protocol followed by the HOR measurement itself (i.e. 1.38 mA/cm^2 (Pt), 2.2 mA/cm^2 (PtRu), 1.68 mA/cm^2 (PtFe), 1.64 mA/cm^2 (PtCo), and 1.23 mA/cm^2 (PtAu), respectively).

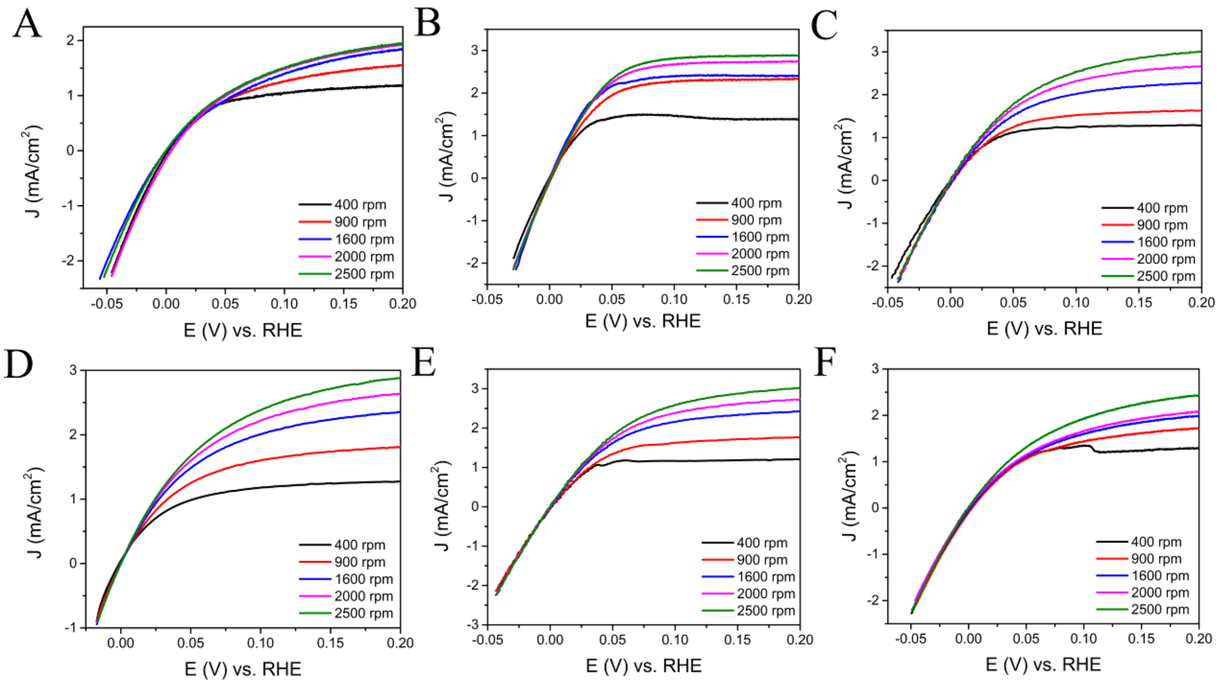

Figure 4.16. Hydrogen oxidation reaction curves acquired in a hydrogen-saturated 0.1 M KOH electrolyte at varying rotation speeds (i.e. 400, 900, 1600, 2000, and 2500 rpm) immediately after catalyst deposition (and prior to running any CVs) for (A) Pt NWs, (B) Pt_7Ru_3 NWs, (C) Pt_7Fe_3 NWs, (D) Pt_7Co_3 NWs, (E) Pt_7Cu_3 NWs, and (F) Pt_7Au_3 NWs, respectively. Reprinted with permission from *ACS Catal.*, **2016**, *6*, pp 3895–3908. Copyright 2016 American Chemical Society.

Catalyst	HOR activity measured after CV data collection (mA/cm^2)	HOR activity obtained prior to CV data collection (mA/cm^2)
Pt	1.38	0.94
PtRu	2.2	2.19
PtFe	1.68	1.59
PtCo	1.64	1.49
PtCu	0.97	1.64
PtAu	1.23	1.07

Table 4.3. Hydrogen oxidation reaction (HOR) activities measured for each catalyst in (i) the presence of prior CV collection and (ii) the absence of any previous CV data acquisition. Activities were obtained at 0.05 V vs. RHE at 1600 rpm and normalized to the geometric surface area of the electrode. Reprinted with permission from *ACS Catal.*, **2016**, *6*, pp 3895–3908. Copyright 2016 American Chemical Society.

Based uon these results, we note that only the PtCu nanowire sample gave rise to a better HOR activity in the absence of CV data collection, a finding which would be consistent with possible surface modification and oxidation of the Cu surface. As for the remaining materials tested including Pt itself, we found that a decreased activity for samples measured without CV data acquisition. That is, taking CVs prior to HOR measurements was actually positively beneficial for almost every sample we looked at. We can therefore attribute this observation to the removal of possible surface impurity species during the cleaning protocol which not only is associated with acquiring both CVs and CO stripping CVs but also was consistently used prior to the actual HOR testing. Furthermore, this finding is consistent with our previous claim that Cu oxide formation at higher potentials (> 0.55 V vs. RHE) inhibits HOR activity[54] by blocking the Pt active sites when re-deposited onto the surface.[53, 55]

We also note that the PtAu catalyst is associated with a worse activity than that of Pt, as had been theoretically predicted.[15] This is an expected finding in many respects, since Au is likely to be primarily localized on the surface and moreover, does not actively participate in hydrogen oxidation.[5, 56, 57] Nevertheless, with the exception of the PtCu system, all measured HOR current densities and the corresponding HBE trends are consistent with one another, with the PtRu system possessing the highest HOR exchange current density (and therefore, activity), whereas elemental Pt NWs and NPs appear to maintain comparatively worse activities.

In addition, the kinetic currents (i_k) for all catalysts were calculated using the Koutecky-Levich equation:[3]

$$\frac{1}{\mathrm{i}}=\frac{1}{\mathrm{i_k}}+\frac{1}{\mathrm{i_D}}$$

wherein i is the measured current and i_D is the diffusion limited current, with the curves being plotted as a function of the overpotential, as seen in Figure 4.17.

As shown in Figure 4.17, the Tafel slope values, collected at low potentials, appear to increase in absolute magnitude in the order of PtRu (|-32.7| mV/dec) < PtCu (|-37.9| mV/dec) < PtFe (|-43.3| mV/dec) < PtCo (|-45.7| mV/dec) < Pt (|-48.1| mV/dec) < PtAu (|-49.6| mV/dec). These data mirror the corresponding XPS trend, earlier discussed in Section 2.1 with the exception of the PtCu system, whose behavior has previously been shown to be impacted by surface oxide formation.

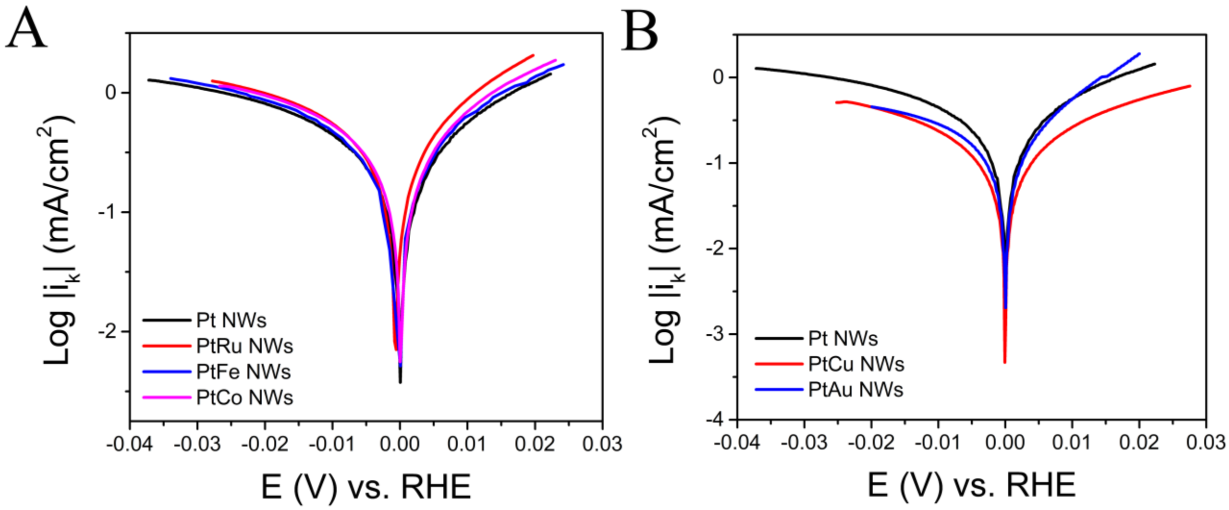

Figure 4.17. Tafel slope analysis of various monometallic and bimetallic nanowire catalysts using a hydrogen-saturated 0.1 M KOH electrolyte, acquired at 20 mV/s at 2500 rpm. Linear fits of the kinetic currents at high current density. (A) Pt NWs (black), Pt_7Ru_3 NWs (red), Pt_7Fe_3 NWs (blue), and Pt_7Co_3 NWs (magenta), as well as (B) Pt NWs (black), Pt_7Cu_3 NWs (red), and Pt_7Au_3 NWs (blue), respectively. Reprinted with permission from *ACS Catal.*, **2016**, *6*, pp 3895–3908. Copyright 2016 American Chemical Society.

4.3. Conclusions

In this Chapter, a simple solution-based method has been employed to synthesize a variety of ultrathin binary alloy nanowire systems which have been subsequently tested as HOR catalysts. The nanowire morphology has been shown to give rise to a better and higher HOR current density and activity as compared with its NP analogue, thereby suggesting the importance of short segments of crystalline planes, decreased amounts of deleterious defect sites, as well as high aspect ratios in determining overall performance. The addition of ‘M’ (wherein M = Fe, Co, Ru, Au, or Cu) to the Pt alloy structure has previously been shown to induce a beneficial response, due to the presence of both (a) the ‘ligand effect’, wherein a metal alters the *d*-band structure and electron density of the second metal, as well as (b) the ‘lattice strain effect’, wherein Pt-Pt bond distances are altered due to the addition of ‘M’, thereby resulting in variations in the electronic properties of the underlying Pt lattice.

Additionally, based upon the XPS results in Figure 4.4, predicted shifts in the Pt *4f* region for each of the binary catalysts analyzed as compared with monometallic Pt NWs can be observed, validating the presence of a ligand effect. Moreover, the CVs presented in Figure 4.9 depict hydrogen adsorption regions shifted to lower potentials for all of the binary alloy catalysts analyzed as compared with Pt, a finding which would suggest variations in their HBEs as compared with Pt alone. Collectively, these data imply a lowering of the HBE for the PtRu, PtFe, PtCo, and PtCu systems, respectively, as compared to monometallic Pt, whereas PtAu would be expected to demonstrate an increase in the magnitude of its HBE.

In fact, our experiments confirm theoretical insights about a clear and correlative dependence between measured activity and chemical composition. We find that the Pt_7Ru_3 NW catalyst exhibiting the highest HOR activity and specifically, exchange current density of 0.493 mA/cm^2, a value even better than that of pure Pt NWs alone. Additionally, all of our binary alloy NW systems, with the exception of the PtCu and PtAu NW systems, outperformed that of our as-synthesized, monometallic Pt NWs, likely due to the addition of 'M' to the Pt lattice, thereby imparting electrochemically favorable ligand and lattice strain effects on the bare Pt structure. In addition, we have been able to correlate the trend found in the calculated HBE values of our various alloyed structures with their actual HOR activities, as previously discussed in Section 2.3. We find that all catalysts generally follow the expected theoretical trend (within experimental error).[15]

To summarize, the significance of this Chapter is several-fold. *First,* we have systematically synthesized a variety of chemically well-defined Pt-based binary alloy systems and correlated their HOR activities in alkaline media as a function of composition. Our work highlights our capability of reproducibly and reliably achieving electrocatalytic enhancements over that of commercial Pt NPs alone with specific, well-chosen alloy compositions.

Second, in our alloy NW samples, we have experimentally elucidated and confirmed the presence of desirable electronic interactions with the introduction of the second metal with Pt. These critically relevant ligand and lattice strain effects have manifested themselves in not only perceptible shifts in the Pt *4f* region associated with the XPS spectra for each binary catalyst tested but also corresponding shifts in both the hydrogen adsorption and oxide regions with respect to Pt. In the case of PtRu, PtFe, PtCo, and PtCu NW alloyed systems, these phenomena may collectively explain the expected decrease in HBE values (versus Pt) because of a transitioning of the *d*-band center away from the Pt Fermi level. On the other hand, for PtAu NW alloys, one would expect a corresponding increase in HBE (versus Pt), which can be ascribed to the *d*-band center moving closer to the Pt Fermi level. In doing so, these results have supported the notion that 'electronic' effects substantively control HBE values and therefore, HOR activity.

Third, we have correlated our observed current densities and hence, resulting measured experimental activities with predicted trends based upon theoretical calculations of near surface alloys possessing identical chemical compositions and in doing so, highlighted possible limitations and caveats associated with existing models. *Finally,* all of our data have confirmed our assertion that morphology, size, and chemical composition need to be rationally and collectively tuned in order to achieve optimal electrochemical performance. Specifically, we have demonstrated that 1D anisotropic motifs, characterized by < 5 nm diameters and Pt-based alloyed compositions (in particular, PtRu), likely represent some of the most promising and intriguing active material platforms for HOR in alkaline media, developed to date.

4.4. References

1. Antolini, E.; Gonzalez, E. R., *J. Power Sources* **2010,** *195* 3431-3450.
2. Durst, J.; Siebel, A.; Simon, C.; Hasche, F.; Herranz, J.; Gasteiger, H. A., *Energy Environ. Sci.* **2014,** *7* 2255-2260.
3. Sheng, W.; Gasteiger, H. A.; Shao-Horn, Y., *J. Electrochem. Soc.* **2010,** *157* B1529-B1536.
4. Markovic, N.; Gasteiger, H.; Ross, P. N., *J. Electrochem. Soc.* **1997,** *144* 1591-1597.
5. Strmcnik, D.; Uchimura, M.; Wang, C.; Subbaraman, R.; Danilovic, N.; van der Vliet, D.; Paulikas, A. P.; Stamenkovic, V. R.; Markovic, N. M., *Nat. Chem.* **2013,** *5* 300-306.
6. Wang, Y.; Wang, G.; Li, G.; Huang, B.; Pan, J.; Liu, Q.; Han, J.; Xiao, L.; Lu, J.; Zhuang, L., *Energy & Environmental Science* **2015,** *8* 177-181.
7. Ribeiro, V. A.; Correa, O. V.; Neto, A. O.; Linardi, M.; Spinacé, E. V., *Appl. Catal., A* **2010,** *372* 162-166.
8. Qiu, H.; Zou, F., *ACS Appl. Mater. Interfaces* **2012,** *4* 1404-1410.
9. Kitchin, J. R.; Nørskov, J. K.; Barteau, M. A.; Chen, J. G., *J. Chem. Phys.* **2004,** *120* 10240-10246.
10. Mavrikakis, M.; Hammer, B.; Nørskov, J. K., *Phys. Rev. Lett.* **1998,** *81* 2819-2822.
11. Jia, Q.; Liang, W.; Bates, M. K.; Mani, P.; Lee, W.; Mukerjee, S., *ACS Nano* **2015,** *9* 387-400.
12. Ruban, A.; Hammer, B.; Stoltze, P.; Skriver, H. L.; Nørskov, J. K., *J. Mol. Catal. A: Chem.* **1997,** *115* 421-429.
13. Jia, Q.; Segre, C. U.; Ramaker, D.; Caldwell, K.; Trahan, M.; Mukerjee, S., *Electrochim. Acta* **2013,** *88* 604-613.
14. Greeley, J.; Mavrikakis, M., *Nat. Mater.* **2004,** *3* 810-815.
15. Kandoi, S.; Ferrin, P. A.; Mavrikakis, M., *Top. Catal.* **2010,** *53* 384-392.
16. Skúlason, E.; Tripkovic, V.; Björketun, M. E.; Gudmundsdóttir, S.; Karlberg, G.; Rossmeisl, J.; Bligaard, T.; Jónsson, H.; Nørskov, J. K., *J. Phys. Chem. C* **2010,** *114* 18182-18197.
17. Elbert, K.; Hu, J.; Ma, Z.; Zhang, Y.; Chen, G.; An, W.; Liu, P.; Isaacs, H. S.; Adzic, R. R.; Wang, J. X., *ACS Catal.* **2015,** *5* 6764-6772.
18. Chen, J. G.; Menning, C. A.; Zellner, M. B., *Surf. Sci. Rep.* **2008,** *63* 201-254.
19. Ferrin, P.; Kandoi, S.; Nilekar, A. U.; Mavrikakis, M., *Surf. Sci.* **2012,** *606* 679-689.
20. Cademartiri, L.; Ozin, G. A., *Adv. Mater.* **2009,** *21* 1013-1020.
21. Koenigsmann, C.; Scofield, M. E.; Liu, H.; Wong, S. S., *J. Phys. Chem. Lett.* **2012,** *3* 3385-3398.
22. Koenigsmann, C.; Santulli, A. C.; Gong, K.; Vukmirovic, M. B.; Zhou, W.-p.; Sutter, E.; Wong, S. S.; Adzic, R. R., *J. Am. Chem. Soc.* **2011,** *133* 9783-9795.
23. Liu, H.; Li, L.; Scofield, M. E.; Wong, S. S., *APL Mat.* **2015,** *3* 1-15.
24. Song, Y.; Garcia, R. M.; Dorin, R. M.; Wang, H.; Qiu, Y.; Coker, E. N.; Steen, W. A.; Miller, J. E.; Shelnutt, J. A., *Nano Lett.* **2007,** *7* 3650-3655.
25. Yang, S.; Hong, F.; Wang, L.; Guo, S.; Song, X.; Ding, B.; Yang, Z., *J. Phys. Chem. C* **2010,** *114* 203-207.
26. Scofield, M. E.; Koenigsmann, C.; Wang, L.; Liu, H.; Wong, S. S., *Energy & Environmental Science* **2015,** *8* 350-363.
27. Long, N. V.; Yang, Y.; Minh Thi, C.; Minh, N. V.; Cao, Y.; Nogami, M., *Nano Energy* **2013,** *2* 636-676.

28. Huang, T.; Liu, J.; Li, R.; Cai, W.; Yu, A., *Electrochem. Commun.* **2009,** *11* 643-646.
29. Sieben, J. M.; Duarte, M. M. E., *Int. J. Hydrogen Energy* **2012,** *37* 9941-9947.
30. Zheng, J.-N.; Li, S.-S.; Ma, X.; Chen, F.-Y.; Wang, A.-J.; Chen, J.-R.; Feng, J.-J., *J. Mater. Chem. A* **2014,** *2* 8386-8395.
31. Kang, W.; Li, R.; Wei, D.; Xu, S.; Wei, S.; Li, H., *RSC Adv.* **2015,** *5* 94210-94215.
32. Chou, H.-Y.; Yeh, T.-K.; Tsai, C.-H., *Int. J. Electrochem. Sci.* **2014,** *9* 5763-5775.
33. Chaisubanan, N.; Pruksathorn, K.; Vergnes, H.; Senocq, F.; Hunsom, M., *Int. J. Electrochem. Sci.* **2016,** *11* 1012-1028.
34. Jeon, M. K.; Zhang, Y.; McGinn, P. J., *Electrochim. Acta* **2010,** *55* 5318-5325.
35. Chen, D.; Zhao, Y.; Peng, X.; Wang, X.; Hu, W.; Jing, C.; Tian, S.; Tian, J., *Electrochim. Acta* **2015,** *177* 86-92.
36. Li, J.; Wang, G.; Wang, J.; Miao, S.; Wei, M.; Yang, F.; Yu, L.; Bao, X., *Nano Res.* **2014,** *7* 1519-1527.
37. Li, J.; Fu, X.; Mao, Z.; Yang, Y.; Qiu, T.; Wu, Q., *Nanoscale Res. Lett.* **2016,** *11* 1-8.
38. Hsu, S.-P.; Liu, C.-W.; Chen, H.-S.; Chen, T.-Y.; Lai, C.-M.; Lee, C.-H.; Lee, J.-F.; Chan, T.-S.; Tsai, L.-D.; Wang, K.-W., *Electrochim. Acta* **2013,** *105* 180-187.
39. Loukrakpam, R.; Shan, S.; Petkov, V.; Yang, L.; Luo, J.; Zhong, C.-J., *J. Phys. Chem. C* **2013,** *117* 20715-20721.
40. Song, P.; Mei, L.-P.; Wang, A.-J.; Fang, K.-M.; Feng, J.-J., *Int. J. Hydrogen Energy* **2016,** *41* 1645-1653.
41. García-Contreras, M. A.; Fernández-Valverde, S. M.; Vargas-García, J. R.; Cortés-Jácome, M. A.; Toledo-Antonio, J. A.; Ángeles-Chavez, C., *Int. J. Hydrogen Energy* **2008,** *33* 6672-6680.
42. Zhao, Y.; Fan, L.; Ren, J.; Hong, B., *Int. J. Hydrogen Energy* **2014,** *39* 4544-4557.
43. Hong, W.; Wang, J.; Wang, E., *Nano Res.* **2015,** *8* 2308-2316.
44. Xu, C.; Li, Q.; Liu, Y.; Wang, J.; Geng, H., *Langmuir* **2012,** *28* 1886-1892.
45. Sheng, W.; Zhuang, Z.; Gao, M.; Zheng, J.; Chen, J. G.; Yan, Y., *Nat. Commun.* **2015,** *6* 1-6.
46. St. John, S.; Atkinson, R. W.; Unocic, K. A.; Unocic, R. R.; Zawodzinski, T. A.; Papandrew, A. B., *ACS Catal.* **2015,** *5* 7015-7023.
47. Mahoney, E. G.; Sheng, W.; Yan, Y.; Chen, J. G., *ChemElectroChem* **2014,** *1* 2058-2063.
48. Farias, M. J. S.; Vidal-Iglesias, F. J.; Solla-Gullón, J.; Herrero, E.; Feliu, J. M., *J. Electroanal. Chem.* **2014,** *716* 16-22.
49. Davies, J. C.; Hayden, B. E.; Pegg, D. J., *Surf. Sci.* **2000,** *467* 118-130.
50. Rheinländer, P. J.; Herranz, J.; Durst, J.; Gasteiger, H. A., *J. Electrochem. Soc.* **2014,** *161* F1448-F1457.
51. Wang, J. X.; Springer, T. E.; Adzic, R. R., *J. Electrochem. Soc.* **2006,** *153* A1732-A1740.
52. St. John, S.; Atkinson, R. W.; Unocic, R. R.; Zawodzinski, T. A.; Papandrew, A. B., *J. Phys. Chem. C* **2015,** *119* 13481-13487.
53. Oezaslan, M.; Hasché, F.; Strasser, P., *J. Electrochem. Soc.* **2012,** *159* B444-B454.
54. Alia, S. M.; Pivovar, B. S.; Yan, Y., *J. Am. Chem. Soc.* **2013,** *135* 13473-13478.
55. Zhang, X.; Yu, S.; Qiao, L.; Zheng, W.; Liu, P., *J. Chem. Phys.* **2015,** *142* 1-9.
56. Angerstein-Kozlowska, H.; Conway, B. E.; Hamelin, A., *J. Electroanal. Chem.* **1990,** *277* 233-252.
57. Henning, S.; Herranz, J.; Gasteiger, H. A., *J. Electrochem. Soc.* **2015,** *162* F178-F189.

Chapter 5 - Correlating the Chemical Composition and Size of Various Metal Oxide Substrates with the Catalytic Activity and Stability of As-Deposited Pt Nanoparticles for the Methanol Oxidation Reaction

5.1. Introduction

Significant strides have been made in terms of advancing direct alcohol fuel cell (DAFC) technology. However, a number of pervasive and potentially deleterious issues can significantly impact upon the overall fuel cell design and specifically reduce electrochemical performance. In particular, the nature of the electrode materials used raises an important and unavoidable concern. In particular, the (i) low activity of the catalyst materials relative to their overall cost, (ii) the poisoning of the active sites due to the presence of carbon monoxide produced during small molecule (methanol, ethanol, and formic acid) oxidation, and (iii) the lack of catalytic stability and durability on the underlying commercial carbon support all represent key inhibitors of catalytic activity and contribute to the operational degradation of electrocatalysts employed, thereby reducing the efficiency of the fuel cell as a whole.[1-3]

Currently, Pt-containing electrocatalysts (such as alloy, core-shell, and hierarchical motifs) are the most widely utilized catalysts, due to the inherently high activity achieved by Pt, which is the most active metal for both MOR and ORR. Nevertheless, the use of carbon as the support medium not only can lead to Pt agglomeration but also is intrinsically problematic, since carbon is easily corroded over time. The net consequence is an overall loss of active Pt sites (i.e. a decrease in the ECSA) and hence, the concomitant degradation of the catalyst.[1] Typically, with the use of carbon black, i.e. the most common carbon support, aggregation and detachment of previously immobilized Pt NPs tend to occur. As a result, the overall surface area needed for the oxygen reduction and methanol oxidation reactions is reduced, and the observed fuel efficiency is effectively lowered.

In order to address this issue and to discover high-performing, relatively inexpensive alternatives to carbon black, research has turned to other supports such as either graphene, CNTs, or metal oxides in order to (i) improve upon favorable physico-chemical coupling interactions of the underlying support with the catalyst and to (ii) enhance the stability of the support under highly acidic electrochemical conditions. Specifically, other groups have previously demonstrated that certain metal oxides such as TiO_2,[4-6] RuO_2,[7-9] and SnO_2[10-12] represent viable and practical alternatives to standard carbon black, due to their (a) increased chemical and electrochemical stability, (b) positive interactions with the coated electrocatalysts,[13] as well as (c) capacity to give rise to an external, outer surface composed of pendant, accessible hydroxyl groups which can conceivably facilitate the removal of poisonous, de-activating species, such as CO.[14] The ability of these metal oxides to adsorb hydroxyl groups is highly advantageous; specifically, these metal oxides possess certain geometrical configurations of metal oxide (M-O) bonds, such that when placed in water, the M-O bonds will interact and form layers of molecular water adsorbates.

Additionally, by either adding in oxygen vacancies or doping with ions such as fluorine, it is likely that these metal oxides can be tailored so as to exhibit even higher electrochemical activities.[13] Although TiO_2 and $SrTiO_3$ are known to be semiconductors in bulk, by contrast, at the nanoscale, a significant amount of defects exist within these materials, and these imperfections ultimately enhance their intrinsic conductivities. For example, it has been shown that nanoscale TiO_2 possesses Ti^{3+} ions which contribute to an increase in their conductivity, and these cations are typically generated by either creating oxygen deficiencies or heating TiO_2

within a reducing atmosphere. These scenarios are analogous to the net effects of our own experimental protocol herein, in which we have fabricated nanoscale TiO_2 by means of hydrothermal synthesis.[15-17]

Indeed, these binary metal oxides have been noted to be particularly advantageous for their corrosion resistance and electrochemical stability under highly acidic conditions, due to their intrinsically high oxidation state, because it is very difficult to oxidize these metal oxides even further. Additionally, metal oxides can act either as co-catalysts or as supports that give rise to beneficial metal-support interactions with their overlying metal catalysts.[15, 18] Typically, metal support interactions are characterized by either partial charge transfer between the support itself and the supported metal catalyst or a change in the lattice parameter of the metal catalyst.[19, 20] This important and helpful interaction can be essentially ascribed to an electronic effect created by the specific metallic component within the support, and has been previously noted with metal oxide supports such as but not limited to TiO_2, CeO_2, MoO_2, WO_2, SnO_2, and RuO_2.[15, 18-21]

To take this concept one step further, it is reasonable and appropriate to consider using either complex metal oxides or perovskites such as ABO_3 (A = Sr, La, and Ca; B = Ti and Ru) as viable metal oxide support materials. In fact, it is well documented that a variety of perovskite materials are electronically conductive, possess very good proton transport properties, and maintain acidic outer surfaces, thereby rendering them as excellent candidates for support materials in highly acidic environments, typically utilized by conventional fuel cells.[22] As a relevant and illustrative example in this context, our group has previously shown[23] that $SrRuO_3$ yields a promising level of methanol oxidation activity, even in the absence of Pt metal as a dispersed catalyst. This result provides for compelling evidence for the ability of the support material itself to actively participate in the oxidation process of methanol.

Moreover, a different team investigated the corresponding methanol oxidation behavior of Pt/$SrRuO_3$, and demonstrated its significant MOR potential.[22] That is, the use of a complex metal oxide material as a support for Pt has been shown to not only lower the overpotential for methanol oxidation but also contribute to the complete oxidation of any methanol present.[14, 24] More importantly, in the presence of water, the perovskite material appears to have the capability to readily absorb surface oxygen atoms that are likely to be heavily protonated on its surface, thereby generating hydroxyl groups which can facilitate and hence promote the desired oxidation process.[25] Some groups have proposed that the metal located at the B site, as opposed to the A site, more significantly influences and contributes to the observed electrochemical abilities of the electrocatalyst lying on its surface.[14]

Specifically, a combinatorial study by Mukasyan et al.[22] evaluated a variety of ABO_3 perovskite structures, with 'A' = La, Sr, and 'B' = Fe, Ru, for instance. In terms of results, they not only found that $SrRuO_3$ as a support is highly active towards methanol oxidation but also, after Pt NP deposition, noted that the Pt likely existed in a higher oxidative state, with the implication that the perovskite material most probably accepted electrons from the adjacent elemental Pt, thereby contributing to a higher observed MOR activity for the overall catalyst. Multiple groups have attempted to determine and differentiate the exact 'catalytic roles' of the atoms localized at both the 'A' and 'B' sites within the perovskite structure, respectively. In particular, Sauvet et al. showed that the Sr present at the 'A' site stabilizes the Ru in its tetravalent configuration at the 'B' site.[26] Additionally, Ponce and co-workers[27] highlighted a similar finding in which the Sr within the perovskite $La_{1-x}Sr_xMnO_3$ ('x' = 0–0.5) played an important role in maintaining the Mn^{4+} state.

Hence, with the ongoing need to find more stable and potentially more active alternatives as compared with conventional carbon black, perovskite materials represent a viable, attractive, and relatively little used substitute for catalytic supports. Moreover, there have been few if any systematic efforts to correlate the chemical composition of these perovskites with the resulting electrochemical performance observed. In this light, the significance of this study is as follows. We aim to differentiate between the various enhancements observed at the catalytic interface as a result of the identity of ‘B’ site within the perovskite structure. That is, by systematically studying various perovskites wherein we have purposely altered ‘B’ but kept ‘A’ constant, we intend to determine whether the metal residing at the ‘B’ site is indeed the driving factor for the observed, enhanced MOR activity. Additionally, we strive to demonstrate the origin of catalytic enhancement, thereby providing a plausible rationale for explaining the improved MOR activity noted.

We have also tested for the effect of surface area and size by analyzing metal oxides of various constituent crystallite sizes. Moreover, we compare our data to binary oxide control samples to deduce between and thereby potentially explain the relevant electrocatalytic performances of simple binary versus ternary (in this case, perovskite) metal oxides. Our results demonstrate that (i) the $SrRuO_3$ substrate coated with Pt NPs gives rise to the best MOR performance observed as compared with the other substrate materials tested herein and that (ii) size is a relatively less important determinant of electrochemical activity as compared with the overriding importance of the chemical composition of the substrate materials themselves.

Furthermore, in order to probe the origin of this enhancement, EELS analysis provided evidence for electron transfer from Pt NPs lying at the surface to surface Ru atoms within the underlying $SrRuO_3$ substrate itself. Interestingly, little if any electron transfer was detected for either the TiO_2 and RuO_2 controls or even analogous $SrTiO_3$ substrates. As additional complementary corroboration of these EELS data, XPS data were acquired and confirmed a decrease in the electron density in the Pt *4f* region when Pt NPs were deposited onto the $SrRuO_3$ supports. These cumulative results would imply that favorable metal support interactions, involving electron transfer between immobilized Pt and the underlying $SrRuO_3$, likely account for the increased MOR activity of the composite catalyst material. Moreover, based on the collected chronoamperometry data, the use of $SrRuO_3$ would also be beneficial in terms of improving the overall stability and long-term effectiveness of the catalytic support as compared with standard commercial carbon black.

5.2. Results & Discussion

In this chapter, we seek to investigate the impact of the chemical composition of the support material itself upon the overall activity of the catalyst. That is, we address the issue of how specifically varying the identity of the 'B' metal site within a perovskite material ultimately promotes and enhances the oxidation of methanol. As a constant 'parameter', Sr was chosen for the invariant 'A' site, since it has been shown to be electrochemically passive.[28] In probing the effect of Ru in particular as the 'B' site, titanium was utilized as a corresponding 'counterbalancing' element, since Ti itself possesses neither a promotional effect nor sufficient conductivity.[29] It has been previously documented that altering the nature of the substituents at the 'B' site can significantly contribute to electrochemical activity.[14, 24] Specifically herein, we demonstrate not only a reproducible electrochemical enhancement when Ru is localized as the 'B' site but also the underlying nature of this enhancement by utilizing EELS analysis. In so doing, we demonstrate electron transfer between Pt and Ru within the $SrRuO_3$ substrate, which may plausibly account for the improved MOR performance. Moreover, in addition to commercial Pt/C, both TiO_2 and RuO_2 served as further controls for these perovskite supports. The structure, morphology, purity, and crystallinity of our perovskite materials both before and after Pt deposition were analyzed using a suite of complementary structural characterization techniques, including XRD, SEM, HRTEM, SAED, XPS, and EELS.

5.2.1. Characterization of the Various Metal Oxide and Perovskite Support Materials

Specifically, Figure 5.1 depicts the powder XRD of various perovskite materials tested, including not only of both sizes of $SrTiO_3$ and $SrRuO_3$ but also of the TiO_2 and RuO_2 control samples. All six metal oxide samples gave rise to the expected crystallographic structure, as demonstrated by the JCPDS database standard of each material. In particular, Figure 5.1A is associated with the anatase form of TiO_2, with peaks corresponding to JCPDS 21-1272. Figure 5.1B can be ascribed to the tetragonal structure of RuO_2, with the peak values and locations consistent with JCPDS 73-1469. Additionally, the $SrTiO_3$ samples (Figure 5.1C & 5.1E) evince a cubic structure similar to JCPDS 86-0179, whereas the $SrRuO_3$ samples (Figure 5.1D & 5.1F) could be readily identified with an orthorhombic structure (JCPDS 85-1907). Moreover, all metal oxide samples displayed the correct structure with little if any obvious impurities, as had been expected, based on the original synthesis protocols.[23, 30-34]

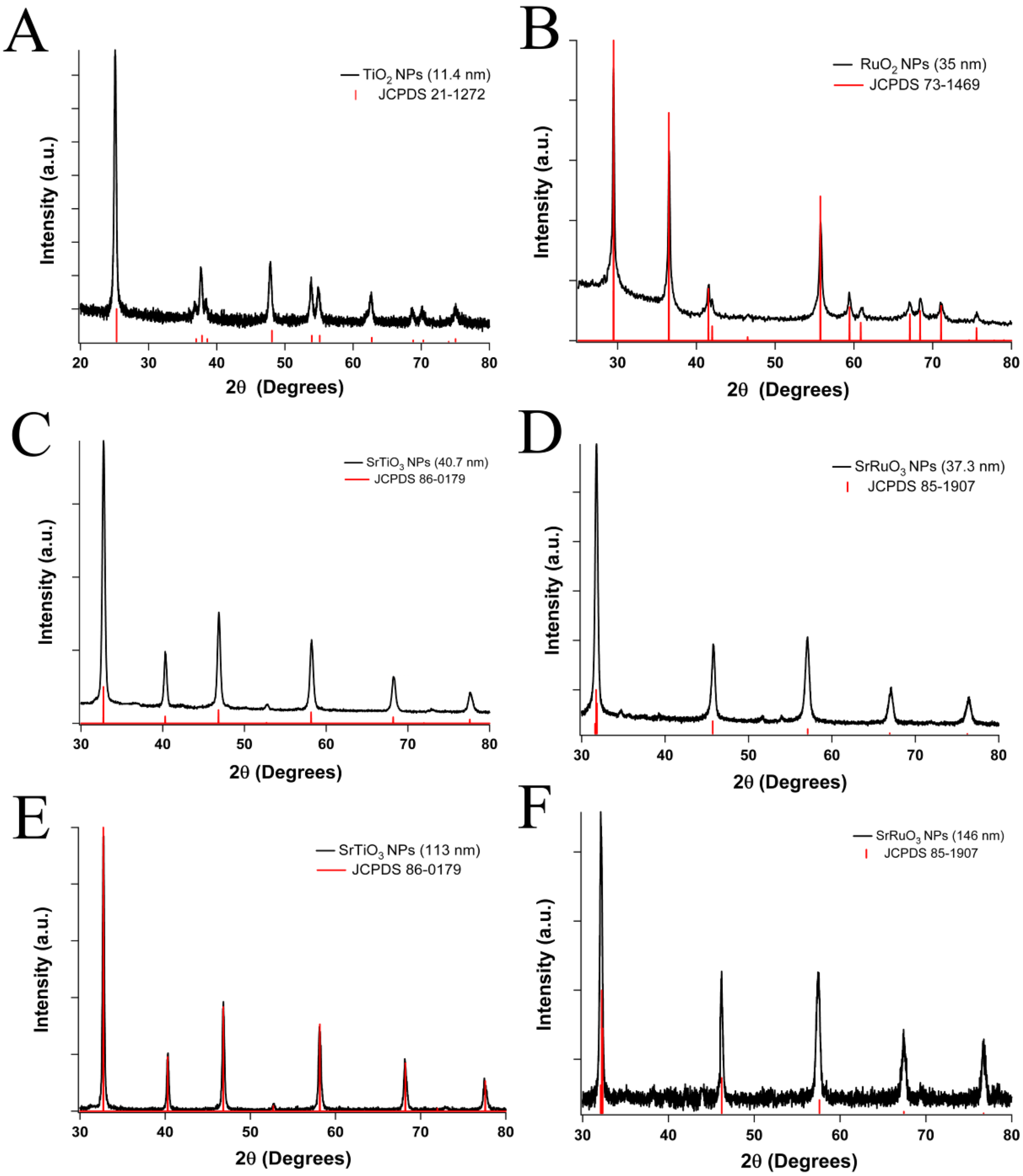

Figure 5.1. XRD patterns (black curves) for (A) TiO_2 NPs (11.4 nm), (B) RuO_2 NPs (35 nm), (C) $SrTiO_3$ NPs (40.7 nm), (D) $SrRuO_3$ NPs (37.3 nm), (E) $SrTiO_3$ NPs (113 nm), and (F) $SrRuO_3$ NPs (146 nm), respectively. All experimental peaks can be correlated with the expected assignments determined from individual JCPDS patterns, shown in red. Reproduced by permission of The Royal Society of Chemistry.

The morphological and chemical compositional characterization data for the various metal oxide and perovskite materials tested are highlighted in Figures 5.2 and 5.3, respectively. These include results obtained from SEM, TEM, HRTEM, as well as SAED analysis. Specific data associated with the average diameters, measured *d*-spacings, and particular crystallographic planes of our binary and ternary metal oxides are listed in Table 5.1.

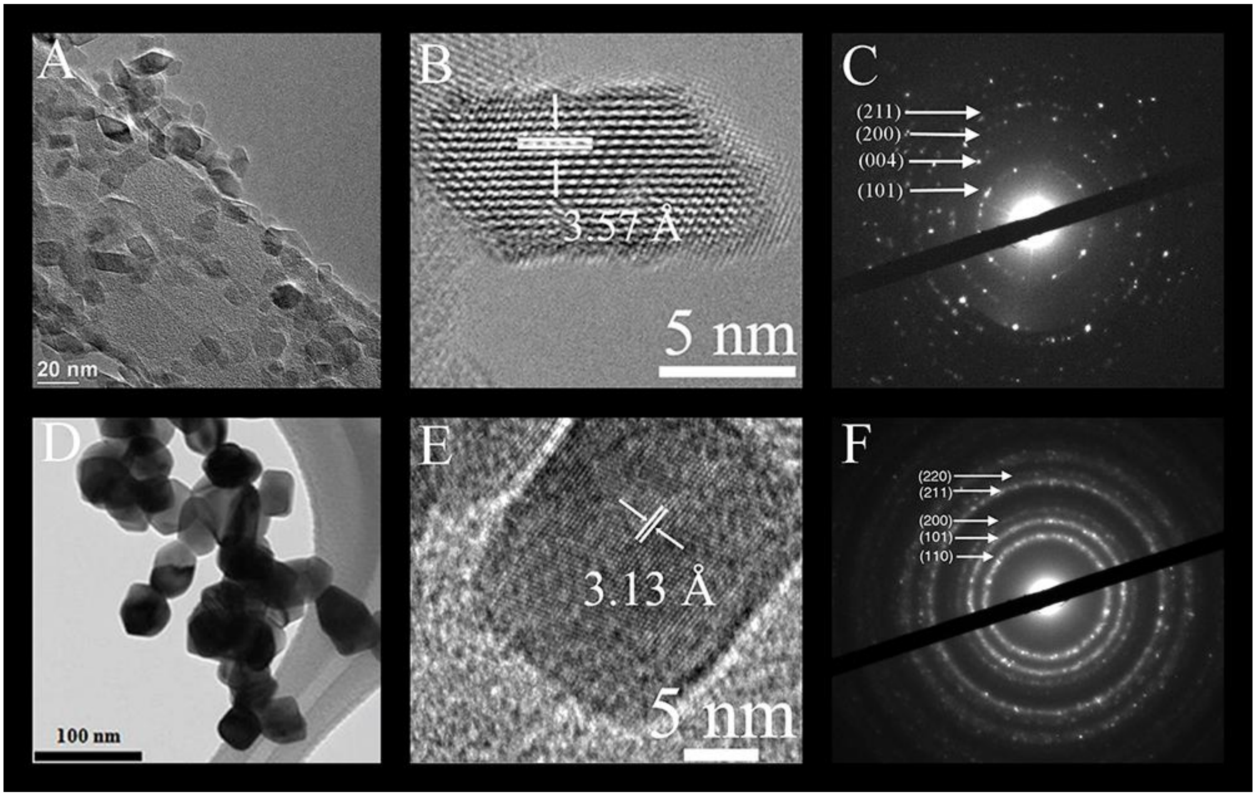

Figure 5.2. Representative TEM image (A & D), higher magnification HRTEM image with the measured *d*-spacing (B & E), and associated single area electron diffraction data (C & F) for binary 11.4 nm TiO_2 (A-C) and 35 nm RuO_2 (D-F) NPs, respectively. Reproduced by permission of The Royal Society of Chemistry.

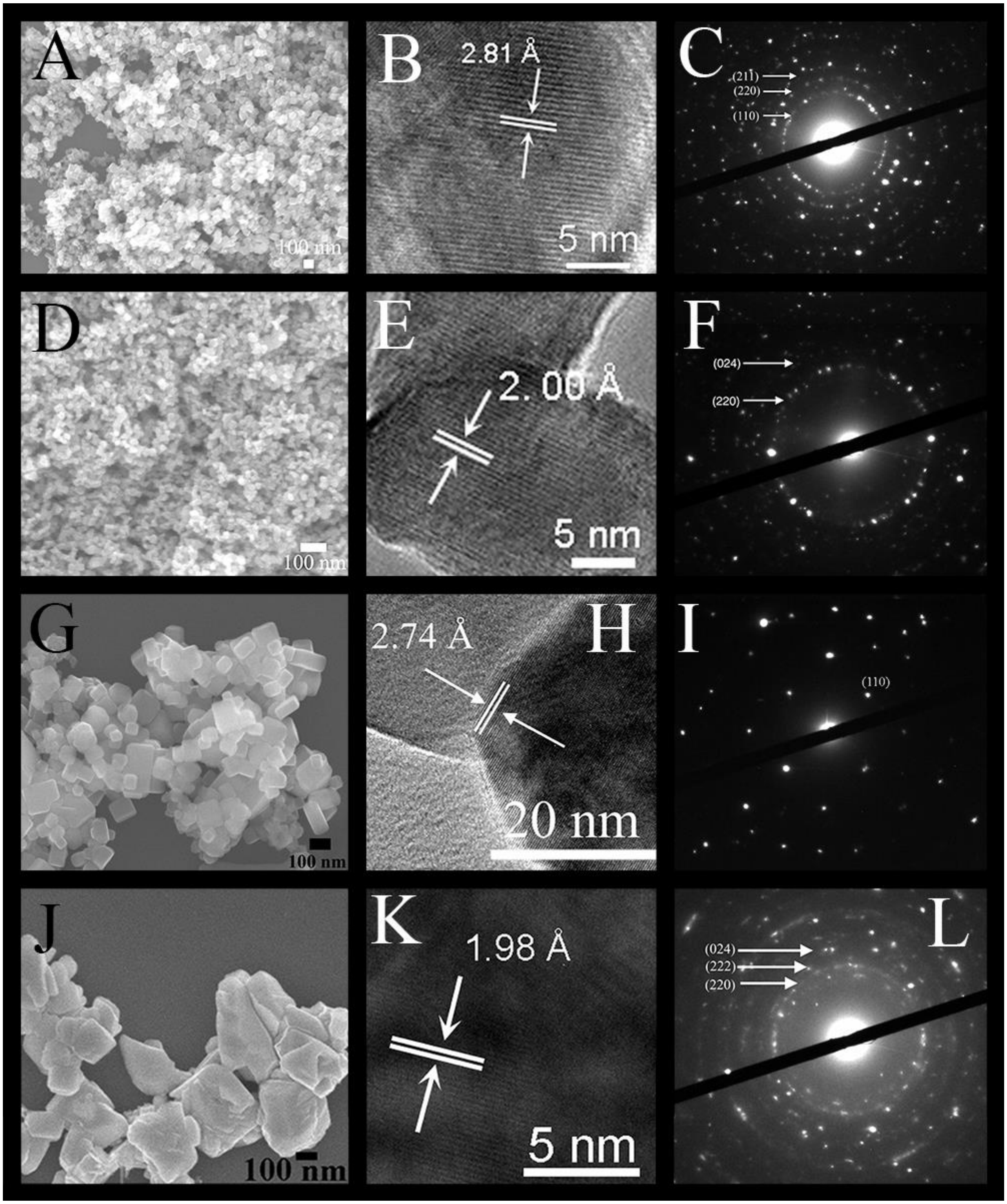

Figure 5.3. Representative SEM images (A, D, G, J), higher magnification HRTEM images with the measured *d*-spacings (B, E, H, K), as well as associated single area electron diffraction data (C, F, I, L) for 40.7 nm $SrTiO_3$ (A-C), 37.3 nm $SrRuO_3$ (D-F), 113 nm $SrTiO_3$ (G-I), and 146 nm $SrRuO_3$ (J-L) NPs, respectively. Reproduced by permission of The Royal Society of Chemistry.

As mentioned earlier, our TiO_2 NPs were fabricated hydrothermally, our RuO_2 NPs were generated by utilizing a sol-gel protocol, and lastly, our perovskite nanostructures were produced using both molten salt techniques as well as hydrothermal methods. Nonetheless, in spite of the variation in synthesis technique, all of our collected data are definitely consistent with the prior results in terms of morphology, degree of monodispersity and homogeneity, crystallinity, as well as chemical composition for these various systems.

The BET analyses for each of the binary metal oxide and ternary complex metal oxide materials along with their respective sizes are presented in Table 5.1. The results obtained from BET characterization are particularly significant for understanding the role and functionality of supports, since materials possessing small surface areas tend to be more prone to potentially deleterious catalyst sintering and Ostwald ripening effects. These mechanisms are responsible for the aggregation of Pt, and can thereby reduce the ECSA of the tested material, thereby ultimately decreasing the number of available sites for methanol oxidation. The measured surface areas were found to increase in the following order: 35 nm RuO_2 < 146 nm $SrRuO_3$ < 113 nm $SrTiO_3$ < 40.7 nm $SrTiO_3$ < 37.3 nm $SrRuO_3$ < 11.4 nm TiO_2. All BET values were found to be consistent with other measured BET data for each metal oxide tested herein, possessing a particular range in size, as noted from prior literature.[14, 23, 35-39] It is also important to note that the synthesis method plays an important role in controlling the overall surface area of the material.

Material	Nanoparticle Size (nm)	BET Surface Area (m^2/g)	Measured *d*-spacing (Å)	Metal Oxide Plane	Actual *d*-spacing (Å)
TiO_2	11.4 ± 2.8	129.32	3.57	(101)	3.51
RuO_2	35.0 ± 3	4.68	3.13	(110)	3.17
$SrTiO_3$	40.7 ± 0.7	29.02	2.81	(110)	2.76
$SrRuO_3$	37.3	54.49	2.00	(220)	1.96
$SrTiO_3$	113.0 ± 40	9.79	2.74	(110)	2.76
$SrRuO_3$	146.0 ± 49	11.43	1.98	(220)	1.96

Table 5.1. Table highlighting the perovskite material, the average measured diameters (nm), the Brunauer–Emmett–Teller (BET) measurements, the measured *d*-spacings (Å) as well as the corresponding lattice planes, in addition to the actual, expected *d*-spacings (Å) associated with these lattice planes. Reproduced by permission of The Royal Society of Chemistry.

5.2.2. Characterization of our Various Metal Oxide and Perovskite Metal Oxide Support Materials after Pt Deposition

The deposition of Pt NPs onto the various metal oxide and perovskite supports was initiated using a $NaBH_4$ reduction method. Therefore, in order to evaluate the optimal Pt loading for methanol oxidation in an H_2SO_4 electrolyte, a systematic series of Pt NPs immobilized onto a TiO_2 support (used as a control) with various mass loadings was tested. As others have previously noted, an optimal Pt mass loading of 50% generated the highest level of MOR activity discerned, with no significant additional increase after 50% loading.[29] Therefore, with the need to utilize the least amount of Pt possible without impacting upon the observed performance, a 50% Pt mass loading was used for each electrocatalyst sample tested. Additionally, based upon the HRTEM results highlighted in Figure 5.4 (which will be described in more detail below), a generally uniform spatial distribution of NPs evenly dispersed onto the underlying metal oxide surface was observed.

HRTEM images of the various metal oxide samples prepared after Pt deposition are shown in Figure 5.4. The Pt NPs possess a rather uniform average particle diameter, ranging from 2-4 nm, for each and every sample analyzed with a relatively homogeneous distribution, as mentioned above. The *d*-spacings corresponding to both the Pt and the metal oxide support for each material, respectively, have been indexed. Table 5.2 incorporates data on the various measured *d*-spacings and the corresponding planes for both the metal oxide substrate as well as the overlying Pt NPs.

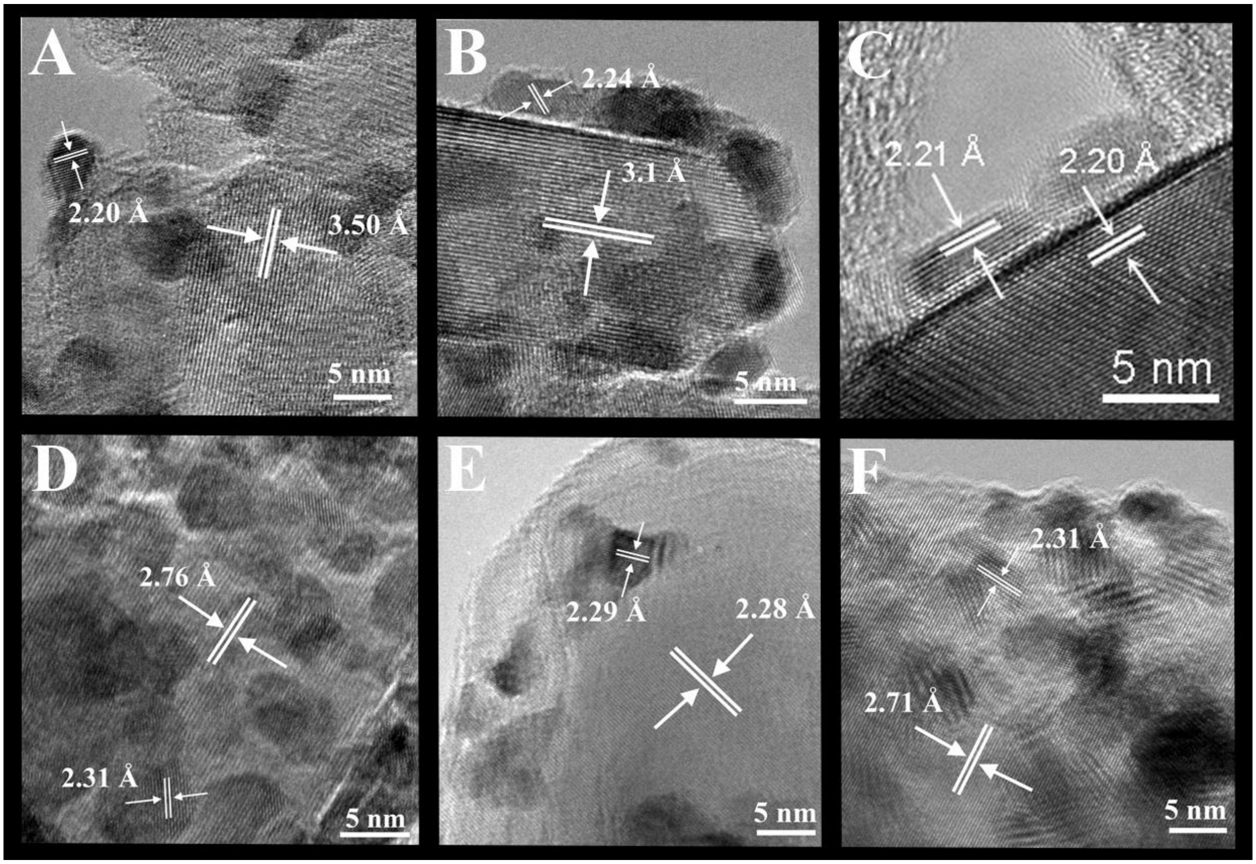

Figure 5.4. Representative high-resolution TEM micrographs with measured *d*-spacings, corresponding to both the Pt NPs and the corresponding supports for (A) Pt/TiO_2 NPs (11.4 nm), (B) Pt/RuO_2 NPs (35 nm), (C) Pt/$SrTiO_3$ NPs (40.7 nm), (D) Pt/$SrRuO_3$ NPs (37.3 nm), (E) Pt/$SrTiO_3$ NPs (113 nm), and (F) Pt/$SrRuO_3$ NPs (146 nm), respectively. Reproduced by permission of The Royal Society of Chemistry.

Overall, all of the measured *d*-spacings can be assigned to the expected crystallographic structures for each of the samples, with the Pt (111) facet noted as the most predominantly exposed facet observed for the adsorbed particles. It should also be mentioned that for both of the analyzed samples incorporating $SrRuO_3$ supports, we observed a ~2% increase in their corresponding Pt *d*-spacings. Although these values fall within the error of the measurement, the increases could also be plausibly attributed to the presence of tension strain imparted onto Pt by the presence of the underlying substrate materials, thereby resulting in an expansion of the Pt lattices, a scenario which has been previously shown to improve methanol oxidation activity.[40] Additionally, SAED patterns possessing rings attributed to both the metal oxides as well as to the Pt NPs present can be found in Figure 5.5.

Support Material	Measured *d*-spacing (Å)	Metal Oxide Plane	Measured Pt *d*-spacing (Å)	Pt Plane
TiO_2 (11.4 nm)	3.50	(101)	2.20	(111)
RuO_2 (35 nm)	3.10	(110)	2.24	(111)
$SrTiO_3$ (40.7 nm)	2.20	(200)	2.21	(111)
$SrRuO_3$ (37.3 nm)	2.76	(020)	2.31	(111)
$SrTiO_3$ (113 nm)	2.28	(111)	2.29	(111)
$SrRuO_3$ (146 nm)	2.71	(020)	2.31	(111)

Table 5.2. Table associated with Figure 5.4, corresponding to the measured *d*-spacings (Å) and lattice planes of various Pt/metal oxide species, incorporating both binary and ternary perovskite oxide materials. Reproduced by permission of The Royal Society of Chemistry.

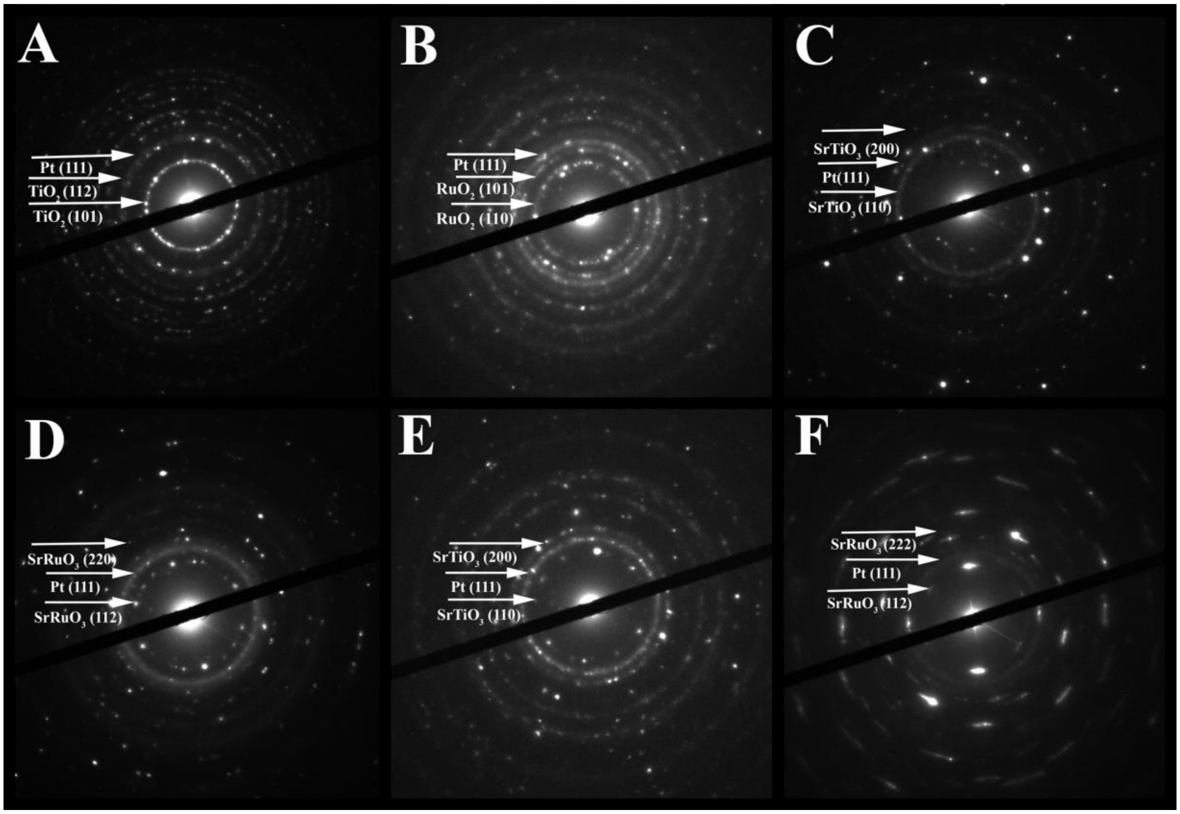

Figure 5.5. Single area electron diffraction patterns of (A) Pt/TiO_2 NPs (11.4 nm), (B) Pt/RuO_2 NPs (35 nm), (C) Pt/$SrTiO_3$ NPs (40.7 nm), (D) Pt/$SrRuO_3$ NPs (37.3 nm), (E) Pt/$SrTiO_3$ NPs (113 nm), and (F) Pt/$SrRuO_3$ NPs (146 nm), respectively. Reproduced by permission of The Royal Society of Chemistry.

5.2.3. Electrochemical Activity of our Metal Oxide and Perovskite Support Materials

Cyclic voltammograms collected in argon-saturated 0.1 M H_2SO_4 electrolyte can be found in Figure 5.6. It is worth remarking that CVs collected on the RuO_2 substrate (Figure 5.5B) in sulfuric acid electrolyte has exhibited similar peak profiles, which others have attributed to the presence of hydroxyl groups.[41, 42] Specifically, these CVs imply that the Ru-containing substrates gives rise to apparent oxygen adsorption features (Figures 5.5B, D, F) whereas there is no evidence for oxygen adsorption in the analogous Ti-containing support data (Figures 5.5A, C, E).

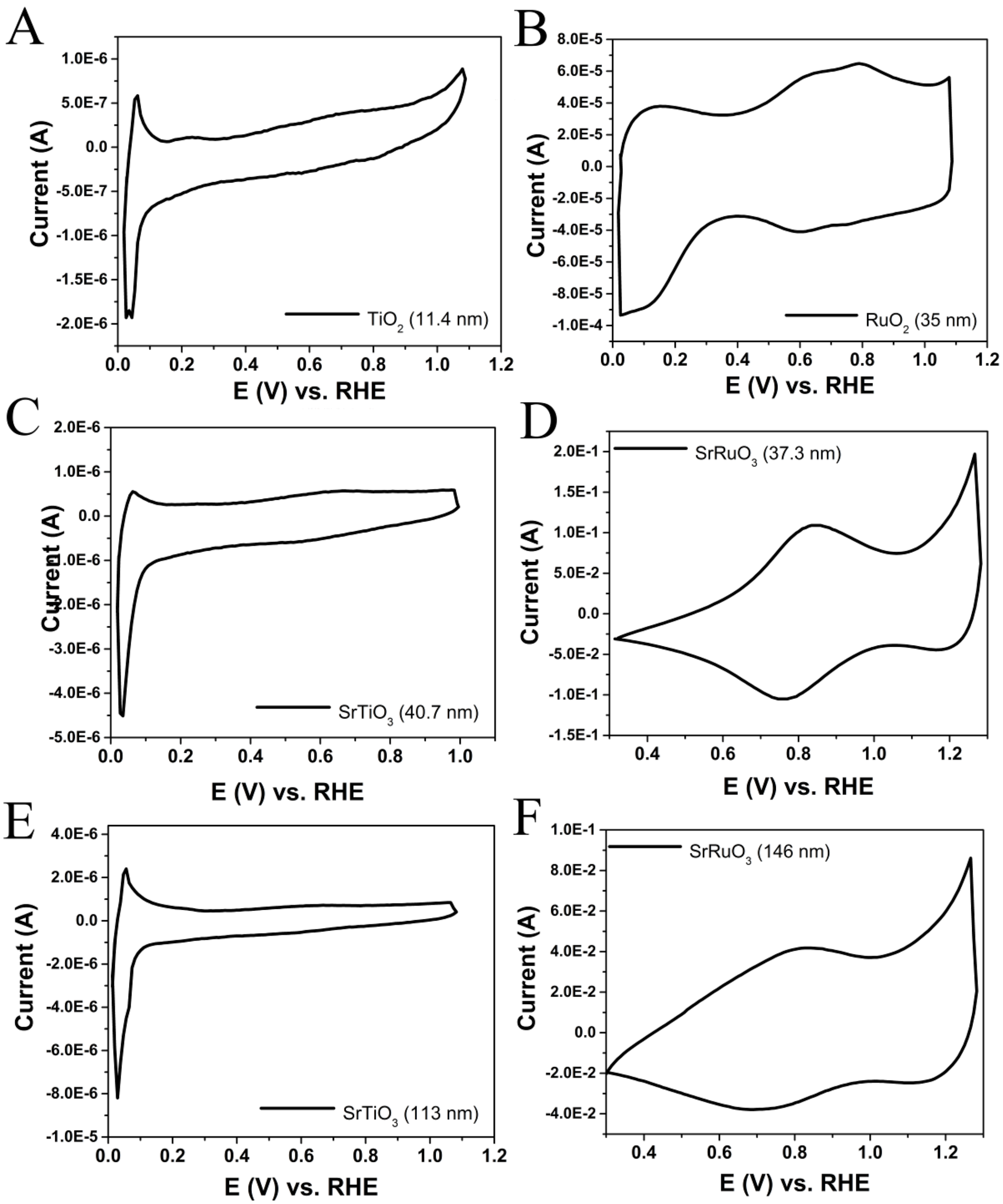

Figure 5.6. Cyclic voltammograms in an argon-saturated 0.1 M H_2SO_4 solution, obtained at a scan rate of 20 mV/s for (A) TiO_2 NPs (11.4 nm), (B) RuO_2 NPs (35 nm), (C) $SrTiO_3$ NPs (40.7 nm), (D) $SrRuO_3$ NPs (37.3 nm), (E) $SrTiO_3$ NPs (113 nm), and (F) $SrRuO_3$ NPs (146 nm), respectively. Reproduced by permission of The Royal Society of Chemistry.

The methanol oxidation reaction activity of the various metal oxide support materials was probed using cyclic voltammetry in a 0.1 M H_2SO_4 solution containing 0.5 M methanol (Figure 5.7). The collected CVs indicate that the bare $SrTiO_3$ substrates evinced noticeably higher MOR activities as compared with other analogous substrates, including Ru-based support materials due to the presence of the anodic current apparent during the negative sweep. The decreased activity of the Ru-containing substrates may be attributed in part to the increased amount of adsorbed hydroxyl species, inhibiting the adsorption and subsequent oxidation of methanol. This assertion is consistent with the nature of the CVs collected prior to methanol oxidation. It is worth noting that although the $SrRuO_3$ supports do not demonstrate an improved MOR activity as compared with analogous $SrTiO_3$ substrates, the addition of Pt NPs should generate Pt-Ru pair sites that will be highly beneficial towards enhancing methanol oxidation activity.

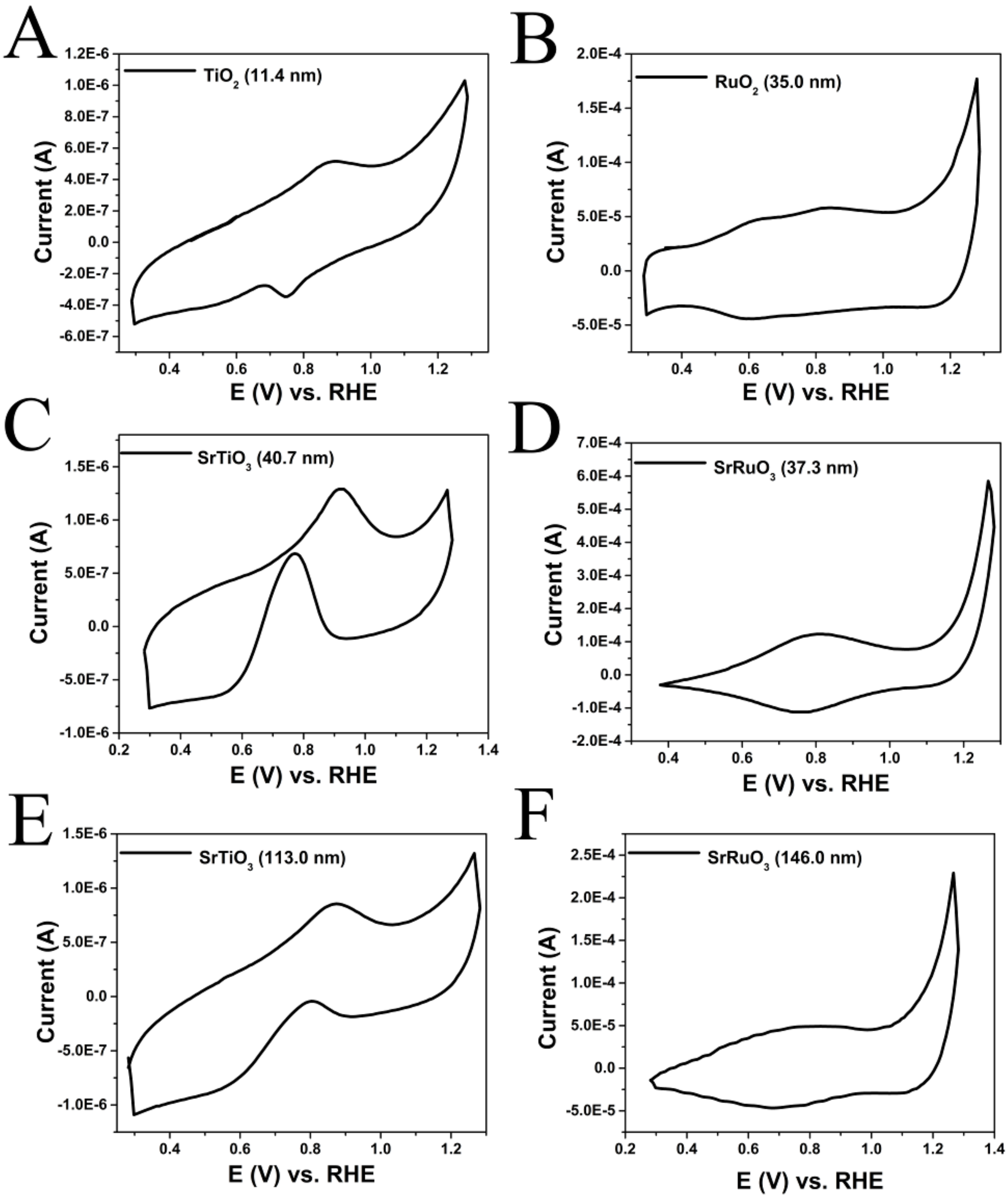

Figure 5.7. Cyclic voltammograms associated with the methanol oxidation reaction in an argon-saturated 0.1 M H_2SO_4 + 0.5 M MeOH solution, obtained at a scan rate of 20 mV/s for (A) 11.4 nm TiO_2 NPs, (B) 35 nm RuO_2 NPs, (C) 40.7 nm $SrTiO_3$ NPs, (D) 37.3 nm $SrRuO_3$ NPs, (E) 113 nm $SrTiO_3$ NPs, and (F) 146 nm $SrRuO_3$ NPs, respectively. Reproduced by permission of The Royal Society of Chemistry.

The overall stability of each of the catalyst support materials has been evaluated and is depicted in Figure 5.8. Specifically, the degree of stability has been tested by cycling each material for 1000 cycles at 250 mV/s in an 0.1 M H_2SO_4 electrolyte in order to evaluate the change in available surface sites as well as in the corresponding electrochemical activity. In particular, the TiO_2, RuO_2, and $SrTiO_3$ samples evince reasonable stability over 1000 cycles, as can be concluded by the reproducible nature of the curves at cycle 1 versus cycle 999. However, an increase in activity is seen with both of the $SrRuO_3$ samples tested. In order to determine the cause for this increase, a TEM analysis of these two samples, post cycling, can be seen in Figure 5.9, and the $SrTiO_3$ samples analyzed measure 38.1 ± 3.9 nm and 194.8 ± 22.6 nm, respectively . Based on these images, it can be observed that the surfaces of both of these $SrRuO_3$ samples are becoming more perceptibly roughened as opposed to experiencing any appreciable change in either size or intrinsic morphology. Therefore, this apparent increase in activity for both $SrRuO_3$ samples can likely be ascribed to the formation of new Ru-O active sites that possess lower coordination numbers and are hence more catalytically active. Hence, on the basis of all of these data, our samples appear to be stable without a distinctive alteration in either size or morphology.

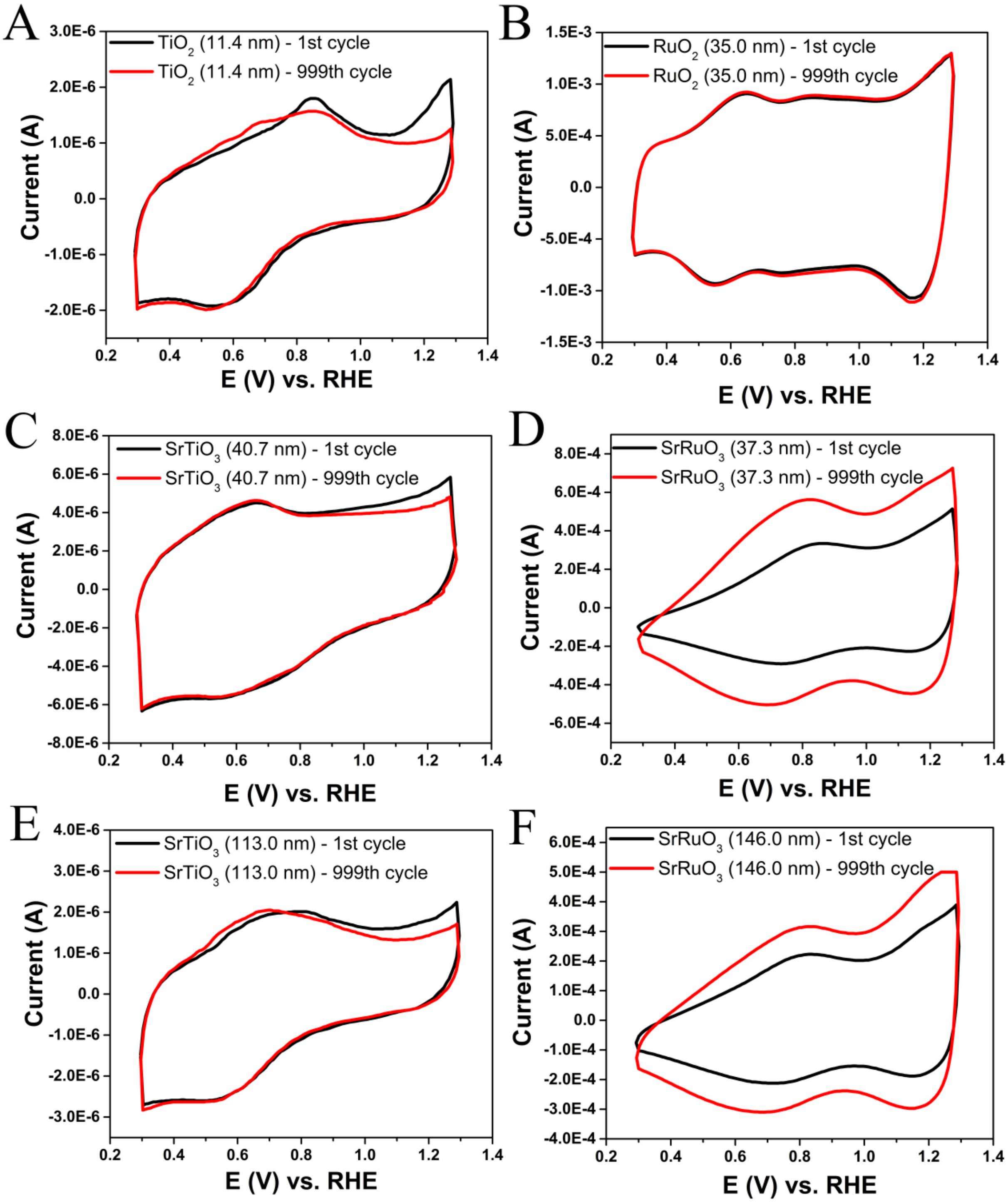

Figure 5.8. Cyclic voltammograms obtained in an argon-saturated 0.1 M H_2SO_4 solution and collected at a scan rate of 250 mV/s for 1000 cycles (only the first and last are included) for (A) 11.4 nm TiO_2 NPs, (B) 35 nm RuO_2 NPs, (C) 40.7 nm $SrTiO_3$ NPs, (D) 37.3 nm $SrRuO_3$ NPs, (E) 113 nm $SrTiO_3$ NPs, and (F) 146 nm $SrRuO_3$ NPs, respectively. Reproduced by permission of The Royal Society of Chemistry.

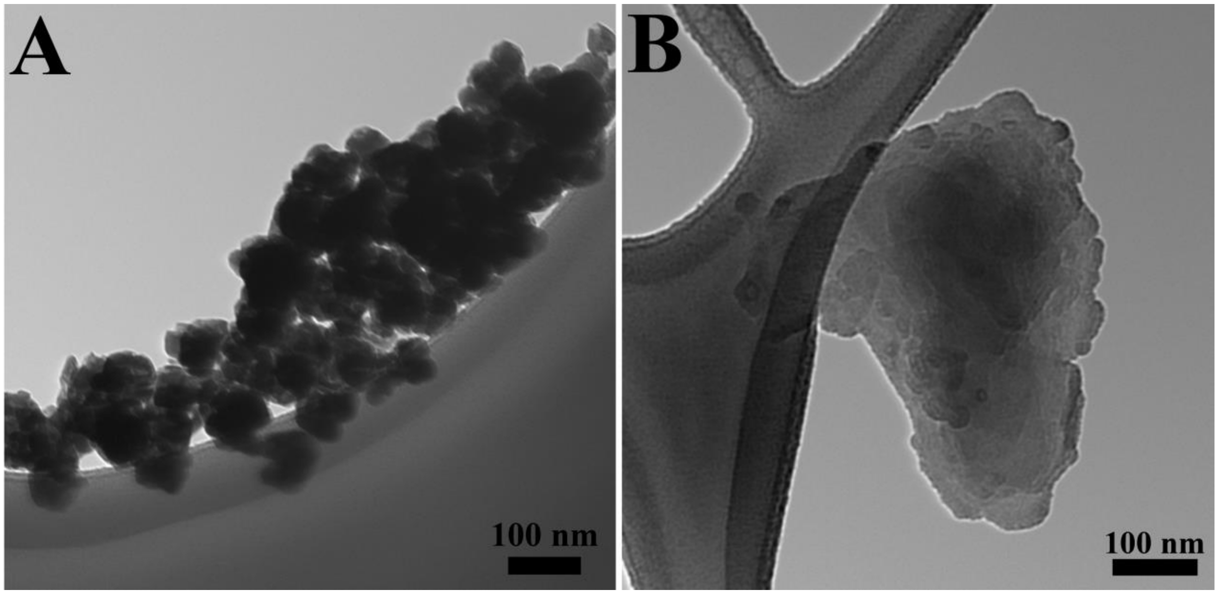

Figure 5.9. TEM images of (A) $SrRuO_3$ NPs (37.3 nm), and of (B) $SrRuO_3$ NPs (146 nm), post stability testing, respectively. Reproduced by permission of The Royal Society of Chemistry.

5.2.4. Electrochemical Activity of our Metal Oxide and Perovskite Support Materials after Pt Deposition

In order to assess the electrochemical activity of our materials after Pt deposition, as shown in Figure 5.10, CVs were collected for each material in 0.1 M H_2SO_4, in order to investigate and correlate the impact of the support materials with the overall electrochemical performance.

Regarding the substructure of the CVs, the shape and location of the observed hydrogen and oxygen adsorption features associated with the Pt/TiO_2 sample are consistent with prior reports.[43] Moreover, the Pt/$SrTiO_3$ samples evince similar attributes to those observed for Pt itself. Interestingly, the peaks in both regions can be solely attributed to the Pt NPs themselves at the surface, an observation indicative of the fact that the identity of the 'A' site metal, Sr, likely does not itself contribute significantly to the adsorption of hydroxyl groups; this assertion is supported by Figure 5.6 as well as by prior reports.[23] In fact, both strontium and titanium are known to be “inactive” and electrochemically passive, since they do not possess obvious active sites for adsorption.[28, 29] By contrast, the RuO_2 and $SrRuO_3$ samples maintain peaks in the hydrogen and oxygen adsorption regions, which are similar to what has been previously observed with Pt/RuO_2 materials.[9, 44]

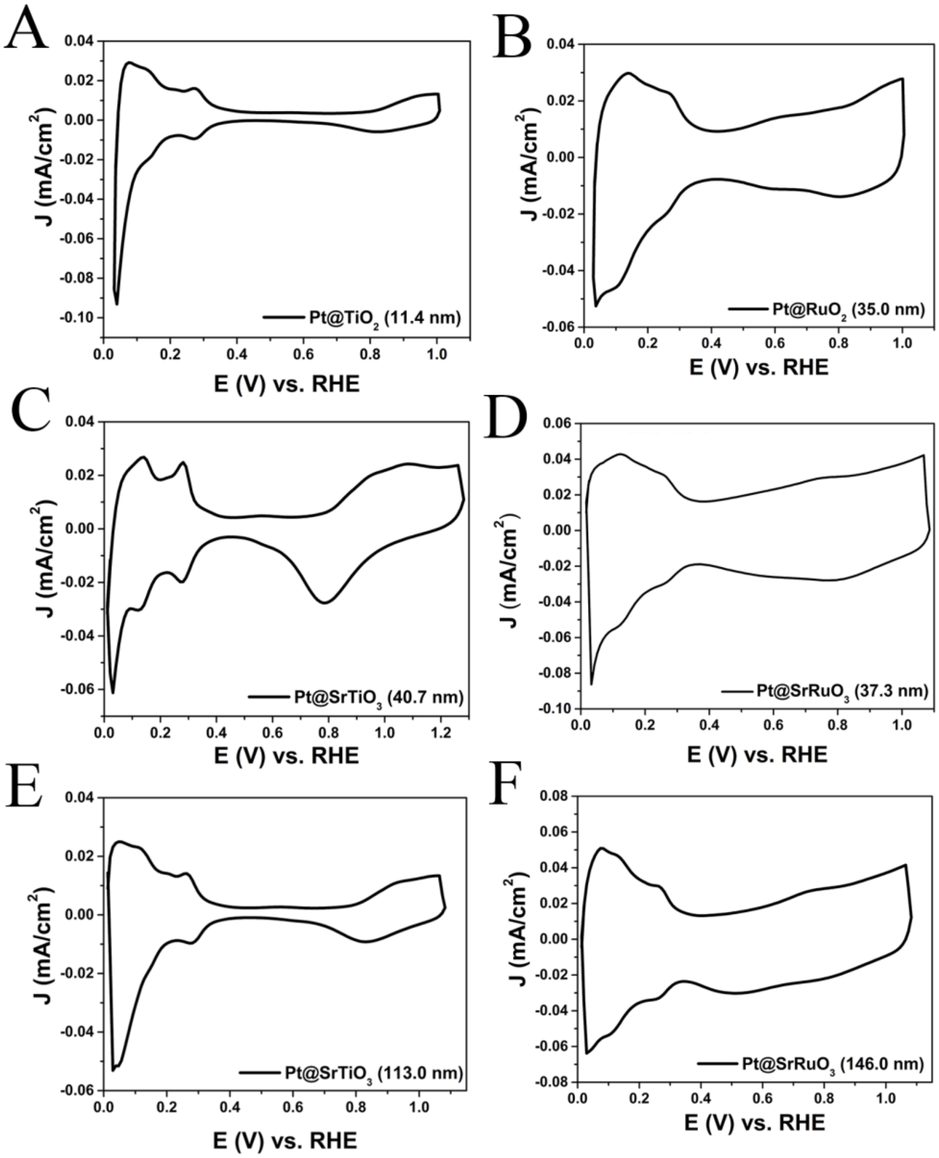

Figure 5.10. Representative CV curves in an argon-saturated 0.1 M H_2SO_4 solution, obtained at a scan rate of 20 mV/s with the current normalized to ECSA for (A) Pt/TiO_2 NPs (11.4 nm), (B) Pt/RuO_2 NPs (35 nm), (C) Pt/$SrTiO_3$ NPs (40.7 nm), (D) Pt/$SrRuO_3$ NPs (37.3 nm), (E) Pt/$SrTiO_3$ NPs (113 nm), and (F) Pt/$SrRuO_3$ NPs (146 nm), respectively. Reproduced by permission of The Royal Society of Chemistry.

Moreover, EELS was employed for the first time to probe the nature of the surface interactions between Pt and these metal oxide support materials in order to gain further insights into the corresponding electrochemical performance. To summarize, because there was little if any difference in the shape of EELS spectra associated with the various TiO_2, RuO_2, and $SrTiO_3$ samples either before or after Pt deposition (Figure 5.11), there was likely no apparent charge transfer in these systems that we could readily distinguish and differentiate. By contrast, both of the $SrRuO_3$ samples gave rise to a suppression of the Ru M_4 edge, in particular after Pt NP coverage, as can be observed in Figure 5.12.[45] This reduction in the Ru M_4 signal, associated with the Ru 4*p* orbitals, is evident and noticeable, and is likely indicative of electron acceptor behavior. This signal suppression would infer that electron transfer is occurring from Pt to Ru within the $SrRuO_3$ support material, and, as a result, there is a decrease in the number of Pt electrons available, as previously demonstrated by prior reports.[46-48]

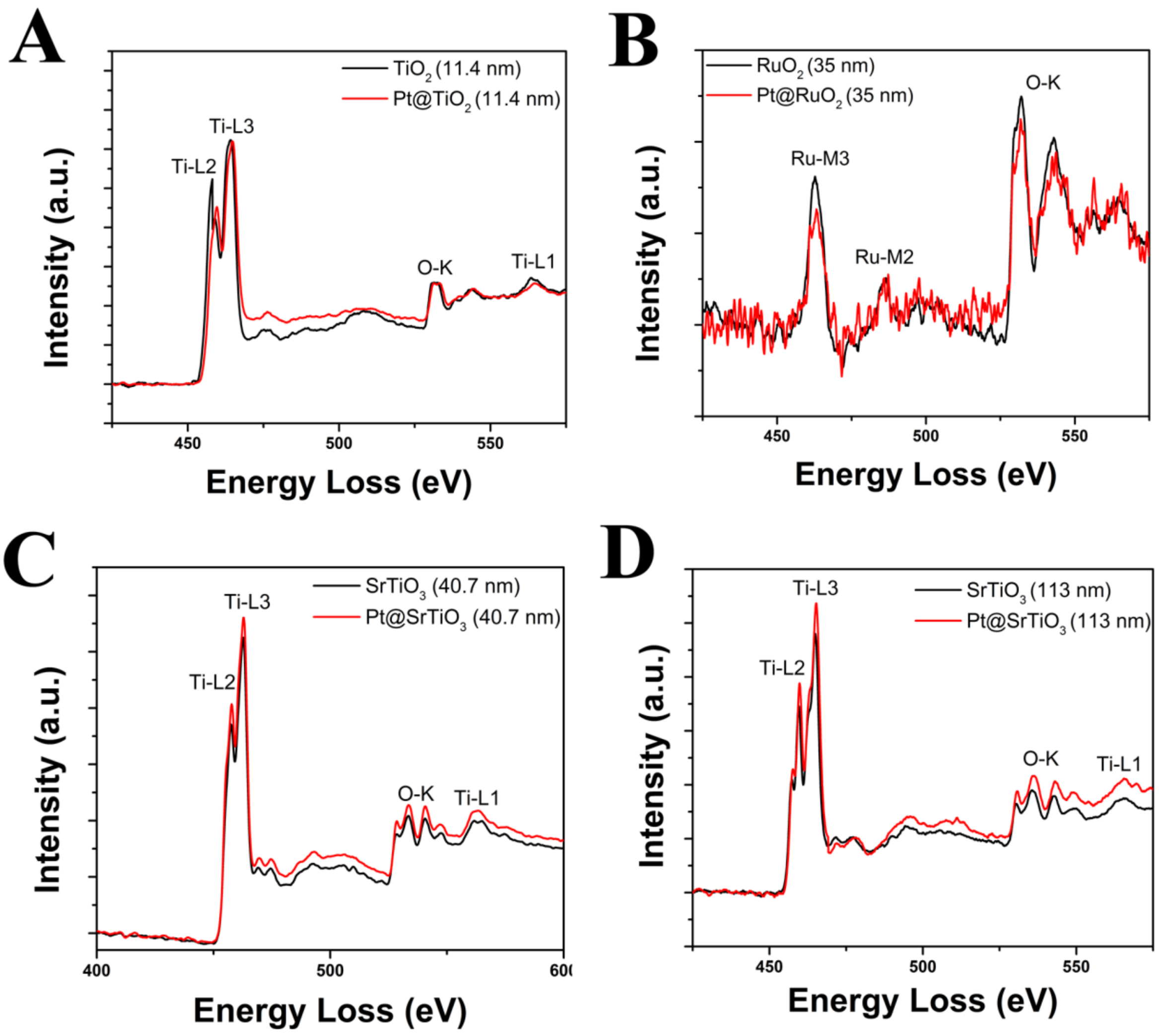

Figure 5.11. Electron energy loss spectra of (A) TiO_2 (red) and Pt/TiO_2 (black) (11.4 nm), (B) RuO_2 (red) and Pt/RuO_2 (black) (35 nm), (C) $SrTiO_3$ (black) and Pt/$SrTiO_3$ (40.7 nm) (red), and (D) $SrTiO_3$ (black) and Pt/$SrTiO_3$ (red) (113 nm), respectively. Reproduced by permission of The Royal Society of Chemistry.

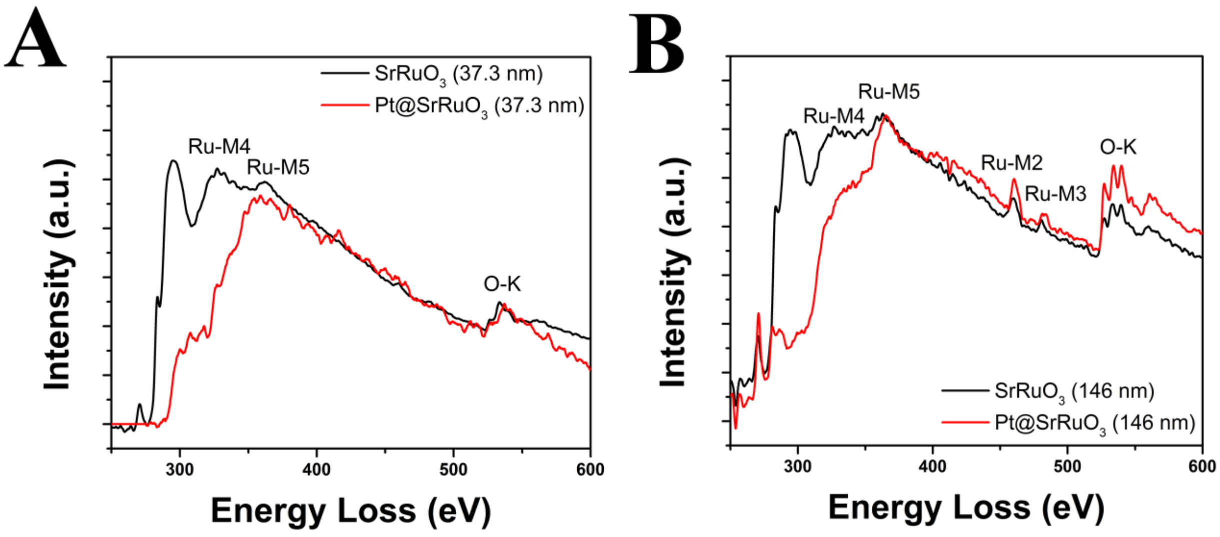

Figure 5.12. Electron energy loss spectra for the series of (A) $SrRuO_3$ (37.3 nm) vs. Pt/$SrRuO_3$ (37.3 nm) and for the corresponding series of (B) $SrRuO_3$ (146 nm) vs. Pt/$SrRuO_3$ (146 nm) samples, respectively. Peaks presented below 300 eV represent the Carbon *K* edge peaks associated with the underlying carbonaceous TEM grid. Reproduced by permission of The Royal Society of Chemistry.

Ultimately, this situation would not only lead to a decrease in the amount of poisonous species potentially blocking Pt active sites but also allow for increased methanol adsorption at these Pt active sites. One group[22] noted that, after Pt deposition onto a $SrRuO_3$ substrate, Pt was likely oxidized to Pt^{+2} from a neutral Pt^0 state, thereby further supporting our EELS-derived notion that the presence of an oxidized Pt species is necessary for high alcohol oxidation activity. It should be noted that the Pt^0 was not likely to have been completely oxidized to the Pt^{+4} state, since the latter species is known to be ineffective at promoting methanol oxidation.[49]

To further probe the nature of the electron transfer from Pt, XPS (Figure 5.13) was used to more closely examine the Pt *4f* region in order to confirm the postulated presence of electron donation from Pt to Ru. The Pt *4f* region contains two peaks, consisting of low energy band ($4f_{7/2}$) and high energy band ($4f_{5/2}$) regions. As noted in Figure 5.13, upshifts in the $4f_{7/2}$ band energy are detected upon deposition of Pt onto both of the $SrRuO_3$ supports tested (i.e. +600 meV and +1.6 eV for the 146 nm $SrRuO_3$ and 37.3 nm $SrRuO_3$ supports, respectively), as compared with a control support of Pt/C itself. This upshift would indicate a loss of electron density within the Pt *4f* region.[50, 51] This result not only supports our EELS findings that electron transfer is indeed occurring from the Pt *4f* to the Ru *4p* orbitals but also corroborates the presence of a metal support interaction between the Pt NPs and the underlying $SrRuO_3$ support.

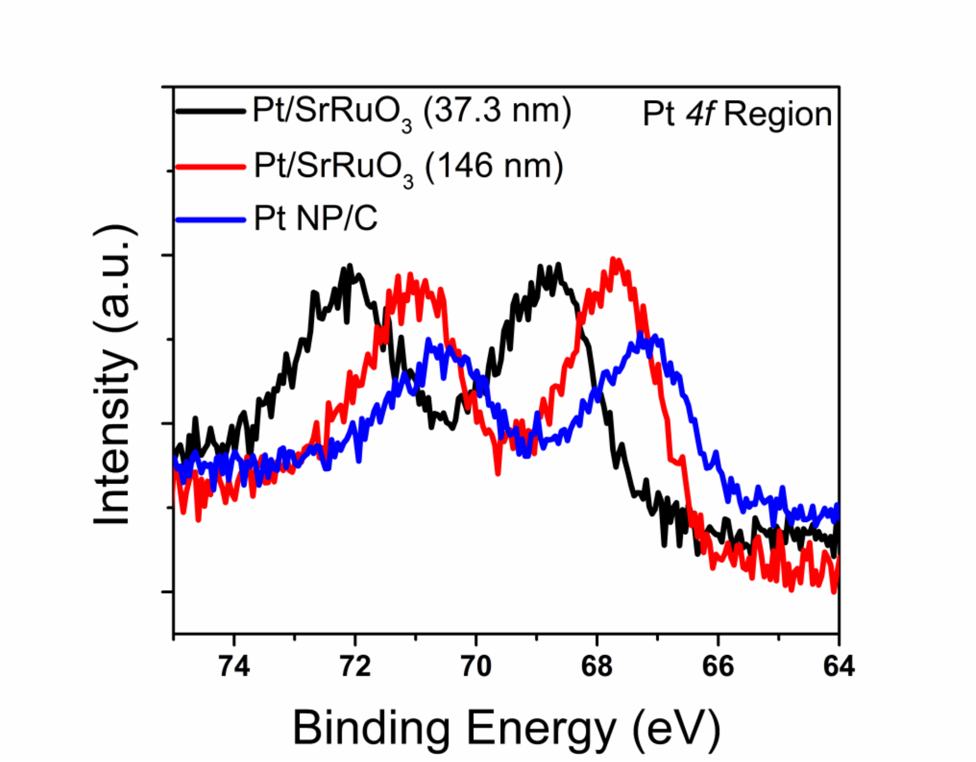

Figure 5.13. XPS spectra associated with the Pt *4f* region for Pt/C, $Pt/SrRuO_3$ (37.3 nm), and $Pt/SrRuO_3$ (146 nm), respectively. A significant upshift is observed when Pt is deposited on both $SrRuO_3$ surfaces as compared with conventional carbon. Reproduced by permission of The Royal Society of Chemistry.

In order to evaluate the methanol oxidation ability of the materials, LSVs are included in Figure 5.14A. The corresponding activities of the various materials probed at 0.55 V vs. RHE are summarized in the bar graph in Figure 5.14B. A complementary set of activities measured at 0.7 V vs. RHE is highlighted in Table 5.3. Specifically, the $Pt/SrRuO_3$ (average diameter of 37.3 nm) sample achieved the highest activity of 1.42 mA/cm^2 with the larger $Pt/SrRuO_3$ sample (average diameter of 146 nm), possessing an activity of 0.57 mA/cm^2, with data on both systems collected at 0.7 V vs. RHE. These measured activities are consistent with the trend in the surface areas of the underlying support materials (Table 5.1). In particular, the higher the surface area, the more uniform the dispersion of Pt, and hence, the more active sites available for methanol oxidation. A similar trend was observed for the 2 sizes of $SrTiO_3$ samples produced with the electrochemical data taken at a slightly higher potential (0.9 V vs. RHE). In this case, Pt/$SrTiO_3$ (average diameter of 40.4 nm) gave rise to a peak activity of 0.82 mA/cm^2, whereas the larger sample, i.e. Pt/$SrTiO_3$ (average diameter of 113 nm), yielded a peak activity of 0.75 mA/cm^2.

It is worth pointing out that even though bare $SrTiO_3$ substrates were indeed more active for methanol oxidation as compared with their uncoated $SrRuO_3$ analogues, the presence of Pt-Ru pair sites created after Pt deposition significantly increased the methanol oxidation activity observed in the presence of $SrRuO_3$. This observation further corroborates the existence of favorable metal-support interactions, facilitated and engendered by the use of $SrRuO_3$ as the support material, an idea which is further reinforced by the EELS/XPS confirmation of electron transfer between the Pt catalyst and the underlying $SrRuO_3$ support material.

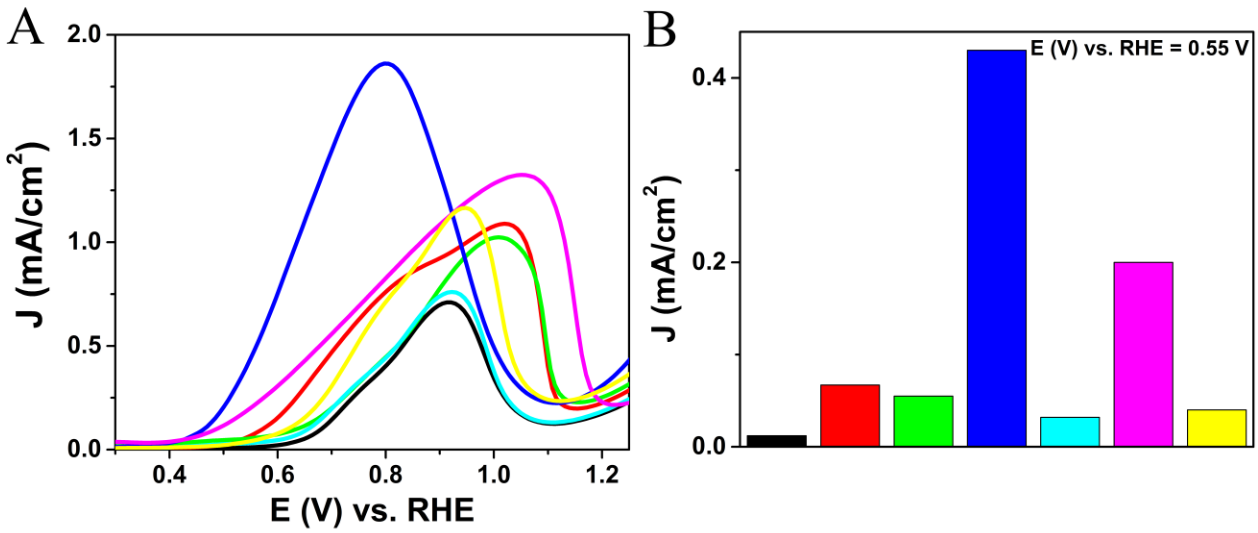

Figure 5.14. (A) Cyclic voltammograms for the methanol oxidation reaction in an argon-saturated 0.1 M H_2SO_4 + 0.5 M MeOH solution, for Pt/TiO_2 NPs (11.4 nm) (black), Pt/RuO_2 NPs (35 nm) (red), Pt/$SrTiO_3$ NPs (40.7 nm) (green), Pt/$SrRuO_3$ NPs (37.3 nm) (blue), Pt/$SrTiO_3$ NPs (113 nm) (cyan), and Pt/$SrRuO_3$ NPs (146 nm) (magenta), respectively, as compared with commercial standards (i.e. Pt NP/C) (yellow), obtained at a scan rate of 20 mV/s with the current normalized to ECSA. (B) Bar graph highlighting the MOR activity data obtained at E (V) vs. RHE = 0.55 V for Pt/TiO_2 NPs (11.4 nm) (black), Pt/RuO_2 NPs (35 nm) (red), Pt/$SrTiO_3$ NPs (40.7 nm) (green), Pt/$SrRuO_3$ NPs (37.3 nm) (blue), Pt/$SrTiO_3$ NPs (113 nm) (cyan), and Pt/$SrRuO_3$ NPs (146 nm) (magenta), respectively, as compared with commercial standards (i.e. Pt NP/C) (yellow). Reproduced by permission of The Royal Society of Chemistry.

By analyzing the onset region of Figure 5.14A, it is apparent that both Pt/$SrRuO_3$ (average diameter of 37.3 nm) and Pt/$SrRuO_3$ (average diameter of 146 nm) maintain very similar onset potentials, i.e. 0.43 V and 0.45 V vs. RHE, respectively. A comparable proximity in onset potentials was also observed for both Pt/$SrTiO_3$ (avg. diameter of 40.7 nm) and Pt/$SrTiO_3$ (avg. diameter of 113 nm) samples; in fact, we measured an onset potential of 0.63 V vs. RHE for both systems. These observations would indicate that the *chemical composition* as opposed to the size of the support is the more significant determinant of the onset potential. As such, it is evident that the use of the Ru-containing supports gave rise to lower onset potentials as compared with those supports containing Ti. Hence, the improvements observed for the Ru-containing substrates as compared with Ti-rich supports would imply that the former are more active for methanol oxidation. Significantly, we emphasize that our data were obtained in the absence of carbon additives, thereby rendering our metal oxide systems as important, relevant, and viable alternatives to the use of conventional carbon black.

Previous studies on the use of Pt/$SrRuO_3$ towards methanol oxidation have implied that the Ru-O surface sites likely play an important role in not only removing CO from Pt active sites but also contributing to the efficacy of methanol oxidation, as was previously shown.[22] In support of this hypothesis, it has been claimed that the increased localized presence of tetravalent Ru species at the surface within $La_{0.7}Sr_{0.3}Cr_xRu_{1-x}O_3$ can significantly contribute to the increased oxidation of CO at Pt active sites.[52] All of these previous results would collectively suggest that the presence of Ru is a positive driving force for increased MOR activity, while the intrinsic perovskite structure enhances the overall stability of the support itself. Based on our results, a slight shift in the MOR onset potential can be seen between the Pt/$SrTiO_3$ samples and the corresponding Pt/TiO_2 control, an observation which would further support the notion that perovskite materials can adsorb hydroxyl groups at their external surfaces in order to facilitate the methanol oxidation process. However, by contrast with Ru, the Pt/TiO_2 and Pt/$SrTiO_3$ samples possess similar peak MOR activities, which would indicate an inability of both Sr and Ti to contribute to the methanol oxidation itself. Previous reports[27] have postulated that the A site within a perovskite structure may actually contribute to the stability of the B site metal as opposed to actively participating in the methanol oxidation reaction itself, thereby further reinforcing our claims herein.

In Figure 5.15, we have attempted to correlate the methanol oxidation activity with the Pt ECSA values associated with the various supports. Specifically, when comparing the $SrRuO_3$ (146 nm) sample, which maintains an ECSA value of 3.35 cm^2, with the analogous $SrTiO_3$ (113 nm) sample, which possesses an ECSA amount of 4.31 cm^2, a higher activity was noted with the former Ru-containing support. It can be inferred that since the Pt ECSA associated with $SrRuO_3$ is actually less than the corresponding ECSA value assigned to $SrTiO_3$, the observed enhancement in methanol oxidation activity with $SrRuO_3$ must be a result of other effects. Therefore, one plausible explanation accounting for our observations with our Pt/$SrRuO_3$ samples would be electron transfer from immobilized Pt NPs to the underlying Ru-containing support, as highlighted by the EELS and XPS analysis shown in Figures 5.11 and 5.12, respectively.

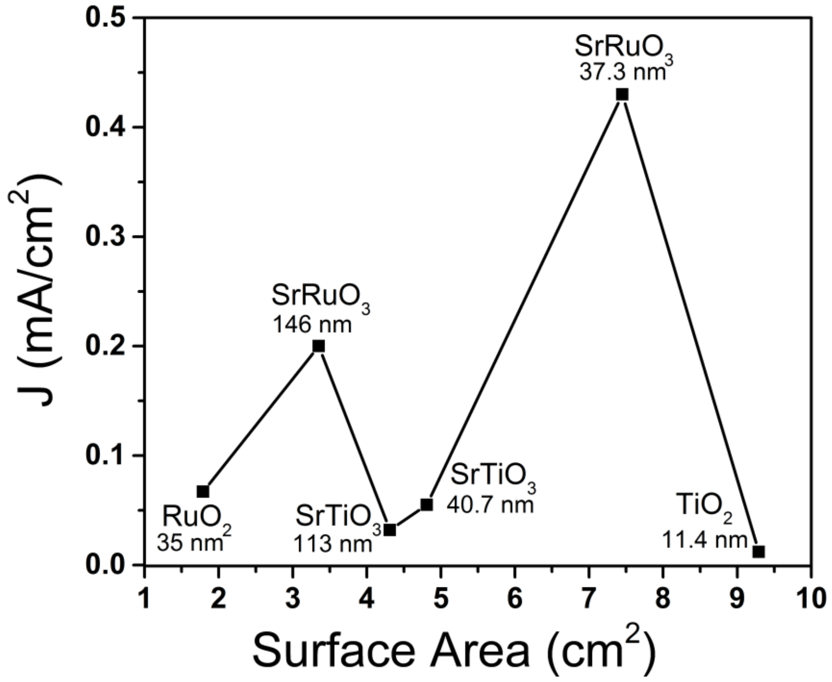

Figure 5.15. Methanol oxidation activity (mA/cm^2) at 0.55 V as a function of Pt electrochemically active surface area (cm^2) for the various Pt/metal oxide catalysts. Reproduced by permission of The Royal Society of Chemistry.

When the inherent support size is reduced to an even smaller scale, an increase in both activity as well as ECSA can be observed. Specifically, when comparing the data associated with the $SrRuO_3$ (37.3 nm) and analogous $SrTiO_3$ (40.7 nm) substrates, the corresponding ESCA values are 7.45 cm^2 and 4.81 cm^2 for $SrRuO_3$ and $SrTiO_3$, respectively. A dramatic increase in activity was noted for $SrRuO_3$, even though the two substrates are comparable in size. Yet, it is unlikely that this performance enhancement could be solely attributed to the greater Pt ECSA value for $SrRuO_3$. Rather, it is plausible that the electronic effects associated with Pt interactions with the underlying $SrRuO_3$ support might also have contributed to the observed result.

The Pt ECSA values of $SrRuO_3$ (146 nm) and $SrRuO_3$ (37.3 nm) are 3.35 and 7.45 cm^2, respectively. In this case, we note that there is a direct correlation between the measured ESCA data and the resulting electrochemical activity measured; specifically, the higher the ESCA, the better the electrochemical performance. Therefore, since similar types of electronic effects and interactions are likely present within both samples, the higher activity ascribed to the smaller 37.3 nm $SrRuO_3$ support would likely be due to its increased Pt ECSA value as compared with the corresponding value for the larger analogous support material. To summarize, our data highlight the fact that the resulting observed electrochemical activity data can be ascribed to a combination not only of the Pt ECSA values but also of the electronic effects induced by the perovksite oxide support onto the immobilized Pt nanoparticles.

In order to evaluate the MOR mechanism responsible for the activity of our best catalyst, namely Pt/$SrRuO_3$ (37.3 nm), Tafel plots were collected at potentials between 0.4 and 0.75 V vs. RHE at a scanning rate of 1 mV s^{-1}. The data are shown in Figure 5.16. In effect, our high-performance system achieved a Tafel slope of 0.112 V/decade, which correlates well with the theoretical value expected of Pt (0.118 V/decade) for a one-electron transfer process.[53-55] This one-electron transfer process is considered to be the rate-determining step within this potential window, and corresponds to the splitting of the first C-H bond of the CH_3OH molecule. A commercial Pt/C catalyst control sample tested gave rise to a Tafel slope value of 0.142 V/decade. This value is also within range of the predicted value for platinum and is similarly suggestive of a one-electron transfer process. However, the slightly smaller value attained by our 'optimal' Pt/$SrRuO_3$ catalyst would imply a beneficially more facile methanol electro-oxidation ability as compared with commercial Pt.[54] Moreover, these data further underline our claim that a metal-support interaction is essential and likely responsible for the improved MOR activity detected, when $SrRuO_3$ is employed as the support material.

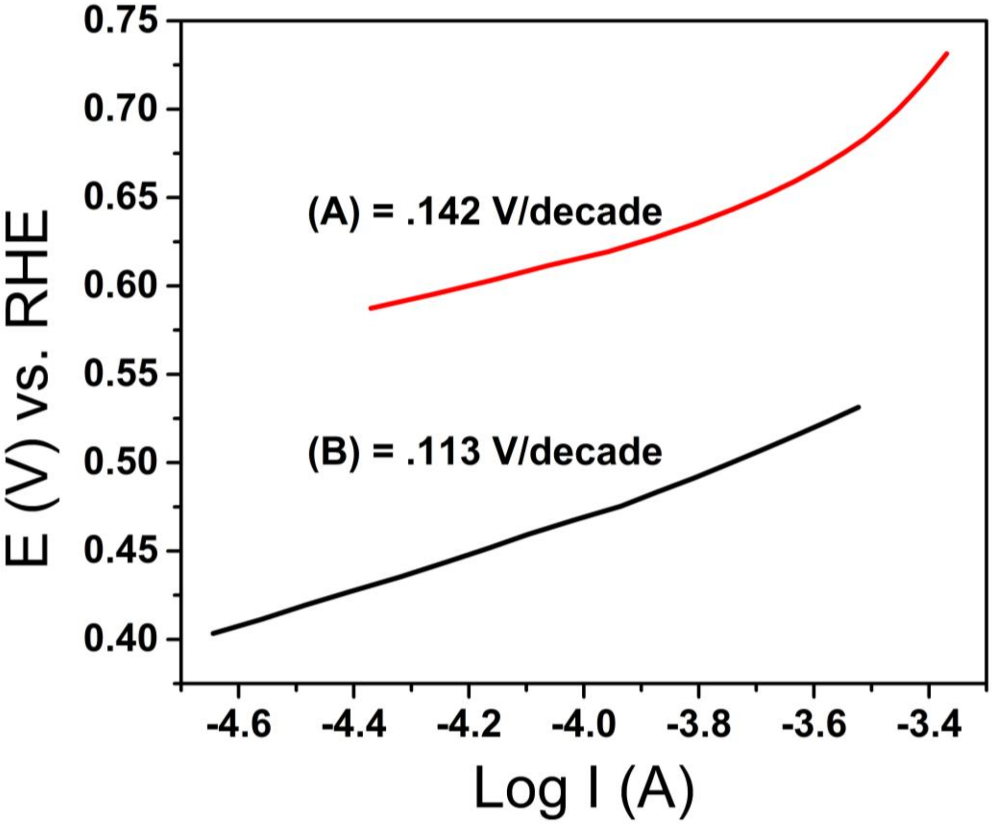

Figure 5.16. Tafel plot data of (A) commercial Pt/C and (B) Pt/$SrRuO_3$ (37.3 nm), collected between 0.4 – 0.75 V vs. RHE at a scanning rate of 1 mV/sec. Reproduced by permission of The Royal Society of Chemistry.

Chronoamperometry testing of our various Pt/metal oxide electrocatalysts is presented in Figure 5.17. The test was conducted over a period of 60 minutes at (E) vs. RHE = 0.7 V, which is located within the methanol oxidation peak current region. The dramatic initial activity loss for all electrocatalysts can be attributed to the presence of the intermediate species CO, potentially poisoning the Pt active sites.[56, 57] As noted, the Ru-containing support materials evinced the highest measured activity over the 60 minute period, with the Pt/$SrRuO_3$ (average diameter of 37.3 nm) sample and the Pt/$SrRuO_3$ (average diameter of 146 nm) sample, giving rise to steady state activities of 2.8 mA/cm^2 and 2.2 mA/cm^2, respectively. The remaining steady state activity values can be found in Table 3.

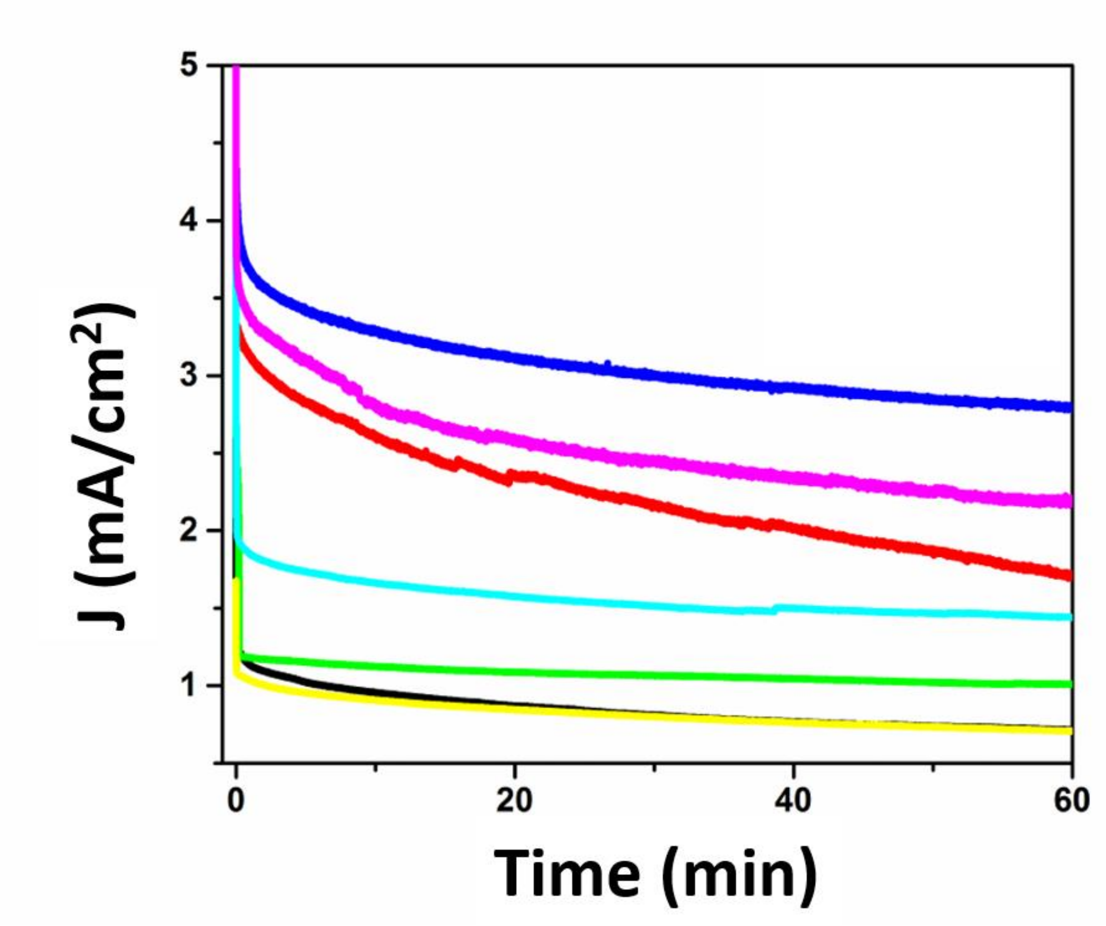

Figure 5.17. Chronoamperometry measurements of catalysts, composed of Pt/TiO_2 NPs (11.4 nm) (black), Pt/RuO_2 NPs (35 nm) (red), Pt/$SrTiO_3$ NPs (40.7 nm) (green), Pt/$SrRuO_3$ NPs (37.3 nm) (blue), Pt/$SrTiO_3$ NPs (113 nm) (cyan), and Pt/$SrRuO_3$ NPs (146 nm) (magenta), respectively, as compared with commercial standards (i.e. Pt NP/C) (yellow) in an argon-saturated 0.1 H_2SO_4 + 0.5 M CH_3OH solution, obtained at a potential of 0.7 V vs. RHE for a test period of 60 min. Reproduced by permission of The Royal Society of Chemistry.

Material	J (mA/cm^2) E(V) vs. RHE = 0.7	Steady State Current Densities after 60 min (mA/cm^2 @ E(V) vs. RHE = 0.7)
Pt/TiO_2 (11.4 nm)	0.15	0.75
Pt/RuO_2 (35 nm)	0.48	1.7
Pt/$SrTiO_3$ (40.7 nm)	0.2	1.05
Pt/$SrRuO_3$ 37.3 nm)	1.42	2.8
Pt/$SrTiO_3$ (113 nm)	0.2	1.5
Pt/$SrRuO_3$ (146 nm)	0.57	2.2
Commercial Pt/C	0.31	0.7

Table 5.3. Table consisting of measured MOR activities (mA/cm^2) and steady state current densities (mA/cm^2), obtained after 60 minutes, for various series of catalyst materials. Reproduced by permission of The Royal Society of Chemistry.

We postulate and confirm that the Ru-containing species would be expected to possess higher steady state current densities due to the presence of Ru active sites that can also participate in the methanol oxidation process. Although the commercial Pt/C exhibited a higher initial activity as compared with the Ti-containing samples, this result is not surprising, considering that Pt/C is more conductive. However, the stability of all of the oxide-containing support materials, even those containing Ti, significantly outperforms that of commercial analogues over time, due to the ability of these metal oxide materials to more effectively and more consistently oxidize harmful CO species at the Pt-metal oxide interface.

5.3. Conclusions

In this study, various metal oxide support materials have been synthesized. These support materials were characterized using a suite of techniques in order to verify their composition, size, morphology, structural integrity, and chemical purity as well as electrochemical ability. Pt NPs were then deposited onto these supports to evaluate methanol oxidation performance. In the case of ABO_3 perovskites used as supports, the effect of using Ru and Ti as the variable 'B' site was explicitly tested, while maintaining Sr as the constant 'A' site. The electrochemical findings indicate a significant electrochemical contribution from Ru at the 'B' site, an observation which had previously been proposed by others[14, 24] and more importantly, confirms prior theoretical hypotheses. In effect, the presence of Ru within the $SrRuO_3$ perovskite structure not only contributed to a significant increase in the methanol oxidation activity but also resulted in an overall shift to lower MOR onset potentials as compared with both analogous $SrTiO_3$ samples and binary metal oxides, used as control samples. Moreover, we confirmed that *chemical composition* as opposed to the size of the support is the more significant indicator of electrochemical behavior. Furthermore, a small shift to lower MOR onset potentials was also noted for $SrTiO_3$ as compared with TiO_2, which may indicate that Sr also plays a small but important role in adsorbing hydroxyl species, thereby facilitating the full oxidation process of methanol.

Additionally, energy electron loss spectroscopy has been employed in order to analyze and interpret the degree of charge transfer happening at the surface between the Pt and the underlying metal oxide interface. As a result, we have shown that electron transfer is occurring between the Pt NPs and the underlying $SrRuO_3$ support, thereby leading to a decreased adsorption of CO species and an increase in the presence of additional available Pt active sites for methanol oxidation. Moreover, XPS demonstrated an upshift associated with the Pt *4f* region for both Pt/$SrRuO_3$ substrates as compared with the analogous Pt/C control sample, indicative of a decrease in the electron density connected to the Pt. In particular, our cumulative data suggest electron transfer from Pt to the Ru in the $SrRuO_3$ material likely occurs via a Pt *4f* to Ru 4*p* transition. In the case of Pt immobilized onto $SrRuO_3$ supports, the magnitude of the Pt ECSA value does correlate with the observed methanol oxidation activity, and as such, helps to explain the higher activities attained of 1.42 mA/cm^2 (Pt/$SrRuO_3$ (average diameter of 37.3 nm)) and 0.57 mA/cm^2 (Pt/$SrRuO_3$ (average diameter of 146 nm)) at E(V) vs. RHE = 0.7 V, respectively, as compared with what has been previously achieved with conventional C-based systems.

Furthermore, a Tafel plot was generated in order to evaluate the methanol oxidation reaction mechanism of our most effective catalyst tested, i.e. Pt/$SrRuO_3$ (37.3 nm), as compared with commercial Pt/C. In effect, our catalyst gave rise to a measured slope value (0.112 V/decade in this case versus 0.142 V/decade for commercial Pt/C), which was numerically very close to what was theoretically expected for a one-electron transfer reaction involving Pt (i.e. 0.118 V/decade). Significantly, these data implied a more facile capability of oxidizing methanol with the use of our Pt/$SrRuO_3$ catalyst. Moreover, the combined results from our Tafel plot analysis as well as from cumulative XPS and EELS data confirm the presence of a beneficial and advantageous metal-support interaction between the Pt nanoparticles and the underlying $SrRuO_3$ support, thereby implying the viability of utilizing this specific perovskite metal oxide-based support as a practical alternative to conventional carbonaceous materials.

5.4. References

1. Kulesza, P. J.; Pieta, I. S.; Rutkowska, I. A.; Wadas, A.; Marks, D.; Klak, K.; Stobinski, L.; Cox, J. A., *Electrochimica Acta* **2013,** *110* 474-483.
2. Campelo, J. M.; Luna, D.; Luque, R.; Marinas, J. M.; Romero, A. A., *ChemSusChem* **2009,** *2* 18-45.
3. Lasch, K.; Hayn, G.; Jörissen, L.; Garche, J.; Besenhardt, O., *Journal of Power Sources* **2002,** *105* 305-310.
4. Hua, H.; Hu, C.; Zhao, Z.; Liu, H.; Xie, X.; Xi, Y., *Electrochimica Acta* **2013,** *105* 130-136.
5. Macak, J. M.; Barczuk, P. J.; Tsuchiya, H.; Nowakowska, M. Z.; Ghicov, A.; Chojak, M.; Bauer, S.; Virtanen, S.; Kulesza, P. J.; Schmuki, P., *Electrochemistry Communications* **2005,** *7* 1417-1422.
6. Hepel, M.; Kumarihamy, I.; Zhong, C. J., *Electrochemistry Communications* **2006,** *8* 1439-1444.
7. Zhao, G.; Zhang, L.; Sun, K.; Li, H., *Journal of Power Sources* **2014,** *245* 892-897.
8. Cao, L.; Scheiba, F.; Roth, C.; Schweiger, F.; Cremers, C.; Stimming, U.; Fuess, H.; Chen, L.; Zhu, W.; Qiu, X., *Angewandte Chemie International Edition* **2006,** *45* 5315-5319.
9. Villullas, H. M.; Mattos-Costa, F. I.; Bulhões, L. O. S., *The Journal of Physical Chemistry B* **2004,** *108* 12898-12903.
10. Santos, A. L.; Profeti, D.; Olivi, P., *Electrochimica Acta* **2005,** *50* 2615-2621.
11. Gercher, V. A.; Cox, D. F.; Themlin, J.-M., *Surface Science* **1994,** *306* 279-293.
12. Saha, M. S.; Li, R.; Sun, X., *Electrochemistry Communications* **2007,** *9* 2229-2234.
13. Penner, S.; Armbrüster, M., *ChemCatChem* **2015,** *7* 374-392.
14. Lan, A.; Mukasyan, A. S., *Industrial & Engineering Chemistry Research* **2008,** *47* 8989-8994.
15. Sharma, S.; Pollet, B. G., *Journal of Power Sources* **2012,** *208* 96-119.
16. Antolini, E.; Gonzalez, E. R., *Solid State Ionics* **2009,** *180* 746-763.
17. Shi, F.; Baker, L. R.; Hervier, A.; Somorjai, G. A.; Komvopoulos, K., *Nano Letters* **2013,** *13* 4469-4474.
18. Scofield, M. E.; Liu, H.; Wong, S. S., *Chemical Society Reviews* **2015,** *44* 5836-5860.
19. Lewera, A.; Timperman, L.; Roguska, A.; Alonso-Vante, N., *The Journal of Physical Chemistry C* **2011,** *115* 20153-20159.
20. Timperman, L.; Lewera, A.; Vogel, W.; Alonso-Vante, N., *Electrochemistry Communications* **2010,** *12* 1772-1775.
21. Hayek, K.; Kramer, R.; Paál, Z., *Applied Catalysis A: General* **1997,** *162* 1-15.
22. Lan, A.; Mukasyan, A. S., *The Journal of Physical Chemistry C* **2007,** *111* 9573-9582.
23. Tiano, A. L.; Santulli, A. C.; Koenigsmann, C.; Feygenson, M.; Aronson, M. C.; Harrington, R.; Parise, J. B.; Wong, S. S., *Chemistry of Materials* **2011,** *23* 3277-3288.
24. White, J. H.; Sammells, A. F., *Journal of The Electrochemical Society* **1993,** *140* 2167-2177.
25. Peña, M. A.; Fierro, J. L. G., *Chemical Reviews* **2001,** *101* 1981-2018.
26. Sauvet, A. L.; Fouletier, J.; Gaillard, F.; Primet, M., *Journal of Catalysis* **2002,** *209* 25-34.
27. Ponce, S.; Peña, M. A.; Fierro, J. L. G., *Applied Catalysis B: Environmental* **2000,** *24* 193-205.

28. Wang, H.; Lu, J.; Marshall, C. L.; Elam, J. W.; Miller, J. T.; Liu, H.; Enterkin, J. A.; Kennedy, R. M.; Stair, P. C.; Poeppelmeier, K. R.; Marks, L. D., *Catalysis Today* **2014,** *237* 71-79.
29. Hasa, B.; Kalamaras, E.; Papaioannou, E. I.; Sygellou, L.; Katsaounis, A., *International Journal of Hydrogen Energy* **2013,** *38* 15395-15404.
30. Chen, C.; Dai, Q.; Miao, C.; Xu, L.; Song, H., *RSC Advances* **2015,** *5* 4844-4852.
31. Mao, Y.; Banerjee, S.; Wong, S. S., *Journal of the American Chemical Society* **2003,** *125* 15718-15719.
32. Mao, Y.; Wong, S. S., *Journal of the American Chemical Society* **2006,** *128* 8217-8226.
33. Walker, J.; Bruce King, R.; Tannenbaum, R., *Journal of Solid State Chemistry* **2007,** *180* 2290-2297.
34. Atta, N. F.; Galal, A.; Ali, S. M., *International Journal of Electrochemical Science* **2012,** *7* 725-746.
35. Santulli, A. C.; Koenigsmann, C.; Tiano, A. L.; DeRose, D.; Wong, S. S., *Nanotechnology* **2011,** *22* 1-13.
36. Sugimoto, W.; Kizaki, T.; Yokoshima, K.; Murakami, Y.; Takasu, Y., *Electrochimica Acta* **2004,** *49* 313-320.
37. Long, J. W.; Swider, K. E.; Merzbacher, C. I.; Rolison, D. R., *Langmuir* **1999,** *15* 780-785.
38. Guan, X.; Guo, L., *ACS Catalysis* **2014,** *4* 3020-3026.
39. Xian, T.; Yang, H., *Advanced Materials Research* **2011,** *418-420* 18-21.
40. Li, M.; Liu, P.; Adzic, R. R., *The Journal of Physical Chemistry Letters* **2012,** *3* 3480-3485.
41. Hepel, T.; Pollak, F. H.; O'Grady, W. E., *Journal of The Electrochemical Society* **1984,** *131* 2094-2100.
42. Vukmirovic, M. B.; Liu, P.; Muckerman, J. T.; Adzic, R. R., *The Journal of Physical Chemistry C* **2007,** *111* 15306-15311.
43. Hua, H.; Hu, C.; Zhao, Z.; Liu, H.; Xie, X.; Xi, Y., *Electrochimica Acta* **2013,** *105* 130-136.
44. Selvaganesh, S. V.; Selvarani, G.; Sridhar, P.; Pitchumani, S.; Shukla, A. K., *Journal of The Electrochemical Society* **2012,** *159* B463-B470.
45. Zhou, J. G.; Fang, H. T.; Hu, Y. F.; Sham, T. K.; Wu, C. X.; Liu, M.; Li, F., *The Journal of Physical Chemistry C* **2009,** *113* 10747-10750.
46. Liu, X.; Pichler, T.; Knupfer, M.; Fink, J.; Kataura, H., *Physical Review B* **2004,** *70* 205405.
47. Lewera, A.; Zhou, W. P.; Hunger, R.; Jaegermann, W.; Wieckowski, A.; Yockel, S.; Bagus, P. S., *Chemical Physics Letters* **2007,** *447* 39-43.
48. Liao, L.; Mai, H. X.; Yuan, Q.; Lu, H. B.; Li, J. C.; Liu, C.; Yan, C. H.; Shen, Z. X.; Yu, T., *The Journal of Physical Chemistry C* **2008,** *112* 9061-9065.
49. Bisht, A.; Zhang, P.; Shivakumara, C.; Sharma, S., *The Journal of Physical Chemistry C* **2015,** *119* 14126-14134.
50. Briggs, D.; Seah, M. P., *Auger and X-ray Photoelectron Spectroscopy*. 2 ed.; Wiley: New York, 1990; Vol. 1.
51. Wakisaka, M.; Mitsui, S.; Hirose, Y.; Kawashima, K.; Uchida, H.; Watanabe, M., *The Journal of Physical Chemistry B* **2006,** *110* 23489-23496.

52. Petrović, S.; Rakić, V.; Jovanović, D. M.; Baričević, A. T., *Applied Catalysis B: Environmental* **2006,** *66* 249-257.
53. Suffredini, H. B.; Tricoli, V.; Vatistas, N.; Avaca, L. A., *Journal of Power Sources* **2006,** *158* 124-128.
54. Masud, J.; Alam, M. T.; Awaludin, Z.; El-Deab, M. S.; Okajima, T.; Ohsaka, T., *Journal of Power Sources* **2012,** *220* 399-404.
55. Franceschini, E. A.; Bruno, M. M.; Williams, F. J.; Viva, F. A.; Corti, H. R., *ACS Applied Materials & Interfaces* **2013,** *5* 10437-10444.
56. Guo, J. W.; Zhao, T. S.; Prabhuram, J.; Chen, R.; Wong, C. W., *Electrochimica Acta* **2005,** *51* 754-763.
57. Kabbabi, A.; Faure, R.; Durand, R.; Beden, B.; Hahn, F.; Leger, J. M.; Lamy, C., *Journal of Electroanalytical Chemistry* **1998,** *444* 41-53.

Chapter 6 - Ambient Synthesis, Characterization, and Electrochemical Activity of $LiFePO_4$ Nanomaterials Derived from Iron Phosphate Intermediates

6.1. Introduction

$LiFePO_4$ materials have become increasingly popular as a cathode material, due to the many benefits they possess including thermal stability, durability, low cost, and long life span. However, to improve the appeal for electrochemical applications, it is necessary to develop a relatively mild and simple synthetic method for the generation of $LiFePO_4$. As a result of the work conducted by Goodenough and co-workers,[1, 2] olivine $LiFePO_4$ has become of significant interest due to its low cost, low toxicity, high thermal stability, and excellent electrochemical properties. Specifically, $LiFePO_4$ exhibits good cycling stability, a high, flat voltage profile, and a high theoretical specific capacity of ~170 mAh/g.[3, 4] This material also gives rise to a high lithium intercalation voltage of 3.5 V as compared with pure lithium.[3, 5] Additionally, a lifetime of more than 2,000 cycles has been measured for a $LiFePO_4$ battery, which is necessary for creating commercial batteries with high stability and durability. Equation 6.1 represents the discharge of $LiFePO_4$:

$$FePO_4 + Li^+ + 1e^- \rightarrow LiFePO_4 \qquad E° = 3.5V \qquad [6.1]$$

$LiFePO_4$ possesses an olivine structure composed of a distorted hexagonal-close packed array of oxygen atoms, wherein 50% of the octahedral sites are occupied by Fe^{2+} and 12.5% are occupied by Li^+.[6] The olivine crystal structure is highly advantageous, due to its stability and lack of a significant volume change during de-lithiation.[7, 8] Conversely, other common battery materials, such as $LiCoO_2$, succumb to significant structural changes, when the lithium content is below a certain amount.[9] Hence, as a result, the olivine crystal structure is considered to be more sturdy and hence preferable for long-term battery applications.

By reducing the dimensions of $LiFePO_4$ materials to the nanoscale, improvements in the lithium ion diffusion rate can be made. For example, a particle size reduction to the nanoscale size regime would minimize the path length for Li^+ ion diffusion and further aid in electron transport through the material. Others have also suggested that when confining the dimensions to the nanoscale, the mechanical strain of the particles is reduced, thereby leading to faster lithium ion diffusion during reversible intercalation and hence, enhanced cycle lifetimes.[4, 10]

As previously mentioned, nanostructured materials of $LiFePO_4$ retain increased surface area-to-volume ratios as compared with their bulk counterparts, which leads to enhanced activity by increasing the contact area with the electrolyte.[4, 6, 10] Moreover, as a result, much research has focused on the synthesis and characterization of $LiFePO_4$ nanomaterials.[11-19] Specifically, one-dimensional (1D) nanomaterials represent an optimal morphology, as they have demonstrated a significant impact upon $LiFePO_4$ battery performance, as a result of uniquely advantageous structural and electronic properties.[3, 4, 20-32]

As an example, computational analysis has shown that the preferred Li^+ ion diffusion pathway is oriented along the *b*-axis (0.55 eV), wherein Li^+ ions form a chain within the $FePO_4$ matrix.[33, 34] Consequently, by growing the nanowire along either the *a*- or *c*- axis to orient the *b*-axis across the Li^+ ion channels along the diameter of the nanowire (i.e. the shortest distance), an increased rate performance can be attained. This would reduce the Li^+ ion diffusion length through the material and also generate better performance at cycling high rates.

Our synthesis method herein forms iron phosphate as the initial product, allowing for direct electrochemical evaluation of the $FePO_4$ moiety. Prior reports have indicated that success in the electrochemical lithiation of iron phosphate materials can be very sensitive to specific structural properties, depending on the crystallinity and the phase of the $FePO_4$ material. For example, a prior report yielded a cycle 2 specific discharge capacity of 76 mAh/g for an amorphous $FePO_4•2H_2O$ material, but only 18 mAh/g for a more crystalline hexagonal $FePO_4$ material prepared at 500°C.[35] Similarly, carbon nanotube-amorphous $FePO_4$ core–shell nanowires realized a specific capacity of 175 mAh/g in lithium batteries[36] and 120 mAh/g in sodium batteries,[37] respectively, characterized by ultra-thin amorphous coatings of $FePO_4$ comprising only a few nm in thickness. A limitation of these prior studies was a lack of discernible X-ray diffraction patterns in each case. By contrast, herein, through directed control of synthesis properties, we can tailor the aspect ratio and size of $FePO_4$ material, thereby providing for an opportunity to evaluate function with respect to electrochemical lithiation for nanowire $FePO_4$ materials relative to bulk-type granular $FePO_4$ samples.

Moreover, a significant amount of reports exist for the generation of 1D $LiFePO_4$ nanomaterials through the employment of hydrothermal and electrospinning techniques.[3, 4, 21-23] Conversely, template-directed methods represent a simple and straightforward synthetic method for the generation of 1D nanostructures,[38] with the template representing a framework for the nucleation and subsequent growth of 1D nanomaterials. The template directs the formation of the material, with the product mimicking the size and morphology of the individual pores. This synthetic method allows for increased flexibility, since the diameters of the 1D material may be controlled by varying the corresponding pore size of the template employed.

Not only does our group have significant experience synthesizing 1D nanomaterials from templates with pore diameters ranging from 15 nm to 200 nm,[25, 29, 31, 32, 39-42] but others have also shown their ability to synthesize high-performing, 1D $LiFePO_4$ nanomaterials as well. For instance, Yang et al. synthesized $LiFePO_4$ nanotubes employing a calcination step at 550°C for 2 hours in a 5%/95% H_2/Ar atmosphere.[43] Additionally, nanowires were generated by submerging a PC template in an aqueous precursor solution of ferric nitrate, lithium hydroxide, phosphoric acid, ascorbic acid, and ammonium hydroxide for 24 hours,[44] with the resulting electrodes achieving a specific capacity of 165 mAh/g (3C discharge rate).

In our synthesis scheme herein, the membranous template is wedged between two half-cells of the so-called “U-tube device”, which is a U-shaped tube. The addition of precursor solutions to the two half-cells of the device enables the “double-diffusion” of precursors into the porous channels. Subsequently, the precursors meet within the spatial confines of the polycarbonate membrane and react within the confined 1D pore space, thereby forming the desired product. This synthetic technique has been extensively developed by our research group to generate a wide range of materials including but not limited to metals, metal oxides, phosphates, sulfides, and fluorides.[3, 20, 22, 25, 28, 29, 31, 38, 41, 42, 45-50] The template-assisted U-tube method offers many advantages for the synthesis of 1D nanostructures, since it is a simple and flexible methodology, often operating in aqueous media and yielding high-quality single-crystalline nanomaterials with high yield and with reliable control over composition, size, and shape. Additionally, the method is compatible with a wide range of relatively benign, sustainable precursor systems, and typically involves rather short reaction times under ambient conditions.

In this Chapter, we investigate the characterization of 1D $LiFePO_4$ nanowires, prepared with a mild template-based U-tube method. The diameter of the amorphous $FePO_4$ nanowires are controlled by the pore size of the specific template employed, with nanowires possessing as-generated diameters of 185 ± 35 nm and 63 ± 14 nm, respectively. The desired olivine-type $LiFePO_4$ NWs were produced by a 2-step protocol, with the first involving a chemical lithiation by LiI, followed by a calcination step under a reducing atmosphere. Additionally, these nanowires will be compared with an as-synthesized $LiFePO_4$ bulk analogue. Various advanced characterization methods will be employed to investigate the morphology, phase, and purity of our as-prepared $LiFePO_4$ nanomaterials. The nanomaterials will then be employed as cathode materials to investigate their electrochemical performance as Li-ion battery materials.

6.2. Results and Discussion

6.2.1. Characterization of Pure, Crystalline, 1D $LiFePO_4$ Nanowires

To demonstrate a proof-of-concept validation for the synthesis of the various $LiFePO_4$ nanomaterials, Figure 6.1 depicts scanning electron microscope (SEM) images in conjunction with the corresponding X-ray diffraction (XRD) patterns. As shown in Figure 6.1A, the particles reveal average diameters of 220 ± 57 nm. The 50 nm $LiFePO_4$ nanowires can be seen in Figure 6.1B. The corresponding average diameter of the 50 nm nanowires is 98 ± 18 nm, with the nanowires exhibiting a roughened surface. Conversely, the 200 nm NWs (Figure 6.1C) possessed an average diameter of 185 ± 35 nm with an average length of 3.0 ± 0.9 μm. Based on the SEM image, particles are evident in the image, which may be a result of the mechanical strain occurring during the sonication step needed to remove the sample from the annealed template. Even though some nanowires with shorter aspect ratios as well as particles are evident, the majority of the sample possesses the nanowire morphology.

The composition and crystallinity of the as-obtained products were evaluated by XRD, high-resolution synchrotron XRD, and high resolution TEM techniques. The XRD patterns for all three lithiated samples are displayed in Figure 6.1D-F, respectively, with all present peaks corresponding to the standard pattern for olivine $LiFePO_4$ (JCPDS #83-2092). This result initially confirmed to a first approximation that the lithiation and crystallization step successfully converted the as-synthesized amorphous materials into phase-pure $LiFePO_4$, with no additional crystalline impurities.

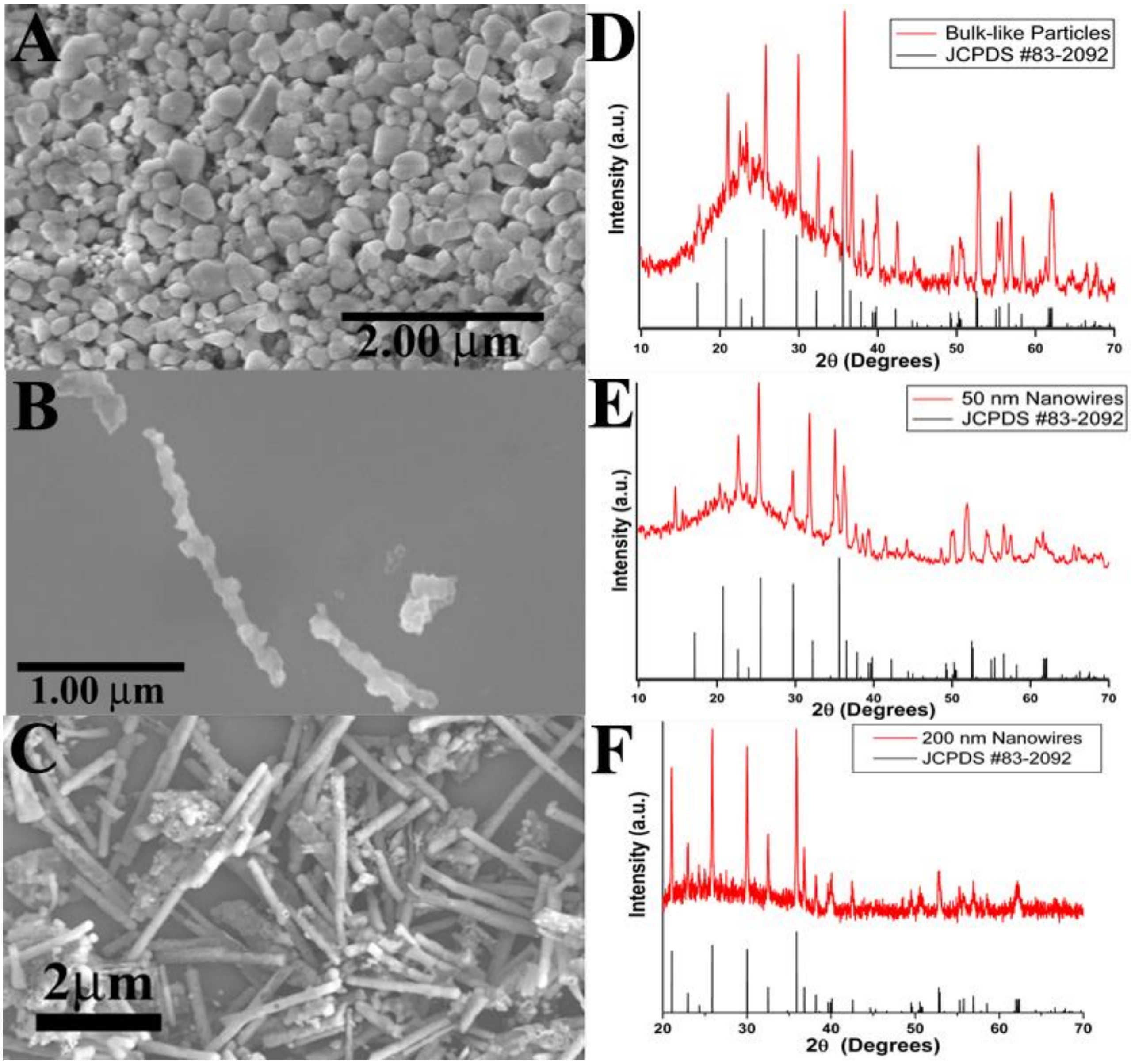

Figure 6.1. Representative SEM images of crystallized chemically lithiated particles (A), nanowires produced from 50 nm pore sized PC templates (B), and nanowires produced from 200 nm pore sized PC templates (C). Corresponding X-ray diffraction patterns of as-prepared bulk and nanomaterials (in red), along with their corresponding crystallographic database standards (in black), are displayed in (D), (E), and (F), respectively. Taken with permission from Reproduced by permission of Springer.

However, to obtain a clearer idea about the purity of our as-prepared samples, additional high-resolution synchrotron XRD data processed in the context of Rietveld refinements were gathered with the intent of more rigorously accounting for the presence of any remnant impurities and possible anti-site disorder for Fe and Li ions in the structure. The data are summarized in Figure 6.2. Our as-prepared bulk-like particles were determined to be a = 10.326(0) Å, b = 6.004(6) Å, and c = 4.690(0) Å with a cell volume of 290.800(6) Å^3. Moreover, the bulk-like sample appeared to co-exist with an approximately 30% Li_3PO_4 impurity, as indicated by the green asterisks in Figure 6.2.The reliability factor for this fit was noted to be an acceptable value of R_{wp} = 3.3%.

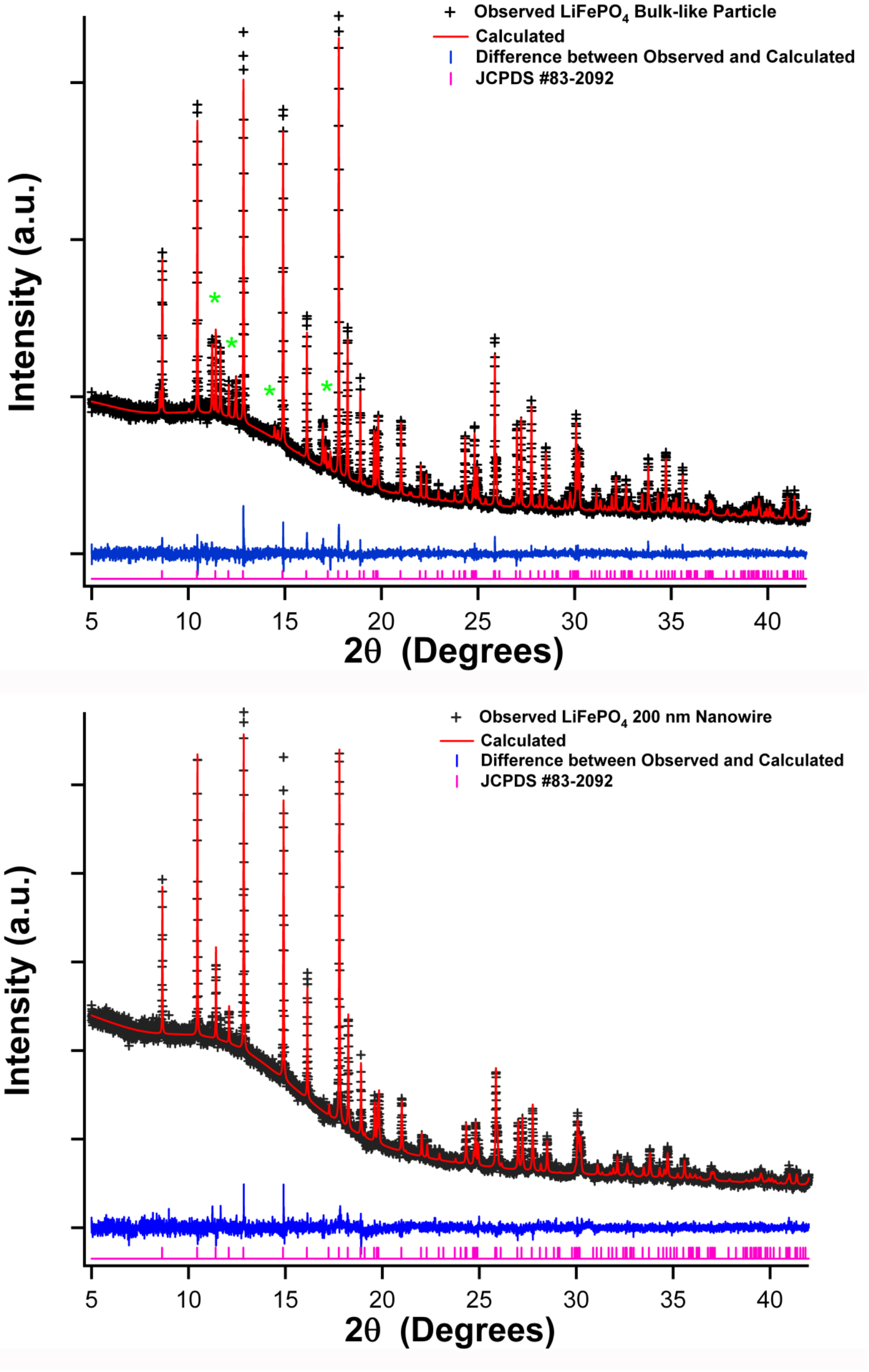

Figure 6.2. High-resolution synchrotron X-ray diffraction patterns (in black) and corresponding Rietveld refinement patterns (red) of (A) bulk-like $LiFePO_4$ particles (green asterisks highlight the presence of a Li_3PO_4 impurity) and of (B) 200 nm $LiFePO_4$ nanowires produced using the PC template with the corresponding database standards shown below (in pink) for each material. Differences between the observed and calculated intensities are plotted in blue. Reproduced by permission of Springer.

The collective crystallographic information obtained, including the cell parameters, volumes, and anti-site defect concentrations, as determined from Rietveld refinement analysis, is shown in Table 6.1. The formation of this impurity likely can be attributed to the presence of an excess quantity of Li ions in the material. However, we should note that the as-prepared Li_3PO_4 was effectively phase segregated from $LiFePO_4$ itself, which exists as the predominant, majority phase and is essentially stoichiometric in nature.[51, 52] The implications of the formation of Li_3PO_4 on the resulting electrochemical behavior of the bulk material will be discussed later.

By contrast, we noted that the $LiFePO_4$ nanowires prepared using the 200 nm template sample do not evince any such impurity, as determined by the absence of any Li_3PO_4 peaks in the high resolution XRD as well as the lack of any other crystalline impurities associated with $LiFePO_4$. The as-obtained lattice constants were not significantly different as compared with those of bulk-like powders. These were computed to a = 10.327(9) Å, b = 6.005(8) Å, and c = 4.692(6) Å with a corresponding cell volume of 291.069(3) $Å^3$. The reliability factor for this fit was determined to be an acceptable value of R_{wp} = 3.3%. Moreover, our nanowires possessed negligible (within the limits of error of the measurement) anti-site disorder for both Li and Fe ions, thereby suggesting that as-obtained $LiFePO_4$ nanowires were high quality in terms of chemical purity. Detailed structural parameters associated with both $LiFePO_4$ bulk-like particles and the corresponding nanowires are shown in Table 6.1.

		200 nm Nanowire		
Atom	**x**	**y**	**z**	**Occupancy**
Li	0.5	0.5	0	1
Fe	0.21853	0.25	0.0267	1
P	0.40479	0.25	0.58445	1
O1	0.40267	0.25	0.2689	1
O2	0.16286	0.54884	0.22128	1
O3	0.04822	0.25	-0.211	1
Space group:	Pmna		**Reliability Factor (Rwp):**	3.29%
Unit Cell Parameters: a = 10.32789 Å, b = 6.00579 Å, c = 4.69261 Å			**Phase:**	100% $LiFePO_4$
Cell Volume:	291.06917 Å^3			

		Bulk-like Sample		
Atom	**x**	**y**	**z**	**Occupancy**
Li	0.5	0.5	0	1
Fe	0.21775	0.25	0.02557	1
P	0.40502	0.25	0.58446	1
O1	0.40029	0.25	0.25635	1
O2	0.16733	0.54493	0.21629	1
O3	0.04563	0.25	-0.20062	1
Space group:	Pmna		**Reliability Factor (Rwp):**	3.29%
Unit Cell Parameters: a = 10.32599 Å, b = 6.00463 Å, c = 4.69005 Å			**Phase:**	71% $LiFePO_4$
Cell Volume:	290.80068 Å^3			29% Li_3PO_4

Table 6.1. Structural parameters, determined from the high-resolution synchrotron X-ray data analysis for both the 200 nm $LiFePO_4$ nanowire (top) and bulk-like $LiFePO_4$ (bottom) samples. Reproduced by permission of Springer.

The HRTEM images presented in Figures 6.3, 6.4, 6.5, 6.6, and 6.7 validate the XRD results. Specifically, a low magnification TEM image of a typical bulk-like particle is shown in Figure 6.3A. Further analysis of the high-resolution TEM (HRTEM) image in Figure 6.3B reveals the perfect long-range crystal ordering with lattice fringes observed for the [-12-1] zone ascribed to the particle. Moreover, direct measurement of the expected lattice spacings, i.e. *d*(111) = 0.348 nm and *d*(-101) = 0.425 nm, along with the optical Fourier Transform pattern shown in the inset also is consistent with the appropriate (*hkl*) reflections expected for the [-12-1] zone associated with the bulk-like $LiFePO_4$ particles. The Fourier diffraction pattern (DP) shown in the inset of Figure 6.3B is in good numerical agreement with the calibrated DP in Figure 6.3C, recorded from a larger area of the nanoparticle, as shown in Figure 6.3A. The diffraction spots can be assigned to the (111), (101), as well as (210) planes, respectively.

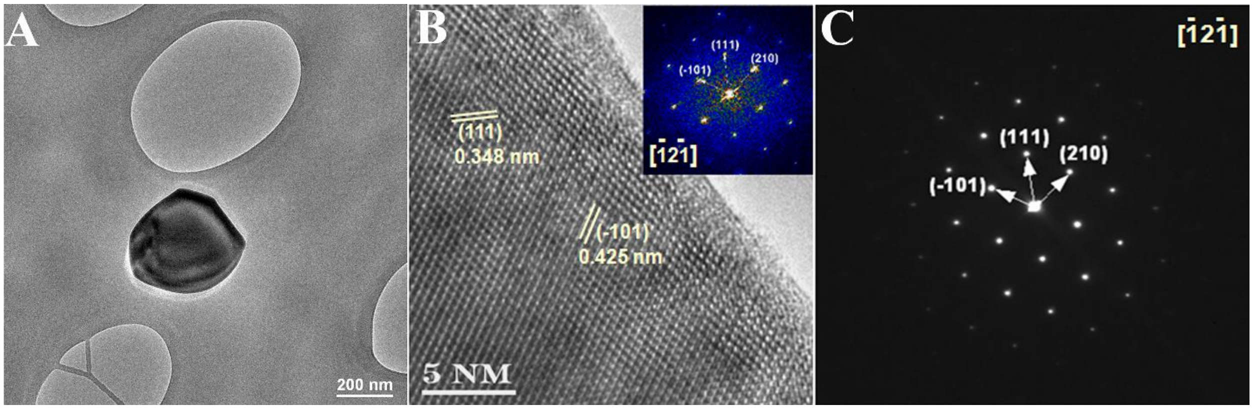

Figure 6.3. A low magnification TEM image of (A) crystalline $LiFePO_4$ particles, (B) Magnified HRTEM image is recorded along the [-12-1] zone direction from the optical Fourier pattern (inset) of $LiFePO_4$ (Pnma) taken from this image. (C) An experimental diffraction pattern (DP) (magnified 1.4x), representing the [-12-1] zone pattern for the 200 nm $LiFePO_4$ nanoparticles, highlighted in the HRTEM image (B). Reproduced by permission of Springer.

Representative nanowires produced from a 50 nm pore size template are highlighted in the dark field TEM image (Figure 6.4C). The surface of the wire appears to be roughened and fractured, as it exhibits low angle grain boundaries, which is consistent with our observations from SEM. The high magnification image in Figure 6.4A indicates that the wire is highly crystalline. Its corresponding SAED pattern is shown in Figure 6.4B. The SAED pattern in Figure 6.4B exhibits a [01-1] zone pattern, which can be attributed to $LiFePO_4$. Diffraction spots have been indexed to the (200) and (011) planes in this specific zone. It can be seen from these data that the 50 nm NWs grow anisotropically along the *a*-axis, although low angle grain boundaries can be seen due to the small diameter of the NWs.

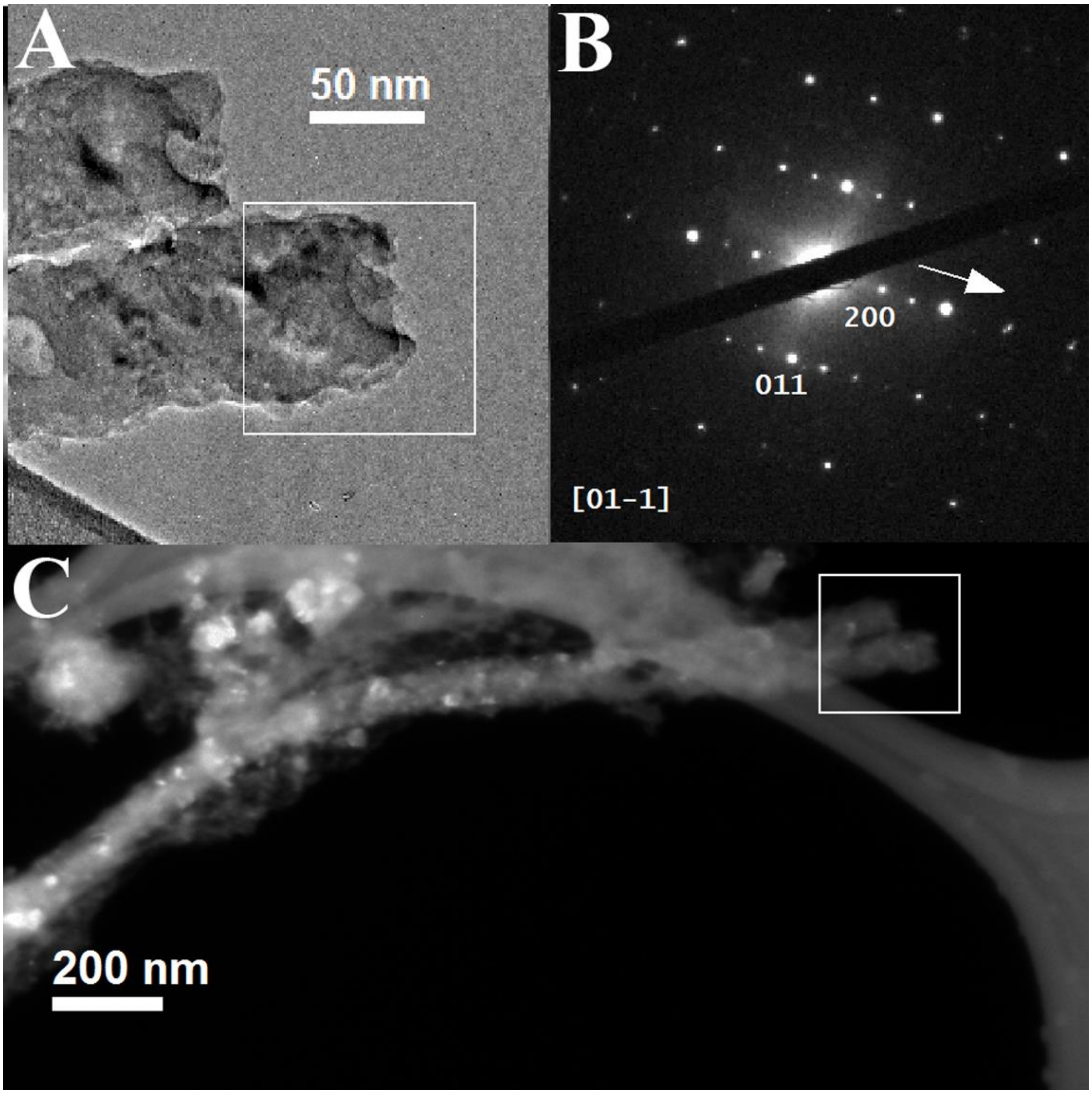

Figure 6.4. HRTEM characterization for the 50 nm $LiFePO_4$ NWs. (A) A magnified HRTEM image of a 50 nm NW tip taken from (C). (B) A single area electron diffraction pattern taken from (A), corresponding to the [01-1] zone of $LiFePO_4$. (C) A dark field image of two 50 nm LFP NWs. Reproduced by permission of Springer.

In Figure 6.5, additional HRTEM characterization was used to further corroborate the assertion that we had synthesized single crystalline 50 nm NWs with the appropriate growth directions. Specifically, in Figure 6.5A, a dark field image of 2 LFP NWs can be seen. This result demonstrates internal consistency in the crystallinity within the NW sample, as the individual crystals lying in the correct Bragg condition are highlighted. In the bottom righthand part of Figure 6.5A, a high magnification image of the boxed area can be observed, further demonstrating the presence of low angle grain boundaries within our 50 nm NWs. In Figure 6.5B, a SAED pattern is included for the area, delineated in Figure 6.5A. This SAED pattern suggests that some of our 50 nm NWs are actually polycrystalline. In the bottom righthand portion of the image, there is a special calibrated ring pattern obtained by the rotational averaging of all diffraction spots observed for that localized region. The diffraction rings obtained by this procedure match well with the expected reference fringes (shown with bright bars in the inset) for appropriate (*hkl*) reflection positions of crystalline $LiFePO_4$. Herein, even though there are a lot of data within this pattern, for the sake of clarity, only seven strong rings are marked with the corresponding referencing bars.

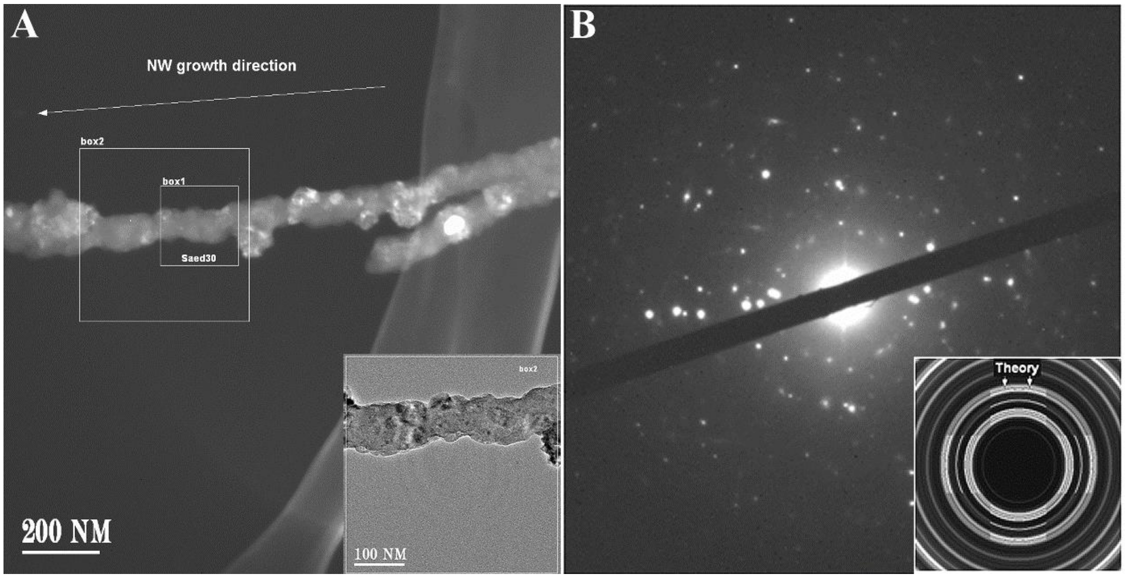

Figure 6.5. (A) Dark field image of 200 nm $LiFePO_4$ NWs. The inset is associated with the boxed area 2 in the main image. (B) An experimental diffraction pattern (DP), corresponding to the inset of Figure 6.5A. The lower right-hand inset for the recorded ED pattern illustrates a rotationally averaged ring pattern, overlaid with a theoretical fringe pattern of $LiFePO_4$ (Pnma) for several *d*-spacings (JCPDS #83-2092), as shown by cross-like fine fringes, labeled by the word "theory". For the sake of clarity, only the first seven rings are indexed with *d*-space fringes. Reproduced by permission of Springer.

HRTEM images corresponding to the 200 nm LFP NWs can be observed in Figure 6.6. Figure 6.6C focuses on a single crystalline 200 nm NW. A higher magnification image can be noted in Figure 6.6B, corresponding to the Fourier transform in Figure 6.6A, identified as the [011] zone of $LiFePO_4$. The NW edge (Figure 6.6C) follows the *a*-axis direction, associated with the (200) spot direction in the FT pattern. Figure 6.6E is a SAED pattern that can be assigned to the [011] zone for $LiFePO_4$, thereby further corroborating the FT shown in Figure 6.6A. The appropriate selected area image of the 200 nm NWs for which the SAED pattern was obtained is described in Figure 6.6D, which provides for additional evidence, supporting the idea of NW growth parallel to the *a*-axis. Figure 6.6F reveals the defocused diffraction pattern for the region shown in Figure 6.6D, which implies a direct relationship between the NW orientation (in the central BF image spot) and the *a*-lattice direction, as defined by the (200) reflection.

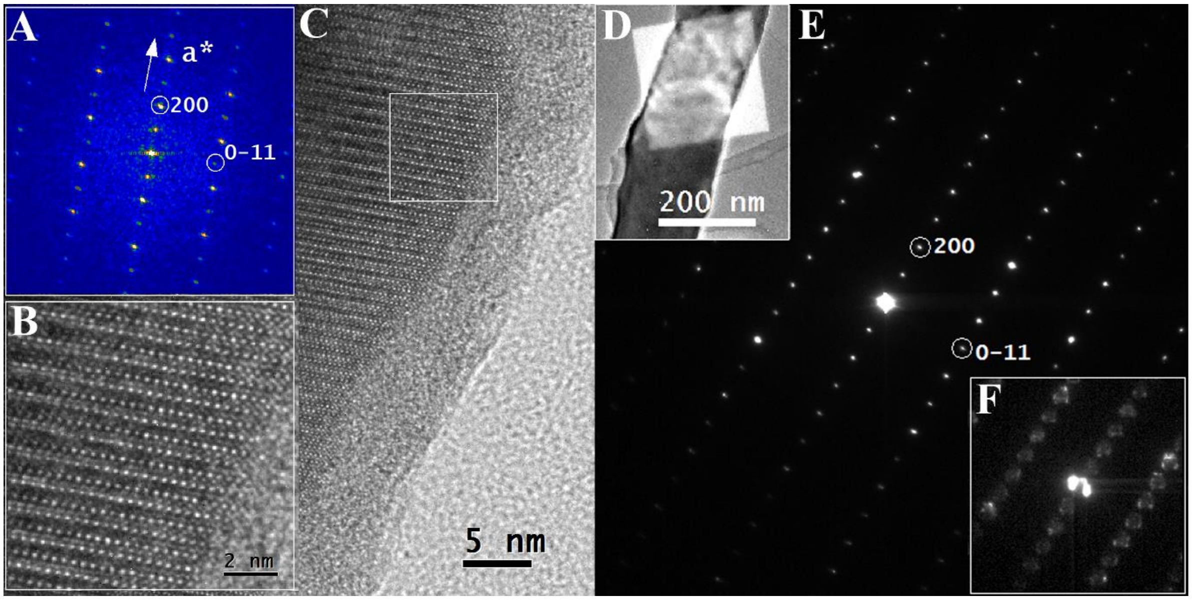

Figure 6.6. HRTEM characterization for the 200 nm $LiFePO_4$ NWs. (A) Fourier transform of an magnified image insert (B), identified as the [011] zone of $LiFePO_4$, (B) A high magnification image of the 200 nm LFP NW used for the FT. (C) The NW edge follows the *a*-axis direction presented by the (200) spot direction in the FT pattern. (D) A high magnification image used for acquiring (E) a selected area electron diffraction image, corresponding to the [011] zone of $LiFePO_4$ (200nm), as well as (F) a defocused diffraction pattern, highlighting the NW orientation (in the central BF image spot),which is almost parallel to the *a*-lattice direction, as defined by the (200) reflection. Reproduced by permission of Springer.

Additional HRTEM images are shown in Figure 6.7. Specifically, Figure 6.7A represents a low magnification TEM image of a typical 200 nm nanowire. The nanowire appears to possess a highly textured surface with regions, featuring uneven color contrast and brightness, thereby implying that the electron diffraction signal fluctuates to some extent throughout the material, likely because of slight spatial variations in thickness and surface roughness within its length. This observation may be indicative of a slightly porous structure. The measured *d*-spacing (Figure 6.7B) of 0.369 nm corresponds to the (0-11) plane aligned parallel with the [100] vector, i.e. the *a*-axis, associated with the $LiFePO_4$ crystal. Such an observation agrees well with the localized diffraction pattern (DP) orientation, seen in Figure 6.7C.

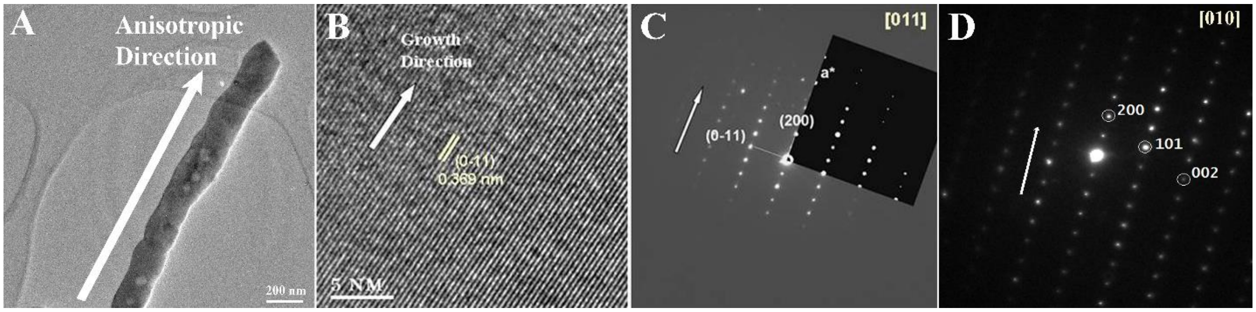

Figure 6.7. (A) A low magnification HRTEM image corresponding to nanowires produced from 200 nm pore size diameter PC templates. (B) A magnified HRTEM image corresponding to 200 nm diameter nanowires, demonstrating the presence of anisotropic growth along the *a*-direction. (C) Magnified (1.4 x) image for a DP of 200 nm-diameter nanowires, as compared with the theoretical DP, calculated for the [011] zone of $LiFePO_4$ (Pnma) thin crystal and overlaid with a DP (in dark color square), thereby confirming an *a*-axis growth direction. (D) A low-index [010] zone of $LiFePO_4$. Reproduced by permission of Springer.

By comparing the DP with a theoretically calculated pattern (as shown by the overlaid dark square), we have been able to conclude that the 200 nm nanowire, as shown in Figure 6.7A, likely has a preferred growth direction associated with the *a*-axis of the crystalline $LiFePO_4$ structure. Specifically, all of the sharp and uniform diffraction spots in Figure 6.7C can be attributed to the [011] zone pattern for a $LiFePO_4$ crystal, implying that the nanowire possesses a long range crystalline ordering with a preferred anisotropic growth direction along the *a*-axis. Moreover, the measured spacings of $d(011) = 0.373$ nm and $d(200) = 0.514$ nm in Figure 6.7C can be ascribed to the reference (*hkl*) reflections of $LiFePO_4$ single crystals (JCPDS #83-2092) and, in particular, for a large *a*-lattice parameter of $2*d(200) = 1.3$ nm. Figure 6.7D represents an additional SAED pattern taken from the low-index [010] zone of $LiFePO_4$. These spots have been indexed to the (200), (010), and (002) reflections, respectively, of $LiFePO_4$, thereby further supporting the idea of *a*-axis growth.

Moreover, we note that both of the preferred growth directions for the 50 nm and 200 nm nanowires, along the *a*-axis, result in an interesting structural consequence. That is, in both cases, one of the lattice normal vectors, i.e. (***a, b***) for the nanowire surfaces, possesses a ***b*** direction for the (010) lattice planes, corresponding to the preferred Li ion transport pathway.[53, 54] Overall, our observations from HRTEM and XRD data suggest that our as-obtained $LiFePO_4$ nanowires are likely to be both single-crystalline and phase-pure.

6.2.2. Electrochemical Performance of 200 nm $LiFePO_4$ Nanowires

Crystalline 200 nm diameter $LiFePO_4$ nanowires were prepared as an electrode for a coin cell battery setup. The incorporation of carbon particles in the electrode has been shown to vastly reduce resistance by assisting in the transport of electrons produced by the $LiFePO_4$ cathode material to the current collector.[53, 55-57] This step is critical to overcoming the low conductivity inherent to $LiFePO_4$, which would typically result in a dramatically reduced specific capacity at high rates, relative to the theoretical value, under practical coin cell conditions.

Constant current charge/discharge experiments were run at room temperature from 2 to 3.6 V at a rate of C/10, and the corresponding data can be observed in Figure 6.8A. The associated charge and discharge profiles of the 200 nm diameter nanowires are presented in Figure 6.9. These experiments were run in order to demonstrate that our 200 nm-diameter NWs were electrochemically active as compared with bulk as a comparative standard. The bulk material showed average electrochemical properties, exhibiting a decrease in specific capacity over the course of 10 cycles, which is indicative of average rate performance and reversibility.

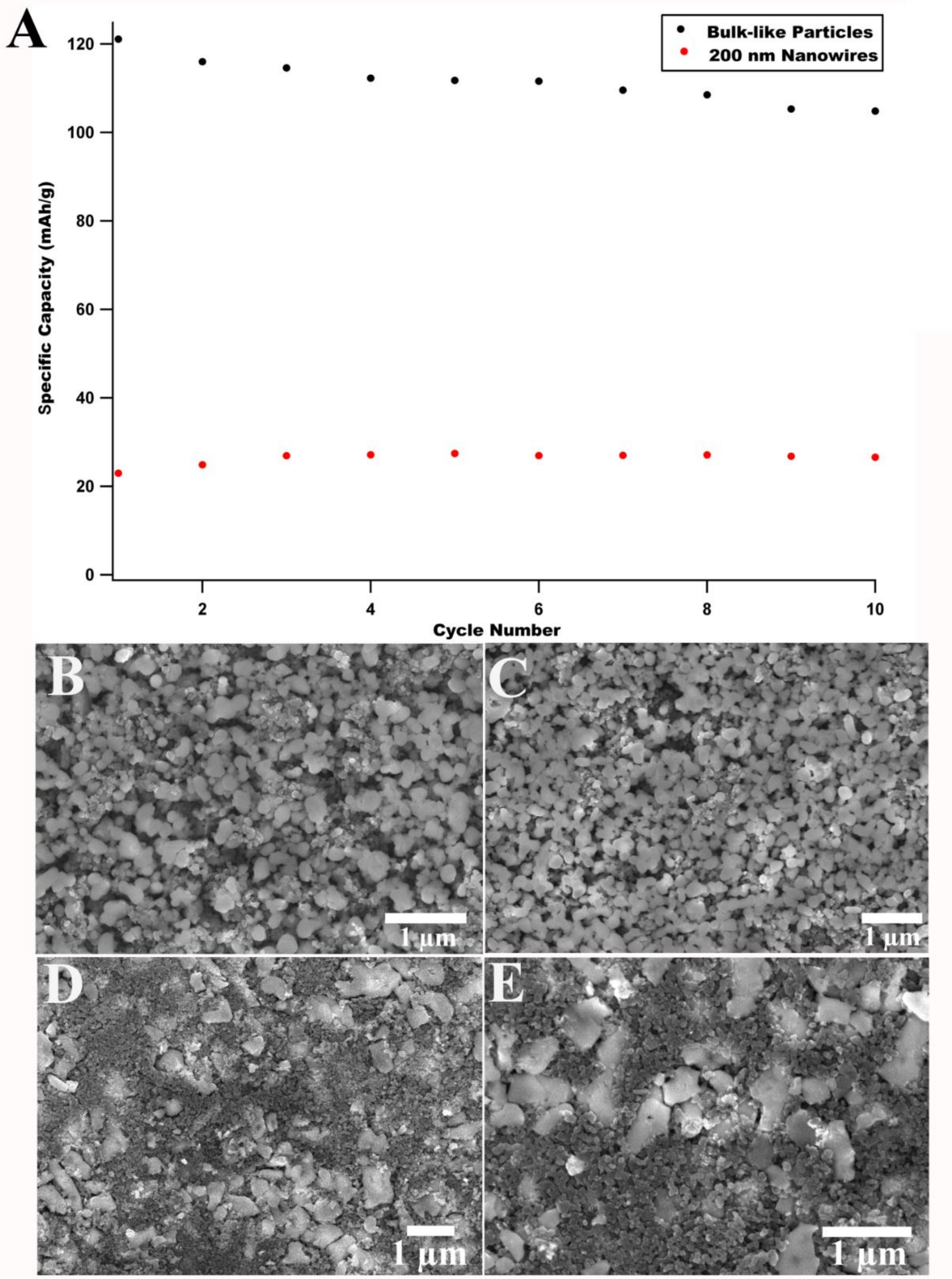

Figure 6.8. (A) Capacity vs. cycle number for both the bulk-like particles as well as 200 nm diameter lithium iron phosphate nanowires. SEM images have been taken both before (B, D) and after (C, E) electrochemical cycling. (B) and (C) are connected with the bulk-like $LiFePO_4$ particles, whereas (D) and (E) are associated with the 200 nm-diameter $LiFePO_4$ nanowire system, both coupled with carbon black and PTFE. Reproduced by permission of Springer.

While it is reasonable to conclude from these data that our chemical lithiation procedure appears not to be as efficient as the corresponding electrochemical lithiation protocol, more experiments must be conducted to confirm this result. The value of the specific capacity after 10 cycles was measured to be 111.5 mAh/g, revealing that the bulk-like particles likely achieved 66% of the theoretical value (i.e. 170 mAh/g). By comparison, the average specific capacity (i.e. 26.4 mAh/g) of our as-synthesized 200 nm NWs, as determined by the relatively small amount of $LiFePO_4$ active material present in the electrode, is significantly below that of the theoretical value (i.e. 170 mAh/g), which may be due to poor electronic conductivity and sheer lack of active material. Moreover, our electrode preparation will need to be optimized, but the main goal of this report was to successfully demonstrate our ability to synthesize chemically pure, crystalline $LiFePO_4$ nanomaterials that are electrochemically active.

Hence, the charge and discharge curves in Figure 6.9 are promising in that they show that our nanowires are at least responsive electrochemically. The plateau seen in this Figure suggests that the potential of 200 nm-diameter nanowires, during the charging process for the oxidation of $Fe^{2+} \rightarrow Fe^{3+}$, is 3.4 V vs. Li/Li^{+}. In fact, the higher than anticipated voltage observed for the 200 nm nanowires (i.e. 3.5 V) can be ascribed to the impedance present within the cell. This increased resistance can be attributed to a number of reasons, including the nature of the electrolyte as well as morphological differences in the samples analyzed (i.e. particles versus wires). In our case, we can potentially attribute the observed increase in impedance to both morphology and poor contact between the active material and the current collector, as the other parameters during coin cell assembly were effectively maintained constant throughout for all of the cells analyzed including those for bulk.

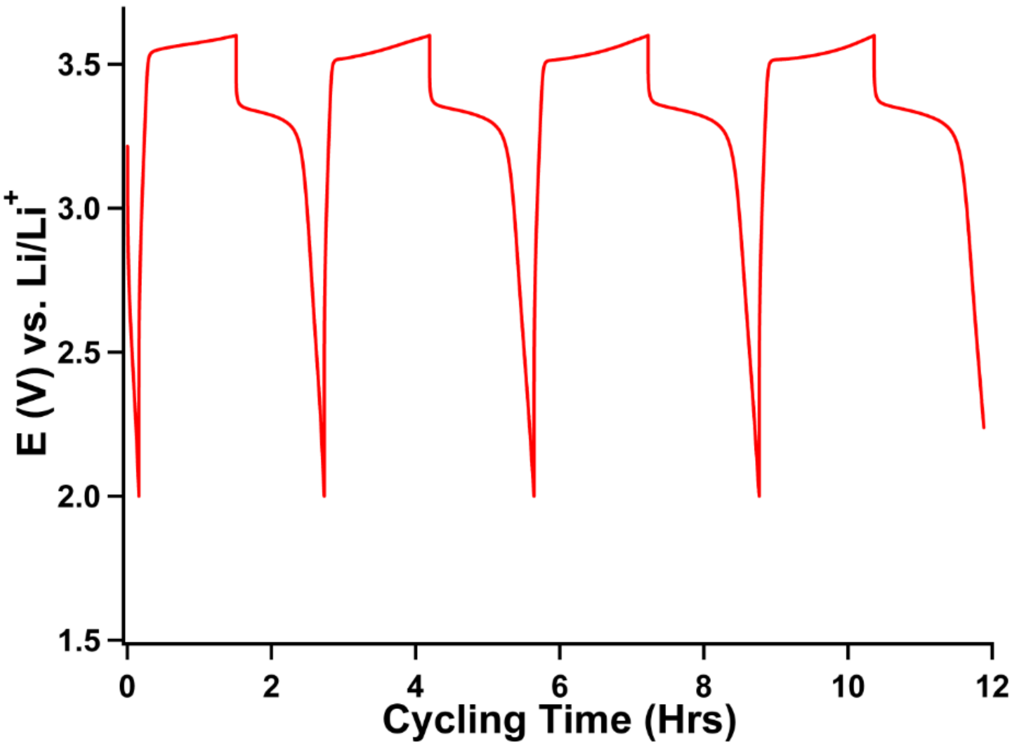

Figure 6.9. Electrochemical cycling of 200 nm $LiFePO_4$ nanowires. The charge-discharge curve is plotted as a function of time. Reproduced by permission of Springer.

Of significance for the interpretation of our electrochemical data, we were unable to conclusively demonstrate the formation of Li-Fe anti-site pair defects in which a Li ion at the M1 site is exchanged with a Fe ion at the M2 site.[57-59] This impurity is actually intrinsic[60] to $LiFePO_4$ and easily forms in olivine structures. Yet, this defect can potentially influence electrochemical performance, because it has been postulated that the presence of Fe ions on lithium sites can block the long-range 1D migration of the corresponding Li channel[55] (in particular, the (010) channel).[53] For instance, hydrothermally grown $LiFePO_4$ nanostructures synthesized by Yang and coworkers possessed about 3-5% of Fe ions, occupying Li sites, as determined by using Rietveld analysis.[58] During the intercalation/de-intercalation process, these Fe ions localized in the M1 sites likely inhibited Li ion transport and concomitantly led to not only a noteworthy decrease in the Li ion diffusion coefficient but also a reduction in the availability of active volume, all of which would have diminished the overall potential capacity of this material. Hence, typically, these materials are heated above 450°C to remove this deleterious defect.[53, 60] Interestingly, our material evinced no such impurities, as indicated by our high resolution synchrotron XRD data, thereby supporting the notion that the presence of these impurities could not be the reason for our poor conductivity.

Furthermore, the observed variation in electrochemical behavior may be ascribed to the differences in size and morphology between the samples herein, which directly impact both electron and lithium ion transport.[54, 61] To analyze and track the morphological evolution of the electrode before and after cycling, scanning electron microscopy was specifically utilized to document these changes. More specifically, the electrode was prepared and imaged prior to assembling the coin cell as well as after 1 cycle, in order to probe the effect of Li intercalation/de-intercalation on the electrode.

Images of individual electrodes containing bulk-like particles (Figure 6.8B and C) and the 200 nm diameter nanowires (Figure 6.8D and E) have been analyzed. Specifically, the electrode, containing 200 nm-diameter $LiFePO_4$ nanowires, shows reasonable surface uniformity, both pre- and post-cycling; it is not as if the Li intercalation/de-intercalation process caused the electrode to fracture and crack after electrochemical cycling. However, there are a few issues that are worth noting. *First*, there is a qualitative difference in physical appearance and packing between the 200 nm $LiFePO_4$ nanowires isolated immediately after synthesis (Figure 6.1C) and when physically incorporated into the electrode (Figure 6.8D). This observation may be as a result of the technique employed to synthesize the electrode, which tends to require a fair amount of mechanical, potentially destructive grinding in order to compact the mixture. *Second*, it is apparent that an inhomogeneous distribution and packing of the cathode material exists throughout the electrode, which may also be detrimental to the overall performance of the resulting cell. As stated previously, the conductivity of the material is directly related to both its size and shape. Hence, the slight but noticeable deterioration in morphology and packing, which presumably affected electrode porosity and which is apparent from Figures 6.8D and 6.8E, before and after cycling, respectively, suggests that this factor had a negative effect upon the wires' overall electrochemical performance.

Moreover, without even considering the characteristics of the active material, the electrochemical measurement technique employed possesses a number of limitations of its own. That is, the specific methodology implemented to put together the coin cell assembly in these studies ultimately decreases the volume energy density of the $LiFePO_4$ used by 25% (i.e. 10% carbon black and 5% PTFE present in the cathode),[14] thereby fundamentally affecting performance. From prior literature, it has been suggested that the electrode fabrication process needs to be specifically and carefully tailored to the type of $LiFePO_4$ material used (i.e. through optimization of the adhesion and miscibility characteristics of the $LiFePO_4$ relative to the other cell components, for instance),[3] in order to inadvertently avoid lowering the volumetric and gravimetric energy density and hence the overall efficiency of the resulting coin cell configuration.[6, 58] Herein our protocols did not necessarily lead to the formation of a homogeneous, uniform electrode, which would represent a minimum and necessary prerequisite for observing reasonable Li intercalation/de-intercalation. However, we reiterate that the reason for choosing this method of electrode synthesis was to use viable, reproducible, and relatively simple techniques, considering the relatively small amounts of $LiFePO_4$ nanowires that we had ambiently formed. Evidently, we learned that the quantity of active $LiFePO_4$ material matters. Hence, future work will rely on working with an optimized electrode set-up using larger quantities of electrochemically active single-crystalline $LiFePO_4$ nanostructures, tailored in terms of size, chemical composition, and morphology.

6.2.3. Electrochemical Lithiation of $FePO_4$ Nanowires

In order to assess the opportunity for electrochemical lithiation of the iron phosphate materials, commercial (bulk-like) and synthesized (nanowire) samples of $FePO_4$ were tested in electrochemical cells versus lithium metal electrodes. The first test of the $FePO_4$ was designed to be consistent with the test of the chemically lithiated material. Cells containing bulk-like $FePO_4$ material were cycled under a voltage range of 2.0 – 3.6 V at a 0.18 mA/cm^2 rate for ten cycles (Figure 6.10). After a lower capacity for the initial cycle, the discharge and charge capacities were measured to be ~ 4 mAh/g for cycles 2 - 10.

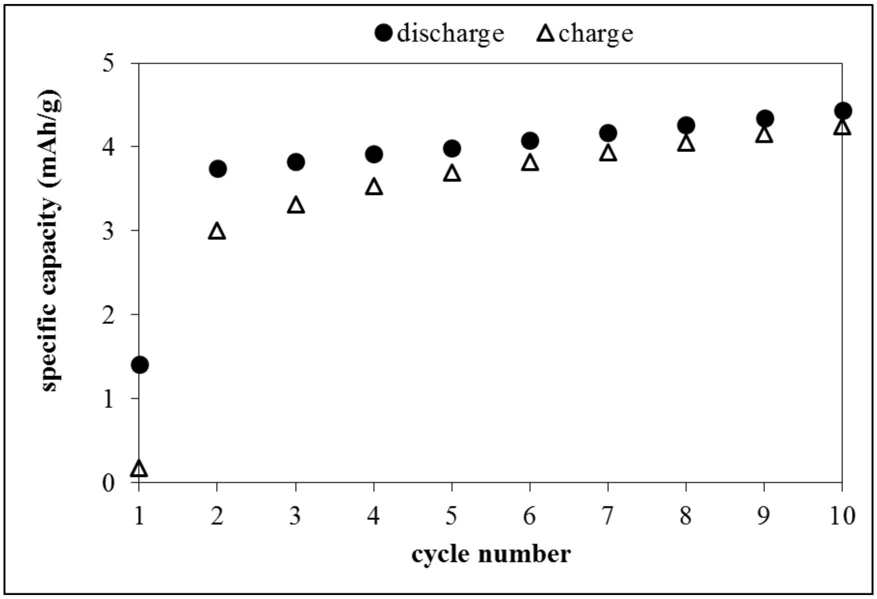

Figure 6.10. Electrochemical cycling of $Li/FePO_4$ cells containing bulk-like $FePO_4$ material under 0.018 mA/cm^2 rate. Specific capacities for discharge and charge are shown as a function of cycle number. Reproduced by permission of Springer.

It was proposed that a lower cycling rate may improve the lithiation of the $FePO_4$ material, and that a nanowire structural motif would impact the delivered capacity of the $FePO_4$ material. Therefore, a second test was undertaken in terms of cycling both bulk-like and nanowire $FePO_4$ materials under a voltage range of 2.0 – 3.6 V at 0.018 mA/cm^2 rate for three cycles (Figure 6.11). For the bulk-like material, the discharge capacities were 16 and 18 mAh/g on cycles 1 and 2, respectively, with no discharge capacity observed on the third cycle (Figure 6.12A). Lithiation of the bulk-like material remained limited, even at this lower rate, with low charge capacities measured of 5 and 8 mAh/g on cycles 2 and 3. For the nanowire material, the discharge capacities were 0.17 and 0.17 mAh/g on cycles 1 and 2, with very little discharge capacity observed for the third cycle (Figure 6.12B). Lithiation of the bulk-like material was in fact very limited even at this lower rate, with capacities < 0.02 mAh/g on all three cycles. The ten-fold lower capacity for the nanowire $FePO_4$ material relative to the bulk-like $FePO_4$ material under this test was similar to the six-fold lower capacity for the nanowire $LiFePO_4$ material, relative to that of the bulk-like $LiFePO_4$ material, as shown in Figure 6.8 above.

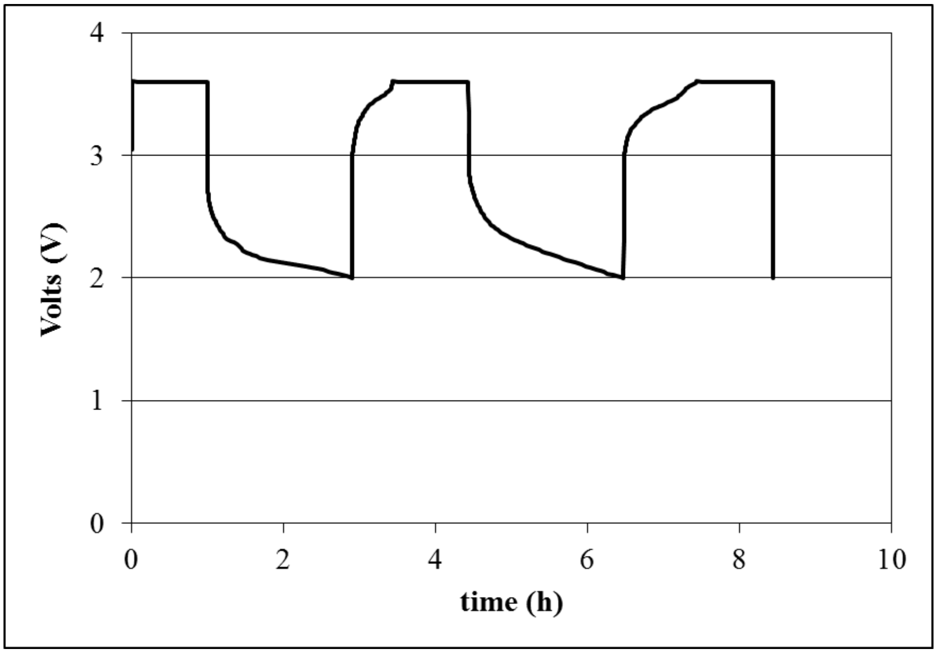

Figure 6.11. Electrochemical cycling of Li/$FePO_4$ cells, containing bulk-like $FePO_4$ material under 0.018 mA/cm^2 rate and a 2.0 – 3.6 V potential window. The charge-discharge curve is plotted as a function of cycling time. Reproduced by permission of Springer.

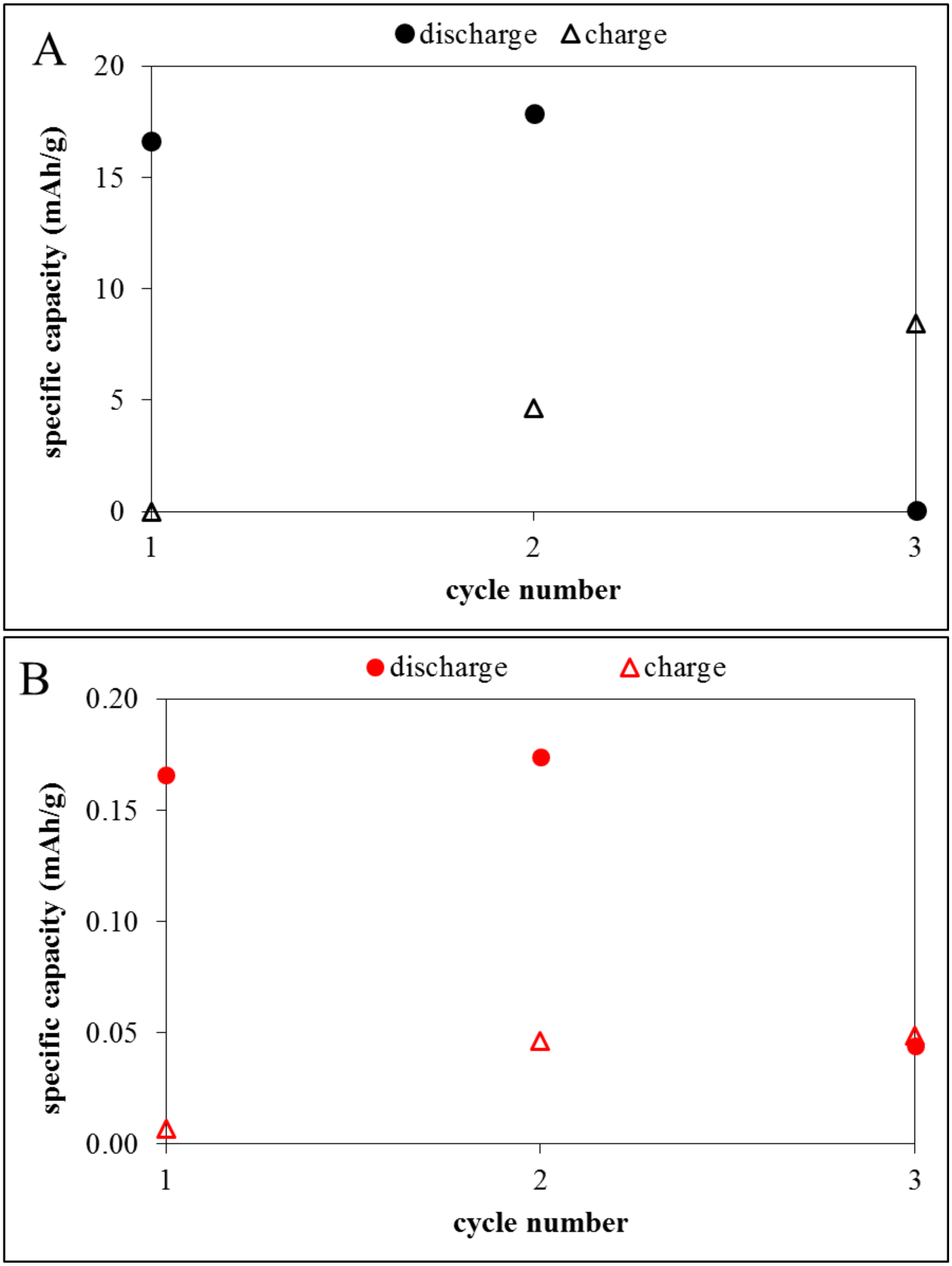

Figure 6.12. Electrochemical cycling of Li/$FePO_4$ cells under a rate of 0.018 mA/cm^2 and a 2.0 – 3.6 V potential window. Specific capacities for discharge and charge are shown as a function of cycle number for bulk-like (black) $FePO_4$ material (A), and nanowires of (red) $FePO_4$ material (B). Reproduced by permission of Springer.

It was further hypothesized that a modification of the voltage window for the discharge-charge rate may improve the lithiation of the $FePO_4$ material. Therefore, a third test was undertaken in terms of cycling both bulk-like and nanowire $FePO_4$ materials under a voltage range of 1.5 – 4.0 V at an 0.018 mA/cm^2 rate for ten cycles (Figure 6.13). For the bulk-like material, the cycle 1 discharge capacity was ~70 mAh/g for Cycle 1 and remained effectively constant at ~30 mAh/g for cycles 2- 10 (Figure 6.14A). The charge capacity remained at 30 – 40 mAh/g for all cycles, showing reasonable cycling efficiency but low capacity for the bulk-like material. For the nanowire material, the discharge capacities were < 4 mAh/g on all cycles, with very low charge capacities of <0.3 mAh/g on all cycles (Figure 6.14B).

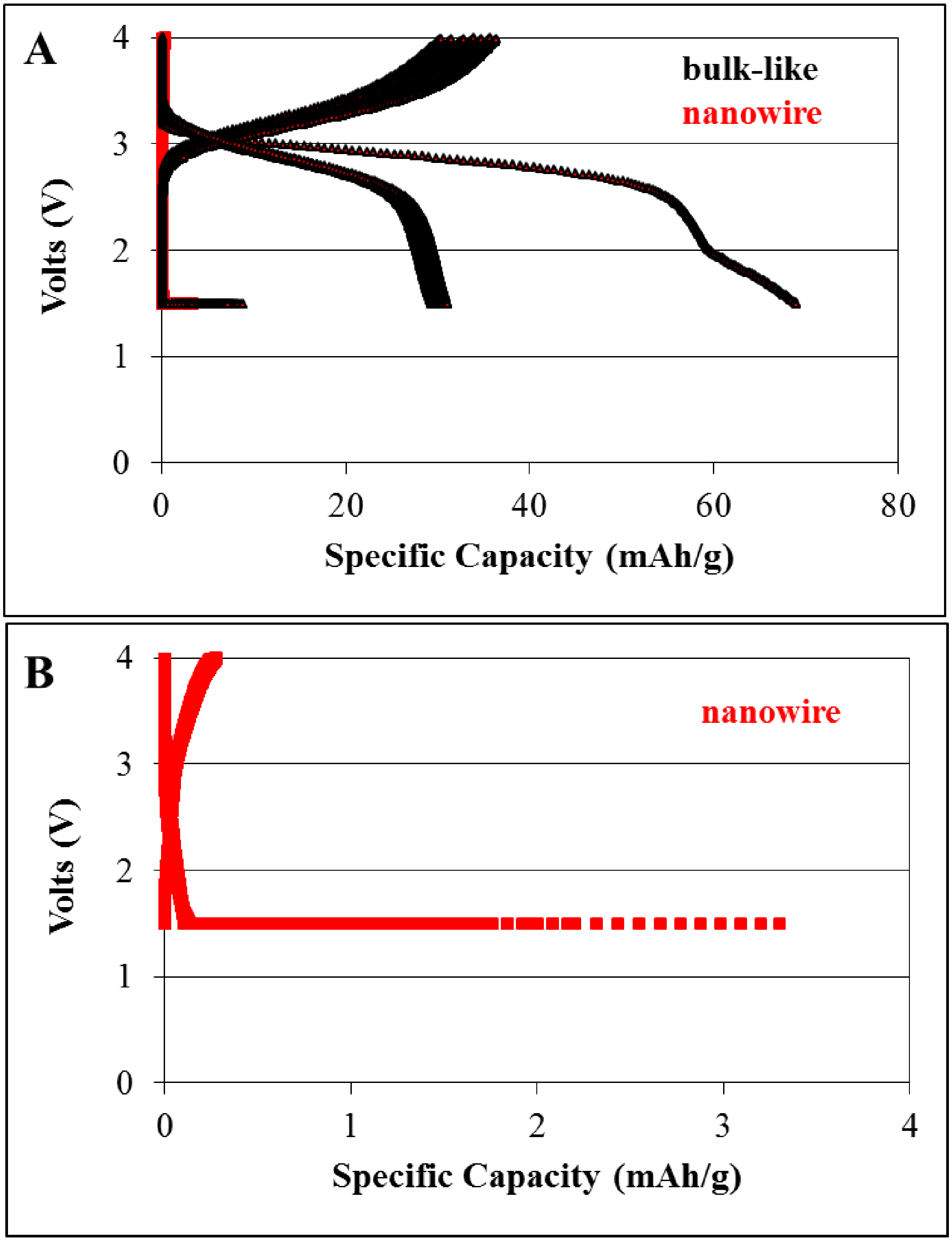

Figure 6.13. Electrochemical cycling of Li/$FePO_4$ cells under a 0.018 mA/cm^2 rate and in a 1.5 – 4.0 V potential window. Voltage versus specific capacity for (A) bulk-like (black) $FePO_4$ material and (B) nanowires (red) of $FePO_4$ material. Reproduced by permission of Springer.

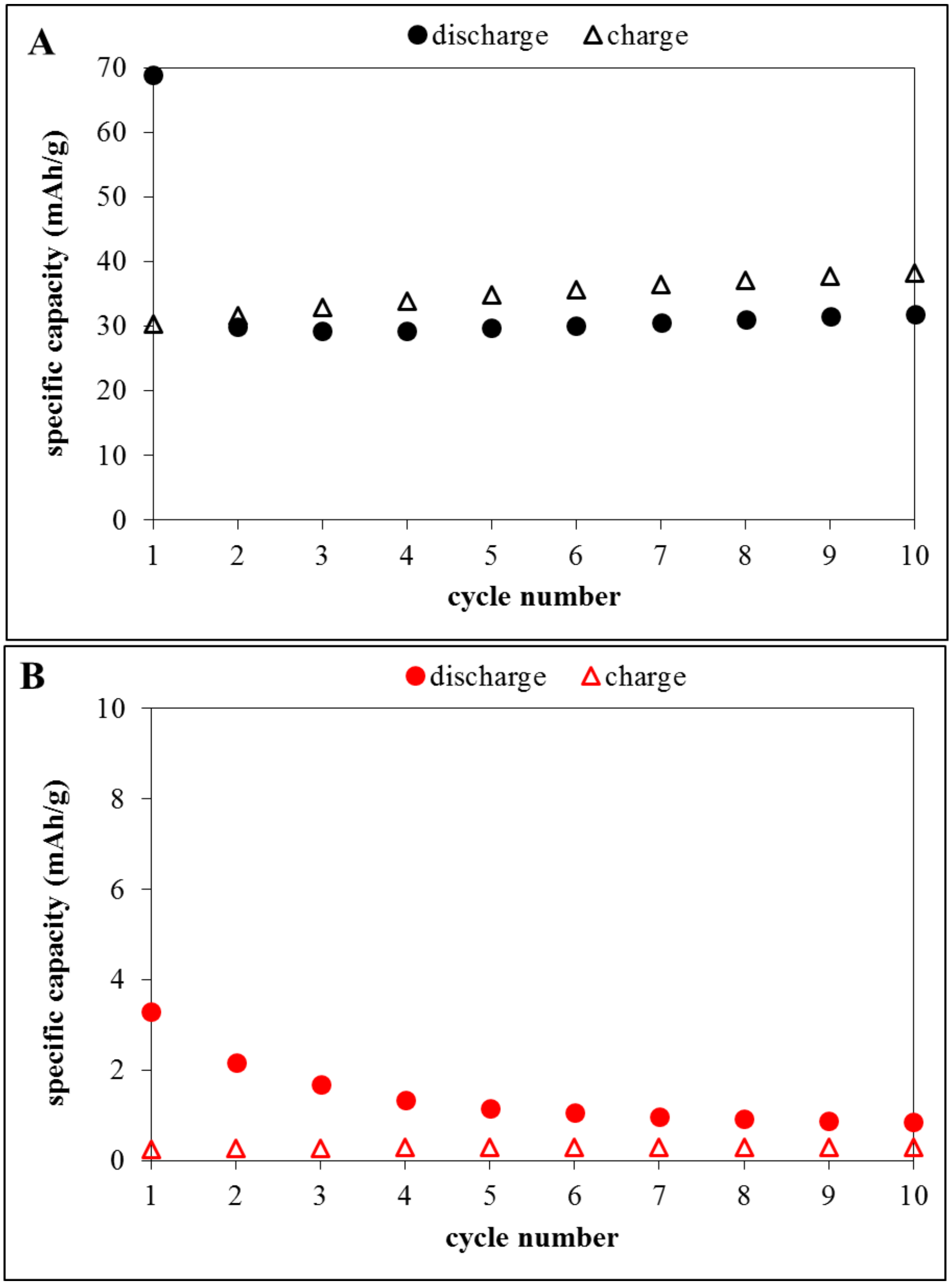

Figure 6.14. Electrochemical cycling of Li/$FePO_4$ cells under 0.018 mA/cm^2 rate and 1.5 – 4.0 V window. Specific capacity versus cycle number for (A) bulk-like (black) $FePO_4$ material and (B) nanowires (red) of $FePO_4$ material. Reproduced by permission of Springer.

Under all electrochemical lithiation conditions tested, the nanowire $FePO_4$ material showed less capability for lithiation relative to the bulk-like $FePO_4$ material. A recent first-principles study of the chemical bonding and conduction behavior of $LiFePO_4$ using maximallylocalized Wannier functions[62] lends additional insight into our empirical observations. Results of the calculations showed that the chemical bonding of Fe–O3 has an important function in the low-temperature conductivity of $LiFePO_4$, as small polaron hopping is mainly mediated by Fe–O3 chemical bonds. Notably, our Rietveld analysis of the bulk-like and nanowire $LiFePO_4$ materials (Table 6.1) showed similar Fe1, O1, and O2 positions, but different O3 positions. Thus, we propose that the Fe-O3 geometry in our nanowire materials may be less favorable than that in the bulk-like materials, providing (to the best of our knowledge) the first empirical evidence with which to support this theory.

6.3. Conclusions

The strength of our contribution lies not only in our ability to generate lithium iron phosphate nanowires using mild reaction conditions with demonstrably high quality, crystallinity, and purity but also in our deliberate approach in including a set of results emanating from the use of a sophisticated toolkit of complementary structural characterization (including synchrotron-based) techniques that have rarely been applied to this material. Specifically, in this study, we have described our success in the diameter and shape-controlled synthesis of 1D $LiFePO_4$ nanostructures under sustainable conditions.

Building upon our previous work, we have utilized an ambient, seedless, surfactantless, wet-solution-based U-tube method to generate 1D amorphous $FePO_4$ precursors through the precipitation of $FeCl_3$ and Na_3PO_4. The precursor chemistry and reaction time were optimized to yield chemically pure, high-quality amorphous $FePO_4$ nanowires, with spatial control over the diameters of the nanowires achieved through appropriately varying the pore size channel of the commercially available template. We have successfully converted our amorphous starting precursor material into the electrochemically active $LiFePO_4$ through chemical lithiation, while maintaining the specified size and 1D morphology.

Structural characterization of the as-prepared 50 nm and 200 nm diameter crystalline $LiFePO_4$ material showed that the one-dimensional samples grew anisotropically along the *a*-axis direction, thereby exposing the *b*-direction. Specifically, a suite of high-resolution TEM techniques, including HAADF, SAED, and defocused diffraction methods, has confirmed the presence of enhanced crystallinity of both the 50 nm and 200 nm nanowires, taken from various regions. Moreover, our as-prepared 200 nm NWs were found to be not only phase pure but also single-crystalline by various additional characterization methods, including but not limited to synchrotron X-ray diffraction.

The size and morphology of these as-synthesized nanowires have had an impact upon their electrochemical efficiency, when employed in a coin cell setup. However, our technique was not necessarily optimal because of low sample quantity considerations, and the mechanical grinding may have fundamentally altered the morphology of our lithium iron phosphate materials when incorporated as a part of a functional electrode. Moreover, the relatively poor electronic conductivity, packing inhomogeneity, and poor contact with the current collector may also have affected the electrochemical performance of our 200 nm-diameter nanowires. Nevertheless, based on the collected charge/discharge curves, we were able to successfully demonstrate that, at a minimum, our $LiFePO_4$ material is electrochemically active. The electrochemical data for the chemically and electrochemically lithiated $FePO_4$materials showed consistent trends for the bulk-like and nanowire material, where the bulk-like materials exhibited higher capacities in each case. The capacity trends may relate to Fe-O3 geometry for materials, as recent calculations showed that the chemical bonding of Fe–O3 has an important function in the low-temperature conductivity of $LiFePO_4$.[62] As a positive step towards understanding and potentially improving upon Li ion diffusion at a structural level, we have demonstrated that our nanowires can be synthetically grown along the *a*-axis in terms of a viable growth direction.

6.4. References

1. Padhi, A. K.; Nanjundaswamy, K. S.; Masquelier, C.; Okada, S.; Goodenough, J. B., *Journal of the Electrochemical Society* **1997,** *144* 1609-1613.
2. Padhi, A. K.; Nanjundaswamy, K. S.; Goodenough, J. B., *Journal of the Electrochemical Society* **1997,** *144* 1188-1194.
3. Sides, C. R.; Croce, F.; Young, V. Y.; Martin, C. R.; Scrosati, B., *Electrochemical and Solid-State Letters* **2005,** *8* A484-A487.
4. Huang, X.; Yan, S.; Zhao, H.; Zhang, L.; Guo, R.; Chang, C.; Kong, X.; Han, H., *Materials Characterization* **2010,** *61* 720-725.
5. Chung, S.-Y.; Bloking, J. T.; Chiang, Y.-M., *Nature Materials* **2002,** *1* 123-128.
6. Xu, B.; Qian, D.; Wang, Z.; Meng, Y. S., *Materials Science and Engineering: R: Reports* **2012,** *73* 51-65.
7. Whittingham, M. S., *Chemical Reviews* **2004,** *104* 4271-4302.
8. Yi, T.-F.; Li, X.-Y.; Liu, H.; Shu, J.; Zhu, Y.-R.; Zhu, R.-S., *Ionics* **2012,** *18* 529-539.
9. Lee, K. T.; Jeong, S.; Cho, J., *Accounts of Chemical Research* **2013,** *46* 1161-1170.
10. Ellis, B.; Kan, W. H.; Makahnouk, W. R. M.; Nazar, L. F., *Journal of Materials Chemistry* **2007,** *17* 3248-3254.
11. Lee, M.-H.; Kim, T.-H.; Kim, Y. S.; Song, H.-K., *The Journal of Physical Chemistry C* **2011,** *115* 12255-12259.
12. Zheng, J.-c.; Li, X.-h.; Wang, Z.-x.; Guo, H.-j.; Zhou, S.-y., *Journal of Power Sources* **2008,** *184* 574-577.
13. Franger, S.; Le Cras, F.; Bourbon, C.; Rouault, H., *Journal of Power Sources* **2003,** *119–121* 252-257.
14. Arnold, G.; Garche, J.; Hemmer, R.; Ströbele, S.; Vogler, C.; Wohlfahrt-Mehrens, M., *Journal of Power Sources* **2003,** *119–121* 247-251.
15. Prosini, P. P.; Carewska, M.; Scaccia, S.; Wisniewski, P.; Passerini, S.; Pasquali, M., *Journal of the Electrochemical Society* **2002,** *149* A886-A890.
16. Kim, J.-K.; Choi, J.-W.; Chauhan, G. S.; Ahn, J.-H.; Hwang, G.-C.; Choi, J.-B.; Ahn, H.-J., *Electrochimica Acta* **2008,** *53* 8258-8264.
17. Hwang, B.-J.; Hsu, K.-F.; Hu, S.-K.; Cheng, M.-Y.; Chou, T.-C.; Tsay, S.-Y.; Santhanam, R., *Journal of Power Sources* **2009,** *194* 515-519.
18. Saravanan, K.; Balaya, P.; Reddy, M. V.; Chowdari, B. V. R.; Vittal, J. J., *Energy & Environmental Science* **2010,** *3* 457-463.
19. Chen, Z.-y.; Zhu, W.; Zhu, H.-l.; Zhang, J.-l.; Li, Q.-f., *Transactions of Nonferrous Metals Society of China* **2010,** *20* 809-813.
20. Liu, X.-h.; Wang, J.-q.; Zhang, J.-y.; Yang, S.-r., *Chinese Journal of Chemical Physics* **2006,** *19* 530-534.
21. Wang, G.; Shen, X.; Yao, J., *Journal of Power Sources* **2009,** *189* 543-546.
22. Teng, F.; Santhanagopalan, S.; Lemmens, R.; Geng, X.; Patel, P.; Meng, D. D., *Solid State Sciences* **2010,** *12* 952-955.
23. Zhu, C.; Yu, Y.; Gu, L.; Weichert, K.; Maier, J., *Angewandte Chemie International Edition* **2011,** *50* 6278-6282.
24. Koenigsmann, C.; Wong, S. S., *Energy & Environmental Science* **2011,** *4* 1161 - 1176.
25. Mao, Y.; Zhang, F.; Wong, S., *Advanced Materials* **2006,** *18* 1895-1899.
26. Santulli, A. C.; Feygenson, M.; Camino, F. E.; Aronson, M. C.; Wong, S. S., *Chemistry of Materials* **2011,** *23* 1000-1008.

27. Tiano, A. L.; Koenigsmann, C.; Santulli, A. C.; Wong, S. S., *Chemical Communications* **2010,** *46* 8093-8130.

28. Zhang, F.; Sfeir, M. Y.; Misewich, J. A.; Wong, S. S., *Chemistry of Materials* **2008,** *20* 5500-5512.

29. Zhang, F.; Wong, S. S., *Chemistry of Materials* **2009,** *21* 4541-4554.

30. Zhou, H.; Park, T.-J.; Wong, S. S., *Journal of Materials Research* **2006,** *21* 2941-2947.

31. Zhou, H.; Wong, S. S., *ACS Nano* **2008,** *2* 944-958.

32. Zhou, H.; Zhou, W.-p.; Adzic, R. R.; Wong, S. S., *Journal of Physical Chemistry C* **2009,** *113* 5460-5466.

33. Fisher, C. A. J.; Hart Prieto, V. M.; Islam, M. S., *Chemistry of Materials* **2008,** *20* 5907-5915.

34. Morgan, D.; Van der Ven, A.; Ceder, G., *Electrochemical and Solid-State Letters* **2004,** *7* A30-A32.

35. Hong, Y.-S.; Ryu, K. S.; Park, Y. J.; Kim, M. G.; Lee, J. M.; Chang, S. H., *Journal of Materials Chemistry* **2002,** *12* 1870-1874.

36. Kim, S.-W.; Ryu, J.; Park, C. B.; Kang, K., *Chemical Communications* **2010,** *46* 7409-7411.

37. Liu, Y.; Xu, Y.; Han, X.; Pellegrinelli, C.; Zhu, Y.; Zhu, H.; Wan, J.; Chung, A. C.; Vaaland, O.; Wang, C.; Hu, L., *Nano Letters* **2012,** *12* 5664-5668.

38. Patete, J. M.; Peng, X.; Koenigsmann, C.; Xu, Y.; Karn, B.; Wong, S. S., *Green Chemistry* **2011,** *13* 482-519.

39. Koenigsmann, C.; Santulli, A. C.; Sutter, E.; Wong, S. S., *ACS Nano* **2011,** *5* 7471-7487.

40. Park, T. J.; Mao, Y. B.; Wong, S. S., *Chemical Communications* **2004,** 2708-2709.

41. Zhou, H.; Yiu, Y.; Aronson, M. C.; Wong, S. S., *Journal of Solid State Chemistry* **2008,** *181* 1539-1545.

42. Koenigsmann, C.; Sutter, E.; Chiesa, T. A.; Adzic, R. R.; Wong, S. S., *Nano Letters* **2012,** *12* 2013-2020.

43. Hernandez-Sanchez, B. A.; Chang, K.-S.; Scancella, M. T.; Burris, J. L.; Kohli, S.; Fisher, E. R.; Dorhout, P. K., *Chemistry of Materials* **2005,** *17* 5909-5919.

44. Yang, Z.; Huang, Y.; Dong, B.; Li, H. L.; Shi, S. Q., *Applied Physics A* **2006,** *84* 117-122.

45. Kuang, Q.; Lin, Z.-W.; Lian, W.; Jiang, Z.-Y.; Xie, Z.-X.; Huang, R.-B.; Zheng, L.-S., *Journal of Solid State Chemistry* **2007,** *180* 1236-1242.

46. Zhang, F.; Wong, S. S., *ACS Nano* **2009,** *4* 99-112.

47. Koenigsmann, C.; Wong, S. S., *ACS Catalysis* **2013,** *3* 2031-2040.

48. Park, T.-J.; Mao, Y.; Wong, S. S., *Chemical Communications* **2004,** 2708-2709.

49. Koenigsmann, C.; Santulli, A. C.; Gong, K.; Vukmirovic, M. B.; Zhou, W.-p.; Sutter, E.; Wong, S. S.; Adzic, R. R., *Journal of the American Chemical Society* **2011,** *133* 9783-9795.

50. Koenigsmann, C.; Sutter, E.; Adzic, R. R.; Wong, S. S., *Journal of Physical Chemistry C* **2012,** *116* 15297-15306.

51. Wang, B.; Qiu, Y.; Ni, S., *Solid State Ionics* **2007,** *178* 843-847.

52. Galoustov, K.; Anthonisen, M.; Ryan, D. H.; MacNeil, D. D., *Journal of Power Sources* **2011,** *196* 6893-6897.

53. Islam, M. S.; Driscoll, D. J.; Fisher, C. A. J.; Slater, P. R., *Chemistry of Materials* **2005,** *17* 5085-5092.

54. Nan, C.; Lu, J.; Li, L.; Li, L.; Peng, Q.; Li, Y., *Nano Research* **2013,** *6* 469-477.

55. Chung, S.-Y.; Choi, S.-Y.; Yamamoto, T.; Ikuhara, Y., *Angewandte Chemie International Edition* **2009,** *48* 543-546.
56. Yang, S.; Song, Y.; Zavalij, P. Y.; Stanley Whittingham, M., *Electrochemistry Communications* **2002,** *4* 239-244.
57. Chen, J.; Graetz, J., *ACS Applied Materials & Interfaces* **2011,** *3* 1380-1384.
58. Axmann, P.; Stinner, C.; Wohlfahrt-Mehrens, M.; Mauger, A.; Gendron, F.; Julien, C. M., *Chemistry of Materials* **2009,** *21* 1636-1644.
59. Lee, M.-H.; Kim, T.-H.; Kim, Y. S.; Park, J.-S.; Song, H.-K., *Journal of Materials Chemistry* **2012,** *22* 8228-8234.
60. Yuan, L.-X.; Wang, Z.-H.; Zhang, W.-X.; Hu, X.-L.; Chen, J.-T.; Huang, Y.-H.; Goodenough, J. B., *Energy & Environmental Science* **2011,** *4* 269-284.
61. Gaberscek, M.; Dominko, R.; Jamnik, J., *Electrochemistry Communications* **2007,** *9* 2778-2783.
62. Kou, X.-j.; Ke, H.; Zhu, C.-b.; Rolfe, P., *Chemical Physics* **2015,** *446* 1-6.

Chapter 7 - Conclusions

7.1. Conclusions

The experiments described within this thesis represent a logical and straightforward approach at synthesizing and characterizing various nanoscale materials. Not only have we been able to tailor and tune chemical composition and morphology, but also control various parameters so as to optimize performance for a number of applications, including fuel cells and batteries. Nanomaterials produced in this thesis were generated by using reasonably ambient and mild synthetic techniques in order to minimize negative environmental impacts while achieving high purity and crystallinity.

In Chapter 3, the synthesis and characterization of ultrathin ternary PtRuFe alloy nanowires were investigated as catalyst materials for the methanol oxidation reaction. An ambient and facile synthesis method was employed to generate nanowire networks with average diameters of 2 nm. 1D nanomaterials are highly advantageous for catalytic reactions, due to their intrinsic stability and reduction in deleterious defects. Moreover, the Pt_7Ru_2Fe NW catalyst evinced the highest MOR activity as compared with the other PtRuFe alloy nanowires, possessing an activity of 1.1 mA/cm^2 at 0.65 V vs. RHE. Additionally, this catalyst exhibited enhanced stability as compared with commercial PtRu NP/C, maintaining a steady state current density of 0.605 mA/cm^2, whereas PtRu NP/C only achieved a current density of 0.051 mA/cm^2. As a result, optimized performance and durability were attributed to the specific ratio between Ru and Fe, with Ru likely promoting methanol oxidation through the indirect pathway, whereas Fe enabled the direct pathway through the formation of a formic acid intermediate.

In Chapter 4, the same synthetic method employing CTAB as an inverse micelle network was utilized to generate multiple binary Pt-based alloy nanowires. Specifically, PtM (M = Ru, Fe, Co, Au, Cu) nanowires were produced as anode catalysts for the hydrogen oxidation reaction in alkaline media. Moreover, the effect of alloying was investigated using a variety of techniques including XPS and EELS in order to make correlations between the presence of *d*-band vacancies and the HBE. In essence, the PtRu NW catalyst yielded the fastest kinetics and highest HOR exchange current density (0.493 mA/cm^2) as compared with Pt NWs (0.209 mA/cm^2), a finding attributable to electron density withdrawal from Pt, thereby producing a more favorable HBE value.

In Chapter 5, the effect of alternative support materials to carbon were investigated. More specifically, binary and ternary metal oxides, including TiO_2, RuO_2, $SrTiO_3$ and $SrRuO_3$, have been employed as supports for Pt NPs, and these oxide materials were subsequently tested for the methanol oxidation reaction. In effect, a favorable metal-support interaction was found between the $SrRuO_3$ substrates and Pt NPs, with the supports withdrawing electron density from the Pt *4f* orbitals. This resulted in an observed enhanced catalytic activity for the Pt/$SrRuO_3$ (37.3 nm) sample, achieving an activity of 1.42 mA/cm^2 as compared with commercial Pt NP/C possessing an activity of 0.31 mA/cm^2, collected at 0.7 V vs. RHE.

Chapter 6 discussed the effect of morphology, electronic structure, and purity of $LiFePO_4$ nanomaterials on the electrochemical performance of Li ion batteries. More specifically, an ambient, surfactantless template-based method was employed to generate highly anisotropic $LiFePO_4$ nanowires with diameters consistent with the pore sizes of the template employed. The NWs exhibited high purity and crystallinity, with a growth direction along the *a*-axis, allowing for the favorable orientation of the *b*-axis along the diameter of the nanowire. Although the observed electrochemical performance was unfavorable, producing low capacities, it was discovered that this result was a consequence of the geometry of the nanowire, specifically the

Fe-O3 geometry which has been shown to significantly influence conductivity under low temperature operations.

7.2. Future Directions

Throughout this thesis, we have demonstrated our ability to not only control the synthesis of our nanostructures but also acquire a basic understanding of data derived from the acquired characterization methods. Moreover, our work highlights significant promise for the development of fuel cell catalysts and cathode materials for Li ion batteries.

Specifically, in terms of trends in the field, many groups are generating non-precious metal catalytic analogues to lower the overall cost of the fuel cell catalyst, which is a large inhibitor for widespread commercialization. As mentioned, Pt is still the most efficient metal for most fuel cell reactions, with PtRu typically employed as an anode catalyst. Currently, catalysts such as but not limited to CoNiMo NPs[1] used for the hydrogen oxidation reaction in alkaline media and $Ni_xCo_{3-x}O_4$[2] catalysts utilized for the methanol oxidation reaction in alkaline media, are being explored and further optimized to compete with Pt-based materials. Conversely, it will be more difficult to generate non-precious metal catalysts for acidic media, since most succumb to dissolution and degradation. Nonetheless, the transition from Pt to other more cost effective and abundant transition metals such as but not limited to Fe, Co, and Ni is necessary for the widespread commercialization of fuel cells.

Additionally, beyond the use of more abundant and cost-effective metals, it will be necessary to expand beyond either a mono-metallic or binary metallic catalyst composition. As suggested above, many groups are leaning towards the development of more complex combinations of ternary or even quaternary nanomaterials, in addition to intricate permutations of different varieties of catalysts.[3-5] This strategy allows for the creation of a 'catalyst' that encompasses an assortment of attributes so as to address a wide range of issues with a particular reaction. For instance, a PtRuOsIr catalyst demonstrated an accelerated reaction process for MOR, thereby leading to enhanced efficiencies for DMFC applications. More specifically, the use of Ir led to better C-H activation for methanol oxidation, whereas the roles of Ru and Os were in promoting water adsorption.[3] Furthermore, the growing knowledge base and associated understanding of reaction mechanisms will continue to lead to the development of more complex and effective catalyst materials, so as to address existing technical obstacles.

Moreover, scientists within the fuel cell field have begun to recognize the significance and advantages associated with the 1D morphology. With the beneficial combination of anisotropy, high aspect ratio, and enhanced stability, efforts have focused on the investigation of alloyed, core-shell, and hierarchical motifs, respectively, of a 1D structure as compared with the traditional nanoparticle morphology.[6-10] For example, Pt@Ru NTs have been developed for the hydrogen oxidation reaction in alkaline media and these evinced a surface specific activity of 2.4 mA/cm^2 at 0.05 V vs. RHE, which is 2.5 times greater than that of Pt NTs.[7] Additionally, Pd@Cu NWs can realize a mass exchange current density of 0.33 A/mg_{PGM}^{-1} for the hydrogen oxidation reaction in basic media and achieve 95% of the activity threshold normally attained for Pt NP/C.[6] The analysis of similar types of 1D nanostructures will continue, as this research area is still relatively nascent.

Regarding support materials, with the ability either to dope carbon-based supports with nitrogen or to partially reduce them to not only improve stability and durability but also provide for beneficial metal-support interactions, carbon materials such as either graphene or CNTs still exist as the primary support material for catalysts.[5, 11-13] However, although metal oxide supports still represent a more stable alternative to carbon-based materials, in most instances, they do not possess the same conductive behavior as carbon yields with respect to as-deposited catalyst material, immobilized on its surface. Recently, research has turned to support materials that contain a combination of these two material support alternatives, i.e. stable metal oxides coupled with carbon-based materials.[14, 15] For example, a graphene-based porous carbon-Pd/SnO_2 nanocomposite has shown enhanced activity for the methanol oxidation reaction, maintaining 85% of its activity after 500 cycles, with the improved performance attributable not only to the enhanced conductivity of the graphene but also to the greater CO tolerance resulting from the addition of the SnO_2.[14]

Additionally, carbon materials combined with Fe-N-C composites have been developed as promising alternative catalysts to Pt.[16-20] These particular catalysts are almost completely unaffected by the presence of small molecules such as methanol or CO, which can significantly hinder and inhibit catalytic reactions. Although this is a highly beneficial attribute, the activities of these composites for either ORR or the oxygen evolution reaction (OER) are unfortunately not even remotely competitive with current commercial catalysts.

Li-ion batteries also represent a clean energy alternative to fossil fuel-based components. However, with the employment of either a carbon or graphene-based anode material, the theoretical capacity is reduced significantly as compared with using Li metal. Moreover, most Li metal batteries suffer from either detrimental side reactions that significantly influence cell lifetimes or safety concerns as a result of Li dendrite formation or unstable electrodeposition. As a way to mitigate for these issues, research has transitioned to the use of less hazardous and more abundant metals such as Al or Na.[21]

Additionally, the employment of metal oxides as cathode materials for Li ion batteries typically results in the formation of insulating metal oxide layers at the interface, which subsequently lead to the formation of high reaction barriers. Therefore, some have begun investigating metal organic frameworks to address and alleviate this particular problem.[22] In both technologies, significant work still needs to be performed and optimized to keep up with the current standards of fossil fuel-based technologies and be utilized as a clean energy alternative.

Moreover, carbon-based materials such as graphene and CNTs are being developed as conductive additives to anode and cathode materials as a result of their low electrical conductivity.[23-26] For instance, reduced graphene oxide possesses high electrical conductivity as well as high surface area, which lead to a capacity retention rate of 93% after 1000 cycles at a 10C rate for reduced graphene oxide-modified $LiMn_{0.75}Fe_{0.25}PO_4$ microspheres.[24]

More recently, research has shifted focus to a more optimal battery, i.e. the Li-air battery. This type of battery oxidizes lithium at the anode and reduces oxygen at the cathode. However, as with Li-ion batteries, the safety concern associated with metallic lithium is still present. Additionally, the cathode materials, in this case, are typically noble metals, which present a significant cost issue, and again, it is likely that more economical alternatives will be developed. Nevertheless, Li-air batteries possesses the highest theoretical capacity as compared with other types of batteries, with the possibility of storing 10 times the amount of energy of that normally associated with Li-ion batteries.

In addition to the optimization of catalysts through chemical means, there is also a significant need to expand upon the characterization tools utilized for analyses of samples used for fuel cell and battery applications. For example, beamline techniques, such as pair distribution function (PDF), which measures the distances between particles and atoms within a material, and inner shell spectroscopy (ISS), which gauges changes in oxidation states under *operando* conditions, would be highly beneficial tools for the characterization of nanomaterials.

Specifically, PDF measurements can enable the analysis of specific distances between atoms within an alloy structure, which in turn would provide insight not only into the type of strain present within the material but also the extent of that strain. These data could then be correlated with the activity of a particular material in question by comparison with that of a pure monometallic standard. The ISS technique moreover would be advantageous for measuring changes in the oxidation state during battery operation.

Other techniques include *in-situ* infrared spectroscopy (*in-situ* IR) and electron microscopy. *In-situ* IR could probe the formation of specific intermediates during a reaction process, allowing for identification of species produced in a particular reaction pathway. For example, the methanol and ethanol oxidation reactions possess a number of plausible pathways, which Adzic and co-workers were able to successfully narrow down to more precise scenarios through the employment of *in-situ* IR.[27] Moreover, liquid cell electron microscopy could also be utilized to investigate the growth mechanism of a particular nanomaterial. For instance, the growth kinetics of Fe_3Pt-Fe_2O_3 core-shell nanoparticles have been investigated using this technique, and insights into a plausible formation pathway were acquired as a result.[28] Such studies would enable information to be acquired about the specific facets and planes that participate in the overall growth process, findings which can hopefully be generalized to further an understanding of the generation of materials possessing a similar class of chemical composition. Hence, advanced characterization techniques will play a major role in the development and optimization of nanomaterials and contribute to the advancement of both fuel cells and batteries.

7.3. References

1. Sheng, W.; Bivens, A. P.; Myint, M.; Zhuang, Z.; Forest, R. V.; Fang, Q.; Chen, J. G.; Yan, Y., *Energy & Environmental Science* **2014,** *7* 1719-1724.
2. Manivasakan, P.; Ramasamy, P.; Kim, J., *Nanoscale* **2014,** *6* 9665-9672.
3. Dimakis, N.; Flor, F. A.; Navarro, N. E.; Salgado, A.; Smotkin, E. S., *The Journal of Physical Chemistry C* **2016,** *120* 10427-10441.
4. Kim, J. H.; Kwon, S. Y.; Bhattacharjya, D.; Chai, G. S.; Yu, J.-S., *Journal of Catalysis* **2013,** *306* 133-145.
5. Zhao, P.; Xu, W.; Hua, X.; Luo, W.; Chen, S.; Cheng, G., *The Journal of Physical Chemistry C* **2016,** *120* 11006-11013.
6. Alia, S. M.; Yan, Y., *Journal of The Electrochemical Society* **2015,** *162* F849-F853.
7. St. John, S.; Atkinson, R. W.; Unocic, K. A.; Unocic, R. R.; Zawodzinski, T. A.; Papandrew, A. B., *ACS Catalysis* **2015,** *5* 7015-7023.
8. Zhang, N.; Guo, S.; Zhu, X.; Guo, J.; Huang, X., *Chemistry of Materials* **2016**.
9. Zhao, Y.; Liu, J.; Liu, C.; Wang, F.; Song, Y., *ACS Catalysis* **2016,** 4127-4134.
10. Wang, Q.-L.; Fang, R.; He, L.-L.; Feng, J.-J.; Yuan, J.; Wang, A.-J., *Journal of Alloys and Compounds* **2016**.
11. Liang, Y.; Wei, J.; Zhang, X.; Zhang, J.; Jiang, S. P.; Wang, H., *ChemCatChem* **2016,** *8* 1-5.
12. Zhang, W.; Yao, Q.; Wu, X.; Fu, Y.; Deng, K.; Wang, X., *Electrochimica Acta* **2016,** *200* 131-141.
13. Zhang, X.; Zhu, J.; Tiwary, C. S.; Ma, Z.; Huang, H.; Zhang, J.; Lu, Z.; Huang, W.; Wu, Y., *ACS Applied Materials & Interfaces* **2016,** *8* 10858-10865.
14. Nan, L.; Fan, Z.; Yue, W.; Dong, Q.; Zhu, L.; Yang, L.; Fan, L., *Journal of Materials Chemistry A* **2016,** *4* 8898-8904.
15. Li, L.; Qian, Y.; Yang, J.; Tan, X.; Dai, Z.; Jin, Y.; Wang, H.; Qu, W.; Chu, Y., *International Journal of Hydrogen Energy* **2016,** *41* 9284-9294.
16. Zhao, S.; Yin, H.; Du, L.; He, L.; Zhao, K.; Chang, L.; Yin, G.; Zhao, H.; Liu, S.; Tang, Z., *ACS Nano* **2014,** *8* 12660-12668.
17. Wang, M.-Q.; Yang, W.-H.; Wang, H.-H.; Chen, C.; Zhou, Z.-Y.; Sun, S.-G., *ACS Catalysis* **2014,** *4* 3928-3936.
18. Liang, J.; Zhou, R. F.; Chen, X. M.; Tang, Y. H.; Qiao, S. Z., *Advanced Materials* **2014,** *26* 6074-6079.
19. Deng, D.; Yu, L.; Chen, X.; Wang, G.; Jin, L.; Pan, X.; Deng, J.; Sun, G.; Bao, X., *Angewandte Chemie International Edition* **2013,** *52* 371-375.
20. Dong, Q.; Zhuang, X.; Li, Z.; Li, B.; Fang, B.; Yang, C.; Xie, H.; Zhang, F.; Feng, X., *Journal of Materials Chemistry A* **2015,** *3* 7767-7772.
21. Tu, Z.; Nath, P.; Lu, Y.; Tikekar, M. D.; Archer, L. A., *Accounts of Chemical Research* **2015,** *48* 2947-2956.
22. Peng, Z.; Yi, X.; Liu, Z. X.; Shang, J.; Wang, D., *ACS Applied Materials & Interfaces* **2016**.
23. Fu, Y.; Wei, Q.; Lu, B.; Wang, X.; Sun, S., *Journal of Alloys and Compounds* **2016**.
24. Kim, M.-S.; Kim, H.-K.; Lee, S.-W.; Kim, D.-H.; Ruan, D.; Chung, K. Y.; Lee, S. H.; Roh, K. C.; Kim, K.-B., *Scientific Reports* **2016,** *6* 26686.

25. Marka, S. K.; Petnikota, S.; Vadali, S. V. S. S.; Reddy, M. V. V.; Adams, S.; Chowdari, B. V. R., *RSC Advances* **2016**.
26. Sun, Y.; Zhao, C.; Shen, M.; Pan, Z.; Liu, X., *Journal of Alloys and Compounds* **2016,** *683* 191-197.
27. Li, M.; Liu, P.; Adzic, R. R., *The Journal of Physical Chemistry Letters* **2012,** *3* 3480-3485.
28. Liang, W.-I.; Zhang, X.; Zan, Y.; Pan, M.; Czarnik, C.; Bustillo, K.; Xu, J.; Chu, Y.-H.; Zheng, H., *Journal of the American Chemical Society* **2015,** *137* 14850-14853.

Chapter 8 - Full List of References

8.1. Full Reference List

1. Garbarino, S.; Ponrouch, A.; Pronovost, S.; Gaudet, J.; Guay, D., *Electrochemistry Communications* **2009,** *11* 1924-1927.
2. Koenigsmann, C.; Wong, S. S., *Energy & Environmental Science* **2011,** *4* 1161-1176.
3. Wang, C.; Waje, M.; Wang, X.; Tang, J. M.; Haddon, R. C.; Yan, *Nano Letters* **2004,** *4* 345-348.
4. Smith, P. A.; Nordquist, C. D.; Jackson, T. N., *Applied Physics Letters* **2000,** *77* 1399-1401.
5. Zhou, W.-P.; Li, M.; Koenigsmann, C.; Ma, C.; Wong, S. S.; Adzic, R. R., *Electrochimica Acta* **2011,** *56* 9824-9830.
6. Liu, H.; Adzic, R. R.; Wong, S. S., *ACS Applied Materials & Interfaces* **2015,** *7* 26145-26157.
7. Winter, M.; Brodd, R. J., *Chemical Reviews* **2004,** *104* 4245-4270.
8. Bockris, J. O. M.; Reddy, A. K. N., *Modern Electrochemistry*. Plenum Press: New York, 1970.
9. Aricò, A. S.; Bruce, P.; Scrosati, B.; Tarascon, J.-M.; van Schalkwijk, W., *Nature Materials* **2005,** *4* 366-377.
10. Scofield, M. E.; Liu, H.; Wong, S. S., *Chemical Society Reviews* **2015,** *44* 5836-5860.
11. Sun, Y.; Zhou, T.; Pan, Q.; Zhang, X.; Guo, J., *RSC Advances* **2015,** *5* 60237-60245.
12. Bullion, J. Platinum price per gram.
13. James, B. D.; Kalinoski, J.; Baum, K., *Manufacturing Cost Analysis of Fuel Cell Systems*. U.S. Department of Energy: Arlington, VA, USA, 2011.
14. Sharma, S.; Pollet, B. G., *Journal of Power Sources* **2012,** *208* 96-119.
15. Kangasniemi, K. H.; Condit, D. A.; Jarvi, T. D., *Journal of The Electrochemical Society* **2004,** *151* E125-E132.
16. Antolini, E.; Gonzalez, E. R., *Solid State Ionics* **2009,** *180* 746-763.
17. Abida, B.; Chirchi, L.; Baranton, S.; Napporn, T. W.; Kochkar, H.; Léger, J.-M.; Ghorbel, A., *Applied Catalysis B: Environmental* **2011,** *106* 609-615.
18. Yu, N.; Kuai, L.; Wang, Q.; Geng, B., *Nanoscale* **2012,** *4* 5386-5393.
19. Hua, H.; Hu, C.; Zhao, Z.; Liu, H.; Xie, X.; Xi, Y., *Electrochimica Acta* **2013,** *105* 130-136.
20. Xiao, Y.; Zhan, G.; Fu, Z.; Pan, Z.; Xiao, C.; Wu, S.; Chen, C.; Hu, G.; Wei, Z., *Electrochimica Acta* **2014,** *141* 279-285.
21. Tauster, S. J., *Accounts of Chemical Research* **1987,** *20* 389-394.
22. Fu, Q.; Wagner, T., *Surface Science Reports* **2007,** *62* 431-498.
23. Tauster, S. J.; Fung, S. C., *Journal of Catalysis* **1978,** *55* 29-35.
24. Baker, R. T. K.; Prestridge, E. B.; McVicker, G. B., *Journal of Catalysis* **1984,** *89* 422-432.
25. Raupp, G. B.; Dumesic, J. A., *Journal of Catalysis* **1986,** *97* 85-99.
26. Baker, R. T. K.; Prestridge, E. B.; Murrell, L. L., *Journal of Catalysis* **1983,** *79* 348-358.
27. Bernal, S.; Calvino, J. J.; Cauqui, M. A.; Gatica, J. M.; Larese, C.; Pérez Omil, J. A.; Pintado, J. M., *Catalysis Today* **1999,** *50* 175-206.

28. Penner, S.; Wang, D.; Su, D. S.; Rupprechter, G.; Podloucky, R.; Schlögl, R.; Hayek, K., *Surface Science* **2003,** *532–535* 276-280.
29. Wang, D.; Penner, S.; Su, D. S.; Rupprechter, G.; Hayek, K.; Schlögl, R., *Journal of Catalysis* **2003,** *219* 434-441.
30. Fu, Q.; Wagner, T.; Olliges, S.; Carstanjen, H.-D., *The Journal of Physical Chemistry B* **2005,** *109* 944-951.
31. Bernal, S.; Calvino, J. J.; Cauqui, M. A.; Gatica, J. M.; López Cartes, C.; Pérez Omil, J. A.; Pintado, J. M., *Catalysis Today* **2003,** *77* 385-406.
32. Raj, R.; Saha, A.; An, L.; Hasselman, D. P. H.; Ernst, P., *Acta Materialia* **2002,** *50* 1165-1176.
33. Yu, Y.; Mark, J.; Ernst, F., *Journal of Materials Science* **2006,** *41* 7785-7797.
34. Antolini, E.; Gonzalez, E. R., *Journal of Power Sources* **2010,** *195* 3431-3450.
35. Snell, K. D.; Keenan, A. G., *Electrochimica Acta* **1982,** *27* 1683-1696.
36. Lamy, C., *Electrochimica Acta* **1984,** *29* 1581-1588.
37. Leiva, E. P. M.; Giordano, M. C., *Journal of The Electrochemical Society* **1983,** *130* 1305-1312.
38. Smirnov, P.; Wakita, H.; Yamaguchi, T., *The Journal of Physical Chemistry B* **1998,** *102* 4802-4808.
39. Teliska, M.; Murthi, V. S.; Mukerjee, S.; Ramaker, D. E., *The Journal of Physical Chemistry C* **2007,** *111* 9267-9274.
40. Olivera, P. P.; Parito, M.; Sellers, H., Electronic structure calculations of polyatomic oxyanions adsorbed on metal surfaces. In *Interfacial Electrochemistry,* Wieckowski, A., Ed. Marcel-Dekker: New York, 1999; p 63.
41. Merle, G.; Wessling, M.; Nijmeijer, K., *Journal of Membrane Science* **2011,** *377* 1-35.
42. Kruusenberg, I.; Mondal, J.; Matisen, L.; Sammelselg, V.; Tammeveski, K., *Electrochemistry Communications* **2013,** *33* 18-22.
43. Xing, Z.; Li, Q.; Wang, D.; Yang, X.; Sun, X., *Electrochimica Acta* **2016,** *191* 841-845.
44. Li, X.; Popov, B. N.; Kawahara, T.; Yanagi, H., *Journal of Power Sources* **2011,** *196* 1717-1722.
45. Sheng, W.; Bivens, A. P.; Myint, M.; Zhuang, Z.; Forest, R. V.; Fang, Q.; Chen, J. G.; Yan, Y., *Energy & Environmental Science* **2014,** *7* 1719-1724.
46. Kadirgan, F.; Beden, B.; Leger, J. M.; Lamy, C., *Journal of Electroanalytical Chemistry and Interfacial Electrochemistry* **1981,** *125* 89-103.
47. Durst, J.; Siebel, A.; Simon, C.; Hasche, F.; Herranz, J.; Gasteiger, H. A., *Energy & Environmental Science* **2014,** *7* 2255-2260.
48. Sheng, W.; Gasteiger, H. A.; Shao-Horn, Y., *Journal of The Electrochemical Society* **2010,** *157* B1529-B1536.
49. Narayan, S. R.; Valdez, T. I., *Electrochem. Soc. Interface* **2008,** *17* 40-45.
50. Wang, C.-H.; Chen, L.-C.; Chen, K.-H., *Electrocatalysis of Direct Methanol Fuel Cells: From Fundamentals to Applications*. John Wiley and Sons: 2009; p 606.
51. Cuesta, A., *Journal of the American Chemical Society* **2006,** *128* 13332-13333.
52. Neurock, M.; Janik, M.; Wieckowski, A., *Faraday Discussions* **2008,** *140* 363-378.
53. Housmans, T. H. M.; Koper, M. T. M., *The Journal of Physical Chemistry B* **2003,** *107* 8557-8567.
54. Lai, S. C. S.; Lebedeva, N. P.; Housmans, T. H. M.; Koper, M. T. M., *Topics in Catalysis* **2007,** *46* 320-333.

55. Chen, Y. X.; Heinen, M.; Jusys, Z.; Behm, R. J., *Angewandte Chemie International Edition* **2006,** *45* 981-985.
56. Yu, X.; Pickup, P. G., *Journal of Power Sources* **2008,** *182* 124-132.
57. Markovic, N. M.; Sarraf, S. T.; Gasteiger, H. A.; Ross, P. N., *Journal of the Chemical Society, Faraday Transactions* **1996,** *92* 3719-3725.
58. Marković, N. M.; Ross Jr, P. N., *Surface Science Reports* **2002,** *45* 117-229.
59. Bagotzky, V. S.; Osetrova, N. V., *Journal of Electroanalytical Chemistry and Interfacial Electrochemistry* **1973,** *43* 233-249.
60. Mahoney, E. G.; Sheng, W.; Yan, Y.; Chen, J. G., *ChemElectroChem* **2014,** *1* 2058-2063.
61. Krischer, K.; Savinova, E. R., *Handbook of Heterogeneous Catalysis*. Wiley-VCH Verlag GmbH & Co. KGaA: 2008.
62. St. John, S.; Atkinson, R. W.; Unocic, K. A.; Unocic, R. R.; Zawodzinski, T. A.; Papandrew, A. B., *ACS Catalysis* **2015,** *5* 7015-7023.
63. Shinagawa, T.; Garcia-Esparza, A. T.; Takanabe, K., *Scientific Reports* **2015,** *5* 13801.
64. Conway, B. E.; Bai, L., *Journal of Electroanalytical Chemistry* **1986,** *198* 149-175.
65. Watanabe, M.; Saegusa, S.; Stonehart, P., *Journal of Electroanalytical Chemistry and Interfacial Electrochemistry* **1989,** *271* 213-220.
66. Song, Y.; Garcia, R. M.; Dorin, R. M.; Wang, H.; Qiu, Y.; Coker, E. N.; Steen, W. A.; Miller, J. E.; Shelnutt, J. A., *Nano Letters* **2007,** *7* 3650-3655.
67. Jambunathan, K.; Jayaraman, S.; Hillier, A. C., *Langmuir* **2004,** *20* 1856-1863.
68. Moore, J. T.; Corn, J. D.; Chu, D.; Jiang, R.; Boxall, D. L.; Kenik, E. A.; Lukehart, C. M., *Chemistry of Materials* **2003,** *15* 3320-3325.
69. Yajima, T.; Uchida, H.; Watanabe, M., *The Journal of Physical Chemistry B* **2004,** *108* 2654-2659.
70. Fachini, E. R.; Díaz-Ayala, R.; Casado-Rivera, E.; File, S.; Cabrera, C. R., *Langmuir* **2003,** *19* 8986-8993.
71. González, M. J.; Peters, C. H.; Wrighton, M. S., *The Journal of Physical Chemistry B* **2001,** *105* 5470-5476.
72. Park, K.-W.; Choi, J.-H.; Sung, Y.-E., *The Journal of Physical Chemistry B* **2003,** *107* 5851-5856.
73. Liu, F.; Lee, J. Y.; Zhou, W., *The Journal of Physical Chemistry B* **2004,** *108* 17959-17963.
74. Casado-Rivera, E.; Volpe, D. J.; Alden, L.; Lind, C.; Downie, C.; Vázquez-Alvarez, T.; Angelo, A. C. D.; DiSalvo, F. J.; Abruña, H. D., *Journal of the American Chemical Society* **2004,** *126* 4043-4049.
75. Villullas, H. M.; Mattos-Costa, F. I.; Bulhões, L. O. S., *The Journal of Physical Chemistry B* **2004,** *108* 12898-12903.
76. Liu, H.; Iglesia, E., *The Journal of Physical Chemistry B* **2005,** *109* 2155-2163.
77. Park, K.-W.; Ahn, K.-S.; Nah, Y.-C.; Choi, J.-H.; Sung, Y.-E., *The Journal of Physical Chemistry B* **2003,** *107* 4352-4355.
78. Xu, C.; Wang, L.; Mu, X.; Ding, Y., *Langmuir* **2010,** *26* 7437-7443.
79. Igarashi, H.; Fujino, T.; Zhu, Y.; Uchida, H.; Watanabe, M., *Physical Chemistry Chemical Physics* **2001,** *3* 306-314.
80. Demirci, U. B., *Journal of Power Sources* **2007,** *173* 11-18.
81. Stamenkovic, V. R.; Mun, B. S.; Arenz, M.; Mayrhofer, K. J. J.; Lucas, C. A.; Wang, G.; Ross, P. N.; Markovic, N. M., *Nature Materials* **2007,** *6* 241-247.

82. Wu, J.; Yang, H., *Accounts of Chemical Research* **2013,** *46* 1848-1857.
83. Stamenkovic, V. R.; Mun, B. S.; Mayrhofer, K. J. J.; Ross, P. N.; Markovic, N. M., *Journal of the American Chemical Society* **2006,** *128* 8813-8819.
84. Watanabe, M.; Uchida, H., Catalysts for the electro-oxidation of small molecules. In *Handbook of Fuel Cells*, John Wiley & Sons, Ltd: 2010.
85. Roth, C.; Benker, N.; Buhrmester, T.; Mazurek, M.; Loster, M.; Fuess, H.; Koningsberger, D. C.; Ramaker, D. E., *Journal of the American Chemical Society* **2005,** *127* 14607-14615.
86. Gojković, S. L.; Vidaković, T. R.; Đurović, D. R., *Electrochimica Acta* **2003,** *48* 3607-3614.
87. Zhou, W.; Zhou, Z.; Song, S.; Li, W.; Sun, G.; Tsiakaras, P.; Xin, Q., *Applied Catalysis B: Environmental* **2003,** *46* 273-285.
88. Permyakova, A. A.; Han, B.; Jensen, J. O.; Bjerrum, N. J.; Shao-Horn, Y., *The Journal of Physical Chemistry C* **2015,** *119* 8023-8031.
89. Huang, W.; Wang, H.; Zhou, J.; Wang, J.; Duchesne, P. N.; Muir, D.; Zhang, P.; Han, N.; Zhao, F.; Zeng, M.; Zhong, J.; Jin, C.; Li, Y.; Lee, S.-T.; Dai, H., *Nature Communications* **2015,** *6*.
90. Mavrikakis, M.; Hammer, B.; Nørskov, J. K., *Physical Review Letters* **1998,** *81* 2819-2822.
91. Qiu, J.-D.; Wang, G.-C.; Liang, R.-P.; Xia, X.-H.; Yu, H.-W., *The Journal of Physical Chemistry C* **2011,** *115* 15639-15645.
92. Guo, S.; Zhang, S.; Sun, X.; Sun, S., *Journal of the American Chemical Society* **2011,** *133* 15354-15357.
93. Huang, T.; Wang, X.; Zhuang, J.; Cai, W.-B.; Yu, A., *Electrochemical and Solid-State Letters* **2009,** *12* B112-B115.
94. Jeon, M. K.; Won, J. Y.; Lee, K. R.; Woo, S. I., *Electrochemistry Communications* **2007,** *9* 2163-2166.
95. Wang, Z.-B.; Yin, G.-P.; Shao, Y.-Y.; Yang, B.-Q.; Shi, P.-F.; Feng, P.-X., *Journal of Power Sources* **2007,** *165* 9-15.
96. Zhao, Y.; Tao, C.; Xiao, G.; Wei, G.; Li, L.; Liu, C.; Su, H., *Nanoscale* **2016,** *8* 5313-5326.
97. Banerjee, S.; Wong, S. S., *Journal of the American Chemical Society* **2004,** *126* 2073-2081.
98. Mao, Y.; Kanungo, M.; Hemraj-Benny, T.; Wong, S. S., *The Journal of Physical Chemistry B* **2006,** *110* 702-710.
99. Wang, L.; Zhang, Y.; Scofield, M. E.; Yue, S.; McBean, C.; Marschilok, A. C.; Takeuchi, K. J.; Takeuchi, E. S.; Wong, S. S., *ChemSusChem* **2015,** *8* 3304-3313.
100. Koenigsmann, C.; Zhou, W.-p.; Adzic, R. R.; Sutter, E.; Wong, S. S., *Nano Letters* **2010,** *10* 2806-2811.
101. Karmazyn, A. D.; Fiorin, V.; Jenkins, S. J.; King, D. A., *Surface Science* **2003,** *538* 171-183.
102. Hammer, B., *Topics in Catalysis 37* 3-16.
103. Kenjo, T., *Journal of The Electrochemical Society* **1985,** *132* 383-386.
104. Kiros, Y.; Schwartz, S., *Journal of Power Sources* **2000,** *87* 101-105.
105. Zhuang, Z.; Giles, S. A.; Zheng, J.; Jenness, G. R.; Caratzoulas, S.; Vlachos, D. G.; Yan, Y., *Nat Commun* **2016,** *7*.

106. Gasteiger, H. A.; Kocha, S. S.; Sompalli, B.; Wagner, F. T., *Applied Catalysis B: Environmental* **2005,** *56* 9-35.
107. Elbert, K.; Hu, J.; Ma, Z.; Zhang, Y.; Chen, G.; An, W.; Liu, P.; Isaacs, H. S.; Adzic, R. R.; Wang, J. X., *ACS Catalysis* **2015,** *5* 6764-6772.
108. Strmcnik, D.; Uchimura, M.; Wang, C.; Subbaraman, R.; Danilovic, N.; van der Vliet, D.; Paulikas, A. P.; Stamenkovic, V. R.; Markovic, N. M., *Nature Chemistry* **2013,** *5* 300-306.
109. Wang, Y.; Wang, G.; Li, G.; Huang, B.; Pan, J.; Liu, Q.; Han, J.; Xiao, L.; Lu, J.; Zhuang, L., *Energy & Environmental Science* **2015,** *8* 177-181.
110. Bard, A. J.; Faulkner, L. R., *ELECTROCHEMICAL METHODS: Fundamentals and Applications*. 2 ed.; JOHN WILEY & SONS, INC.: 2001.
111. Tarascon, J.-M.; Armand, M., *Nature* **2001,** *414* 359.
112. Tiano, A. L.; Papaefthymiou, G. C.; Lewis, C. S.; Han, J.; Zhang, C.; Li, Q.; Shi, C.; Abeykoon, A. M. M.; Billinge, S. J. L.; Stach, E.; Thomas, J.; Guerrero, K.; Munayco, P.; Munayco, J.; Scorzelli, R. B.; Burnham, P.; Viescas, A. J.; Wong, S. S., *Chemistry of Materials* **2015,** *27* 3572-3592.
113. Tiano, A. L.; Santulli, A. C.; Koenigsmann, C.; Feygenson, M.; Aronson, M. C.; Harrington, R.; Parise, J. B.; Wong, S. S., *Chemistry of Materials* **2011,** *23* 3277-3288.
114. Santulli, A. C.; Feygenson, M.; Camino, F. E.; Aronson, M. C.; Wong, S. S., *Chemistry of Materials* **2011,** *23* 1000-1008.
115. Patete, J. M.; Han, J.; Tiano, A. L.; Liu, H.; Han, M.-G.; Simonson, J. W.; Li, Y.; Santulli, A. C.; Aronson, M. C.; Frenkel, A. I.; Zhu, Y.; Wong, S. S., *The Journal of Physical Chemistry C* **2014,** *118* 21695-21705.
116. Lewis, C. S.; Wang, L.; Liu, H.; Han, J.; Wong, S. S., *Crystal Growth & Design* **2014,** *14* 3825-3838.
117. Han, J.; McBean, C.; Wang, L.; Jaye, C.; Liu, H.; Fischer, D. A.; Wong, S. S., *The Journal of Physical Chemistry C* **2015,** *119* 3826-3842.
118. Koenigsmann, C.; Semple, D. B.; Sutter, E.; Tobierre, S. E.; Wong, S. S., *ACS Applied Materials & Interfaces* **2013,** *5* 5518-5530.
119. Koenigsmann, C.; Sutter, E.; Adzic, R. R.; Wong, S. S., *The Journal of Physical Chemistry C* **2012,** *116* 15297-15306.
120. Domènech, B.; Bastos-Arrieta, J.; Amanda Alonso, J. M. s.; Muñoz, M.; Muraviev, D. N., *Bifunctional Polymer-Metal Nanocomposite Ion Exchange Materials*. InTech: 2012.
121. Byrappa, K.; Adschiri, T., *Progress in Crystal Growth and Characterization of Materials* **2007,** *53* 117-166.
122. Lu, A.-H.; Salabas, E. L.; Schüth, F., *Angewandte Chemie International Edition* **2007,** *46* 1222-1244.
123. Greene, L. E.; Law, M.; Goldberger, J.; Kim, F.; Johnson, J. C.; Zhang, Y.; Saykally, R. J.; Yang, P., *Angewandte Chemie International Edition* **2003,** *42* 3031-3034.
124. Zhang, C.; Zhu, Y., *Chemistry of Materials* **2005,** *17* 3537-3545.
125. Liang, Y.; Wang, H.; Sanchez Casalongue, H.; Chen, Z.; Dai, H., *Nano Research* **2010,** *3* 701-705.
126. Demir-Cakan, R.; Hu, Y.-S.; Antonietti, M.; Maier, J.; Titirici, M.-M., *Chemistry of Materials* **2008,** *20* 1227-1229.
127. Mao, Y.; Wong, S. S., *Journal of the American Chemical Society* **2006,** *128* 8217-8226.
128. Chen, C.; Dai, Q.; Miao, C.; Xu, L.; Song, H., *RSC Advances* **2015,** *5* 4844-4852.
129. Mao, Y.; Park, T.-J.; Zhang, F.; Zhou, H.; Wong, S. S., *Small* **2007,** *3* 1122-1139.

130. Segal, D., *Journal of Materials Chemistry* **1997,** *7* 1297-1305.
131. Lux, H., *Zeitschrift für Elektrochemie* **1939,** *45* 303-309.
132. Deng, H.; Qiu, Y.; Yang, S., *Journal of Materials Chemistry* **2009,** *19* 976-982.
133. Peng, R.; Wu, N.; Zheng, Y.; Huang, Y.; Luo, Y.; Yu, P.; Zhuang, L., *ACS Applied Materials & Interfaces* **2016,** *8* 8474-8480.
134. Tseng, L.-T.; Luo, X.; Bao, N.; Ding, J.; Li, S.; Yi, J., *Materials Letters* **2016,** *170* 142-146.
135. Chen, J.; Xing, X.; Watson, A.; Wang, W.; Yu, R.; Deng, J.; Yan, L.; Sun, C.; Chen, X., *Chemistry of Materials* **2007,** *19* 3598-3600.
136. Mao, Y.; Banerjee, S.; Wong, S. S., *Journal of the American Chemical Society* **2003,** *125* 15718-15719.
137. Cushing, B. L.; Kolesnichenko, V. L.; O'Connor, C. J., *Chemical Reviews* **2004,** *104* 3893-3946.
138. Livage, J.; Henry, M.; Sanchez, C., *Progress in Solid State Chemistry* **1988,** *18* 259-341.
139. Hench, L. L.; West, J. K., *Chemical Reviews* **1990,** *90* 33-72.
140. Niederberger, M., *Accounts of Chemical Research* **2007,** *40* 793-800.
141. Zorkipli, N. N. M.; Kaus, N. H. M.; Mohamad, A. A., *Procedia Chemistry* **2016,** *19* 626-631.
142. Rajammal, K.; Sivakumar, D.; Duraisamy, N.; Ramesh, K.; Ramesh, S., *Ionics* **2016,** 1-6.
143. de Biasi, R. S.; de Souza Lopes, R. D., *Ceramics International* **2016,** *42* 9315-9318.
144. Yang, H.; Duh, J.-G., *RSC Advances* **2016,** *6* 37160-37166.
145. Walker, J.; Bruce King, R.; Tannenbaum, R., *Journal of Solid State Chemistry* **2007,** *180* 2290-2297.
146. Koenigsmann, C.; Sutter, E.; Chiesa, T. A.; Adzic, R. R.; Wong, S. S., *Nano Letters* **2012,** *12* 2013-2020.
147. Lakshmi, B. B.; Patrissi, C. J.; Martin, C. R., *Chemistry of Materials* **1997,** *9* 2544-2550.
148. Limmer, S. J.; Seraji, S.; Wu, Y.; Chou, T. P.; Nguyen, C.; Cao, G. Z., *Advanced Functional Materials* **2002,** *12* 59-64.
149. Patete, J. M.; Scofield, M. E.; Volkov, V.; Koenigsmann, C.; Zhang, Y.; Marschilok, A. C.; Wang, X.; Bai, J.; Han, J.; Wang, L.; Wang, F.; Zhu, Y.; Graetz, J. A.; Wong, S. S., *Nano Research* **2015,** *8* 2573-2594.
150. Wang, X.; Li, Y., *Inorganic Chemistry* **2006,** *45* 7522-7534.
151. Tiano, A. L.; Koenigsmann, C.; Santulli, A. C.; Wong, S. S., *Chemical Communications* **2010,** *46* 8093-8130.
152. Gunnewiek, R. F. K.; Mendes, C. F.; Kiminami, R. H. G. A., *Advanced Powder Technology*.
153. Balamurugan, C.; Lee, D. W.; Maheswari, A. R.; Parmar, M., *RSC Advances* **2014,** *4* 54625-54630.
154. Wang, D.; Song, C., *The Journal of Physical Chemistry B* **2005,** *109* 12697-12700.
155. Scofield, M. E.; Koenigsmann, C.; Wang, L.; Liu, H.; Wong, S. S., *Energy & Environmental Science* **2015,** *8* 350-363.
156. Scofield, M. E.; Zhou, Y.; Yue, S.; Wang, L.; Su, D.; Tong, X.; Vukmirovic, M. B.; Adzic, R. R.; Wong, S. S., *ACS Catalysis* **2016,** 3895-3908.
157. Drenth, J., *Principles of Protein X-Ray Crystallography*. Springer-Verlag New York: New York, 2007; p XIV, 332.

158. Morgan, P.; Drews, J.; Dhiman, R.; Nielson, P., Nanostructured Materials in Different Dimensions for Sensing Applications. In *Nanotechnological Basis for Advanced Sensors*, Reithmaier, J. P.; Paunovic, P.; Kulisch, W.; Popov, C.; Petkov, P., Eds. Springer: 2011; p 257.
159. Goldstein, J., *Scanning Electron Microscopy and X-ray Microanalysis: Third Edition*. Plenum: 2003.
160. Leapman, R., EELS Quantitative Analysis. In *Transmission Electron Energy Loss Spectrometry in Materials Science and The EELS Atlas*, Wiley-VCH Verlag GmbH & Co. KGaA: 2005; pp 49-96.
161. von Harrach, H.; Klenov, D.; Freitag, B.; Schlossmacher, P.; Collins, P.; Fraser, H., *Microscopy and Microanalysis* **2010,** *16* 1312-1313.
162. Langmuir, I., *Journal of the American Chemical Society* **1916,** *38* 2221-2295.
163. Masel, R. I., *Principles of Adsorption and Reaction on Solid Surfaces*. Wiley Interscience: 1996.
164. Brunauer, S.; Emmett, P. H.; Teller, E., *Journal of the American Chemical Society* **1938,** *60* 309-319.
165. Bard, A.; Faulkner, L., *Electrochemical Methods: Fundamentals and Applications*. John Wiley & Sons, Inc: 2001.
166. Zhang, L. L.; Zhao, X. S., *Chemical Society Reviews* **2009,** *38* 2520-2531.
167. Parsons, R.; VanderNoot, T., *Journal of Electroanalytical Chemistry and Interfacial Electrochemistry* **1988,** *257* 9-45.
168. Motoo, S.; Furuya, N., *Journal of Electroanalytical Chemistry and Interfacial Electrochemistry* **1985,** *184* 303-316.
169. Yang, H.; Zhang, J.; Sun, K.; Zou, S.; Fang, J., *Angewandte Chemie International Edition* **2010,** *49* 6848-6851.
170. Jayaraman, S.; Jaramillo, T. F.; Baeck, S.-H.; McFarland, E. W., *The Journal of Physical Chemistry B* **2005,** *109* 22958-22966.
171. Liu, Z.; Ling, X. Y.; Su, X.; Lee, J. Y., *The Journal of Physical Chemistry B* **2004,** *108* 8234-8240.
172. Wang, J.; Xi, J.; Bai, Y.; Shen, Y.; Sun, J.; Chen, L.; Zhu, W.; Qiu, X., *Journal of Power Sources* **2007,** *164* 555-560.
173. Attard, G. A.; Brew, A.; Hunter, K.; Sharman, J.; Wright, E., *Physical Chemistry Chemical Physics* **2014,** *16* 13689-13698.
174. Rheinländer, P. J.; Herranz, J.; Durst, J.; Gasteiger, H. A., *Journal of The Electrochemical Society* **2014,** *161* F1448-F1457.
175. Schmidt, T. J.; Ross Jr, P. N.; Markovic, N. M., *Journal of Electroanalytical Chemistry* **2002,** *524–525* 252-260.
176. Yang, S.; Hong, F.; Wang, L.; Guo, S.; Song, X.; Ding, B.; Yang, Z., *The Journal of Physical Chemistry C* **2010,** *114* 203-207.
177. Liu, H.; Koenigsmann, C.; Adzic, R. R.; Wong, S. S., *ACS Catalysis* **2014,** *4* 2544-2555.
178. Atta, N. F.; Galal, A.; Ali, S. M., *International Journal of Electrochemical Science* **2012,** *7* 725-746.
179. Mayavan, S.; Mandalam, A.; Balasubramanian, M.; Sim, J.-B.; Choi, S.-M., *Materials Research Bulletin* **2015,** *67* 215-219.
180. Zhou, H.; Yiu, Y.; Aronson, M. C.; Wong, S. S., *Journal of Solid State Chemistry* **2008,** *181* 1539-1545.

181. Zhang, F.; Mao, Y.; Park, T.-J.; Wong, S. S., *Advanced Functional Materials* **2008,** *18* 103-112.
182. Duan, T. L.; Pan, J. S.; Ang, D. S., *ECS Journal of Solid State Science and Technology* **2015,** *4* P364-P368.
183. Song, Y.; Yang, S.; Zavalij, P. Y.; Whittingham, M. S., *Materials Research Bulletin* **2002,** *37* 1249-1257.
184. Yuan, L.-X.; Wang, Z.-H.; Zhang, W.-X.; Hu, X.-L.; Chen, J.-T.; Huang, Y.-H.; Goodenough, J. B., *Energy & Environmental Science* **2011,** *4* 269-284.
185. Choi, W. C.; Jeon, M. K.; Kim, Y. J.; Woo, S. I.; Hong, W. H., *Catalysis Today* **2004,** *93-95* 517-522.
186. Wasmus, S.; Küver, A., *Journal of Electroanalytical Chemistry* **1999,** *461* 14-31.
187. Kang, D. K.; Noh, C. S.; Kim, N. H.; Cho, S.-H.; Sohn, J. M.; Kim, T. J.; Park, Y.-K., *Journal of Industrial and Engineering Chemistry* **2010,** *16* 385-389.
188. Qiu, H.; Zou, F., *ACS Applied Materials & Interfaces* **2012,** *4* 1404-1410.
189. Joo, S. H.; Choi, S. J.; Oh, I.; Kwak, J.; Liu, Z.; Terasaki, O.; Ryoo, R., *Nature* **2001,** *412* 169-172.
190. Huang, T.; Liu, J.; Li, R.; Cai, W.; Yu, A., *Electrochemistry Communications* **2009,** *11* 643-646.
191. Long, N. V.; Yang, Y.; Thi, C. M.; Minh, N. V.; Cao, Y.; Nogami, M., *Nano Energy* **2013,** *2* 636-676.
192. Sieben, J. M.; Duarte, M. M. E., *International Journal of Hydrogen Energy* **2012,** *37* 9941-9947.
193. Gómez de la Fuente, J. L.; Martínez-Huerta, M. V.; Rojas, S.; Hernández-Fernández, P.; Terreros, P.; Fierro, J. L. G.; Peña, M. A., *Applied Catalysis B: Environmental* **2009,** *88* 505-514.
194. Ribeiro, V. A.; Correa, O. V.; Neto, A. O.; Linardi, M.; Spinacé, E. V., *Applied Catalysis A: General* **2010,** *372* 162-166.
195. Godoi, D. R. M.; Perez, J.; Villullas, H. M., *The Journal of Physical Chemistry C* **2009,** *113* 8518-8525.
196. Wang, H.; Alden, L. R.; DiSalvo, F. J.; Abruña, H. c. D., *Langmuir* **2009,** *25* 7725-7735.
197. Strasser, P.; Fan, Q.; Devenney, M.; Weinberg, W. H.; Liu, P.; Norskov, J. K., *The Journal of Physical Chemistry B* **2003,** *107* 11013-11021.
198. Velázquez-Palenzuela, A.; Brillas, E.; Arias, C.; Centellas, F.; Garrido, J. A.; Rodríguez, R. M.; Cabot, P.-L., *Journal of Power Sources* **2012,** *208* 306-315.
199. Liu, F.; Lee, J. Y.; Zhou, W. J., *Small* **2006,** *2* 121-128.
200. Wang, Z. B.; Yin, G. P.; Shi, P. F.; Sun, Y. C., *Electrochemical and Solid-State Letters* **2006,** *9* A13-A15.
201. Huang, T.; Liu, J.; Li, R.; Cai, W.; Yu, A., *Electrochemistry Communications* **2009,** *11* 643-646.
202. Strasser, P.; Fan, Q.; Devenney, M.; Weinberg, W. H.; Liu, P.; Nørskov, J. K., *The Journal of Physical Chemistry B* **2003,** *107* 11013-11021.
203. Kawaguchi, T.; Rachi, Y.; Sugimoto, W.; Murakami, Y.; Takasu, Y., *Journal of Applied Electrochemistry* **2006,** *36* 1117-1125.
204. Kageyama, S.; Murakami, A.; Ichikawa, S.; Seino, S.; Nakagawa, T.; Daimon, H.; Ohkubo, Y.; Kugai, J.; Yamamoto, T. A., *Journal of Materials Research* **2012,** *27* 1037-1045.
205. Koenigsmann, C.; Wong, S., *Energy and Environmental Science* **2011,** *4* 1045-1528.

206. Yuan, Q.; Huang, D.-B.; Wang, H.-H.; Zhou, Z.-Y., *Langmuir* **2014,** *30* 5711-5715.

207. Cademartiri, L.; Ozin, G. A., *Advanced Materials* **2009,** *21* 1013-1020.

208. Jeon, M. K.; Lee, K. R.; Daimon, H.; Nakahara, A.; Woo, S. I., *Catalysis Today* **2008,** 123-126.

209. Koenigsmann, C.; Scofield, M.; Liu, H.; Wong, S., *The Journal of Physical Chemistry Letters* **2012,** *3*.

210. Yang, S.; Hong, F.; Wang, L.; Guo, S.; Song, X.; Ding, B.; Yang, Z., *The Journal of Physical Chemistry C* **2009,** *114* 203-207.

211. Koenigsmann, C.; Santulli, A. C.; Gong, K.; Vukmirovic, M. B.; Zhou, W.-p.; Sutter, E.; Wong, S. S.; Adzic, R. R., *Journal of the American Chemical Society* **2011,** *133* 9783-9795.

212. Antolini, E., *Materials Chemistry and Physics* **2003,** *78* 563-573.

213. Toda, T.; Igarashi, H.; Uchida, H.; Watanabe, M., *Journal of The Electrochemical Society* **1999,** *146* 3750-3756.

214. Xu, C.; Li, Q.; Liu, Y.; Wang, J.; Geng, H., *Langmuir* **2012,** *28* 1886-1892.

215. Strasser, P.; Koh, S.; Anniyev, T.; Greeley, J.; More, K.; Yu, C.; Liu, Z.; Kaya, S.; Nordlund, D.; Ogasawara, H.; Toney, M. F.; Nilsson, A., *Nature Chemistry* **2010,** 454-460.

216. Toda, T.; Igarashi, H.; Watanabe, M., *Journal of The Electrochemical Society* **1998,** *145* 4185-4188.

217. Stolbov, S.; Ortigoza, M. A.; Adzic, R.; Rahman, T. S., *The Journal of Chemical Physics* **2009,** *130* 124714/1-124714/5.

218. Sasaki, K.; Wang, J. X.; Balasubramanian, M.; McBreen, J.; Uribe, F.; Adzic, R. R., *Electrochimica Acta* **2004,** *49* 3873-3877.

219. Zhang, X.; Zhang, F.; Guan, R.-F.; Chan, K.-Y., *Materials Research Bulletin* **2007,** *42* 327-333.

220. Ehteshami, S. M. M.; Jia, Q.; Halder, A.; Chan, S. H.; Mukerjee, S., *Electrochimica Acta* **2013,** *107* 155-163.

221. Zhong, W. H.; Liu, Y. X.; Zhang, D. J., *Journal of Physical Chemistry C* **2012,** *116* 2994-3000.

222. Yuan, D.; Gong, X.; Wu, R., *Journal of Chemical Physics* **2008,** *128* 064706.

223. Rossmeisl, J.; Ferrin, P.; Tritsaris, G. A.; Nilekar, A. U.; Koh, S.; Bae, S. E.; Brankovic, S. R.; Strasser, P.; Mavrikakis, M., *Energy and Environmental Science* **2012,** *5* 8335-8342.

224. Wang, H.; Loffler, T.; Baltruschat, H., *Journal of Applied Electrochemistry* **2001,** *31* 759-765.

225. Wang, S.; Jiang, S. P.; Wang, X.; Guo, J., *Electrochimica Acta* **2011,** *56* 1563-1569.

226. Si, F.; Ma, L.; Liu, C.; Zhang, X.; Xing, W., *RSC Advances* **2012,** 401-403.

227. Xia, B. Y.; Wu, H. B.; Yan, Y.; Lou, X. W. D.; Wang, X., *Journal of the American Chemical Society* **2013,** *135* 9480-9485.

228. Lai, S. C. S.; Lebedeva, N. P.; Housmans, T. H. M.; Koper, M. T. M., *Topics in Catalysis* **2007,** *46* 320-333.

229. Xu, J.; Yuan, D.; Yang, F.; Mei, D.; Zhang, Z.; Chen, Y.-X., *Physical Chemistry Chemical Physics* **2013,** *15* 4367-4376.

230. Antolini, E.; Gonzalez, E. R., *Journal of Power Sources* **2010,** *195* 3431-3450.

231. Durst, J.; Siebel, A.; Simon, C.; Hasche, F.; Herranz, J.; Gasteiger, H. A., *Energy and Environmental Science* **2014,** *7* 2255-2260.

232. Sheng, W.; Gasteiger, H. A.; Shao-Horn, Y., *Journal of the Electrochemical Society* **2010,** *157* B1529-B1536.

233. Markovic, N.; Gasteiger, H.; Ross, P. N., *Journal of the Electrochemical Society* **1997,** *144* 1591-1597.
234. Strmcnik, D.; Uchimura, M.; Wang, C.; Subbaraman, R.; Danilovic, N.; van der Vliet, D.; Paulikas, A. P.; Stamenkovic, V. R.; Markovic, N. M., *Nature Chemistry.* **2013,** *5* 300-306.
235. Ribeiro, V. A.; Correa, O. V.; Neto, A. O.; Linardi, M.; Spinacé, E. V., *Applied Catalysis, A* **2010,** *372* 162-166.
236. Qiu, H.; Zou, F., *ACS Applied Materials & Interfaces* **2012,** *4* 1404-1410.
237. Kitchin, J. R.; Nørskov, J. K.; Barteau, M. A.; Chen, J. G., *Journal of Chemical Physics* **2004,** *120* 10240-10246.
238. Mavrikakis, M.; Hammer, B.; Nørskov, J. K., *Physical Review Letters* **1998,** *81* 2819-2822.
239. Jia, Q.; Liang, W.; Bates, M. K.; Mani, P.; Lee, W.; Mukerjee, S., *ACS Nano* **2015,** *9* 387-400.
240. Ruban, A.; Hammer, B.; Stoltze, P.; Skriver, H. L.; Nørskov, J. K., *Journal of Molecular Catalysis A: Chemical* **1997,** *115* 421-429.
241. Jia, Q.; Segre, C. U.; Ramaker, D.; Caldwell, K.; Trahan, M.; Mukerjee, S., *Electrochimica Acta* **2013,** *88* 604-613.
242. Greeley, J.; Mavrikakis, M., *Nature Materials* **2004,** *3* 810-815.
243. Kandoi, S.; Ferrin, P. A.; Mavrikakis, M., *Topics in Catalysis* **2010,** *53* 384-392.
244. Skúlason, E.; Tripkovic, V.; Björketun, M. E.; Gudmundsdóttir, S.; Karlberg, G.; Rossmeisl, J.; Bligaard, T.; Jónsson, H.; Nørskov, J. K., *Journal of Physical Chemstry C* **2010,** *114* 18182-18197.
245. Elbert, K.; Hu, J.; Ma, Z.; Zhang, Y.; Chen, G.; An, W.; Liu, P.; Isaacs, H. S.; Adzic, R. R.; Wang, J. X., *ACS Catalysis* **2015,** *5* 6764-6772.
246. Chen, J. G.; Menning, C. A.; Zellner, M. B., *Surface Science Reports* **2008,** *63* 201-254.
247. Ferrin, P.; Kandoi, S.; Nilekar, A. U.; Mavrikakis, M., *Surface Science* **2012,** *606* 679-689.
248. Cademartiri, L.; Ozin, G. A., *Advanced Materials* **2009,** *21* 1013-1020.
249. Koenigsmann, C.; Scofield, M. E.; Liu, H.; Wong, S. S., *Journal of Physical Chemstry Letters* **2012,** *3* 3385-3398.
250. Koenigsmann, C.; Santulli, A. C.; Gong, K.; Vukmirovic, M. B.; Zhou, W.-p.; Sutter, E.; Wong, S. S.; Adzic, R. R., *Journal of the Amercian Chemical Society* **2011,** *133* 9783-9795.
251. Liu, H.; Li, L.; Scofield, M. E.; Wong, S. S., *APL Materials* **2015,** *3* 1-15.
252. Song, Y.; Garcia, R. M.; Dorin, R. M.; Wang, H.; Qiu, Y.; Coker, E. N.; Steen, W. A.; Miller, J. E.; Shelnutt, J. A., *Nano Letters* **2007,** *7* 3650-3655.
253. Yang, S.; Hong, F.; Wang, L.; Guo, S.; Song, X.; Ding, B.; Yang, Z., *Journal of Physical Chemistry C* **2010,** *114* 203-207.
254. Long, N. V.; Yang, Y.; Minh Thi, C.; Minh, N. V.; Cao, Y.; Nogami, M., *Nano Energy* **2013,** *2* 636-676.
255. Huang, T.; Liu, J.; Li, R.; Cai, W.; Yu, A., *Electrochemical Communications* **2009,** *11* 643-646.
256. Sieben, J. M.; Duarte, M. M. E., *International Journal of Hydrogen Energy* **2012,** *37* 9941-9947.
257. Zheng, J.-N.; Li, S.-S.; Ma, X.; Chen, F.-Y.; Wang, A.-J.; Chen, J.-R.; Feng, J.-J., *Journal of Matererials Chemistry A* **2014,** *2* 8386-8395.
258. Kang, W.; Li, R.; Wei, D.; Xu, S.; Wei, S.; Li, H., *RSC Advances* **2015,** *5* 94210-94215.

259. Chou, H.-Y.; Yeh, T.-K.; Tsai, C.-H., *International Journal of Electrochemical Science* **2014,** *9* 5763-5775.
260. Chaisubanan, N.; Pruksathorn, K.; Vergnes, H.; Senocq, F.; Hunsom, M., *International Journal of Electrochemical Science* **2016,** *11* 1012-1028.
261. Jeon, M. K.; Zhang, Y.; McGinn, P. J., *Electrochimica Acta* **2010,** *55* 5318-5325.
262. Chen, D.; Zhao, Y.; Peng, X.; Wang, X.; Hu, W.; Jing, C.; Tian, S.; Tian, J., *Electrochimica Acta* **2015,** *177* 86-92.
263. Li, J.; Wang, G.; Wang, J.; Miao, S.; Wei, M.; Yang, F.; Yu, L.; Bao, X., *Nano Research* **2014,** *7* 1519-1527.
264. Li, J.; Fu, X.; Mao, Z.; Yang, Y.; Qiu, T.; Wu, Q., *Nanoscale Research Letters* **2016,** *11* 1-8.
265. Hsu, S.-P.; Liu, C.-W.; Chen, H.-S.; Chen, T.-Y.; Lai, C.-M.; Lee, C.-H.; Lee, J.-F.; Chan, T.-S.; Tsai, L.-D.; Wang, K.-W., *Electrochimica Acta* **2013,** *105* 180-187.
266. Loukrakpam, R.; Shan, S.; Petkov, V.; Yang, L.; Luo, J.; Zhong, C.-J., *Journal of Physical Chemistry C* **2013,** *117* 20715-20721.
267. Song, P.; Mei, L.-P.; Wang, A.-J.; Fang, K.-M.; Feng, J.-J., *International Journal of Hydrogen Energy* **2016,** *41* 1645-1653.
268. García-Contreras, M. A.; Fernández-Valverde, S. M.; Vargas-García, J. R.; Cortés-Jácome, M. A.; Toledo-Antonio, J. A.; Ángeles-Chavez, C., *International Journal of Hydrogen Energy* **2008,** *33* 6672-6680.
269. Zhao, Y.; Fan, L.; Ren, J.; Hong, B., *International Journal of Hydrogen Energy* **2014,** *39* 4544-4557.
270. Hong, W.; Wang, J.; Wang, E., *Nano Research* **2015,** *8* 2308-2316.
271. Sheng, W.; Zhuang, Z.; Gao, M.; Zheng, J.; Chen, J. G.; Yan, Y., *Nature Communications* **2015,** *6* 1-6.
272. St. John, S.; Atkinson, R. W.; Unocic, K. A.; Unocic, R. R.; Zawodzinski, T. A.; Papandrew, A. B., *ACS Catalysis* **2015,** *5* 7015-7023.
273. Farias, M. J. S.; Vidal-Iglesias, F. J.; Solla-Gullón, J.; Herrero, E.; Feliu, J. M., *Journal of Electroanalitical Chemistry* **2014,** *716* 16-22.
274. Davies, J. C.; Hayden, B. E.; Pegg, D. J., *Surface Science* **2000,** *467* 118-130.
275. Rheinländer, P. J.; Herranz, J.; Durst, J.; Gasteiger, H. A., *Journal of the Electrochemical Society* **2014,** *161* F1448-F1457.
276. Wang, J. X.; Springer, T. E.; Adzic, R. R., *Journal of the Electrochemical Society* **2006,** *153* A1732-A1740.
277. St. John, S.; Atkinson, R. W.; Unocic, R. R.; Zawodzinski, T. A.; Papandrew, A. B., *Journal of Physical Chemistry C* **2015,** *119* 13481-13487.
278. Oezaslan, M.; Hasché, F.; Strasser, P., *Journal of the Electrochemical Society* **2012,** *159* B444-B454.
279. Alia, S. M.; Pivovar, B. S.; Yan, Y., *Journal of the American Chemical Society* **2013,** *135* 13473-13478.
280. Zhang, X.; Yu, S.; Qiao, L.; Zheng, W.; Liu, P., *Journal of Chemical Physics* **2015,** *142* 1-9.
281. Angerstein-Kozlowska, H.; Conway, B. E.; Hamelin, A., *J. Electroanal. Chem.* **1990,** *277* 233-252.
282. Henning, S.; Herranz, J.; Gasteiger, H. A., *Journal of the Electrochemical Society* **2015,** *162* F178-F189.

283. Kulesza, P. J.; Pieta, I. S.; Rutkowska, I. A.; Wadas, A.; Marks, D.; Klak, K.; Stobinski, L.; Cox, J. A., *Electrochimica Acta* **2013,** *110* 474-483.
284. Campelo, J. M.; Luna, D.; Luque, R.; Marinas, J. M.; Romero, A. A., *ChemSusChem* **2009,** *2* 18-45.
285. Lasch, K.; Hayn, G.; Jörissen, L.; Garche, J.; Besenhardt, O., *Journal of Power Sources* **2002,** *105* 305-310.
286. Hua, H.; Hu, C.; Zhao, Z.; Liu, H.; Xie, X.; Xi, Y., *Electrochimica Acta* **2013,** *105* 130-136.
287. Macak, J. M.; Barczuk, P. J.; Tsuchiya, H.; Nowakowska, M. Z.; Ghicov, A.; Chojak, M.; Bauer, S.; Virtanen, S.; Kulesza, P. J.; Schmuki, P., *Electrochemistry Communications* **2005,** *7* 1417-1422.
288. Hepel, M.; Kumarihamy, I.; Zhong, C. J., *Electrochemistry Communications* **2006,** *8* 1439-1444.
289. Zhao, G.; Zhang, L.; Sun, K.; Li, H., *Journal of Power Sources* **2014,** *245* 892-897.
290. Cao, L.; Scheiba, F.; Roth, C.; Schweiger, F.; Cremers, C.; Stimming, U.; Fuess, H.; Chen, L.; Zhu, W.; Qiu, X., *Angewandte Chemie International Edition* **2006,** *45* 5315-5319.
291. Santos, A. L.; Profeti, D.; Olivi, P., *Electrochimica Acta* **2005,** *50* 2615-2621.
292. Gercher, V. A.; Cox, D. F.; Themlin, J.-M., *Surface Science* **1994,** *306* 279-293.
293. Saha, M. S.; Li, R.; Sun, X., *Electrochemistry Communications* **2007,** *9* 2229-2234.
294. Penner, S.; Armbrüster, M., *ChemCatChem* **2015,** *7* 374-392.
295. Lan, A.; Mukasyan, A. S., *Industrial & Engineering Chemistry Research* **2008,** *47* 8989-8994.
296. Shi, F.; Baker, L. R.; Hervier, A.; Somorjai, G. A.; Komvopoulos, K., *Nano Letters* **2013,** *13* 4469-4474.
297. Lewera, A.; Timperman, L.; Roguska, A.; Alonso-Vante, N., *The Journal of Physical Chemistry C* **2011,** *115* 20153-20159.
298. Timperman, L.; Lewera, A.; Vogel, W.; Alonso-Vante, N., *Electrochemistry Communications* **2010,** *12* 1772-1775.
299. Hayek, K.; Kramer, R.; Paál, Z., *Applied Catalysis A: General* **1997,** *162* 1-15.
300. Lan, A.; Mukasyan, A. S., *The Journal of Physical Chemistry C* **2007,** *111* 9573-9582.
301. White, J. H.; Sammells, A. F., *Journal of The Electrochemical Society* **1993,** *140* 2167-2177.
302. Peña, M. A.; Fierro, J. L. G., *Chemical Reviews* **2001,** *101* 1981-2018.
303. Sauvet, A. L.; Fouletier, J.; Gaillard, F.; Primet, M., *Journal of Catalysis* **2002,** *209* 25-34.
304. Ponce, S.; Peña, M. A.; Fierro, J. L. G., *Applied Catalysis B: Environmental* **2000,** *24* 193-205.
305. Wang, H.; Lu, J.; Marshall, C. L.; Elam, J. W.; Miller, J. T.; Liu, H.; Enterkin, J. A.; Kennedy, R. M.; Stair, P. C.; Poeppelmeier, K. R.; Marks, L. D., *Catalysis Today* **2014,** *237* 71-79.
306. Hasa, B.; Kalamaras, E.; Papaioannou, E. I.; Sygellou, L.; Katsaounis, A., *International Journal of Hydrogen Energy* **2013,** *38* 15395-15404.
307. Santulli, A. C.; Koenigsmann, C.; Tiano, A. L.; DeRose, D.; Wong, S. S., *Nanotechnology* **2011,** *22* 1-13.
308. Sugimoto, W.; Kizaki, T.; Yokoshima, K.; Murakami, Y.; Takasu, Y., *Electrochimica Acta* **2004,** *49* 313-320.

309. Long, J. W.; Swider, K. E.; Merzbacher, C. I.; Rolison, D. R., *Langmuir* **1999,** *15* 780-785.
310. Guan, X.; Guo, L., *ACS Catalysis* **2014,** *4* 3020-3026.
311. Xian, T.; Yang, H., *Advanced Materials Research* **2011,** *418-420* 18-21.
312. Li, M.; Liu, P.; Adzic, R. R., *The Journal of Physical Chemistry Letters* **2012,** *3* 3480-3485.
313. Hepel, T.; Pollak, F. H.; O'Grady, W. E., *Journal of The Electrochemical Society* **1984,** *131* 2094-2100.
314. Vukmirovic, M. B.; Liu, P.; Muckerman, J. T.; Adzic, R. R., *The Journal of Physical Chemistry C* **2007,** *111* 15306-15311.
315. Selvaganesh, S. V.; Selvarani, G.; Sridhar, P.; Pitchumani, S.; Shukla, A. K., *Journal of The Electrochemical Society* **2012,** *159* B463-B470.
316. Zhou, J. G.; Fang, H. T.; Hu, Y. F.; Sham, T. K.; Wu, C. X.; Liu, M.; Li, F., *The Journal of Physical Chemistry C* **2009,** *113* 10747-10750.
317. Liu, X.; Pichler, T.; Knupfer, M.; Fink, J.; Kataura, H., *Physical Review B* **2004,** *70* 205405.
318. Lewera, A.; Zhou, W. P.; Hunger, R.; Jaegermann, W.; Wieckowski, A.; Yockel, S.; Bagus, P. S., *Chemical Physics Letters* **2007,** *447* 39-43.
319. Liao, L.; Mai, H. X.; Yuan, Q.; Lu, H. B.; Li, J. C.; Liu, C.; Yan, C. H.; Shen, Z. X.; Yu, T., *The Journal of Physical Chemistry C* **2008,** *112* 9061-9065.
320. Bisht, A.; Zhang, P.; Shivakumara, C.; Sharma, S., *The Journal of Physical Chemistry C* **2015,** *119* 14126-14134.
321. Briggs, D.; Seah, M. P., *Auger and X-ray Photoelectron Spectroscopy*. 2 ed.; Wiley: New York, 1990; Vol. 1.
322. Wakisaka, M.; Mitsui, S.; Hirose, Y.; Kawashima, K.; Uchida, H.; Watanabe, M., *The Journal of Physical Chemistry B* **2006,** *110* 23489-23496.
323. Petrović, S.; Rakić, V.; Jovanović, D. M.; Baričević, A. T., *Applied Catalysis B: Environmental* **2006,** *66* 249-257.
324. Suffredini, H. B.; Tricoli, V.; Vatistas, N.; Avaca, L. A., *Journal of Power Sources* **2006,** *158* 124-128.
325. Masud, J.; Alam, M. T.; Awaludin, Z.; El-Deab, M. S.; Okajima, T.; Ohsaka, T., *Journal of Power Sources* **2012,** *220* 399-404.
326. Franceschini, E. A.; Bruno, M. M.; Williams, F. J.; Viva, F. A.; Corti, H. R., *ACS Applied Materials & Interfaces* **2013,** *5* 10437-10444.
327. Guo, J. W.; Zhao, T. S.; Prabhuram, J.; Chen, R.; Wong, C. W., *Electrochimica Acta* **2005,** *51* 754-763.
328. Kabbabi, A.; Faure, R.; Durand, R.; Beden, B.; Hahn, F.; Leger, J. M.; Lamy, C., *Journal of Electroanalytical Chemistry* **1998,** *444* 41-53.
329. Padhi, A. K.; Nanjundaswamy, K. S.; Masquelier, C.; Okada, S.; Goodenough, J. B., *Journal of The Electrochemical Society* **1997,** *144* 1609-1613.
330. Padhi, A. K.; Nanjundaswamy, K. S.; Goodenough, J. B., *Journal of The Electrochemical Society* **1997,** *144* 1188-1194.
331. Sides, C. R.; Croce, F.; Young, V. Y.; Martin, C. R.; Scrosati, B., *Electrochemical and Solid-State Letters* **2005,** *8* A484-A487.
332. Huang, X.; Yan, S.; Zhao, H.; Zhang, L.; Guo, R.; Chang, C.; Kong, X.; Han, H., *Materials Characterization* **2010,** *61* 720-725.

333. Chung, S.-Y.; Bloking, J. T.; Chiang, Y.-M., *Nature Materials* **2002,** *1* 123-128.
334. Xu, B.; Qian, D.; Wang, Z.; Meng, Y. S., *Materials Science and Engineering: R: Reports* **2012,** *73* 51-65.
335. Whittingham, M. S., *Chemical Reviews* **2004,** *104* 4271-4302.
336. Yi, T.-F.; Li, X.-Y.; Liu, H.; Shu, J.; Zhu, Y.-R.; Zhu, R.-S., *Ionics* **2012,** *18* 529-539.
337. Lee, K. T.; Jeong, S.; Cho, J., *Accounts of Chemical Research* **2013,** *46* 1161-1170.
338. Ellis, B.; Kan, W. H.; Makahnouk, W. R. M.; Nazar, L. F., *Journal of Materials Chemistry* **2007,** *17* 3248-3254.
339. Lee, M.-H.; Kim, T.-H.; Kim, Y. S.; Song, H.-K., *The Journal of Physical Chemistry C* **2011,** *115* 12255-12259.
340. Zheng, J.-c.; Li, X.-h.; Wang, Z.-x.; Guo, H.-j.; Zhou, S.-y., *Journal of Power Sources* **2008,** *184* 574-577.
341. Franger, S.; Le Cras, F.; Bourbon, C.; Rouault, H., *Journal of Power Sources* **2003,** *119–121* 252-257.
342. Arnold, G.; Garche, J.; Hemmer, R.; Ströbele, S.; Vogler, C.; Wohlfahrt-Mehrens, M., *Journal of Power Sources* **2003,** *119–121* 247-251.
343. Prosini, P. P.; Carewska, M.; Scaccia, S.; Wisniewski, P.; Passerini, S.; Pasquali, M., *Journal of The Electrochemical Society* **2002,** *149* A886-A890.
344. Kim, J.-K.; Choi, J.-W.; Chauhan, G. S.; Ahn, J.-H.; Hwang, G.-C.; Choi, J.-B.; Ahn, H.-J., *Electrochimica Acta* **2008,** *53* 8258-8264.
345. Hwang, B.-J.; Hsu, K.-F.; Hu, S.-K.; Cheng, M.-Y.; Chou, T.-C.; Tsay, S.-Y.; Santhanam, R., *Journal of Power Sources* **2009,** *194* 515-519.
346. Saravanan, K.; Balaya, P.; Reddy, M. V.; Chowdari, B. V. R.; Vittal, J. J., *Energy & Environmental Science* **2010,** *3* 457-463.
347. Chen, Z.-y.; Zhu, W.; Zhu, H.-l.; Zhang, J.-l.; Li, Q.-f., *Transactions of Nonferrous Metals Society of China* **2010,** *20* 809-813.
348. Liu, X.-h.; Wang, J.-q.; Zhang, J.-y.; Yang, S.-r., *Chinese Journal of Chemical Physics* **2006,** *19* 530-534.
349. Wang, G.; Shen, X.; Yao, J., *Journal of Power Sources* **2009,** *189* 543-546.
350. Teng, F.; Santhanagopalan, S.; Lemmens, R.; Geng, X.; Patel, P.; Meng, D. D., *Solid State Sciences* **2010,** *12* 952-955.
351. Zhu, C.; Yu, Y.; Gu, L.; Weichert, K.; Maier, J., *Angewandte Chemie International Edition* **2011,** *50* 6278-6282.
352. Koenigsmann, C.; Wong, S. S., *Energy & Environmental Science* **2011,** *4* 1161 - 1176.
353. Mao, Y.; Zhang, F.; Wong, S., *Advanced Materials* **2006,** *18* 1895-1899.
354. Santulli, A. C.; Feygenson, M.; Camino, F. E.; Aronson, M. C.; Wong, S. S., *Chemistry of Materials* **2011,** *23* 1000-1008.
355. Zhang, F.; Sfeir, M. Y.; Misewich, J. A.; Wong, S. S., *Chemistry of Materials* **2008,** *20* 5500-5512.
356. Zhang, F.; Wong, S. S., *Chemistry of Materials* **2009,** *21* 4541-4554.
357. Zhou, H.; Park, T.-J.; Wong, S. S., *Journal of Materials Research* **2006,** *21* 2941-2947.
358. Zhou, H.; Wong, S. S., *ACS Nano* **2008,** *2* 944-958.
359. Zhou, H.; Zhou, W.-p.; Adzic, R. R.; Wong, S. S., *Journal of Physical Chemistry C* **2009,** *113* 5460-5466.
360. Fisher, C. A. J.; Hart Prieto, V. M.; Islam, M. S., *Chemistry of Materials* **2008,** *20* 5907-5915.

361. Morgan, D.; Van der Ven, A.; Ceder, G., *Electrochemical and Solid-State Letters* **2004,** *7* A30-A32.
362. Hong, Y.-S.; Ryu, K. S.; Park, Y. J.; Kim, M. G.; Lee, J. M.; Chang, S. H., *Journal of Materials Chemistry* **2002,** *12* 1870-1874.
363. Kim, S.-W.; Ryu, J.; Park, C. B.; Kang, K., *Chemical Communications* **2010,** *46* 7409-7411.
364. Liu, Y.; Xu, Y.; Han, X.; Pellegrinelli, C.; Zhu, Y.; Zhu, H.; Wan, J.; Chung, A. C.; Vaaland, O.; Wang, C.; Hu, L., *Nano Letters* **2012,** *12* 5664-5668.
365. Patete, J. M.; Peng, X.; Koenigsmann, C.; Xu, Y.; Karn, B.; Wong, S. S., *Green Chemistry* **2011,** *13* 482-519.
366. Koenigsmann, C.; Santulli, A. C.; Sutter, E.; Wong, S. S., *ACS Nano* **2011,** *5* 7471-7487.
367. Park, T. J.; Mao, Y. B.; Wong, S. S., *Chemical Communications* **2004,** 2708-2709.
368. Hernandez-Sanchez, B. A.; Chang, K.-S.; Scancella, M. T.; Burris, J. L.; Kohli, S.; Fisher, E. R.; Dorhout, P. K., *Chemistry of Materials* **2005,** *17* 5909-5919.
369. Yang, Z.; Huang, Y.; Dong, B.; Li, H. L.; Shi, S. Q., *Applied Physics A* **2006,** *84* 117-122.
370. Kuang, Q.; Lin, Z.-W.; Lian, W.; Jiang, Z.-Y.; Xie, Z.-X.; Huang, R.-B.; Zheng, L.-S., *Journal of Solid State Chemistry* **2007,** *180* 1236-1242.
371. Zhang, F.; Wong, S. S., *ACS Nano* **2009,** *4* 99-112.
372. Koenigsmann, C.; Wong, S. S., *ACS Catalysis* **2013,** *3* 2031-2040.
373. Park, T.-J.; Mao, Y.; Wong, S. S., *Chemical Communications* **2004,** 2708-2709.
374. Koenigsmann, C.; Sutter, E.; Adzic, R. R.; Wong, S. S., *Journal of Physical Chemistry C* **2012,** *116* 15297-15306.
375. Wang, B.; Qiu, Y.; Ni, S., *Solid State Ionics* **2007,** *178* 843-847.
376. Galoustov, K.; Anthonisen, M.; Ryan, D. H.; MacNeil, D. D., *Journal of Power Sources* **2011,** *196* 6893-6897.
377. Islam, M. S.; Driscoll, D. J.; Fisher, C. A. J.; Slater, P. R., *Chemistry of Materials* **2005,** *17* 5085-5092.
378. Nan, C.; Lu, J.; Li, L.; Li, L.; Peng, Q.; Li, Y., *Nano Research* **2013,** *6* 469-477.
379. Chung, S.-Y.; Choi, S.-Y.; Yamamoto, T.; Ikuhara, Y., *Angewandte Chemie International Edition* **2009,** *48* 543-546.
380. Yang, S.; Song, Y.; Zavalij, P. Y.; Stanley Whittingham, M., *Electrochemistry Communications* **2002,** *4* 239-244.
381. Chen, J.; Graetz, J., *ACS Applied Materials & Interfaces* **2011,** *3* 1380-1384.
382. Axmann, P.; Stinner, C.; Wohlfahrt-Mehrens, M.; Mauger, A.; Gendron, F.; Julien, C. M., *Chemistry of Materials* **2009,** *21* 1636-1644.
383. Lee, M.-H.; Kim, T.-H.; Kim, Y. S.; Park, J.-S.; Song, H.-K., *Journal of Materials Chemistry* **2012,** *22* 8228-8234.
384. Gaberscek, M.; Dominko, R.; Jamnik, J., *Electrochemistry Communications* **2007,** *9* 2778-2783.
385. Kou, X.-j.; Ke, H.; Zhu, C.-b.; Rolfe, P., *Chemical Physics* **2015,** *446* 1-6.
386. Manivasakan, P.; Ramasamy, P.; Kim, J., *Nanoscale* **2014,** *6* 9665-9672.
387. Tu, Z.; Nath, P.; Lu, Y.; Tikekar, M. D.; Archer, L. A., *Accounts of Chemical Research* **2015,** *48* 2947-2956.
388. Peng, Z.; Yi, X.; Liu, Z. X.; Shang, J.; Wang, D., *ACS Applied Materials & Interfaces* **2016**.

389. Sheng, W.; Bivens, A. P.; Myint, M.; Zhuang, Z.; Forest, R. V.; Fang, Q.; Chen, J. G.; Yan, Y., *Energy & Environmental Science* **2014,** *7* 1719-1724.
390. Manivasakan, P.; Ramasamy, P.; Kim, J., *Nanoscale* **2014,** *6* 9665-9672.
391. Dimakis, N.; Flor, F. A.; Navarro, N. E.; Salgado, A.; Smotkin, E. S., *The Journal of Physical Chemistry C* **2016,** *120* 10427-10441.
392. Kim, J. H.; Kwon, S. Y.; Bhattacharjya, D.; Chai, G. S.; Yu, J.-S., *Journal of Catalysis* **2013,** *306* 133-145.
393. Zhao, P.; Xu, W.; Hua, X.; Luo, W.; Chen, S.; Cheng, G., *The Journal of Physical Chemistry C* **2016,** *120* 11006-11013.
394. Alia, S. M.; Yan, Y., *Journal of The Electrochemical Society* **2015,** *162* F849-F853.
395. St. John, S.; Atkinson, R. W.; Unocic, K. A.; Unocic, R. R.; Zawodzinski, T. A.; Papandrew, A. B., *ACS Catalysis* **2015,** *5* 7015-7023.
396. Zhang, N.; Guo, S.; Zhu, X.; Guo, J.; Huang, X., *Chemistry of Materials* **2016**.
397. Zhao, Y.; Liu, J.; Liu, C.; Wang, F.; Song, Y., *ACS Catalysis* **2016,** 4127-4134.
398. Wang, Q.-L.; Fang, R.; He, L.-L.; Feng, J.-J.; Yuan, J.; Wang, A.-J., *Journal of Alloys and Compounds* **2016**.
399. Liang, Y.; Wei, J.; Zhang, X.; Zhang, J.; Jiang, S. P.; Wang, H., *ChemCatChem* **2016,** *8* 1-5.
400. Zhang, W.; Yao, Q.; Wu, X.; Fu, Y.; Deng, K.; Wang, X., *Electrochimica Acta* **2016,** *200* 131-141.
401. Zhang, X.; Zhu, J.; Tiwary, C. S.; Ma, Z.; Huang, H.; Zhang, J.; Lu, Z.; Huang, W.; Wu, Y., *ACS Applied Materials & Interfaces* **2016,** *8* 10858-10865.
402. Nan, L.; Fan, Z.; Yue, W.; Dong, Q.; Zhu, L.; Yang, L.; Fan, L., *Journal of Materials Chemistry A* **2016,** *4* 8898-8904.
403. Li, L.; Qian, Y.; Yang, J.; Tan, X.; Dai, Z.; Jin, Y.; Wang, H.; Qu, W.; Chu, Y., *International Journal of Hydrogen Energy* **2016,** *41* 9284-9294.
404. Zhao, S.; Yin, H.; Du, L.; He, L.; Zhao, K.; Chang, L.; Yin, G.; Zhao, H.; Liu, S.; Tang, Z., *ACS Nano* **2014,** *8* 12660-12668.
405. Wang, M.-Q.; Yang, W.-H.; Wang, H.-H.; Chen, C.; Zhou, Z.-Y.; Sun, S.-G., *ACS Catalysis* **2014,** *4* 3928-3936.
406. Liang, J.; Zhou, R. F.; Chen, X. M.; Tang, Y. H.; Qiao, S. Z., *Advanced Materials* **2014,** *26* 6074-6079.
407. Deng, D.; Yu, L.; Chen, X.; Wang, G.; Jin, L.; Pan, X.; Deng, J.; Sun, G.; Bao, X., *Angewandte Chemie International Edition* **2013,** *52* 371-375.
408. Dong, Q.; Zhuang, X.; Li, Z.; Li, B.; Fang, B.; Yang, C.; Xie, H.; Zhang, F.; Feng, X., *Journal of Materials Chemistry A* **2015,** *3* 7767-7772.
409. Fu, Y.; Wei, Q.; Lu, B.; Wang, X.; Sun, S., *Journal of Alloys and Compounds*.
410. Kim, M.-S.; Kim, H.-K.; Lee, S.-W.; Kim, D.-H.; Ruan, D.; Chung, K. Y.; Lee, S. H.; Roh, K. C.; Kim, K.-B., *Scientific Reports* **2016,** *6* 26686.
411. Marka, S. K.; Petnikota, S.; Vadali, S. V. S. S.; Reddy, M. V. V.; Adams, S.; Chowdari, B. V. R., *RSC Advances* **2016**.
412. Sun, Y.; Zhao, C.; Shen, M.; Pan, Z.; Liu, X., *Journal of Alloys and Compounds* **2016,** *683* 191-197.
413. Li, M.; Liu, P.; Adzic, R. R., *The Journal of Physical Chemistry Letters* **2012,** *3* 3480-3485.

414. Liang, W.-I.; Zhang, X.; Zan, Y.; Pan, M.; Czarnik, C.; Bustillo, K.; Xu, J.; Chu, Y.-H.; Zheng, H., *Journal of the American Chemical Society* **2015,** *137* 14850-14853.